

# **Sonic Boom Minimization through Vehicle Shape Optimization and Probabilistic Acoustic Propagation**

A Dissertation  
Presented to  
The Academic Faculty

by

**Sriram Rallabhandi**

In Partial Fulfillment  
of the Requirements for the Degree  
Doctor of Philosophy

School of Aerospace Engineering  
Georgia Institute of Technology  
April 2005

Copyright © 2005 by Sriram Rallabhandi

# Sonic Boom Minimization through Vehicle Shape Optimization and Probabilistic Acoustic Propagation

Approved by:

Dr. Dimitri N. Mavris, Advisor  
College of Engineering  
*Georgia Institute of Technology*

Dr. Daniel Schrage  
College of Engineering  
*Georgia Institute of Technology*

Dr. Lakshmi Sankar  
College of Engineering  
*Georgia Institute of Technology*

Mr. Robert Wolz  
*Gulfstream Aerospace Corporation*

Dr. Krishan Ahuja  
College of Engineering  
*Georgia Institute of Technology*

Date Approved: April 15, 2005

*To my parents and brother, people who have supported me throughout my  
life.*

# ACKNOWLEDGEMENTS

First and foremost, I want to thank my advisor Dr. Dimitri Mavris for giving me this opportunity to come and work in Aerospace Systems Design Lab at Georgia Tech. I want to thank my committee members, Dr. Sankar, Dr. Ahuja, Dr. Schrage and Mr. Robert Wolz who have agreed to be on my thesis committee..

There are so many people in ASDL who have helped and influenced my work that I'm afraid I might forget someone. If I do forget someone, please accept my apologies in advance. First and foremost, I want to thank Rob McDonald for the suggestions, ideas, enthusiasm and guidance he provided me from the very beginning in Aerodynamics and other design studies. My first team project at Georgia Tech, the AIAA graduate aircraft design competition helped me to get along and communicate with other team members and induced a team spirit in me. I'm glad Nick Borer and Erol Cagatay were in my team. I had a great time during that project and learned quite a lot from that experience. I would like to thank Michael Buonanno for allowing me to borrow some of his work. I wish to thank Peter DeBaets, Peter Hollingsworth, Brian German, Travis Danner, Bryce Roth, Yongjun Zhao, Chirag Patel, Michelle Kirby, Dan Delaurentis, Eunsuk Yang, Neil Weston and many others at ASDL who have helped me in one way or other during my stay here.

I'm very thankful to Suraj Unnikrishnan for all the fruitful discussions I had with him. He helped in many ways and I thoroughly enjoyed the late afternoon coffee breaks I had with him everyday in the last 2 years. Ramachandra Sattigeri provided me with various political and technical perspectives to various things and I am thankful for that. It was a good reprieve from the gruelling research work. He is a great source of information on most day to day topics.

I have had so many room mates during my four and half year stay here. I would like to thank my room mates, current and ex, Yuvraj Dhillon, Aditya Utturwar, Vijay Ganugapati, Naveen Gopal, Amol Kane, Vijay Kasi and Chirag Patel for all their support. I would also

like to take this opportunity to thank my cousin, Nittala Lakshminarayana, for all the advice and suggestions he gave me during my stay here at Georgia Tech.

Finally, I would like to thank my parents and my brother who have supported through out my life. They stood by me and encouraged me at every step of my life. This thesis would not have been possible without their loving support and help. Thank you.

# TABLE OF CONTENTS

<b>DEDICATION</b>	<b>iii</b>
<b>ACKNOWLEDGEMENTS</b>	<b>iv</b>
<b>LIST OF TABLES</b>	<b>x</b>
<b>LIST OF FIGURES</b>	<b>xi</b>
<b>LIST OF SYMBOLS OR ABBREVIATIONS</b>	<b>xv</b>
<b>SUMMARY</b>	<b>xvii</b>
<b>CHAPTER 1 INTRODUCTION</b>	<b>1</b>
1.1 Motivation	1
1.1.1 Preliminary Aerodynamic Design	3
1.1.2 Sonic boom near-field prediction tools	6
1.1.3 Atmospheric propagation	8
1.1.4 Sonic Boom Minimization	12
1.2 Optimization techniques	14
1.3 Basic foundations and assumptions	16
1.4 Research Questions	19
<b>CHAPTER 2 BACKGROUND</b>	<b>20</b>
2.1 Linearized near field prediction	23
2.1.1 Equivalent area due to volume and wave drag estimation	26
2.1.2 Equivalent area due to Lift	27
2.2 Far field pressure propagation	28
2.3 Complete linearized sonic boom prediction	32
2.4 Sonic boom minimization	32
2.5 Miscellaneous design studies	39
2.6 Industry designs and knowledge base	41
2.6.1 Concorde	41
2.6.2 Aerion Design	43
2.6.3 Gulfstream Design	44

2.6.4	Lockheed-Martin Design . . . . .	46
2.6.5	Other Designs . . . . .	47
<b>CHAPTER 3</b>	<b>IMPROVED DESIGN TOOLS . . . . .</b>	<b>48</b>
3.1	Geometry generation . . . . .	48
3.1.1	Bezier Curves . . . . .	51
3.1.2	NURBS surfaces . . . . .	53
3.1.3	Using Bezier and NURBS surfaces in geometry generation . . . . .	57
3.1.4	Other Nose cone shapes . . . . .	59
3.2	Surface refinement and discretization . . . . .	59
3.3	Improvements to the equivalent area estimation . . . . .	63
3.4	Automatic CFD transfer capability . . . . .	67
3.5	Validation of the improved tools . . . . .	70
3.6	Pressure propagation . . . . .	71
3.6.1	PCBOOM . . . . .	71
3.7	Effect of Nacelle Interference . . . . .	74
3.8	Perceived loudness minimization tool . . . . .	78
3.8.1	Modifications to the SGD analysis . . . . .	84
3.8.2	Validation of the SGD analysis method . . . . .	90
3.8.3	Additional insights of modified SGD analysis . . . . .	95
3.9	Optimization tool . . . . .	97
3.10	Summary of improved tools . . . . .	98
<b>CHAPTER 4</b>	<b>IMPLEMENTATION DETAILS AND FRAMEWORK FOR- MULATION . . . . .</b>	<b>100</b>
4.1	Metamodelling . . . . .	100
4.1.1	Response Surface Equations . . . . .	100
4.1.2	Kriging and co-kriging . . . . .	101
4.1.3	Neural Networks . . . . .	103
4.2	Metamodel estimation of minimum area distribution . . . . .	105
4.2.1	SGD analysis approximation . . . . .	106
4.2.2	Modified SGD approximation . . . . .	110

4.3	Parallelization . . . . .	116
4.3.1	Message Passing Interface . . . . .	116
4.3.2	Coarse grained Parallel Genetic Algorithms . . . . .	117
4.4	Probabilistic and statistical propagation . . . . .	118
4.4.1	Anderson-Darling test statistic . . . . .	118
4.5	PROBLEM FORMULATION . . . . .	120
4.5.1	Analysis Constraints . . . . .	120
4.5.2	Direct Design . . . . .	122
4.5.3	Bi-level Reverse Design . . . . .	123
4.6	Hierarchical cross-over operation . . . . .	124
4.7	Optimization flowcharts . . . . .	126
4.7.1	Direct Design . . . . .	126
4.7.2	Bi-level reverse design . . . . .	126
4.8	Proof of concept - SSBD . . . . .	128
<b>CHAPTER 5</b>	<b>SHAPE OPTIMIZATION RESULTS . . . . .</b>	<b>132</b>
5.1	Direct optimization . . . . .	132
5.2	Bi-level reverse optimization from SGD perspective . . . . .	136
5.2.1	Using SGD analysis . . . . .	137
5.2.2	Using generalized SGD analysis . . . . .	141
5.3	Low boom designs under varying conditions . . . . .	152
5.4	Final comments . . . . .	154
<b>CHAPTER 6</b>	<b>CONCLUSIONS AND RECOMMENDATIONS . . . . .</b>	<b>158</b>
6.1	Summary of research contributions . . . . .	158
6.2	Answering Research questions through the results obtained . . . . .	159
6.2.1	Improved geometry handling (Question 1) . . . . .	159
6.2.2	Improvements in near field prediction tools (Question 2) . . . . .	159
6.2.3	Pressure propagation tools(Question 3) . . . . .	160
6.2.4	Sonic boom minimization technique (Question 4) . . . . .	161
6.2.5	Generalized SGD equations for Sonic Boom minimization (Question 5)	161
6.2.6	Flexible design framework (Question 6) . . . . .	161



6.3	Recommendations . . . . .	162
6.3.1	Variable Fidelity Optimization . . . . .	162
6.3.2	Near field approximation improvements . . . . .	164
6.3.3	Inverse Design . . . . .	165
6.3.4	Indoor and other effects . . . . .	165
6.3.5	Practical considerations . . . . .	166
<b>APPENDIX A</b>	<b>AIRCRAFT EQUIVALENT AREA REPRESENTATION</b>	<b>167</b>
<b>APPENDIX B</b>	<b>WHITHAM'S F-FUNCTION . . . . .</b>	<b>171</b>
<b>APPENDIX C</b>	<b>MATLAB CODE FOR MODIFIED SGD ANALYSIS . .</b>	<b>179</b>
<b>APPENDIX D</b>	<b>MATLAB CODE FOR NEURAL NETWORK APPROX- IMATION . . . . .</b>	<b>187</b>
<b>REFERENCES</b>	<b>. . . . .</b>	<b>190</b>
<b>VITA</b>	<b>. . . . .</b>	<b>200</b>

# LIST OF TABLES

1	Discrete parameters . . . . .	50
2	Important continuous parameters . . . . .	50
3	Varying knot vectors for B-spline basis . . . . .	55
4	Sample values of design variables for NURBS nose cone . . . . .	58
5	Inputs and outputs for a sample run . . . . .	85
6	Fixed values of some parameters for sample run . . . . .	88
7	Variable values in sample run comparison . . . . .	89
8	Comparison of outputs for different F-functions . . . . .	90
9	Inputs for test case 1 . . . . .	91
10	Additional inputs for modified SGD analysis . . . . .	91
11	Comparison of original analysis with modified SGD analyses . . . . .	92
12	Comparison of original analysis with modified SGD analyses . . . . .	93
13	Effect of varying slopes in F-function . . . . .	96
14	Ranges for SGD input variables . . . . .	106
15	Ranges for modified SGD input variables . . . . .	113
16	Various implementations of MPI . . . . .	117
17	Geometric constraints . . . . .	121
18	Different tools and their functions . . . . .	127
19	Ranges of design variables for step 1 . . . . .	137
20	Variable Ranges for parameters modified SGD optimization . . . . .	142
21	Final loudness values . . . . .	146
22	DoE table inputs and outputs . . . . .	157
23	Inputs and outputs for the Program . . . . .	180

# LIST OF FIGURES

1	Great circle distance of 5000nm from select cities [119] . . . . .	2
2	Different stages of design [68] . . . . .	5
3	Typical aerodynamic design process [47] . . . . .	5
4	Poor geometry representation . . . . .	7
5	Geometry representation by Harris wave drag code . . . . .	8
6	Parametric atmospheric temperature model . . . . .	10
7	Joint probability distribution of the overpressure and loudness levels . . . . .	11
8	A sample sonic boom signature . . . . .	13
9	Comparison of the actual and standard temperature profile in Atlanta . . . . .	18
10	Shock coalescence during boom propagation [76] . . . . .	22
11	Ray tube area changes in different planes [30] . . . . .	29
12	Theory of atmospheric propagation [30] . . . . .	29
13	Pressure signature as seen by waveform parameter method . . . . .	30
14	Comparison of focused U-wave and conventional N-wave . . . . .	31
15	Computation of shock location . . . . .	34
16	Comparison of two different F-functions . . . . .	35
17	F-function shape for minimizing pressure rise . . . . .	37
18	Concorde layout [19] . . . . .	42
19	Reduction in Sonic Boom overpressure level just from size reduction [81] . . . . .	43
20	Aerion Design for SBJ [1] . . . . .	44
21	Expected loudness gains from Gulfstream QSP study [131] . . . . .	45
22	Gulfstream Design for QSP [39] . . . . .	45
23	Lockheed-SAI QSST Design [99] . . . . .	46
24	Expected loudness gains from Lockheed-SAI QSST study [100] . . . . .	47
25	Sample Wire-frame geometry generated by the parametric geometry generation tool . . . . .	51
26	Sample Bezier curve . . . . .	52
27	Sample Airfoil Bezier curve . . . . .	52
28	B-spline basis dependence on knot vector . . . . .	54

29	Local control of B-splines . . . . .	55
30	Rational B-spline basis of order 4 . . . . .	56
31	Local control of B-splines . . . . .	57
32	Side view of some nose cone NURBS surfaces . . . . .	58
33	Sample sketch showing parameters for nose cone . . . . .	59
34	Sears-Haack nose . . . . .	60
35	Wire-frame geometry and its refined counterpart . . . . .	61
36	Triangulated individual components of aircraft . . . . .	62
37	Fully triangulated aircraft . . . . .	63
38	Equivalent area due to volume comparison for a Sears-Haack body . . . . .	64
39	Sample wing-body-canard geometry . . . . .	65
40	Equivalent area due to volume comparison on a wing-body-canard geometry . . . . .	65
41	Equivalent area due to volume for geometries with engines . . . . .	66
42	Pressure contours obtained from Cartesian CFD solver . . . . .	68
43	Residual history of the flow solution . . . . .	69
44	Iteration history of the drag coefficient . . . . .	69
45	Discretized Sears-Haack body . . . . .	70
46	Random atmospheric Wind profiles . . . . .	72
47	Hyperbolic shock structure . . . . .	74
48	Near field signature with nacelle under the wing . . . . .	75
49	Near field signature with a nacelle on top of wing . . . . .	76
50	Two configuration differing only in the nacelle location . . . . .	76
51	Comparison of equivalent area for top and bottom nacelles . . . . .	77
52	Ground pressure signature comparison . . . . .	78
53	Sample SGD F-function shape for minimizing pressure perturbations . . . . .	85
54	Sample SGD total equivalent area distribution . . . . .	86
55	Sonic Boom minimization strategy [73] . . . . .	86
56	New F-function . . . . .	87
57	Modifications to the original S-G-D F-function . . . . .	89
58	Corresponding ground pressure signatures . . . . .	90

59	Comparison of F-functions for case 1 . . . . .	92
60	Comparison of total equivalent areas for case 1 . . . . .	93
61	Comparison of F-functions for case 2 . . . . .	94
62	Comparison of total equivalent areas for case 2 . . . . .	94
63	Sample F-functions with varying slopes . . . . .	95
64	Sample ground signatures with varying slopes . . . . .	96
65	Sketch of NSGA II . . . . .	98
66	Performance of NSGA on a two objective optimization problem . . . . .	99
67	Artificial Neuron . . . . .	104
68	Single hidden layer Neural Network . . . . .	104
69	Neural Network training for SGD equations . . . . .	108
70	Neural Network testing for SGD equations . . . . .	109
71	Expected vs. Predicted plot for H . . . . .	110
72	Expected vs. Predicted plot for C . . . . .	111
73	Expected vs. Predicted plot for D . . . . .	111
74	Expected vs. Predicted plot for $\lambda$ . . . . .	112
75	Expected vs. Predicted plot for $Y_r$ . . . . .	112
76	Neural Network training for modified SGD equations . . . . .	114
77	Neural Network testing for modified SGD equations . . . . .	115
78	The perceived loudness level from CDF . . . . .	120
79	Sample Cross-over . . . . .	125
80	Sample Crossover sketch . . . . .	125
81	Flow chart of the optimization process . . . . .	126
82	Reverse design: Step 1 . . . . .	127
83	Reverse Design: Step 2 . . . . .	128
84	Modified F-5E . . . . .	129
85	Equivalent area due to volume for Modified F-5E . . . . .	130
86	Boom signature comparison . . . . .	131
87	Some configurations from the initial population . . . . .	133
88	Progression of populations through generations . . . . .	134

89	Best Designs from direct optimization . . . . .	135
90	Iteration history of the minimum loudness at each generation . . . . .	135
91	Pareto-front for the first step of optimization . . . . .	138
92	The target equivalent area distribution chosen for step 2 . . . . .	139
93	Comparison of total equivalent areas . . . . .	139
94	Pareto-front for the second step of optimization . . . . .	140
95	Three candidate configurations in the Pareto-front . . . . .	141
96	Speed-up of the Parallel GA . . . . .	142
97	Pareto-front for the first step of optimization . . . . .	143
98	Iteration history of the minimum PLdB at each generation . . . . .	144
99	The optimum F-function chosen from step 1 . . . . .	144
100	The target equivalent area distribution chosen for step 2 . . . . .	145
101	The ground pressure signature . . . . .	145
102	Area perturbations . . . . .	147
103	Comparison of F-functions corresponding to perturbed area distributions . .	148
104	Comparison of ground signatures corresponding to perturbed area distributions	148
105	Pareto front of the Nose matching . . . . .	149
106	Comparison of total equivalent areas after nose area matching . . . . .	150
107	Pareto front after perturbing wing and tail geometries . . . . .	151
108	Comparison of final total equivalent areas . . . . .	151
109	Four view sketch of one of the best designs . . . . .	152
110	Comparison of F-functions . . . . .	153
111	Comparison of ground signatures . . . . .	153
112	Prediction profiler for the responses . . . . .	155
113	Conical domain of dependence . . . . .	167
114	Mach plane replacing Mach cones . . . . .	169
115	F-function rear shock characteristics [129] . . . . .	176
116	F-function with a kink in rear region [129] . . . . .	177

# LIST OF SYMBOLS OR ABBREVIATIONS

$\alpha, B, C, D$	Parameters in F-function signature.
$\alpha_a$	Angle of attack.
$\alpha_y$	Non-linear advance of the acoustic rays.
$\beta$	$\sqrt{M^2 - 1}$ .
$\delta A$	Sum of squared error of area distributions.
$\delta p$	Local pressure perturbation.
$\frac{p_f}{p_r}$	Ratio of front to rear shocks in boom signature.
$\gamma$	Ratio of specific heats 1.4.
$\lambda$	Axial position at which F-function becomes negative.
$\phi$	Perturbation potential.
$\rho$	Local density.
$A$	Total equivalent area.
$A^2$	Anderson-Darling test statistic.
$b_1$	Input layer bias vector.
$b_2$	Output layer bias vector.
$CAD$	Computer Aided Design.
$Camb$	Camber function of nose cone.
$Cdia$	Cabin Diameter.
$CFD$	Computational Fluid Dynamics.
$d_1, d_2, \dots d_m$	Discrete shape parameters.
$D_w$	Wave drag at zero lift.
$DARPA$	The Defense Advanced Research Projects Agency.
$f$	Lineal source density.
$F$	F-function.
$FoM$	Seebass-George Figure of Merit.
$G$	Area of F-function to front balance point.
$GTS$	GNU Triangulated Surface library.

$H$	Width of forward spike in F-function.
$h$	Flight altitude.
$HSCT$	High Speed Civil Transport.
$l$	Length of the body.
$M$	Mach number.
$NASA$	National Aeronautics and Space Administration.
$NASCART$	Numerical Aerodynamic Simulation via CARTesian Grid Techniques.
$NSGA$	Non-dominated Sorting Genetic Algorithm.
$NV$	Hidden layer network weights.
$NW$	Output layer network weights.
$Nx$	Neural Network inputs.
$p_0$	Reference pressure.
$P_c$	Critical Probability.
$PDE$	Partial Differential Equation.
$PLdB$	Perceived loudness level dB.
$QSP$	Quiet Supersonic Platform.
$r$	Radial distance.
$RA$	Ray tube area.
$S$	Projected Mach plane intersection area.
$s_1, s_2, \dots s_n$	Continuous shape parameters.
$SL$	Slope of balancing line.
$U$	Local free-stream velocity.
$W$	Weight of aircraft.
$x, s$	Axial Locations.
$x_n$	Angle of attack corrected axial locations.
$y_f$	Width of forward spike in F-function.
$y_r$	Position of rear area balancing.
$yN$	Neural Network outputs.



# SUMMARY

Future aircraft designs should overcome technical challenges like sonic-boom annoyance if they are to fly at supersonic speeds over land. The first step towards that goal is to shape the aircraft so that the flow field shock structure does not cause loud bangs on the ground. Choosing the right shape reflecting the design requirements is a fundamental and most important step which is usually over simplified in the conceptual stages of design by resorting to a qualitative selection of a baseline configuration. Linearized methods or non-linear CFD tools are then used on this baseline configuration to adjust the shape to optimize the design objectives. While this may seem to be an acceptable approach, minor shape modifications of a baseline configuration may not yield a large improvement in the objectives, especially when the baseline is chosen without a rigorous analysis procedure.

The main objective of this work is the development of an automated design framework that encompasses numerous varying fidelity tools to conduct aerodynamic shape optimization in conceptual stages of design. The framework is formulated as a combination of four basic steps.

The first step involves geometry generation and discretization. Geometry generation is accomplished using shape parameters for each component. This component decomposition allows for local shape control. Discretization involves component agglomeration using efficient geometric algorithms. This unique and powerful procedure provides adequate flexibility and control desired for down-selecting configurations from a vast design space. The second step is the near field prediction which involves calculation of the pressure perturbation around the body. For the purpose of performing linearized analysis, an equivalent area approach is used, except now the true geometry would be used instead of the usual wire-frame approximation. The third step is a novel probabilistic procedure. This entails parameterizing atmospheric temperature and wind profiles using random variables and performing acoustic propagation to yield a probabilistic estimate of the loudness metric using

statistical techniques. The sensitivity of the sonic boom ground signature to the atmospheric parameters can be measured.

The fourth and final step is the actual shape optimization procedure. In this study, parallel genetic algorithms have been used for optimization because they are capable of achieving the global optima without requiring sensitivity derivatives. Two different approaches are studied. The first one is that of direct design where the shape of the aircraft is modified based on the objective function values. This is called the direct optimization procedure. The second approach is a reverse optimization technique where the shape of the aircraft is changed based on the nearness to an intermediate function or a target value or distribution that drives the shape of the aircraft.

The results of these approaches are presented and discussed. The salient features of the final designs are explained. Future research recommendations are made.

# CHAPTER I

## INTRODUCTION

Aircraft design is a complex procedure wherein numerous analyses and sub-systems come together synergistically to yield a final aircraft system. The design process is guided by the design requirements. For supersonic aircraft, the requirements are extremely stringent due to the 1) formation and propagation of shock waves to the ground leading to community annoyance and 2) engine emissions, generated by the enormous amounts of fuel burnt to produce the required amount of thrust, causing an undesirable environmental impact. In addition to these, there are other subsonic and supersonic requirements which have to be satisfied.

Aircraft designers in the past have relied on analytical solutions to arrive at optimal shapes, for example, the Sears-Haack body for minimum wave drag in supersonic flow. However, such an approach compromises other metrics in a multi-objective scheme and most often over-simplifies the design process. The design process brings together various disciplines and weighs them according to the design requirements. Therefore, aircraft shapes which offer the best compromise between various disciplines may have to be solved numerically and are not readily available as various analytical shapes. The technique of obtaining a suitable aircraft shape to meet the design requirements came to be known as shape optimization and today it is one of the most researched areas in aircraft and configuration design. After it had been introduced, numerous research efforts have been undertaken to obtain the best shape of an aircraft in order to meet various requirements and constraints.

### ***1.1 Motivation***

According to market studies conducted by various organizations [22], there is a need for an efficient, low noise airplane that could travel at high transonic speeds or supersonic speeds. If efficient supersonic travel were possible, it would dramatically cut down the flight time.

Figure 1 [119] shows the great circle distance of 5000nm from select cities in the United States. This figure shows that most of the world, except South Asia and Australia, can be reached with this range. Significant time savings could be achieved with non-stop flights from continental USA to countries in Europe and Japan. However, to compete with the subsonic market, supersonic travel should be comparably priced. This means that the operating costs for supersonic travel should not be substantially higher than those for subsonic travel. These considerations lead to many challenges in supersonic flight. There have been many studies conducted in the past to overcome the challenges associated with commercial supersonic flight. The most important of these challenges are minimization of sonic boom, engine emissions and airport noise [108] while maintaining the required performance metrics. During the high speed research initiative, *NASA* concluded that a commercial transport sized aircraft cannot be reshaped to have acceptable sonic boom signature without revolutionary advances in various technologies. To provide a successful stepping stone for future supersonic research, many of the recent studies have concentrated on achieving acceptable sonic boom levels for small supersonic business jets. This is because smaller aircraft have lesser weight and thus produce lower sonic boom levels. This is explained in detail in the next chapter.

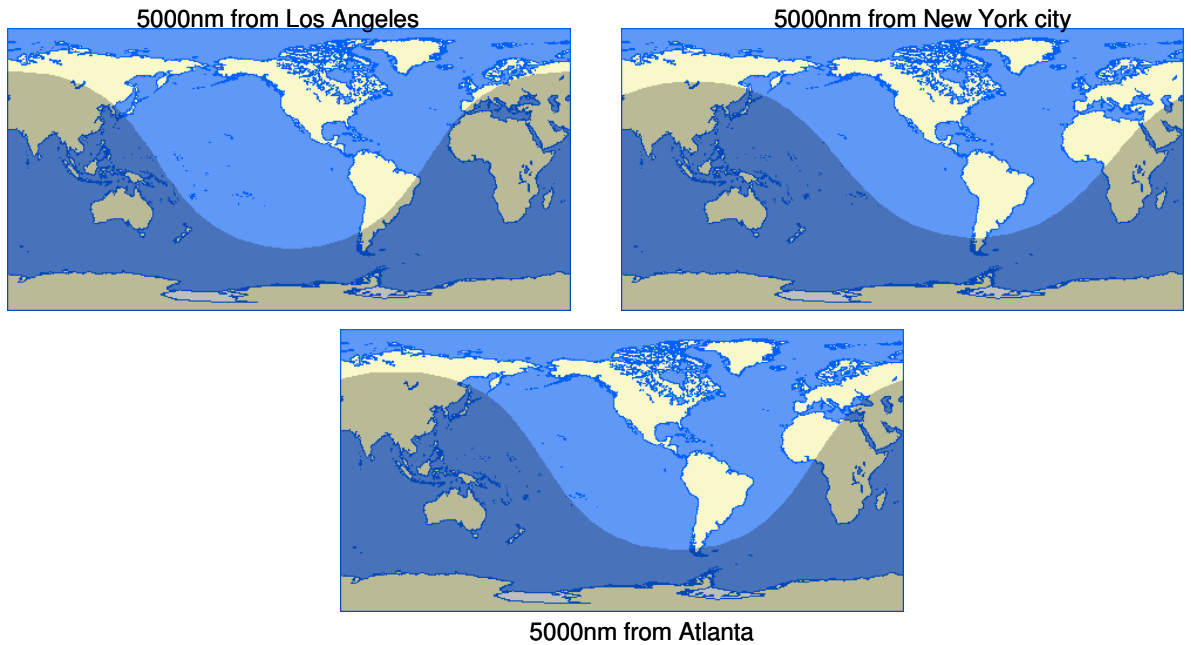


**Figure 1:** Great circle distance of 5000nm from select cities [119]

Most of the research efforts have focused on changing an accepted baseline configuration to meet the requirements using computational fluid dynamics. No significant efforts have been undertaken to down-select the optimum aircraft shapes from a large domain of possible shapes in the conceptual phases of design. One of the main objectives of this thesis is to compress the vast design space up-front to a manageable size to be then passed over to the preliminary design where high fidelity CFD techniques could be used. Thus, this thesis contributes to the development of conceptual design of supersonic aircraft by examining and analyzing alternative and novel computational strategies including improved linearized tools and efficient geometric algorithms.

### **1.1.1 Preliminary Aerodynamic Design**

Of all the challenges posed by commercial supersonic flight, the most important aspect perhaps is that of efficient aerodynamic design for sonic boom mitigation. The field of aerodynamic design has been studied from the beginning of this century. However, with the ever increasing computational power available to designers, new methods and solution strategies for efficient and accurate prediction of aerodynamic loads are still being proposed. Geometry holds the key to an efficient aerodynamic design. The conceptual design phase should be carried out carefully so as to explore the vast design space. Such an exploration may not be feasible in further stages of design due to the extremely high computational costs involved. Using these new techniques in the early phases of design could lead to significant improvements in the overall design cycle of the aircraft because better point of departure designs could be created very early in the design cycle using the improved strategies.

Before presenting a new conceptual architecture for designing supersonic aircraft for sonic boom reduction, it seems appropriate to look into the aspects of traditional design process. In a traditional design process, simple analyses are initially applied to the proposed concept and in the later stages of design, advanced computational aerodynamic packages are used. Most of the advanced analyses are multidisciplinary in nature with iterations between aerodynamics, structures, flight mechanics and propulsion. Multidisciplinary analysis is computationally very intensive and is dependent upon the concept provided from the initial

stages. Thus, one cannot overlook the role played by the conceptual design.

Figure 2 presents a classic chart showing the different stages of design. In this figure, the dashed lines represent the design process as has been carried out in the past and the solid lines represent a notional future design strategy. Many important shortcomings of the traditional design process can be observed from this chart. In the initial stages, the designer has a lot of design freedom to choose the best possible configuration. As design progresses into later stages, this freedom is reduced and the cost committed is increased. The designer should have a thorough knowledge of the effect of various aspects on the performance of the system to make a judicious choice as to what portion of the design space has to be discarded and what is to be retained. This choice is based on the analyses tools used in the conceptual stages. As seen from the dashed lines, using the existing design set-up, the designer loses much of the design freedom and creates a huge cost overhead without knowing much about the system. The aim of the future design strategies should be to use better analyses methods up-front so that more is known about the system. In addition, a thorough design space exploration should be performed so as to improve the design freedom. Doing this would imply that feasible designs are carried on to further stages without discarding them and thus would lead to an improved design freedom. This new paradigm would allow the designer to avoid serious and costly alterations in design in the later stages. It would also ensure that a bigger design space is explored.

Figure 3 shows the aerodynamic design process followed in the industry and academia. There are three major feedback loops. The inner loop is an aerodynamic design loop involving just the computational aerodynamic tools, the outer loop is a multi-disciplinary loop comprising analyses from other disciplines such as aero-elasticity and finally the major design cycle loop involves wind tunnel testing in addition to the aerodynamics and other disciplines. The starting point of this aerodynamic optimization process is the configuration provided by the conceptual analyses.

If the overall time in the above loops has to be minimized, conceptual level analysis codes have to be improved to provide reasonably accurate initial solutions to reflect the design requirements so that costly iterations could be minimized. It is to be noted that

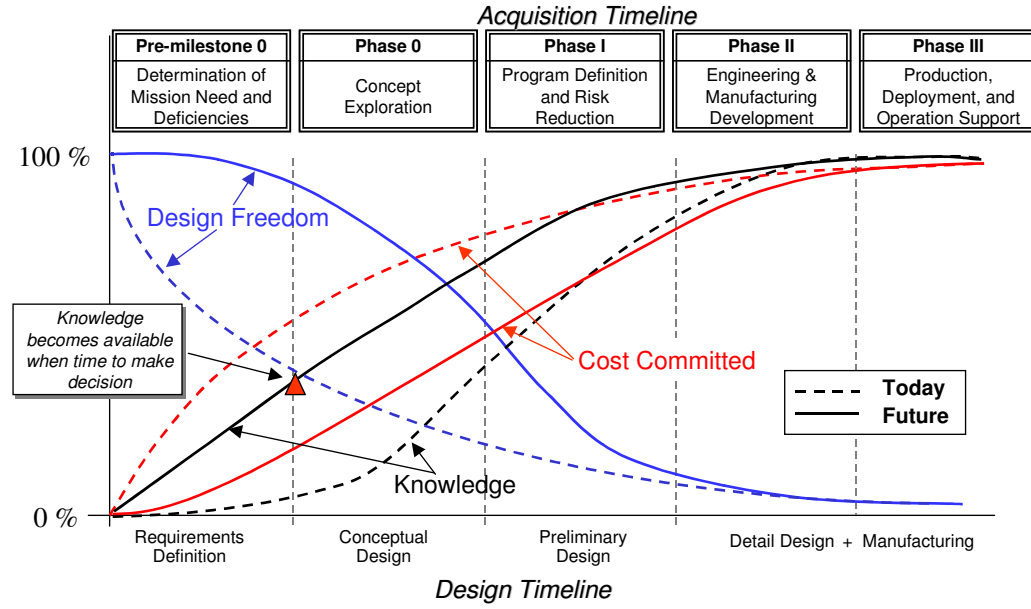


Figure 2: Different stages of design [68]

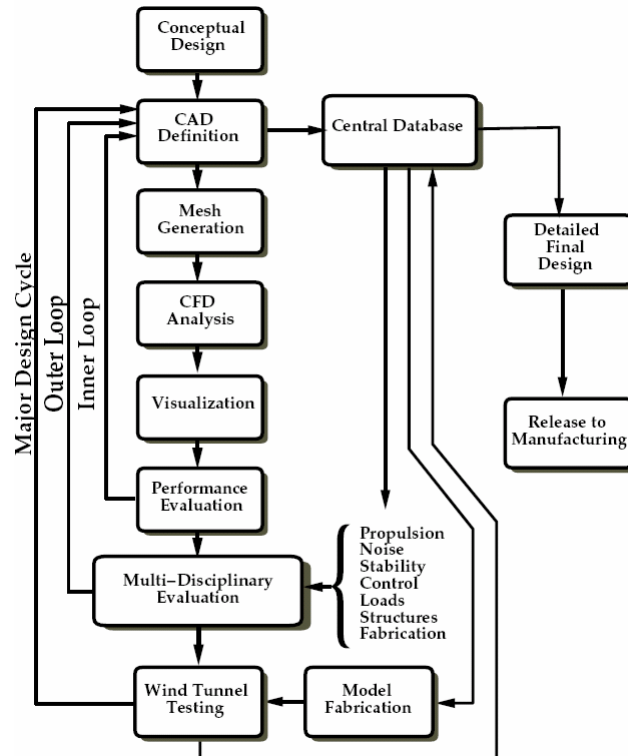


Figure 3: Typical aerodynamic design process [47]

geometry is the key to conceptual aircraft aerodynamic designs. Most of the concepts are dictated by different geometric parameters. There is a need to develop conceptual design tools that are geometry centric.

In the present design setting, the preliminary and advanced tools operate on different levels of geometric fidelity. While conceptual tools operate on crude approximations of true geometry, computational fluid dynamics is applied on CAD like geometries. If a smooth transition is desired from initial stages to advanced design, the setup should be such that the same geometry definition is used for all analysis. This provides transparency in analysis as well a fair platform for comparison of different fidelity analysis. This is one of the objectives of this research.

### **1.1.2 Sonic boom near-field prediction tools**

Sonic boom has been identified as one of the most important technical show-stoppers for the supersonic aircraft design. The prediction of sonic boom signature on the ground involves [13] prediction of near field pressure signature and its propagation [126] to the ground. Numerous research efforts have been undertaken to use linearized methods as well as computational fluid dynamic analysis to predict the near field pressure signature of an aircraft. As long as the free-stream Mach number is not greater than 3.0, it has been shown that linearized tools with non-linear propagation corrections do provide a reasonable estimate of the near field pressure signature [21].

Linearized near field analysis involves the determination of equivalent area due to volume and lift. A detailed explanation of the aircraft equivalent area concepts is given in appendix A. Equivalent area due to volume is usually calculated using Harris wave drag code (AWAVE). Following the equivalent area representation, AWAVE proceeds to compute the volume contribution of each aircraft component separately. The geometry representation of the aircraft comprises loosely connected geometric entities.

Apart from approximating the geometry in terms of awkward control cards, this program does not consider the aircraft as a single object. Since the geometry is read as a wire-frame model, it usually ends up accounting for portions of components which pass through each



other twice. The sketch in Figure 4 illustrates the case for a conventional area-ruled wing-fuselage combination. AWAVE representation can be one of the sketches shown on the right side of the figure where the shaded region is either ignored or accounted for more than once. The reason for this is that the program can only handle straight wing sections and has no strategy to deal with the component intersections. This leads to an incorrect area and volume distribution resulting in an erroneous wave drag and equivalent area distribution. Since AWAVE deals with approximations of conventional geometries, coke bottled fuselages as well as interesting concepts like joined-wing, channel-wing and oblique-wing configurations cannot be handled accurately with this setup.

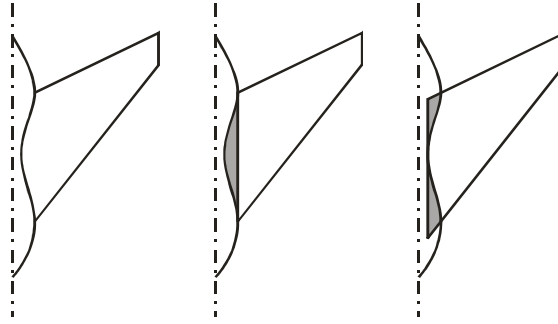


**Figure 4:** Poor geometry representation

AWAVE obtains the Mach plane intersection of each component of the aircraft and sums these individual contributions without ever accounting for the intersections between components. To avoid counting the intersection areas twice, within Aerospace Systems design lab, AWAVE has since been modified to trim the components just before an intersection occurs. This could lead to gaps in the geometry presented to AWAVE. As clearly seen from Figure 5, for a simple canard-wing geometry, AWAVE geometry representation is inadequate with gaps at the wing root sections. A demonstration of the effect of these inaccuracies in the determination of sonic boom ground signatures is given in a later chapter.

Equivalent area due to lift computes the cumulative lift along the aircraft longitudinal axis that contributes to the near-field pressure signature of the aircraft. Theoretically, all the lift producing components of the aircraft contribute to the equivalent area due to lift.

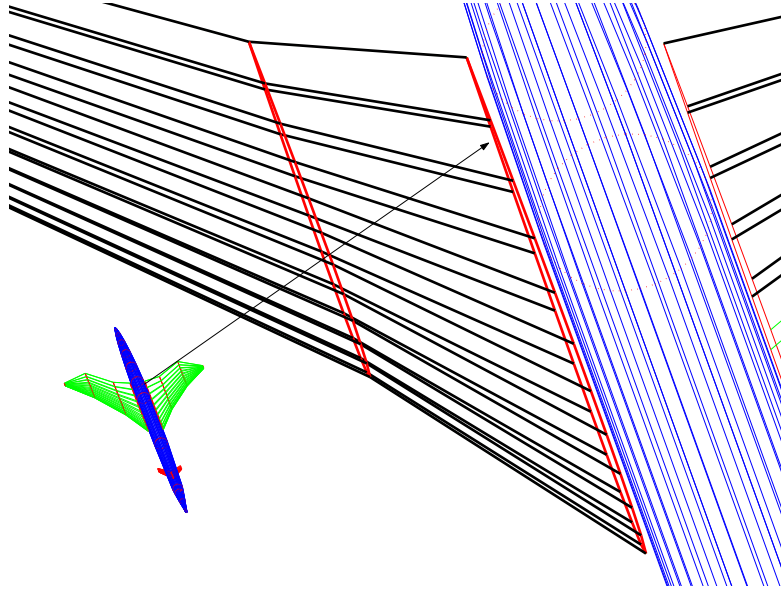


**Figure 5:** Geometry representation by Harris wave drag code

However, in practise, only the effect of the wing contribution is considered in the conceptual stages of design as the analysis tools used at this stage cannot model the fuselage and interference lift effects. The equivalent area due to lift is traditionally calculated using a simple Mach box method which computes just the wing contribution to lift. This method works on a planar version of the wing and so camber and thickness effects cannot be modelled accurately. Since the lift contribution is crucial to a near-field signature, it is important to consider lift contributions from components other than the wing.

A look at the above linearized analysis methods reveals that there is an evident gap in geometric fidelity between the true geometry and that provided to these analyses. The challenge in this area is to develop or use robust analysis routines which use the exact aircraft shape or try to model the effects in a more rigorous fashion to calculate near field pressure perturbation. This would ensure that the exact effect of the true geometry is considered.

### 1.1.3 Atmospheric propagation

Once a near field pressure signature is calculated, a propagation model is needed to propagate this signature to the ground. Conventional propagation models assume standard atmospheric properties to obtain the pressure and temperature values at different altitudes which are then used to obtain the sonic boom pressure signature on the ground. Linearized propagation

models with non-linear corrections are approximations of the true pressure propagation. Effects like atmospheric absorption, molecular relaxation, turbulence and anomalies in temperature and wind profiles influence the ground pressure signature. Some of these effects are extremely difficult to model and such studies are in their fundamental research stages. However, other effects can be modelled.

The cumulative effect of atmospheric absorption, molecular relaxation, atmospheric turbulence and atmospheric fluctuations produce the final pressure signature on the ground. Since these properties are constantly varying in a real atmosphere, an identical aircraft flying over the same location at same Mach number at different times could produce two completely different sounding sonic booms as shown by [7]. In other words, the sensitivity of the ground boom signatures to the variation of the atmospheric parameters may be huge. The existing propagation routines are thus limited in their method of simulating the rise times and other characteristics of the boom signature. The challenge in this area is to carry out the wave propagation with atmospheric variation considered.

Atmosphere is composed of many layers such as troposphere, stratosphere, thermosphere, mesosphere etc. Troposphere extends from the earth's surface to an altitude of about 11 km. and it is a region of rising and falling packets of air. The stratosphere follows next to an altitude of about 47 km. with the air flow mostly horizontal. Aircraft do not cruise beyond the stratosphere and so atmospheric layers beyond the stratosphere are not considered here. Based on several observations, a simple standard atmospheric model has been formed which specifies the temperature variation within these layers and the altitudes that separate them. Pressure and density are well predicted by the standard atmosphere. However, the standard atmosphere temperature predictions are correct only in an average sense and could in general vary with time, season, humidity, latitude, etc.

To study the effect of change in lapse rate, a uniform distribution with a range of  $1.5^{\circ}C/km$  is assumed around a mean of  $-6.5^{\circ}C/km$ . This range is based on observations of the atmospheric temperature profiles measured by Radiosonde experiments [78] at various locations and seasons. Furthermore, since the altitudes might also change, distributions with varying ranges are put around the mean altitudes separating different layers of the standard

atmosphere. Figure 6 shows a parametric atmospheric model using which different models can be generated. The thick solid line in this figure represents the standard atmosphere.

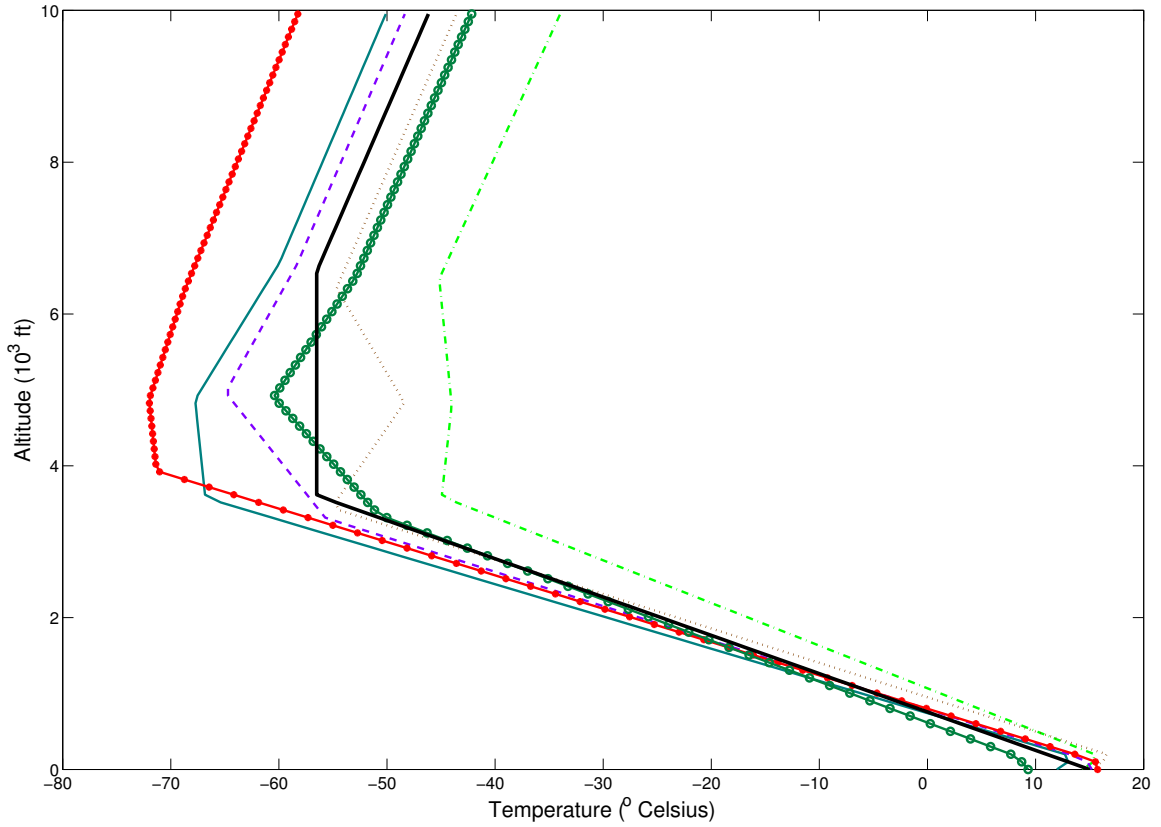


**Figure 6:** Parametric atmospheric temperature model

In addition to the temperature profiles, the wind profiles have also been parameterized by random variables. With random fluctuations in both temperature and wind, Monte Carlo simulation was performed and the joint probability distribution for shock overpressure and the perceived loudness of the ground boom signature is shown in Figure 7. The propagation has been performed on an arbitrary configuration cruising at Mach 1.6, Gross weight of 100,000 lbs and at altitude of 60,000 ft. As can be seen from the figure, the shock overpressure ranges from 0.67 to 0.68 psf and the perceived loudness ranges from 89.2 PLdB to 91.4 PLdB. This figure shows that there can be quite a bit of variability in the perceived loudness level if the atmospheric conditions were to change from the standard conditions. The important idea to be grasped from this figure is that using the shock overpressure as the objective may mask the complete effect of the atmospheric variations because the probability plot spans a

small portion of the overpressure axis. On the contrary, the importance of considering the fluctuations is reflected in the perceived loudness calculations, where a huge variability is observed. Perceived loudness level metric combines the effect of various crucial ingredients in the pressure signature and hence is a better metric to keep track of rather than shock overpressure or other pressure perturbations.

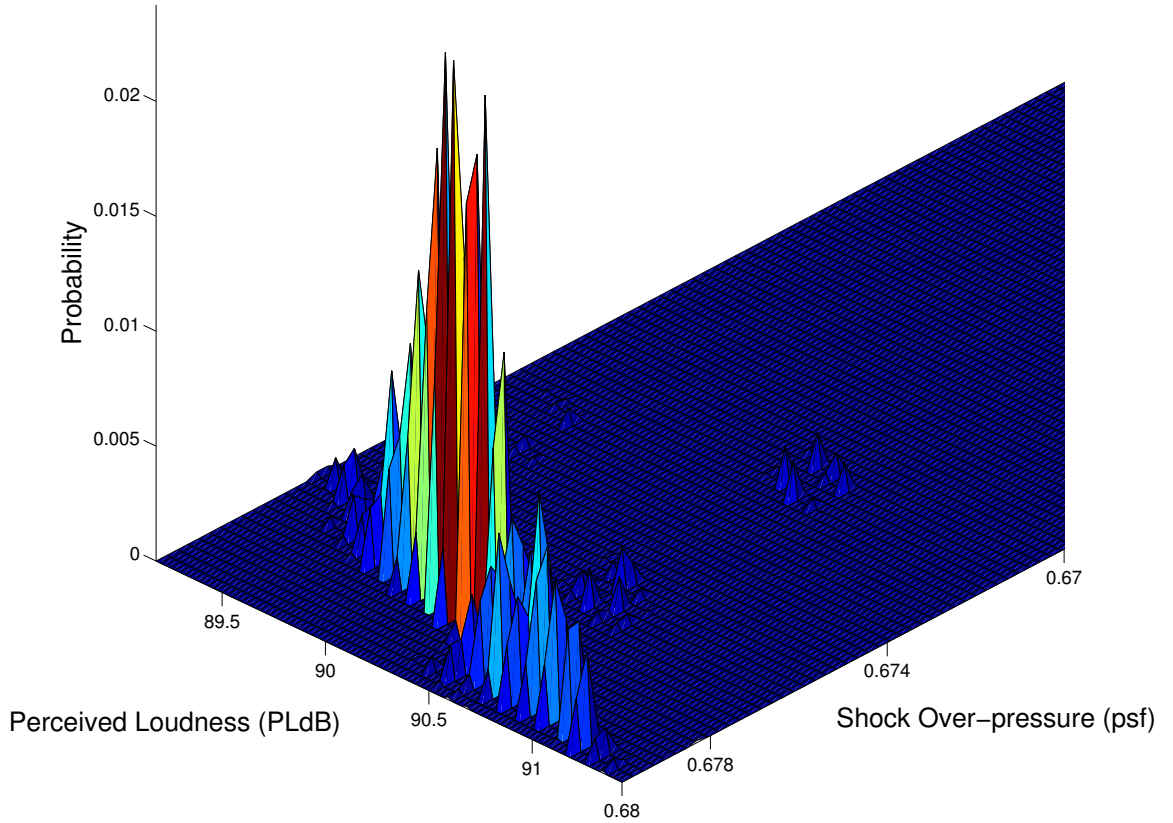


**Figure 7:** Joint probability distribution of the overpressure and loudness levels

A small digression is made here to justify the usage of PLdB as a metric for perceived level of noise. Various procedures of computing the noise levels have been suggested [117] including Mark VI, PNdB and Mark VII. Before Mark VII, the reference frequency used for loudness calculation was 1000 Hz. However various inadequacies of such a reference frequency have been suggested [117]. A new reference frequency of 3150 Hz. has been used in PLdB calculation using Mark VII for two main reasons. Firstly, a frequency of 3150 Hz. is the minimum frequency on the equal perceived magnitude contours. Secondly, the frequency

around 3150 Hz. is in the region of human ear's greatest sensitivity. For these reasons, PLdB calculated by Mark VII is used as the loudness metric. The reader should be aware that even though PLdB calculated by Mark VII method is a unit of the sound pressure level, it is used as a metric to label most figures.

#### **1.1.4 Sonic Boom Minimization**

The key requirement for a new generation civil supersonic transport is that it be capable of unrestricted supersonic flight over land. Based on this requirement alone considerable focus has been placed on sonic boom minimization for a 100,000 lb class aircraft flying around Mach 1.6. The reasons for choosing such a weight and Mach number are presented in the next chapter.

Before the sonic boom minimization concepts are discussed further, it is probably worthwhile to mention that some in the industry (Aerion) [1] have argued that sonic boom minimization is a huge leap in commercial aviation and suggest the use of supersonic corridors for supersonic flight over land and subsonic flight outside these restricted corridors. These corridors are regions that are sparsely populated so that only a limited number of people are affected by the sonic boom produced by supersonic flight. This may compromise the time savings expected due to supersonic flight because the flight has to pass through these corridors, thus increasing the total distance travelled and the time taken. Other companies have recognized that sonic boom mitigation with unrestricted supersonic flight over land is a requirement for a successful business case. Such a design would actually help maximize the time savings.

The sonic boom minimization concepts have been proposed more than two decades ago and resultant low boom constraints are used even today to aid in supersonic aircraft design. However, these constraints do not include any information about the loudness of the ground signature. Even though these theories are mathematically sound, they fail to predict the F-function or equivalent area shapes that minimize loudness of the boom signature.

The most important issue in minimization studies is to choose a criterion to minimize the ground signature. Unfortunately, there is no single standard objective used for sonic

boom minimization. Various researchers have used one or more of the important parameters associated with a ground pressure signature. These parameters include initial shock pressure rise, maximum overpressure, the time it takes to reach the maximum overpressure and the impulse or energy contained in the signature. A sample sonic boom signature is shown in Figure 8 with a finite rise time  $\tau$  and maximum overpressure  $P_o$ . Note the presence of two strong shocks, one at front and the other at the back. The individual shocks from various vehicle components coalesce as they propagate away from the aircraft to result in N-wave looking shapes. Boom minimization theory of Seebass and George [105] and Darden [20], henceforth referred to as SGD theory, develops expressions for the near field signatures that minimize the shock pressure rise or the over-pressure of the ground signature. This theory provides low boom constraints, which are then used as guidelines to drive the optimizer to achieve those near field values by changing the shape of the aircraft.

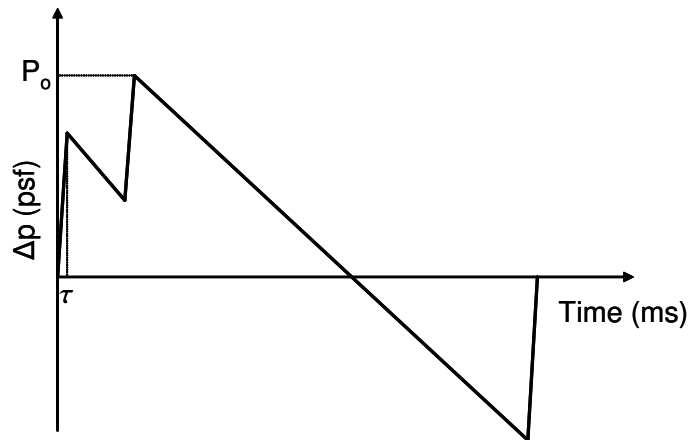


**Figure 8:** A sample sonic boom signature

Recent research shows that, perhaps, the most important parameter that should be used for minimization is the loudness level of the pressure signature that is perceived by humans and structures. After all, supersonic flight over land would be possible if the noise generated does not have a significant effect on humans and does not create any damage to buildings. Perceived loudness calculation is sensitive to the shock rise time and other propagation effects. The existing minimization theory does not provide lower bounds for perceived loudness. Minimizing overpressure or shock pressure rise, as in SGD theory, does not necessarily minimize the perceived loudness and therefore the near field signature predicted by

this theory may not yield a ground signature of minimum loudness.

Perceived loudness level depends heavily on the rise time of the shock waves. Asymmetry of the signature also has an effect on the loudness as studied by [58]. These characteristics are affected by the prevailing atmospheric conditions. Thus, there is a need to predict the near field signature that would minimize loudness by considering atmospheric fluctuations.

## ***1.2 Optimization techniques***

The foregoing sections summarized various methods to improve the sonic boom prediction in the conceptual design phase. In order to use those analysis tools in the design process, an efficient optimization technique is required to realize designs with minimum boom and related metrics. This section introduces the basics of optimization process and discusses the need for numerical optimization in the design of complex systems.

One might ask: Why is optimization important in design? To answer this question, a brief introduction on optimization is presented next. Every designer designs an aircraft to meet certain goals or requirements. How best to change the design settings to meet these goals is up to the designer. Before computers were introduced, designers used their intuition and knowledge base to make those decisions. However, as the systems got complex, relatively small design changes could lead to significant benefits. For example, by slightly modifying the airfoil section shapes, drag could be reduced to a large extent. These types of changes are unlikely to be discovered using trial and error techniques. It is for this reason that quantitative optimization techniques are very important in design. Optimization techniques enhance the designer's ability to produce optimal systems and help to understand the effect of different variables on the performance of the system.

Numerical optimization [123] methods can be classified into two main groups based on the particular algorithm that is used to drive the problem to an optimum value. The first is the gradient optimization technique where the sensitivity of the objective function to the changes in parameters is used in conjunction with the objective value itself to find the optimum. The second is based solely on the objective function value and is termed zero order method. Gradient optimization methods are efficient if the gradient of the objective



function can be computed easily. However, these methods are known to yield local optima and optimization may have to be carried out more than once from different initial guesses to obtain a global optima.

Many real world problems involve simultaneous optimization of multiple conflicting objectives. In these situations, there is no single optimum. Optimal solutions form a finite set in which an improvement in one objective would lead to a degradation in other metrics. This optimal set of non-dominated solutions is termed as the Pareto-optimal set. Multi-objective optimization can be handled in two ways. Firstly, the multi-objective optimization can be transformed into a single objective optimization problem by creating a weighted sum of all the objectives, the so called overall evaluation criterion (OEC) [53]. Using such a scheme, the obtained solution is highly sensitive to the weights chosen. In addition, there might exist more than one optimum solution to the problem. Using an OEC strategy, only a single optimum can be obtained for each run. Hence in order to obtain all the optima, the optimization may have to be performed multiple times and therefore is not desirable. This leads us to the second way of handling multi-objective optimization problems in which a population of points is used at each iteration rather than a single point. All the Pareto-optimal solutions could be obtained in a single run. Even though population based methods produce a Pareto solution front, one could attribute two main disadvantages to these methods. These are computationally expensive and are not intuitive if the number of objectives is large. These algorithms are known to make progress towards the Pareto-optimal set but none of these guarantee a convergence to the true Pareto optimal front. In spite of these disadvantages, these methods are widely used because they offer an easy way to obtain global optima.

A further classification of optimization techniques is the mode in which they are used. Engineering optimization could be run in two different modes. One is the usual direct design where the design variables are modified to minimize the objective function by running the analysis. The design variables are updated depending upon the sensitivity of the objectives to the design variables and the direction of minimization of the objectives. Inverse design, on the other hand, is an approach where the optimizer tries to match the objective to a target objective function or value. In such a case, the target values should be chosen wisely because

there might not exist a feasible solution to meet the target values. The mapping between the design variables and the objective function value could be a non-physical function. However, if a reasonable target distribution is chosen, the set of design variables needed to meet that target function could be obtained efficiently.

Optimization algorithms, however different, share one thing in common. All of them try to obtain a set of design variables that would optimize the prescribed objective function subject to a set of constraints that define the boundaries of the solution space. The choice of the design variables is made by the designer to suit his needs. Constraints may have to be imposed either to satisfy the physics of the problem or to generate a realistic solution.

### ***1.3 Basic foundations and assumptions***

With the basic understanding of the sonic boom theory and the limitations and challenges of the existing methods presented earlier, this section outlines the assumptions made in this research effort. The first and most important assumption for conceptual design is that in the early stages of aerodynamic design, linearized methods provide a reasonable estimate of the near field pressure distribution. Although this is the fundamental assumption, all the tools in this study have been developed with a variable fidelity analysis in mind so that in future design studies, a combination of linear and non-linear methods could be integrated seamlessly. Note that by resorting to linearized analysis, local three dimensional effects are being neglected. Though this is not accurate, the analysis produces values which can be used in conceptual design.

In order to perform a conceptual design of supersonic aircraft, an efficient trade-off analysis has to be carried out to weigh various criteria. This trade-off analysis has to include the shape of the aircraft. Thus, the second assumption is that it is possible to obtain optimum aircraft shapes to satisfy low boom constraints and at the same time improve the performance measure of the aircraft. Seebass-George proposition that the sonic boom signature on the ground can be controlled by shaping the aircraft has been proven recently [17] by the flight tests conducted on August 27, 2003 on a modified nose F-5E, better known as the shaped sonic boom demonstration. More on this flight tests is provided later in this thesis.

Existing linearized methods are approximations of the accurate flow-field physics in two ways. The first is the mathematical approximation according to which these methods are only accurate to the first order. The other approximation made by these methods is the geometric approximation. The true geometry of the body is tweaked to suit the linearized computational programs. For a shape optimization study, where exact geometry is very crucial, such approximations compromise the whole procedure and could lead to potential inaccuracies in the optimized design. It is therefore important to improve the geometric fidelity of the aircraft models used in linearized codes. The third assumption for this study is that geometric handling of the configurations can be improved in the conceptual stages of design.

With the improved geometric fidelity, the existing linearized routines for volume contribution have to be heavily modified or entirely rewritten. Most design studies run either linearized methods or non-linear CFD methods for their lift contribution. With increase in computational power, CFD analyses is being used much earlier in the design than has been used in the past. Before the actual CFD flow solution is attempted, pre-processing is required where a computational mesh needs to be created surrounding the body of interest. Mesh generation is a separate field in itself and could be computationally very expensive. Linearized methods on the other hand require a simple discretization of an approximate geometry. The philosophy of linearized methods is thus completely different from CFD methods. After obtaining an optimized solution using linearized methods, significant time is usually invested to obtain a grid suitable to run CFD over the optimized geometry for advanced analysis. There is a need to bring the above two philosophies closer together so that CFD solution could be attempted without further effort. The fourth assumption is that it is possible for the designer to create and discretize complex geometries so that the linearized tools operate over the same configuration used for CFD analysis. With the improved geometry handling proposed here, the issue of mesh generation and CFD pre-processing can be minimized.

There are significant atmospheric variations at any location that could have a big impact on the pressure signatures on the ground. Figure 9 shows the actual weather balloon data of the atmospheric temperature near Atlanta obtained from Radiosonde measurements of

[78]. This figure compares the temperature profiles in three different months at the same location with the temperature profile predicted by standard atmospheric model. As can be seen from the figure, there is a large discrepancy between the actual data and that predicted from the standard atmosphere. The slope of the temperature profile changes with season and the temperature in the stratosphere is not constant as predicted by standard atmosphere. Note also that there could be a temperature inversion close to the ground in real data where temperature increases with altitude. The characteristics of the predicted boom signatures could be quite different in all these cases. The effect due to this discrepancy should be studied in detail. It is assumed in this study that, probabilistic wave propagation considering atmospheric variations would produce a robust sonic boom prediction environment.

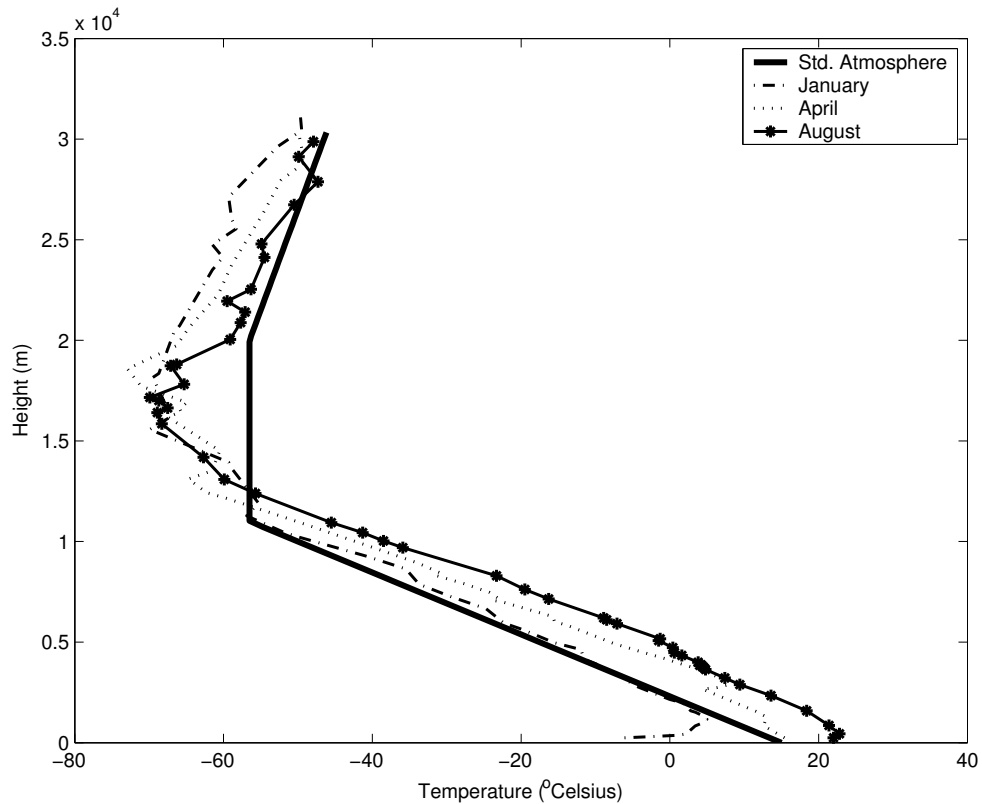


**Figure 9:** Comparison of the actual and standard temperature profile in Atlanta

Seebass and George [105] and Darden [20] present analytical expressions for F-function and equivalent area distributions for producing ground signatures with minimum overpressure or minimum shock pressure rise. A detailed introduction to F-functions is given in Appendix B. It is understood that in addition to these metrics, other metrics like perceived

loudness level that consider the sensitivity of human ears, should be used in a sonic boom minimization study. One has to study how the perceived loudness minimization is going to change the F-function and equivalent distributions predicted by low boom constraints. Low sonic boom constraints for minimum perceived loudness level, instead of the traditional overpressure or shock pressure minimization, can provide a new bench-mark for minimum boom strength.

## ***1.4 Research Questions***

In order to answer the above requirements and needs, the following research questions are posed.

**Question 1:** Is it possible to run linearized and non-linear CFD analysis using the same geometric fidelity?

**Question 2:** Is it possible to improve the fidelity and efficiency of the present sonic boom linearized methods for near field prediction?

**Question 3:** Is it possible to perform a probabilistic sonic boom study with uncertain atmospheric parameters? If so, how will the results differ with those predicted by deterministic models?

**Question 4:** Does loudness minimization affect the F-function distribution predicted by the SGD theory which minimizes pressure perturbations? If so, by how much?

**Question 5:** Can sonic boom minimization procedure be generalized further for aircraft design trade-off studies?

**Question 6:** Is it possible to build a flexible design framework for performing various vehicle shape optimization studies for sonic boom minimization?

# CHAPTER II

## BACKGROUND

Now that the motivation and the objectives of this research effort have been presented, this chapter presents some background theory into the working details of various analysis.

Linearized supersonic flow physics dictate the formation of a conical domain of influence of the aircraft that intersects the ground at a distance downstream of the aircraft. Linearized theory follows the slender body approximation that assumes that the length of the aircraft is far greater than the other two dimensions. In such a case, the potential flow around the body can be modelled by sources, sinks, vortices or doublets. The non-lifting flow is usually modelled as caused by a superposition of source distributions. The perturbation potential in such case is given by the Equation 1 [3] and the corresponding perturbation velocity,  $u$ , is given by Equation 2. In these equations  $x, s$  represent the axial locations,  $\phi$  is the perturbation potential,  $\beta = \sqrt{M^2 - 1}$  and  $f$  is the linear source density.

$$\phi = \int_0^{x-\beta r} \frac{f(s)}{\sqrt{((x-s)^2 - \beta^2 r^2)}} ds \quad (1)$$

$$u = \frac{\partial \phi}{\partial x} = \int_0^{x-\beta r} \frac{f'(s)}{\sqrt{((x-s)^2 - \beta^2 r^2)}} ds \quad (2)$$

By a suitable substitution, the above equation can be converted into a form where it can be clearly seen that the potential disturbances propagate along cones. Using the flow tangency boundary condition, the linearized potential equation can be solved to obtain the slender body potential flow results. Before probing deeper into the mathematics of the near field pressure prediction, it is important to understand the physics of the supersonic flow-field in simple terms.

When an airplane travels at a speed faster than the speed of sound, density waves pile up against each other and result in the formation of shocks. The shock waves propagate through the atmosphere and usually appear as a boom signature on the ground. An observer on the ground experiences the rapid pressure perturbations in an infinitesimally small amount of time resulting in an annoying sonic bang. From an observer's point of view, a conical domain of dependence could be sketched which has its apex at the observer location and intersects the aircraft at various locations as the aircraft maneuvers through the atmosphere. The region between the domain of influence and dependence has a combination of shocks and expansions. As the signature passes through the atmosphere it undergoes various processes like shock coalescence, atmospheric absorption, scattering, refraction etc. and the resultant signature at the ground level is perceived as abrupt pressure jumps in an extremely small time interval.

Generally, sonic boom refers to just the signature directly below the aircraft because it has the maximum intensity. In reality, since shock waves travel in all directions within the Mach cone, there are additional regions where similar, but lesser intensity signatures called secondary booms [24] are observed. This is due to the refraction of the signature through the atmosphere. Various sonic boom carpets have been identified depending on different parameters. The primary boom carpet is usually the strongest and is due to the wave propagation through only that part of the atmosphere directly below the aircraft. The disturbances in this region involve high over-pressures, steep rise times and have substantial high frequency content. Propagation distances are the shortest for primary booms and the disturbances adversely affect community response. The secondary boom carpet involves the portion of the atmosphere both above and below the airplane. The exposed areas are more remote from the ground track and the overpressure levels are much less intense than in the primary carpet.

Atmospheric temperature and wind are the two most important parameters in the propagation of the pressure fields and thus are very important parameters in obtaining the range, direction and magnitude of the boom carpets. The pressure signatures emitted from the aircraft follow ray paths [126], which curve toward regions where the temperature is lower

and where the wind component in the ray direction is greater. The over-pressures experienced in the primary and secondary carpet areas not only depend upon the atmospheric characteristics and distance travelled by the shock waves, but also upon their initial strength and direction. More complex signatures are measured close to the aircraft and the individual shock waves from the aircraft tend to coalesce as distance from the aircraft increases as shown in Figure 10 due to atmospheric properties. Four different altitude levels are shown in this figure. The plane a few body lengths away from the aircraft is called a near field plane where a complex pressure signature exists. It is the effective interface between a *CFD* solver and propagation analysis. *CFD* far field indicates the far field boundary of the computational mesh for a *CFD* solver. Mid field indicates a plane where sufficient coalescence has taken place and ground plane is where the signature is actually measured. The pressure signature calculated at the near field boundary is supplied to the propagation program to obtain the ground level pressure signature.

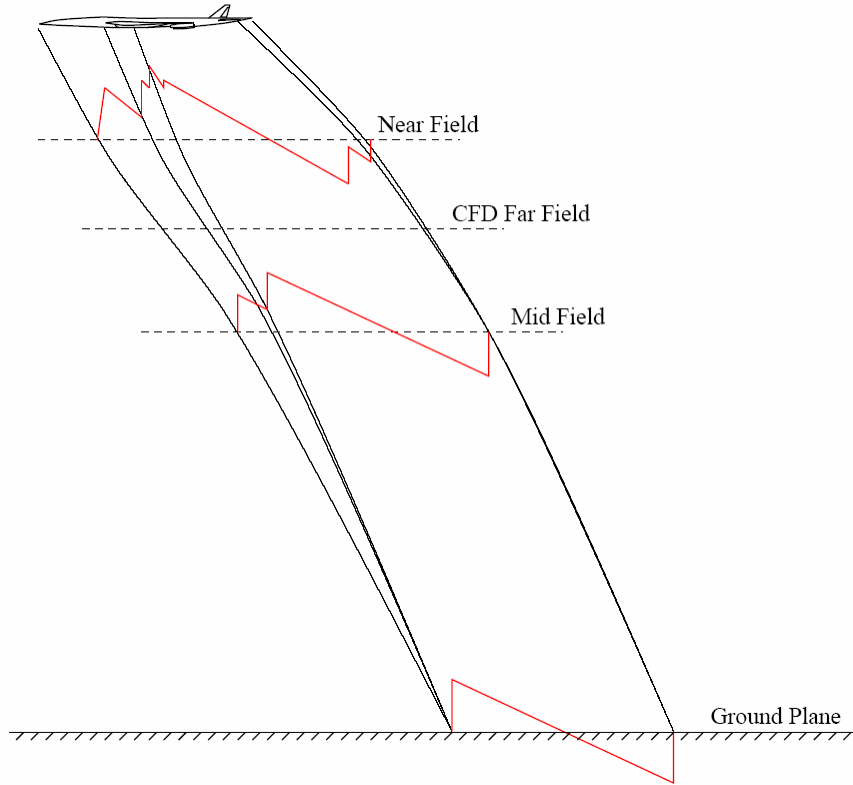


**Figure 10:** Shock coalescence during boom propagation [76]

Sonic boom prediction is thus a complex amalgamation of aerodynamics, aero-acoustics



and atmospheric science and improvements in any of the above fields lead to improved sonic boom prediction techniques. A detailed introduction to the sonic boom generation theory has been given by many authors. Some of the earliest complete explanations are contained in papers by [107] and [13]. A brief introduction to the individual elements of sonic boom generation is presented next.

## 2.1 *Linearized near field prediction*

As has been mentioned in the previous section, the first step in sonic boom prediction is the estimation of near field signature. Whitham [129] was the first to provide a complete first order approximation of the solution of supersonic flow past a slender, axisymmetric body-wake combination. According to Whitham, linear theory had to be corrected slightly to be able to provide better prediction of the near field. He proposed that the characteristic lines  $x - \beta r = \text{constant}$  of the linear theory should be replaced by  $\tau(x, r) = \text{constant}$  as a more accurate representation of the characteristic curves. Replacing  $x - \beta r$  with  $\tau$  in Equation 2 and approximating with  $r \gg \tau$ , Equation 3 is obtained for the perturbation velocity.

$$u = -\frac{F(\tau)}{\sqrt{2\beta r}} \quad (3)$$

where, the F-function,  $F$  is obtained in terms of the second derivative of the equivalent area,  $S$  as shown in Equation 4.

$$F(\tau) = \frac{1}{2\pi} \int_0^\tau \frac{S''(t)}{\sqrt{(\tau - t)}} dt \quad (4)$$

Using the linearized theory expression relating the pressure perturbation and perturbation velocity, Equation 3 could be used to generate a relation between the near field pressure perturbation  $\delta p$  and the F-function in terms of  $M$ ,  $\beta$ ,  $\gamma$ ,  $p_0$  and  $r$  as shown in Equation 5. F-function represents the effect of a distribution of singularities which cause the same disturbance as the aircraft at a distance far away from the aircraft and is thus analogous to an acoustic source term [86]. F-function has a direct relation to the geometry of the aircraft

due to its dependence on the second derivative of the area distribution. This property could be used to control the shape of the aircraft by modifying the F-function. Various other important properties of the F-function and its importance in linearized theory were given by Whitham in his pioneering work.

$$\delta p = p_0 \frac{\gamma M^2 F(\tau)}{\sqrt{(2\beta r)}} \quad (5)$$

The linear theory corrections relevant to the sonic boom calculation [125] are briefly presented here. Along the characteristic curves  $\tau(x, r)$ , Equation 6 is to be satisfied that specifies the slope of the characteristic curves.

$$\frac{dx}{dr} = \cot(\mu + \epsilon) = \beta - \left( \frac{(\gamma + 1)M_\infty^4 F(\tau) r^{1/2}}{2^{1/2} \beta^{3/2}} \right) \quad (6)$$

where

$$\epsilon = \tan^{-1} \left( \frac{v}{u} \right) \quad (7)$$

and

$$v = \frac{\partial \phi}{\partial y} \quad (8)$$

In the above equations,  $\mu = \sin^{-1}(1/M)$  is the slope of the characteristic lines.  $\epsilon$  is the local perturbation in the flow direction. After a little algebra, the corrected characteristic curves can be approximated as given in Equation 9 after higher order terms have been neglected.

$$\tau = x - \beta r + \left( \frac{(\gamma + 1)M_\infty^4 F(\tau) r^{1/2}}{2^{1/2} \beta^{3/2}} \right) \quad (9)$$

So far in the discussion, only characteristic waves have been considered. When shock waves are present in the flow field, the characteristic waves are modified due to their presence.

If the shock wave is given by  $\tau = T(r, \theta)$ , then the characteristic curve slope is given by Equation 10. Note that in this expression, the shock waves have 2 independent parameters.  $r$  represents the radial location and  $\theta$  represents the azimuthal variation.

$$\frac{dx}{dr} = \beta - \frac{(\gamma + 1)M_\infty^4 F(T, \theta)}{2^{3/2}\beta^{3/2}r^{1/2}} + \frac{dT}{dr} \left( 1 - \frac{(\gamma + 1)M_\infty^4 F'(T, \theta) r^{1/2}}{2^{1/2}\beta^{3/2}} \right) \quad (10)$$

Introducing the condition that the shock bisects the intersecting characteristics, Equation 11 can be obtained.

$$\frac{dx}{dr} = \beta - \frac{(\gamma + 1)M_\infty^4 F(T, \theta)}{2^{5/2}\beta^{3/2}r^{1/2}} \quad (11)$$

Using equations 10 and 11, the slope of the shock can be obtained as given in Equation 12.

$$\frac{dT}{dr} = \frac{(\gamma + 1)M_\infty^4 F'(T, \theta) r^{1/2}}{2^{1/2}\beta^{3/2}} \frac{dT}{dr} + \frac{(\gamma + 1)M_\infty^4 F(T, \theta)}{2^{5/2}\beta^{3/2}r^{1/2}} \quad (12)$$

Finally, multiplying both sides of Equation 12 by  $2F(T)$  and integrating yields Equation 13.

$$r^{1/2} = \frac{(2\beta)^{3/2}}{(\gamma + 1)M_\infty^4} \frac{\int_0^T F(\tau, \theta) d\tau}{F^2(T, \theta)} \quad (13)$$

In the limit of large distances from the aircraft axis, i.e.  $r \gg$  aircraft length,  $T$  is assumed to be near  $T_0$ , where  $F(T_0, \theta) = 0$ . For such a far field, the pressure perturbation can be approximated by the expression given in Equation 14. This equation shows that the pressure perturbation decreases as three-fourths power of the altitude of the initial pressure signature.

$$\frac{p - p_\infty}{p_\infty} = \gamma M_\infty^2 \left( \frac{(2\beta)^{1/2}}{(\gamma + 1)M_\infty^4} \int_0^{T_0} F(\tau, \theta) d\tau \right)^{1/2} \frac{1}{r^{3/4}} \quad (14)$$

The position of the shock wave relative to the linear characteristic is given by Equation 15. The important aspect about this equation is that, the location of the shock is determined by the area under the positive portion of the F-function curve.

$$T_0 = \frac{(\gamma + 1)M_\infty^4}{2^{1/2}\beta^{3/2}} \left( \frac{(2\beta)^{3/2} \int_0^{T_0} F(\tau, \theta) d\tau}{(\gamma + 1)M_\infty^4} \right)^{1/2} r^{1/4} \quad (15)$$

This linearized correction procedure is used again to mathematically obtain signatures minimizing sonic boom pressure perturbations as shown in a later section.

### 2.1.1 Equivalent area due to volume and wave drag estimation

For linearized sonic boom prediction, the main ingredient of aerodynamic analysis is the equivalent area representation. As has been said earlier, the flow perturbation by the aircraft can be modelled as due to a linear source distribution for volume contribution and vortex distribution for lift effects. To an observer on the ground, only the singularities that lie in the observer's fore cone would influence the flow conditions at his location following the domain of influence principle of supersonic flows. It can be shown that the strength of the source distribution is related to the gradient of the normal projection of Mach cone intercepted area of the aircraft. When the observer is at a sufficient distance from the aircraft, the cones could be replaced by planes. The airplane could be effectively replaced by an equivalent body of revolution for far field effects.

The wave drag of a slender body is closely related to the Mach cone intercepted area. The wave drag  $D_w$  expression could be analytically derived in terms of  $\rho$ ,  $l$ ,  $S$  and  $U$ . The expression is given in Equation 16 for a body whose area gradient is zero at the ends [127].

$$D_w = \frac{-\rho U^2}{4\pi} \int_0^l \int_0^l S''(x_1) S''(x_2) L_n |x_1 - x_2| dx_1 dx_2 \quad (16)$$

Harris [33] developed one of the first programs to estimate zero lift wave drag of aircraft based on linear theory. This code is usually referred to as AWAVE. Most conceptual design studies use AWAVE for zero lift wave drag prediction even though it is realized that this

code only works on tweaked geometries. Wave drag results from this are based on zeroth order Eminton-Lord [25] theory according to which the computed wave drag is independent of the Mach number. This is inconsistent with theory [50] because it is known that drag should decrease with Mach number in the supersonic regime. From the days the theory was proposed, no significant advance has been made to improve the fidelity of the equivalent area due to volume estimation using linearized methods. [91] introduced a new computational method by which zero lift wave drag and equivalent area due to volume are accurately computed for any arbitrary geometry using linearized methods. This procedure is explained at length in a later section.

### 2.1.2 Equivalent area due to Lift

The equivalent area due to lift is obtained by the integration of the forces acting on the Mach plane intercepted sections of the aircraft. This is directly related to the property of domain of influence. A point on the aircraft axis is influenced by all the points that lie in its fore Mach cone. Thus, at any point on the equivalent body axis, all the forces generated in its fore Mach cone contribute to the force acting at this location. The accumulated lifting force is converted into area contribution by using the multiplication factor  $(-\beta/2q) \sin \theta$ . To obtain the true equivalent area distribution, lifting effects should include wing twist, camber, interference and trim effects and maneuver loads. Traditionally, most linearized methods use a Mach box method to discretize the wing geometry into rectangular boxes and solve the linearized equations.

For large supersonic transports like *HSCT*, the relative significance of the lift contribution is greater than that of the volume contribution especially for high lift conditions and high altitudes. For a supersonic fighter aircraft, the opposite is true with the volume effect being more dominant. A small supersonic business jet would have both the lift and volume effects comparable.

As mentioned by Darden [21], linearized methods fail to provide reasonable results beyond a Mach number of 3.0. There have been many efforts to include higher fidelity lift contribution methods. Page and Plotkin [79] introduced a matching methodology between

CFD near field and signature propagation far field based on acoustic multipole expansions. Various analyses including modified method of characteristics, Euler and Navier-Stokes equations have been used to obtain the lift contribution. Unlike linearized methods, CFD does not distinguish between lift and volume contributions. These two effects are combined into one for near field pressure signature.

## ***2.2 Far field pressure propagation***

The near field signature has to be propagated through the atmosphere to ground level according to the ray tracing method of geometric acoustics. According to this method, acoustic energy propagates along rays and is contained within ray tubes. The theory behind pressure propagation was explained by [30]. The strength of the pressure perturbation is determined from Equation 17, where  $E$  is the energy invariant along a ray tube with area  $RA$ .

$$E = \delta p \sqrt{(RA/\rho a)} \quad (17)$$

The quantity  $\rho a$  is called acoustic impedance. As the signature propagates downwards, the signature has to pass through layers of higher density and higher speed of sound. This causes the rays to bend and ray tube area decreases in the x-z plane while the area increases in the y-z plane [30] as shown in Figure 11. Snell's law could be used to obtain the area of a ray tube area at a distance below the aircraft axis. Using the above energy equation, acoustic impedance and ray tube area corrections cause the movement of point  $K$  to  $K'$  as shown in Figure 12. In this figure, the solid line represents the undisturbed pressure perturbation and the dashed-dotted line is the pressure perturbation after atmospheric impedance and ray tube area changes. Further distortion occurs due to atmospheric non-linearities. The disturbance propagates at the local speed of sound plus the local convective speed and not at the ambient sound speed which is the case for infinitesimal acoustic waves. Therefore, the positive portion of the wave arrives earlier than acoustic waves and the negative portion arrives later and a point  $K'$  moves to a new point  $K''$  as shown in Figure 12. These corrections to the pressure perturbation cause a multi-valued pressure signature which is non-physical. Shocks are then

inserted which make the pressure perturbation a single valued function keeping the area under the curve constant.

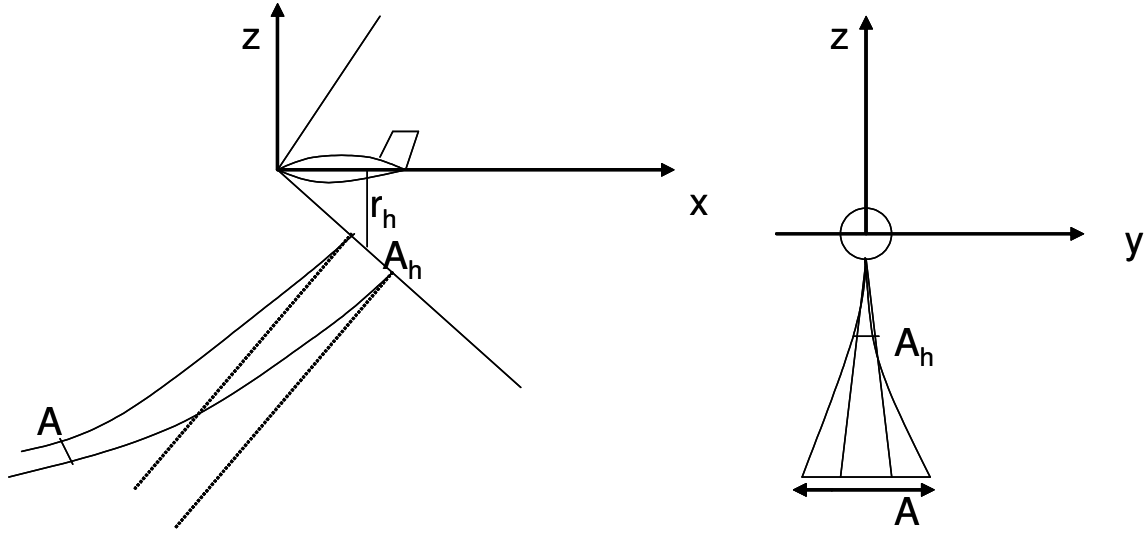


**Figure 11:** Ray tube area changes in different planes [30]

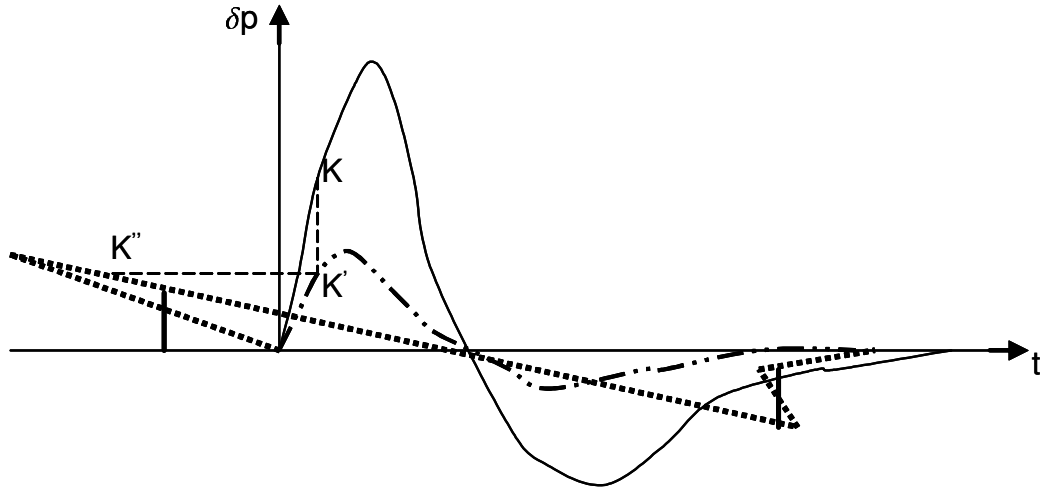


**Figure 12:** Theory of atmospheric propagation [30]

Using the geometric acoustics concepts, Hayes [35] introduced for the first time a complete propagation code whose features included boom for maneuvering aircraft using the propagation concepts provided here. Hayes [126] developed a computer code called ARAP for implementing the above propagation scheme. This method is used even now for initial estimates and is commonly referred to as the F-function method.

Another method, called the waveform parameter method [120] was introduced in the early

1970's to compute the sonic boom signatures by extrapolation through the atmosphere. The fundamental concept behind this method is the same energy invariance principle mentioned earlier. However, this method differs from the F-function method in the way non-linear effects are accounted for.

In the F-function method, an age variable is used to distort the pressure signature as it propagates through the atmosphere and then shocks are inserted according to area balancing technique as discussed before. This way of introduction of shocks is ambiguous to a certain extent. To overcome this ambiguity, the waveform parameter approach approximates the pressure signature waveform by an arbitrary number of linear segments with each segment having three waveform parameters  $m_i$ ,  $\delta p_i$  and  $\lambda_i$ .  $m_i$  is the slope  $\partial p / \partial t$  of segment  $i$ ,  $\delta p_i$  is the pressure rise across the shock at the intersection of sections  $i-1$  and  $i$ .  $\lambda_i$  is the time duration of segment  $i$ . A sample pressure signature with these parameters is depicted in Figure 13.

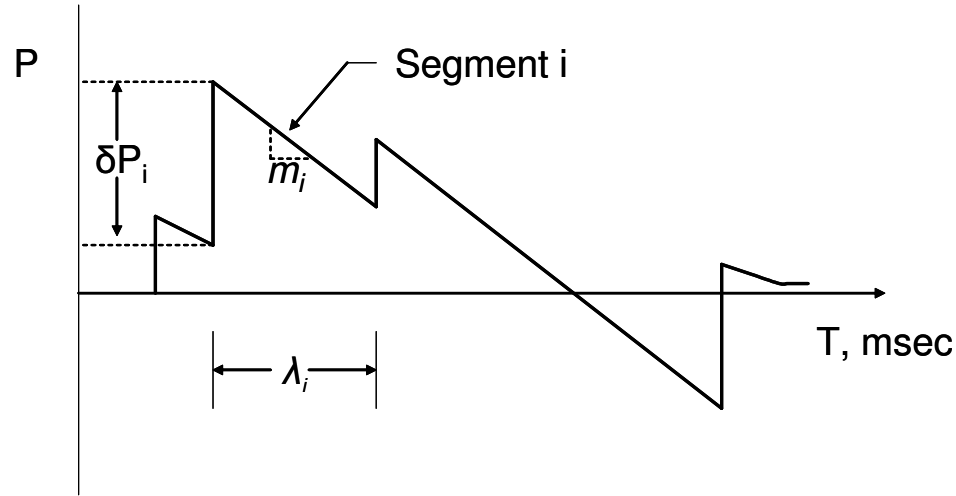


**Figure 13:** Pressure signature as seen by waveform parameter method

Starting with the energy invariance relation, equations can be obtained for the time rates of change of the waveform parameters. These equations can then be numerically integrated over small time increments to yield the final waveform parameters. This method, thus does not need any further assumption on the placement of shocks because a signature with shocks has been assumed from the start.

Various effects such as atmospheric absorption, molecular relaxation, turbulence effects,



etc. are not modelled in ARAP or the waveform parameter method of Thomas [120]. These factors may have a significant effect on the rise times and other important characteristics of the sonic boom ground signature. Pierce and Maglieri [85] introduced the effects of atmospheric irregularities on sonic-boom propagation. The presence of these atmospheric effects could cause the formation of focused boom signatures or caustics where the overpressure values can be far higher than predicted by linearized methods. These focused booms are referred to as "U" waves similar to the conventional "N" waves. A sample "U" wave is shown in Figure 14 along with a conventional "N" wave.

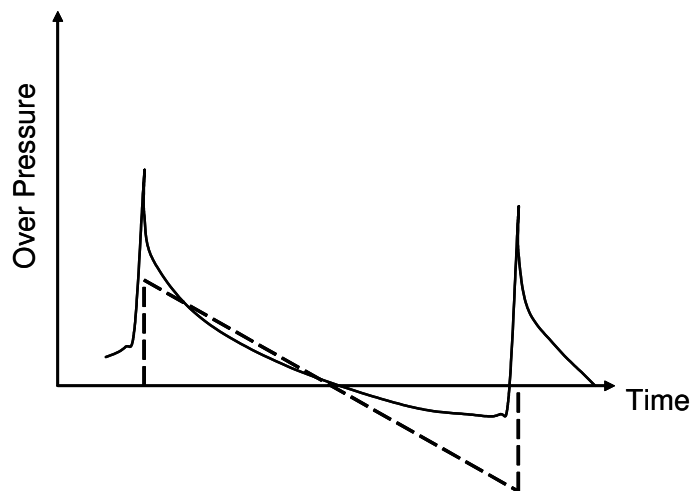


**Figure 14:** Comparison of focused U-wave and conventional N-wave

Bass [40] proposed a new algorithm to account for some of these non-linearities. Recently Auger [4] introduced a method to numerically simulate sonic boom focusing. Effect of turbulence levels on rise times was studied by Pierce [84] and a simple Fourier series approximation to the turbulence effect was proposed by Morgenstern [74] recently. However, these phenomena are still at the research level. The industry standard is a code called PC-BOOM [87], which is a computer program written by Wyle Labs. This code can propagate a three dimensional signature to the ground along with calculations to compute the rise time. PCBOOM has been used extensively in this work and is introduced in a later section.

Plotkin [88] presents the limitations of theoretical results when it comes to rise time prediction even by using the most advanced propagation codes available today. The reason for this is that the effect of factors contributing to rise time have not been completely

understood. Flight tests have shown the shocks to be substantially thicker than predicted due to atmospheric absorption mechanisms. These non-linear effects are beyond the scope of the present research.

## ***2.3 Complete linearized sonic boom prediction***

The aerodynamic near field and acoustic far field have to be combined to yield a sonic boom prediction tool. Middleton and Carlson [69] developed one of the first numerical programs to evaluate the sonic boom signatures based on equivalent body theory. Carlson and Harris [12] extended that study to include the aerodynamic analyses and propagation to provide a complete sonic boom prediction environment. The correlation of the linearized sonic boom theory with wind tunnel data was studied [11]. AWAVE, ALIFT and ARAP codes have been integrated into a single unified program for sonic boom prediction [18] and the resulting executable was named PBOOM. The results generated using PBOOM are limited due to the inaccuracies of the individual tools mentioned in the previous sections.

## ***2.4 Sonic boom minimization***

Sonic boom minimization has been of fundamental importance to the supersonic aircraft design from the early half of this century. [9] suggested that the volume effect leading to boom signature can be theoretically overcome but the lift contribution is inescapable. This is because lift has to be provided to overcome the weight of the aircraft and this is inevitably transferred to the ground through the atmosphere.

Most sonic boom minimization concepts are derived from the basic physics and mathematical expressions relating perturbation pressure, altitude, length and other parameters. It is known that when two shock waves coalesce, the resulting shock strength is stronger than the individual shock strengths. From this simple result, the initial sonic boom minimization concepts were proposed to reduce the strength of the shocks near the aircraft. Furthermore, it was realized that undesirable features of the signature can be avoided by special aerodynamic designs which gave rise to shape optimization studies. [34] was the first to show that under the assumption of a stratified atmosphere, the signature reaches an asymptotic value

beyond which there is no further non-linear distortion of the pressure wave. In other words, the waveform is frozen at a particular height. Some minimization studies used the waveform freezing idea to reduce boom strengths.

Sonic boom minimization is usually accompanied with a deterioration of aircraft performance metrics in that the aircraft drag is increased. Sonic boom minimization usually leads to a blunt nose with the result that the configuration has substantial drag. The reason for this can be explained by analyzing the shock attenuation pattern of the near field pressure signature. A blunt nose creates a strong bow shock and so the secondary shocks are weak and do not overtake and enhance the front shock. The result is that in the far field, the bow shock signature attenuates to produce a much weaker pressure signature. But the drag is substantially increased due to the strong bow shock. In contrast, when the nose is sharp, the secondary shocks are stronger and coalesce with the front shock as they propagate, causing an increase in the shock strength and pressure perturbations far away from the aircraft. A trade-off between these conflicting objectives is usually a compromised design balancing both these effects.

The original sonic boom minimization concepts were proposed independently by [56, 10] to calculate the lower bounds of the sonic boom pressure values under the assumption of far field. According to this theory, the overpressure values are functions of only the weight, length, volume of the aircraft and flight conditions. The mathematical basics of the original minimization are a direct realization of the theory presented in Section 2.2.

Following our discussion on Whitham's corrections to linear theory, Equation 13 can be rewritten in the form given by Equation 18.

$$F^2(T, \theta) = \frac{(2\beta)^{3/2}}{(\gamma + 1)M_\infty^4 r^{1/2}} \int_0^T F(\tau, \theta) d\tau \quad (18)$$

If one has to minimize the pressure perturbations, the F-function value has to be minimized following the relation between pressure and F-function. The above equation shows that the F-function value at the shock location has a direct relation to the area under the

F-function computed to that location. Therefore, as long as the area is not altered, the magnitude of the F-function at the shock can be obtained by a simple geometric interpretation as shown in Figure 15. In this figure, a straight line with slope  $\tan^{-1}(1/kr^{1/2})$ , where  $k$  is given by Equation 19 is used to obtain the appropriate value for the front shock location,  $y_B$  such that the areas A and B are equal.

$$k = \frac{(\gamma + 1)M_{\infty}^4 r^{1/2}}{\sqrt{\beta^{3/2}}} \quad (19)$$

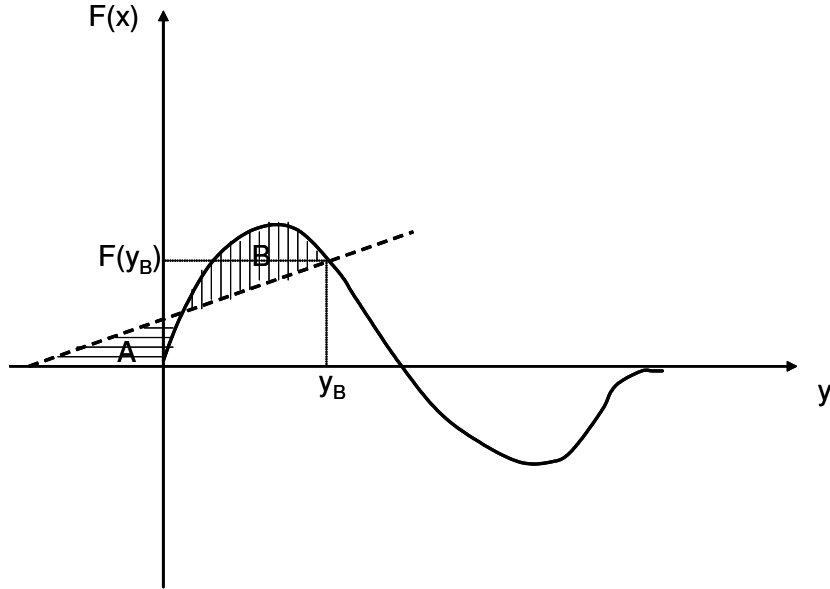


**Figure 15:** Computation of shock location

Before proceeding to show the F-functions which minimize pressure perturbations, another additional constraint has to be introduced. The lift produced by the aircraft is related to the F-function by the Equation 20. In this equation,  $\eta$  is a non-dimensional length coordinate and  $S$  is the equivalent area distribution of the body.

$$S(1) - S(0) + \frac{\beta}{2q}L = 4 \int_0^1 F(\eta) \sqrt{1 - \eta} d\eta \quad (20)$$

In order to show the type of F-functions which offer a reduction in the far field pressure perturbations, the procedure laid down in [56] is followed. In addition to the F-function shown in Figure 15, consider an additional F-function superposed with the earlier one. The

dashed-dotted curve in Figure 16 represents the new F-function. These curves differ only in the interval  $[\eta_1, \eta_3]$ . Both the curves have to satisfy the lift constraint given in Equation 20. The same straight line as used in Figure 15 is superimposed in this figure.

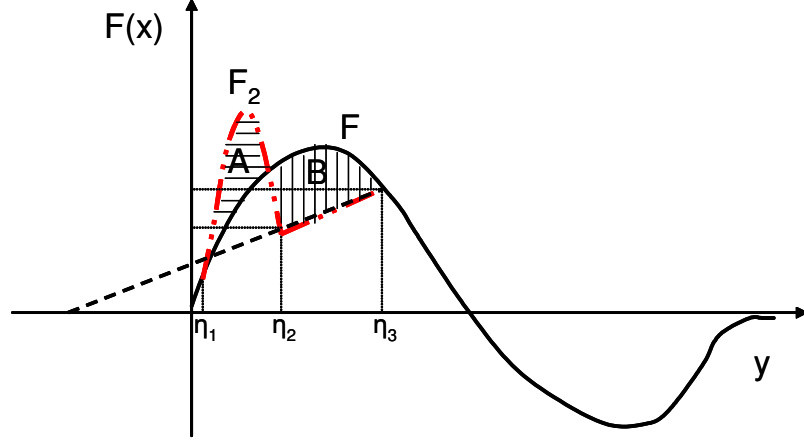


**Figure 16:** Comparison of two different F-functions

According to the lift constraint introduced earlier, Equation 21 has to be satisfied.

$$\begin{aligned} \int_{\eta_1}^{\eta_3} \left[ F_2(\eta) - F(\eta_1) - \frac{1}{kr^{1/2}} (\eta - \eta_1) \right] \sqrt{1 - \eta} d\eta = \\ \int_{\eta_1}^{\eta_2} \left[ F(\eta) - F(\eta_1) - \frac{1}{kr^{1/2}} (\eta - \eta_1) \right] \sqrt{1 - \eta} d\eta \end{aligned} \quad (21)$$

Since the new F-function has a higher value at lower  $\eta$  value, Equation 22 has to be satisfied. In other words the shaded area A is less than the shaded area B in Figure 16.

$$\begin{aligned} \int_{\eta_1}^{\eta_3} \left( F_2(\eta) - F(\eta_1) - \frac{1}{kr^{1/2}} (\eta - \eta_1) \right) d\eta < \\ \int_{\eta_1}^{\eta_2} \left( F(\eta) - F(\eta_1) - \frac{1}{kr^{1/2}} (\eta - \eta_1) \right) d\eta \end{aligned} \quad (22)$$

Following the balancing line logic explained in Figure 15, in order to satisfy Equation 18, the slope of the balancing line has to be decreased. This produces a lower value of  $F(y_B)$  thus leading to a lower shock pressure perturbation.

The final result of all the above mathematical analysis is that, for minimizing sonic boom pressures measured on the ground, the F-function should have a high value close to the nose region of the aircraft, which in the limiting case is a Dirac-Delta function near the nose.

Far field analysis was later extended by Jones [57] to include rear shocks as well. Near field lower bounds were then calculated by George [28] and Seebass [104] and the low sonic boom constraints were laid out. The basis for these constraints is the expression relating perturbation pressure and F-function. Seebass-George provide a specific form of the F-function as given in Equation 23, which minimizes the pressure perturbation in the sonic boom signature. The introduction of the Dirac-delta function at the nose causes a spike in the F-function thus achieving a large value desired of the F-function near the nose.

$$F(y) = \begin{cases} \alpha\delta(y) + By + C & 0 \leq y \leq \lambda \\ By - D & \lambda \leq y \leq l \end{cases} \quad (23)$$

Seebass and George [105, 106] showed that by shaping the equivalent area of a body of revolution, the sonic boom could be mitigated. Using the above F-function, the corresponding area,  $A$ , was obtained in terms of  $\alpha, B, C, D$  as shown in Equation 24.

$$A(y) = 4\alpha y^{1/2} + \frac{16}{15}By^{5/2} + \frac{8}{3}Cy^{3/2} - 1(\lambda)\frac{8}{3}(C + D)(y - \lambda)^{3/2} \quad (24)$$

Conditions were imposed to solve the coefficients of the F-function so as to minimize various boom signature parameters. Simple algebraic expressions were calculated for the minimum shock pressure rise and the minimum overpressure of the sonic boom signature on the ground. Results were published by George and Seebass [29] for conditions under which the front and rear shocks could be eliminated. The important result realized from their study was that if sufficiently long and light weight aircraft can be built, the sonic boom can be mitigated. This method was an elegant mathematical way to ensure that minimum ground pressures were obtained for the specific F-function.

Various research efforts followed the Seebass-George theory for boom minimization. Ferri and Ismail [26] showed that proper positioning of the lifting surfaces affects the lengthwise lift distribution and hence the sonic boom pressures. It was observed that all the sonic boom minimizing designs obtained using Seebass-George minimization theory had blunt aircraft nose thus increasing their drag values. Darden [20] extended the Seebass-George

minimization scheme by introducing a nose-bluntness factor which could then be used to study the trade-off between boom and drag minimization. This was done by considering the F-function to be of the form given in Equation 25.

$$F(y) = \begin{cases} \frac{2yH}{y_f} & 0 \leq y \leq y_f/2 \\ C(\frac{2y}{y_f} - 1) - H(\frac{2y}{y_f} - 2) & y_f/2 \leq y \leq y_f \\ B(y - y_f) + C & y_f \leq y \leq \lambda \\ B(y - y_f) - D & \lambda \leq y \leq l \end{cases} \quad (25)$$

The function representing the above equation is shown in Figure 17. The relevant equations needed for low boom constraints were derived by Seebass and George and are given in equations 26 through 30. These equations are used to solve for  $H$ ,  $C$ ,  $D$ ,  $\lambda$  and  $y_r$  with given values for  $W$ ,  $y_f$ ,  $\frac{p_f}{p_r}$ ,  $B$ ,  $M$ ,  $h$ ,  $z$ ,  $l$  and calculated values for  $G$ ,  $\alpha_y$  and  $SL$ . This produces the required F-function and equivalent area distribution. Equation 26 assumes that the effects due to aircraft wake and engine exhaust can be neglected and that the aircraft volume contribution at the base is zero. Equations 27 and 28 are manifestations of the area balancing rule, introduced in Figure 15, at the front and rear regions of the F-function. Equation 29 specifies the ratio of the front to rear shocks as a function of the desired parameters. This ratio is usually given a value of one. Finally, to ensure that  $y_r$  is the intersection of F-function and the balancing line, Equation 30 is used.

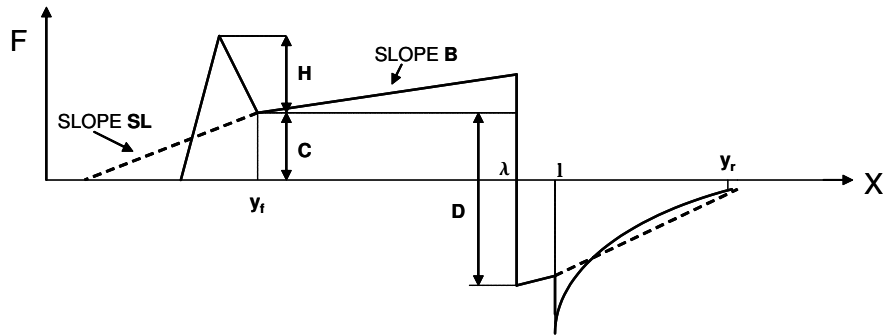


**Figure 17:** F-function shape for minimizing pressure rise

$$A_e(l) = \frac{\beta W}{\rho U^2} = 4 \int_0^l F(y) \sqrt{(l-y)} dy \quad (26)$$

$$\int_0^{y_f} F(y)dy = G = \frac{\alpha_y}{2}C \quad (27)$$

$$\begin{aligned} \int_l^{y_r} F(y)dy &= \frac{-2}{\pi} \int_0^l F(x) \tan^{-1}\left(\sqrt{\frac{y_r-l}{l-x}}\right)dx = \\ \frac{1}{2}[B(l-y_f) - D + F(y_r)](y_r-l) \end{aligned} \quad (28)$$

$$\frac{p_f}{p_r} = \frac{C}{D - B(l-y_f) + F(y_r)} \quad (29)$$

$$F(y_r) = SL(y_r - l) + B(l - y_f) - D \quad (30)$$

These equations are solved simultaneously to yield F-functions, and hence equivalent area distributions, that produce minimum pressure rise signatures on the ground. This minimization strategy is used widely in sonic boom minimization studies. Recently Seebass [109] revisited the minimization problem and provided a figure of merit, given in Equation 31, which is proportional to the aircraft's weight divided by the three halves power of the length. Further they provide a series of important conclusions based on recent studies on sonic boom acceptability.

$$FoM = \left[ \frac{\beta W}{P_g l^{3/2} \sqrt{h}} \right] e^{\frac{h}{2HS}} 10^3 \quad (31)$$

In order to design an aircraft for minimizing certain objective, the designer should know what criteria are to be used. In the case of sonic boom minimization, the right criteria for acceptable levels of pressure signature are not fully known even today. When work began on boom minimization nearly 30 years ago, overpressure and shock pressure rise were minimized. Researchers looked for the best criterion to minimize sonic boom strength. A single better quantity to characterize a sonic boom called "characteristic overpressure",



which is a function of the impulse of the signature, was suggested by Warren [128]. As more has been learnt about the various parameters affecting the boom signature, it is probably not sufficient to minimize just the overpressure, characteristic overpressure or the shock pressure rise of the signature. It is also necessary to minimize the rise time or the perceived loudness affecting humans and structures. While the shock pressure rise, overpressure and the perceived loudness levels are highly correlated, the loudness metric is more sensitive to the atmospheric fluctuations. The perceived loudness depends on various factors and the method presented by Stevens [117] is usually used. However, much research needs to be done in this area to determine human and structural response to these booms. One of the earliest studies conducted to determine the effect of boom signature on human response is documented by von Gierke and Nixon [124]. Brown and Haglund [7] compare the effect of various metrics on the noise level sensitivities. Boom asymmetry affects the perceived loudness and was studied by Leatherwood and Sullivan [58]. Sonic boom simulation studies as presented by Shepherd [110] and subjective human response are ongoing research areas.

## ***2.5 Miscellaneous design studies***

Based on the above concepts and tools, various design studies have been undertaken for the purpose of sonic boom minimization. Much of the work done in the 1980's and early 1990's related to the sonic boom reduction of *HSC*T type vehicles as described by Haglund [32]. A two cycle design process to meet the target equivalent area distribution based on low sonic boom constraints is introduced by Mack and Needleman [64]. In the first cycle, planform is optimized and in the second cycle camber and twist of wings are modified to meet the target equivalent area distribution. Pei Li and Sobieczky [82] studied the sonic boom of oblique flying wing because of its efficient subsonic operation. With the increase in computational power, higher fidelity non-linear near field solutions are being used in conjunction with linear acoustics for propagation. Euler analysis is used by Yoshida [133] to change the wing geometry for minimum drag and then the fuselage shape is changed to produce a low sonic boom. Axisymmetric fuselage is assumed and the fuselage radius is obtained at various locations based on the total equivalent area from minimization theory.

This procedure produces a unique configuration as against other methods which provide a unique total equivalent area distribution with various combinations of the lift and volume contributions. Statistical fits are used by Makino [135] for the signature rise times based on molecular relaxation theory and empirical equations. A numerical optimization of fuselage geometry is performed to modify the sonic boom signature. A combination of linear and non-linear methods for sonic boom prediction is presented by Alonso and Kroo [2]. In addition, an efficient non-linear coupled adjoint method for the calculation of the sensitivity of ground signatures to modifications in the aircraft shape is introduced. The adjoint method is powerful because the sensitivity calculations do not depend on the number of design variables.

A design method with both active sonic boom suppression through off-body energy addition and passive suppression through vehicle shaping was presented by Miles [94]. The study was performed to devise an energy adding mechanism to reduce sonic boom. Farhat and Nikbay [14] proposed a shape optimization methodology where linearized methods were combined with Euler or Navier-Stokes flow solver to reduce the sonic boom initial pressure rise. The shape perturbations were parameterized and the optimizer is allowed to select these perturbation parameters which minimize the objective. The effect of engine placement on sonic boom is studied by Howe [43] using *CFD* methods. the study concluded that placing the engines over the wings causes the shielding of shocks thus reducing the sonic boom loudness on the ground. Vazquez and Koobus [61] used *CAD* free parameterization and multi-level optimization to minimize a volume integral of the squared pressure gradient in a control volume below the object. A shape modification procedure was used by Makino and Yoshida [134] where initially the wing was modified to reduce drag. The sum of equivalent area contribution of all components except the fuselage is added to the equivalent area due to lift. The result is then subtracted from the desired equivalent area distribution from the low boom constraints. The fuselage shape is then driven from this result. Sonic boom reduction studies using non-axisymmetric configuration shaping was studied by Howe [44]. Low boom Wing-canard-fuselage configurations were optimized through genetic algorithms by Sasaki and Obayashi [103].

To reduce the computational complexity associated with non-linear methods, metamodels have been used to replace costly computations from CFD based methods. A kriging meta-model, introduced by Chung and Alonso [46], is used for boom and aerodynamic performance prediction along with a genetic algorithm for shape optimization. The kriging study was extended to use co-kriging [16] approximation models using adjoint sensitivity equations to augment the kriging models. Nadarajah and Alonso [113] developed a set of adjoint equations to quantify the influence of the geometric changes on the pressure distribution at an arbitrary location from the aircraft.

Most of these design studies present their recommendations and identify the areas that need to be stressed to achieve a low boom aircraft. Many organizations are actively involved at present to design a feasible and economically viable Quite Supersonic Platform (*QSP*). The progress made by Gulfstream Aerospace in this aspect is summarized by Wolz [132]. Key technology research areas for successful supersonic flight over land were identified by Hartwich and Wiler [83] of the Boeing company. Some of the industry designs and their salient features are discussed next.

## ***2.6 Industry designs and knowledge base***

### **2.6.1 Concorde**

The first commercial supersonic aircraft to operate successfully was the Concorde. The Soviet TU144 was built and flown at supersonic speeds before Concorde. However, the program was cancelled after a couple of fatal crashes. When it was introduced in the 1970's, Concorde was considered an engineering marvel. Concorde was designed in the 1960's and early 1970's by the combined efforts of British Aerospace and ONERA. Figure 18 presents a schematic [19] of Concorde. There are various features to the Concorde design. Firstly, because of its needle shaped design, the pilots would not be able to see the runway during take-off and landing. So to help improve the view, the nose is drooped down to  $5^\circ$  for take-off and  $12.5^\circ$  for landing, where the aircraft is pitched up at a very high angle of attack. The wing planform is given a smooth continuously varying sweep. Nacelles are placed under the wing and there is no horizontal tail or a canard surface. The stability is achieved by

fly-by-wire controls and stability augmentation systems. While transitioning from subsonic to supersonic regime, the design allowed for fuel to be moved to change the location of center of gravity. However, supersonic flight over land was not possible because of an unacceptably loud sonic boom.



**Figure 18:** Concorde layout [19]

From the early 1990's, various industry partners have been investigating the technologies needed to make commercial supersonic flight possible with unrestricted supersonic flight over land. However, instead of working through the design requirements on a small demonstration aircraft, initial efforts were focused on a 300 passenger commercial supersonic transport called the High Speed Civil Transport. *HSCT* design studies were conducted to provide a better alternative to Concorde for commercial supersonic flight.

After various design studies, it was concluded that feasible designs of a large aircraft such as *HSCT* would require a combination of revolutionary technologies. Since many of the revolutionary technologies would not have been proven, *HSCT* design studies were abandoned. More recently, with renewed interest and lessons learned from *HSCT* studies, various companies and academic institutions have started designing smaller supersonic business jets which have the potential of meeting the design requirements. The reduction in the shock overpressure levels by reducing the size of the aircraft is demonstrated in the Figure 19 [81]. This figure goes on to show that as the weight is reduced from 750,000 lbs. to around 150,000 lbs. , the shock overpressure can be reduced from 3.0 psf to about 1.6 psf. Thus, a

significant improvement can be achieved by weight reduction alone. Further reduction can be achieved by aircraft shaping and other technologies. In the next few paragraphs, the salient features and drawbacks of the latest industry designs are presented.

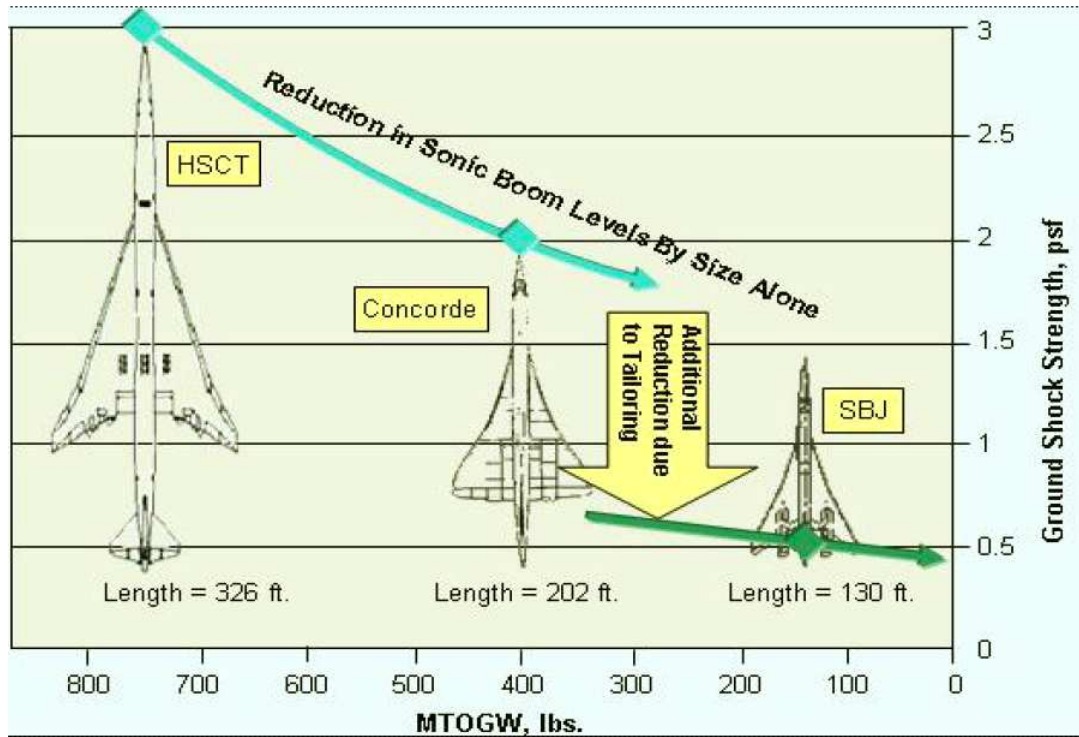


**Figure 19:** Reduction in Sonic Boom overpressure level just from size reduction [81]

## 2.6.2 Aerion Design

Unlike all other companies, Aerion Corporation [1] is not looking at unrestricted supersonic flight over land. Instead, it has been relying on the natural laminar flow on the wings to reduce the drag at various speeds. Aerion claims that straight wing with natural laminar flow, conventional airframe and existing engine technology make its design a low risk alternative with efficient performance over a wide range of speeds. It's design is depicted in Figure 20.

The main drawback for this design is probably that for supersonic flight overland, the aircraft has to stick to pre-specified supersonic corridors. This might increase the distance travelled and result in reduced time savings. Further, it is not fully known whether the natural laminar flow could be sustained over the complete speed regime. Nonetheless, they have continued with their design.



**Figure 20:** Aerion Design for SBJ [1]

### 2.6.3 Gulfstream Design

Gulfstream has been involved in the *DARPA QSP* study for the last four years. The company has an excellent perspective on the market available for supersonic business jets due to its success in subsonic business jets. Gulfstream also has considerable experience with manufacturing and customer requirements.

Gulfstream [131], [39] has conducted conceptual and preliminary studies on some concepts and finally proposed a patented boom-spike [45] concept recently to overcome the sonic boom loudness. The projected loudness gains from their QSP design over the other aircraft is given in Figure 21. In this figure, Gulfstream claims that with advanced shaping and other technologies, approximately  $35dB$  reduction could be achieved in the loudness levels compared to Concorde.

Their design, without the boom spike, is depicted in Figure 22. The nose consists of a retractable spike. The main purpose of the spike is to increase the effective length of the aircraft and to cause multiple low strength oblique shocks instead of a strong single shock. The length of the spike and the position of these spike shocks should be such that they do not coalesce during the pressure signature propagation to the ground.

The spike has been provided with a retraction mechanism [111] so the subsonic performance is not deteriorated. At the same time, having an extended spike would cause storage and other problems on the ground. In order to provide good aerodynamic performance in the supersonic and subsonic regimes, the wing has been given a swing wing shape. During

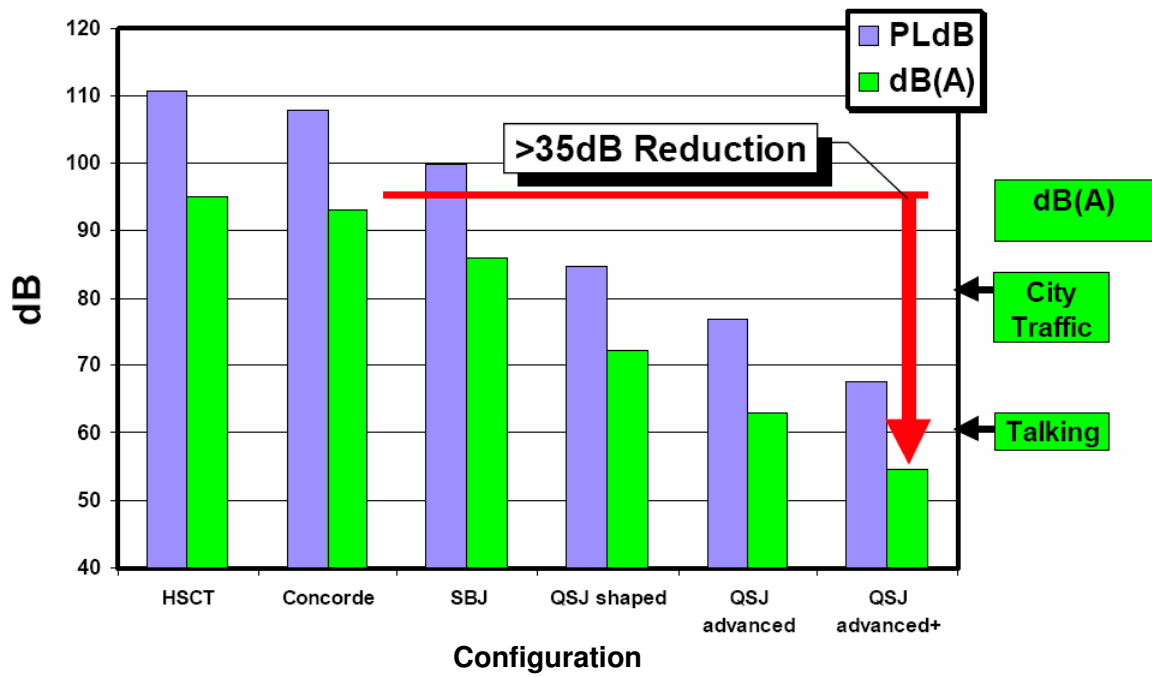


**Figure 21:** Expected loudness gains from Gulfstream QSP study [131]

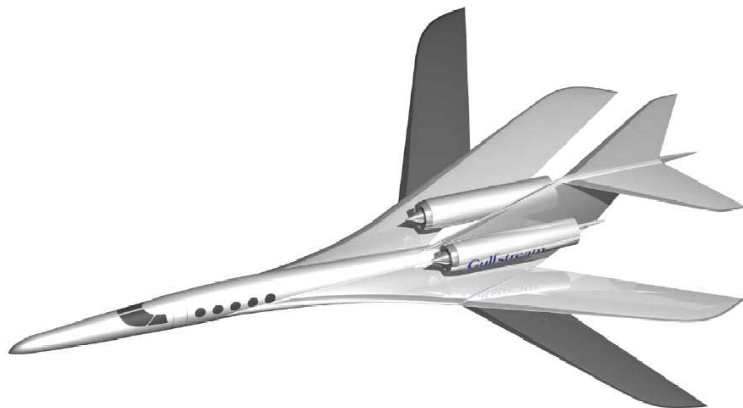


**Figure 22:** Gulfstream Design for QSP [39]

supersonic operations, the wings would be swept back using a swinging mechanism [112]. Following Gulfstream studies [44], the engine nacelles are placed over the wing and to the aft of the aircraft. Positioning the nacelles over the wing causes shielding of the shock waves to a certain extent. The aft positioning is to have sufficient separation between the shocks induced by the wing and the nacelle.

Looking at the design and the corresponding literature, there are some aspects which are not quite satisfactory. Firstly, there is weight penalty associated with the spike retraction mechanism as well as the wing swinging mechanism. Stability and aero-elastic issues have to be studied and detailed wind tunnel tests have to be performed.

#### 2.6.4 Lockheed-Martin Design

Lockheed-Martin has also been conducting their own study to design a quiet supersonic transport (QSST) with funding from Supersonic Aerospace International (SAI) [99]. Their design [60] is based on patented [72] idea of tail-braced wing for sonic-boom suppression. Lockheed's design is depicted in Figure 23.



**Figure 23:** Lockheed-SAI QSST Design [99]

Unlike the Gulfstream design where the nacelles were placed above the wing, Lockheed design has the nacelles under the wing. In order to remove the adverse effect of the nacelle interference, the wing is reflexed to counteract the negative effect of the nacelles. This is different from the traditional wing reflexing in that in addition to the camber slope change, the thickness slope is also changed to make the flow on the top surface of the wing unchanged while at the same time cancelling the shock reflection from the lower surface of the wing. The tail-braced joined wing design provides sufficient structural stiffness to the aircraft and



also increases the effective length of the aircraft because joined wing designs cause the lift to be carried by the anhedral rear wing. This causes stability concerns as well as increased trim force required to maintain level flight. In order to compensate for this, the tail is designed to carry less than 25% of the total lift. In addition, with the electronic stability augmentations systems, stability problem can be overcome. High wing sweep in conjunction with low tail sweep reduce the length of the tail. This feature along with low tail taper create a high buckling resistance in the structure. The design, thus, has better aero-elastic properties. The end result of the above features is a design with projected loudness gains as depicted in Figure 24 [100]. This figure compares the QSST design with other designs. Lockheed claims to have achieved a  $dBA$  of around 55, which is less than the loudness level while talking normally.

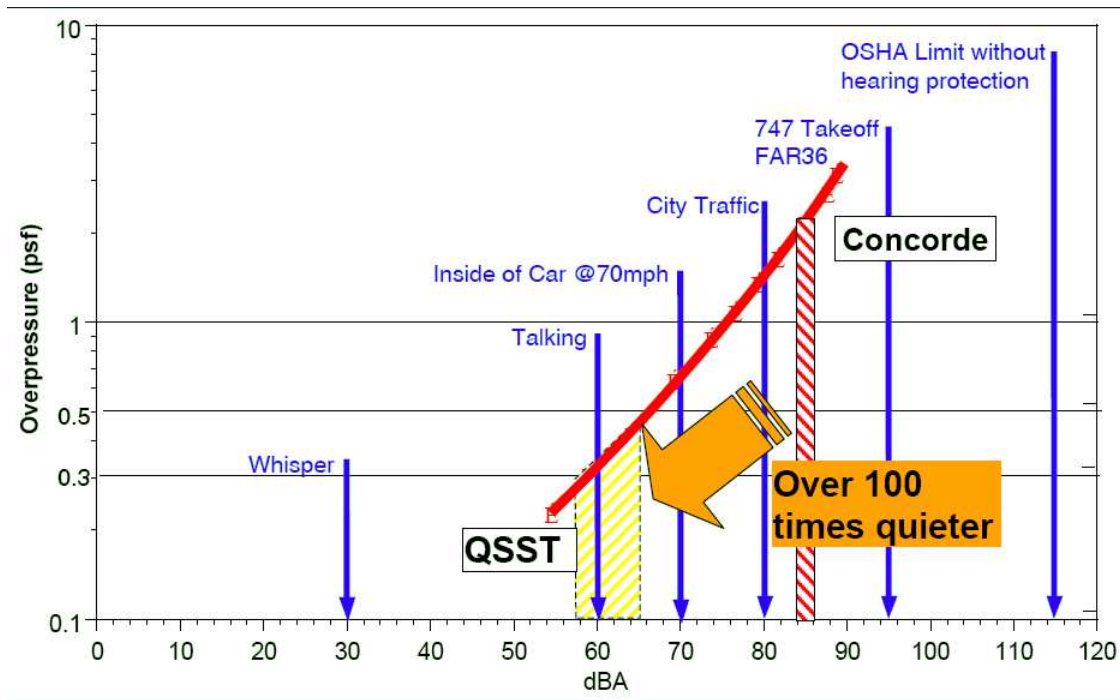


**Figure 24:** Expected loudness gains from Lockheed-SAI QSST study [100]

### 2.6.5 Other Designs

Various other companies and organizations including Boeing, Northrop-Grumman and INRIA [61] are believed to be actively pursuing their designs behind closed doors. Similar activities are also being pursued in Japan [42], [134] and Russia [118].

# CHAPTER III

## IMPROVED DESIGN TOOLS

### *3.1 Geometry generation*

An efficient shape parameterization strategy is a prerequisite for performing aerodynamic shape optimization. Geometry generation is a key issue in shape optimization studies. Various techniques have been introduced in the past to create efficient parametric geometries. Bloor and Wilson [6] introduced a partial differential equation approach to obtain arbitrary aircraft configurations by solving a bi-harmonic partial differential equation (*PDE*). Smith and Thomas [95] extended the PDE approach to generate arbitrary configurations along with volume grid generation and grid sensitivity. Various geometry generation tools and their important features were presented by Kerr and Posenau [80]. Samareh [101, 102] provides an excellent compilation of different shape parameterization techniques.

The above techniques, though very useful to create mathematically closed surfaces in further stages of design, consume a significant set-up and computational time. What is needed in conceptual design is a technique by which many geometries can be analyzed in a quick and efficient manner to obtain the same or better level of fidelity achieved by the tools mentioned in the previous paragraph. Importance has to be given to automation and computational time. A MATLAB based geometry generation and discretization method has been developed and demonstrated by Rallabhandi and Mavris [92] to create water-tight geometries quickly and efficiently.

The idea is to use variables to control the shape as well as the configuration of the aircraft. The configuration variables are discrete and different values for these produce different types of components as shown in Table 1. As can be seen from this table, various shapes are already programmed into the geometric tool and this results in a wide variety of configurations that can be generated. For example, depending on the value of discrete wing parameter, the

wing geometry can be a conventional, delta, double-delta, multi-section or a swing-wing design. Canard, conventional or T-tail geometries and configurations with various engine configurations can be generated. From Table 1, if all components have to exist, there could be 1728 discrete types of configurations. In addition, within each configuration, there are various continuous parameters to define the shape of each component. This is explained briefly in the next paragraph.

Table 2 presents some of the important continuous parameters to determine the shape of individual components. Included here are various planform parameters, control points for NURBS surfaces and bezier curves. Fuselage shapes produced by the formulation include axisymmetric and non-axisymmetric fuselages which are pointed or blunt or area-ruled. Wing shape parameters include twist, camber, control points for leading edge bezier curve and various other parameters. Other parameters are simply dimensions and planform locations of components. The maximum number of parameters used to create a single configuration is 75.

Figure 25 shows a sample geometry generated using this parameterization strategy. Once geometry is obtained, surface discretization is done. However, before geometric operations are presented, a brief review of the parametric curves and surfaces is provided next.

**Table 1:** Discrete parameters

Component	Component type parameter					
	0	1	2	3	4	5
Fuselage	No Fuselage	Nose specified -bezier curve	Full Fuselage - bezier curves	NURBS nose, rest-bezier curves	Fuselage in cross-sections	Area ruled Fuselage
Wing	No wing	Conventional wing	Delta wing	Double delta wing	Concorde like multi-section wing	Swing-wing
H-Tail	No H-Tail	Canard	Conventional	T-tail	T-tail + Canard	Joined wing
V-Tail	No V-Tail	Conventional				
Engine	No Engines	Wing mounted, 2 below wing	Fuselage mounted	Wing mounted, 2 above wing	Wing mounted, 4 below wing	
						Sears-Haack Nose
						Raytheon like multi-section wing

**Table 2:** Important continuous parameters

Component	Important continuous parameters	
	Important continuous parameters	
Fuselage	Length, Maximum diameter, Max. diameter location, bezier control points for nose, mid-section and aft region, Camber, Camber location, blunt-ness parameter, parameters for non-axisymmetric nose section	
Wing	Wing location, $t/c$ , camber, camber location, twist distribution, dihedral, Bezier control points for leading edge,sweep, span	
H-Tail	Aspect ratio, taper ratio, sweep, $t/c$ , longitudinal location, vertical location	
V-Tail	Aspect ratio, taper ratio, sweep, $t/c$ , longitudinal location	
Engine	Engine location, radius, hub to tip ratio, engine length	

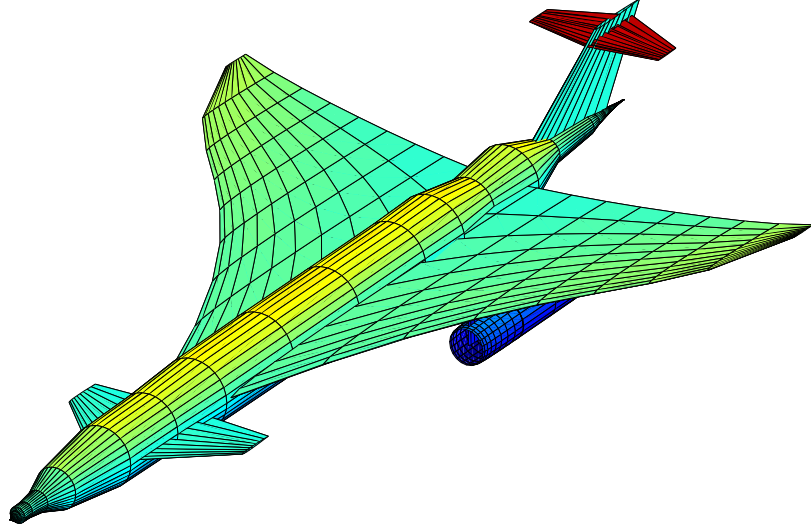


**Figure 25:** Sample Wire-frame geometry generated by the parametric geometry generation tool

### 3.1.1 Bezier Curves

A bezier curve is a smooth parametric curve determined by the vertices of a polygon using known set of basis functions. A bezier curve is represented mathematically as shown in Equation 32

$$P(t) = \sum_{i=0}^n B_i J_{n,i}(t), 0 \leq t \leq 1 \quad (32)$$

where the basis functions are given by

$$J_{i,n}(t) = \binom{n}{i} t^i (1-t)^{n-i} \quad (33)$$

The  $B_i$  are the vertices of the control polygon. Figures 26 and 27 show sample bezier curves along with the corresponding polygons. These figures show that smooth curves could be obtained using a few parameters if Bezier basis functions are used. There are various aspects of the Bezier curves that can be grasped from the definition above and the figures. The degree of the curve is one less than the number of vertices in the polygon. The curve

follows the shape of the polygon and the slopes of the curve near the end points of the polygon match with the slopes of the first and last line segments of the polygon.

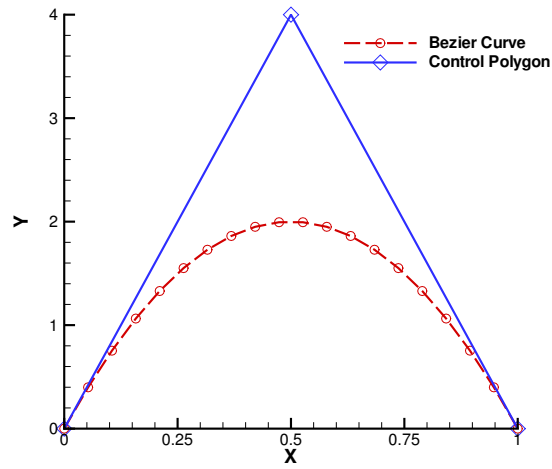


**Figure 26:** Sample Bezier curve

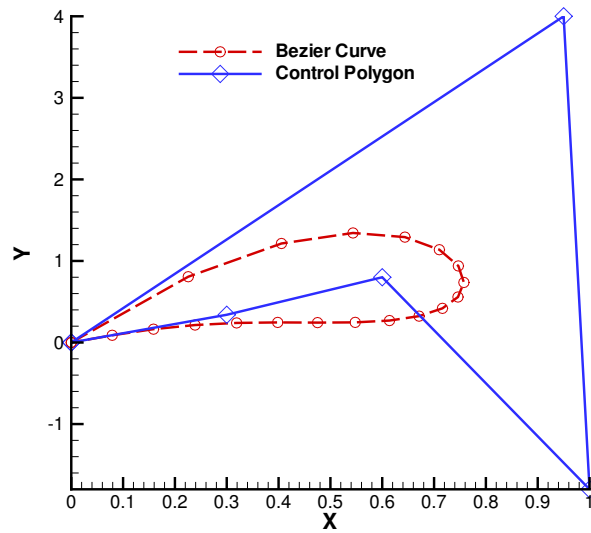


**Figure 27:** Sample Airfoil Bezier curve

Using control points as parameters, many practical curves could be generated for various components such as fuselage or wing profile.

### 3.1.2 NURBS surfaces

All of the commercially available CAD packages use Non-uniform Rational B-Spline (NURBS) surfaces to represent the surface of a three dimensional solid body. The basic ingredient of NURBS is a B-spline curve. Even though Bezier curves are extremely useful in representing smooth curves with very few parameters, they suffer from two major drawbacks. Firstly, the degree of the Bezier curves is one less than the number of vertices in the control polygon. So, if the degree of the curve has to be changed, the number of vertices have to be changed. Secondly, the basis functions for the Bezier definition are global in nature. This means that the basis functions are non-zero over the entire curve or in other words, all of them contribute to the value of the curve at any point. Thus, if one were to change the location of a vertex, the whole curve is changed and eliminates the ability to change the curve locally.

In order to overcome these drawbacks, B-splines were introduced. They are generated according to the Equation 34

$$P(t) = \sum_{i=1}^{n+1} B_i N_{i,k}(t), t_{min} \leq t \leq t_{max}, 2 \leq k \leq n+1 \quad (34)$$

The normalized B-spline basis functions of degree  $k - 1$  are defined using the recursion formulae given in equations 35 and 36. In these equations,  $x_i$  represent elements from a non-decreasing knot vector sequence.

$$N_{i,1}(t) = \begin{cases} 1 & x_i \leq t \leq x_{i+1} \\ 0 & otherwise \end{cases} \quad (35)$$

$$N_{i,k}(t) = \frac{(t - x_i)N_{i,k-1}(t)}{x_{i+k-1} - x_i} + \frac{(x_{i+k} - t)N_{i+1,k-1}(t)}{x_{i+k} - x_{i+1}} \quad (36)$$

The various properties of B-spline curves can be obtained from Rogers [96]. The B-spline curve is affected by various aspects. Firstly, the control polygon vertices control the shape of the curve as in the case of Bezier curves. In addition, the kind of knot vector used affects the shape of the B-spline basis functions thus influencing the shape of the B-spline curve.

Finally, the degree of the B-spline can be changed independently of the number of vertices in the control polygon. All three aspects contribute to the final B-spline curve. Figure 28 depicts the comparison of the basis functions of order  $k = 3$  with varying knot vector sequence as given in Table 3. As can be seen from the figure, for third order b-splines, there are 5 basis functions as specified by  $N_1, N_2, N_3, N_4$  and  $N_5$ . Each basis function is non-zero over  $k + 1$  knots. The end knots have multiplicity of  $k$  so as to achieve any suitable value at the end points by coefficient scaling. Note also that by increasing the multiplicity of the interior knots, the degree of continuity of the basis functions decreases. This is clearly seen from sketch (d) where the third basis function is not differentiable at 1.5 because of the knot vector chosen. Thus, varying basis function shapes with the required level of continuity properties could be obtained by varying the knot sequence.

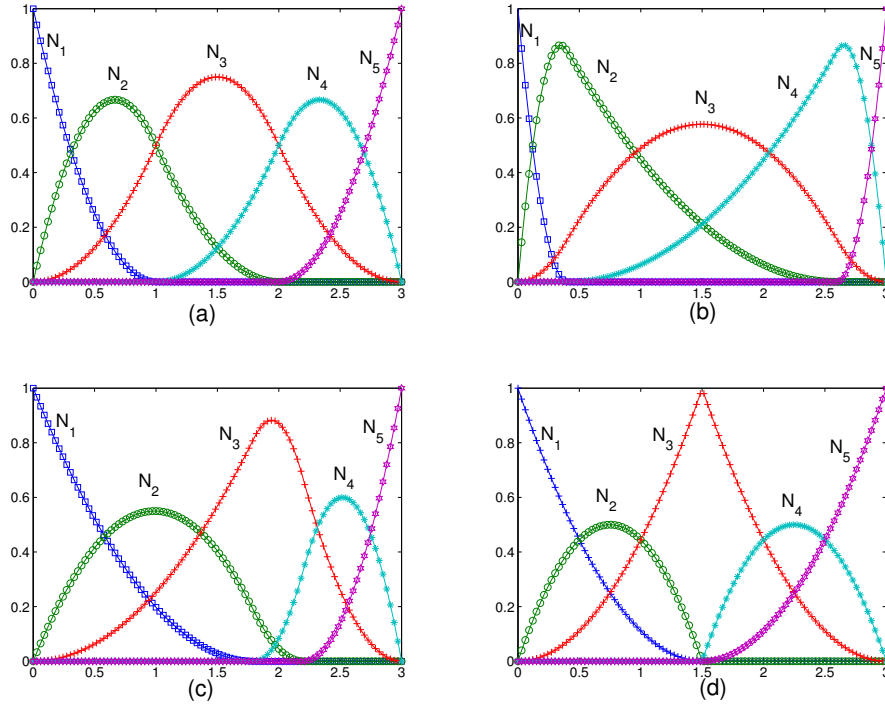


**Figure 28:** B-spline basis dependence on knot vector

Figure 29 shows the local control that is possible with B-splines. The solid lines represent the control polygon. The local control can be demonstrated by changing the fifth vertex of the control polygon. As the fifth vertex is moved from  $B_5$  to  $B_5^1$  to  $B_5^2$ , only the middle



**Table 3:** Varying knot vectors for B-spline basis

Sketch	Knot Vector
(a)	[0 0 0 1 2 3 3 3]
(b)	[0 0 0 0.4 2.6 3 3 3]
(c)	[0 0 0 1.8 2.2 3 3 3]
(d)	[0 0 0 1.5 1.5 3 3 3]

portion of the curve varies. This sort of local control is not possible with Bezier curves as has been discussed earlier.

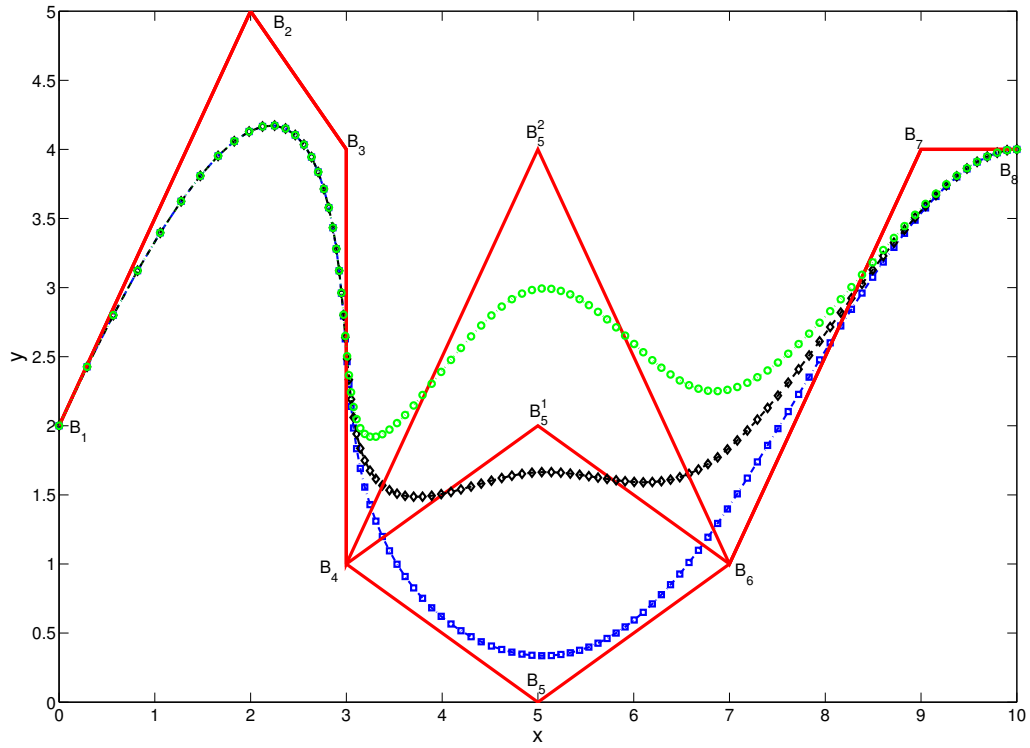


**Figure 29:** Local control of B-splines

Rational B-splines are an extension to the B-spline curves discussed above. They form the projection of the B-spline curve defined in four dimensional homogenous space back into the three dimensional physical space. In other words, the rational B-spline curves are defined using Equation 37 with  $B_i$  being the three dimensional control polygon vertices. The basis functions are now slightly changed and are given as in Equation 38.

$$P(t) = \frac{\sum_{i=1}^{n+1} B_i h_i N_{i,k}(t)}{\sum_{i=1}^{n+1} h_i N_{i,k}(t)} = \sum_{i=1}^{n+1} B_i R_{i,k}(t) \quad (37)$$

$$R_{i,k}(t) = \frac{h_i N_{i,k}(t)}{\sum_{i=1}^{n+1} h_i N_{i,k}(t)} \quad (38)$$

Figure 30 compares the basis functions of the non-rational and rational b-spline basis function of order 4. The rational basis have been obtained using the homogenous co-ordinates [1111010111]. The fourth and fifth basis functions are heavily weighed and this leads to a higher contribution from this basis functions as shown in the figure. However, since the summation of all the basis functions at each point in the domain should add to 1, the other basis functions are correspondingly reduced in the region where the fourth and fifth basis functions exist.

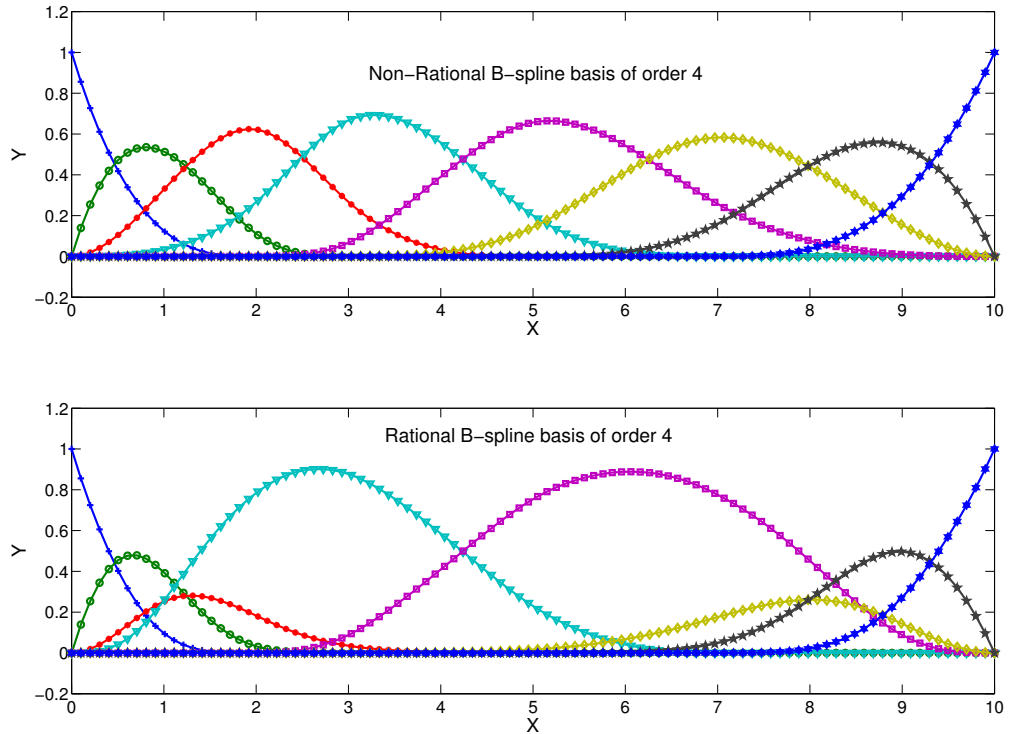


**Figure 30:** Rational B-spline basis of order 4

The important aspect of the rational B-splines is that they provide additional control using the homogenous co-ordinate. The higher the value of the homogenous co-ordinate, the

higher is the contribution of the particular control polygon vertex in the final curve. This is depicted in Figure 31. The control polygon is the same as used in Figure 29. However, due to the rational nature, the curves are pushed towards the fourth and fifth vertices.

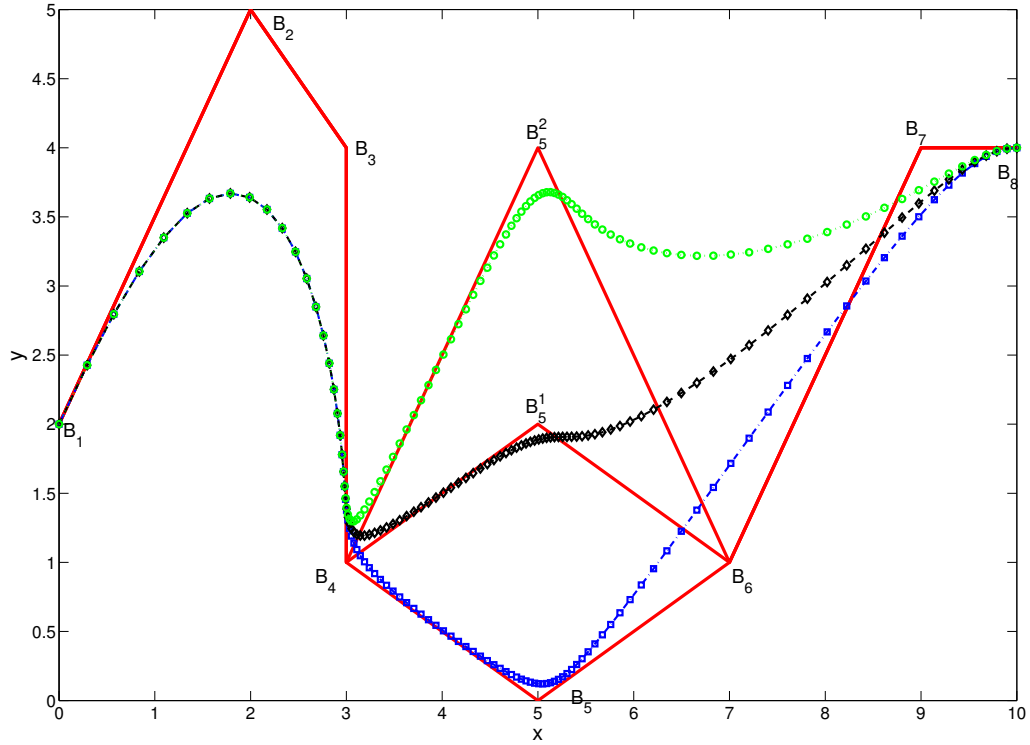


**Figure 31:** Local control of B-splines

### 3.1.3 Using Bezier and NURBS surfaces in geometry generation

As described above, Bezier curves and NURBS surfaces provide a standard form of the geometry definition used in numerous computer aided design packages. The use of NURBS surfaces in creating aircraft nose shapes is demonstrated here. Shown in Table 4 are the variables cabin diameter,  $Cdia$  and nose length, used to generate the shapes shown in Figure 32. As can be seen from this figure, a variety of nose shapes can be generated with this strategy.

The control points used for the NURBS surface are obtained as a function of the design variables shown in Table 4 with the definitions given in sketch 33. The camber function,  $Camb$ , of the nose cone is a quadratic expression with an input parameter  $t_4$ , shown as  $Camb(t_4)$  in the sketch. The parameter  $h$  in the sketch shows the homogenous coordinate

**Table 4:** Sample values of design variables for NURBS nose cone

Design Variable	Value
Nose maximum diameter (Cdia)	2.0
Nose length	4.0
$t_1$	Value $\in [0,1]$
$t_2$	Value $\in [0,1]$
$t_3$	Value $\in [0,1]$
$t_4$	Value $\in [0,1]$
$t_5$	Value $\in [0,1]$

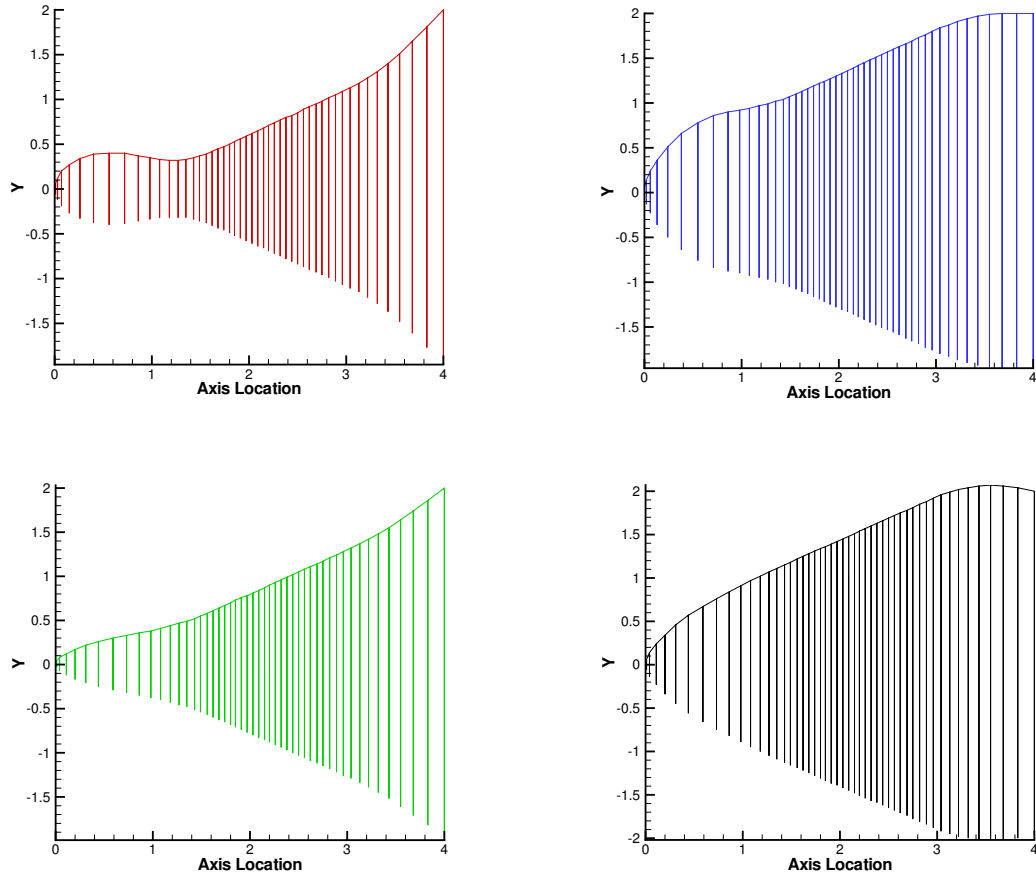


**Figure 32:** Side view of some nose cone NURBS surfaces

in the NURBS definition. The axial locations,  $y$  and  $z$  represent the cartesian coordinates of the control points. These parameters are used so as to give a varying cross-section shape to the nose.

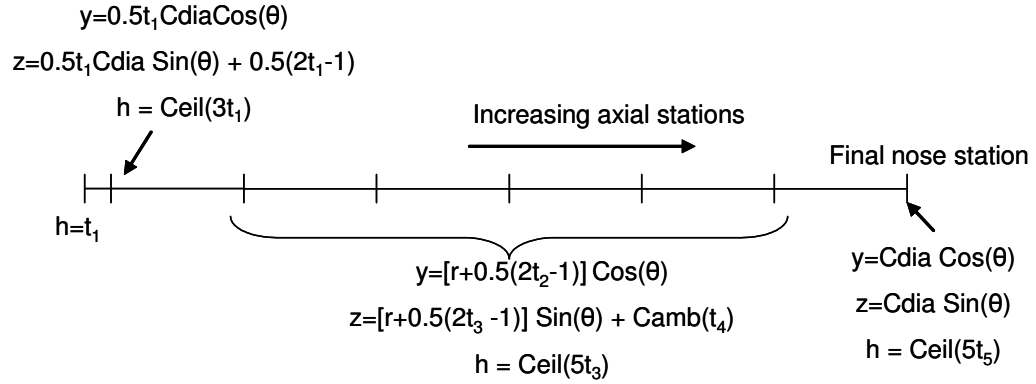


**Figure 33:** Sample sketch showing parameters for nose cone

### 3.1.4 Other Nose cone shapes

In addition to the NURBS surface nose, it was also decided to include a half Sears-Haack body for the aircraft nose as shown in Figure 34. The reason for including this is that a Sears-Haack body has the least wave drag. The optimizer could theoretically achieve these shapes after certain number of iterations. However, since these shapes are known to produce less drag values, a special case to include these could improve the convergence time. In order to create the nose, the parameters used are the cabin diameter and cabin location of the aircraft. Assuming that the cabin location is half the length of a Sears-Haack body, the geometry of the nose cone can be constructed.

## 3.2 *Surface refinement and discretization*

Once a geometry has been created, it should be discretized for numerical analysis. The shapes obtained by the design process are of not much use for further analysis if these shapes cannot be translated into a CAD definition for manufacturing. Ability to manufacture should be induced into the design process right from the conceptual level. This could reduce the time during design iteration and thus reduce the total life cycle cost of the final end product. It is therefore essential to create an integrated design procedure, where generated

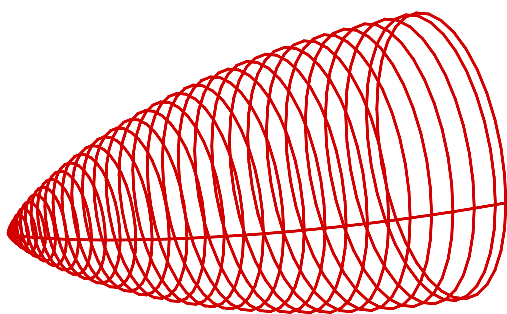


**Figure 34:** Sears-Haack nose

configurations are easily and automatically translated into water-tight CAD geometries. Apart from manufacturing, a CAD definition provides a common geometry format for various analyses and disciplines.

Given a wire-frame geometry composed of various components, the first job is to refine the geometry to ensure better quality surface mesh. A geometry refining tool has been written to accomplish this task automatically. This tool works by progressively introducing cross-sections and computing the aspect ratio of the quadrilaterals. The refining process is terminated once the aspect ratio of all the quadrilaterals is at least equal to that specified by the user. Figure 35 shows a geometry created by the geometry engine explained in the previous section along with a refined version of the same geometry. Note that by doing this operation, long isosceles triangles are eliminated in the surface triangulation as explained later, thus improving numerical accuracy of the solution.

In order to perform numerical analysis, the geometry has to be suitably discretized. A useful library called GNU triangulated surface library (GTS) [89] is used to obtain a surface discretization of the aircraft. An application has been created using this library which reads one component at a time from the geometry file and operates on it to triangulate it. Care is taken to fill openings in each component such as engine inlets and wing tips with triangles.

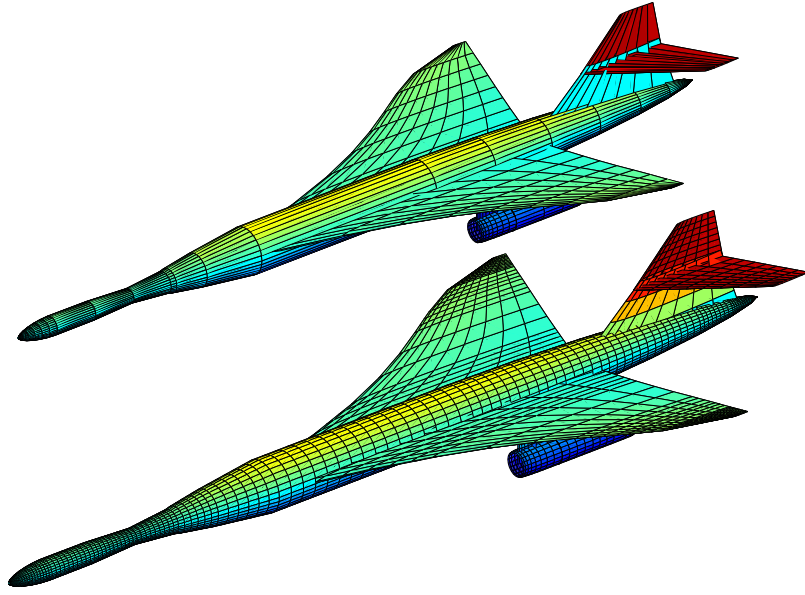


**Figure 35:** Wire-frame geometry and its refined counterpart

Each such closed component is placed in a stack sequentially.

After this, surface boolean operations are performed on components taken in turn from the stack of components. GTS provides a simple object-oriented structure giving easy access to the topological properties of the surfaces and performs robust union, intersection and difference operations on three dimensional surfaces. Surface boolean operations within GTS perform an efficient job of calculating the three dimensional curve of intersection between components and cropping the surfaces beyond this curve. This procedure is continued till all the components in the stack are used up.

Figure 36 shows the triangulated individual components. Note that each component of the aircraft has been triangulated and sealed so that each component is water-tight. Depending on the location of components on the stack, they are taken in turn from the stack and combined together two at a time. If a certain combination does not intersect a component in the stack, the next component is tried. The final result of these geometric operations is shown in Figure 37. This procedure ensures that there is no volume duplication. The generated configuration provides a basic geometry platform on which different aerodynamic analyses could operate. Note also that surfaces can be distinguished from each other by using

a different color for each component. This makes it easy in the later stages of design if the mesh over a particular component, for example wing, has to be refined without disturbing the mesh resolution over other components. It is also useful if a particular component is subject to a boundary condition different from other components. It thus provides adequate flexibility to the configuration designer to play with different components of the aircraft. A meshed surface geometry could be achieved in about 2-3 seconds on a desktop computer. *GTS* also provides algorithms to control the quality of the surface triangles and also routines to output stereolithography format for immediate use in a CAD package. *GTS* provides routines to refine or coarsen the surface triangulation.

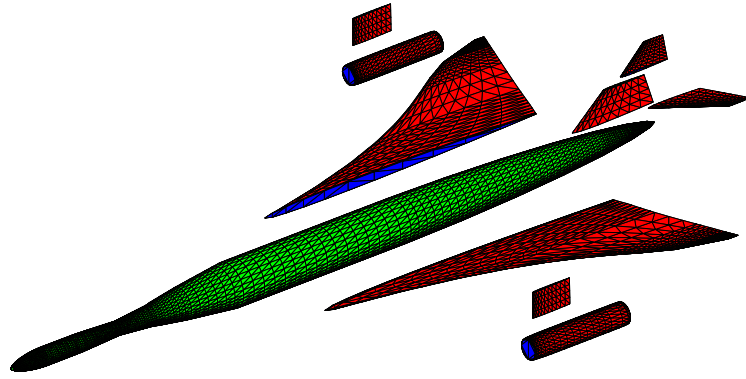


**Figure 36:** Triangulated individual components of aircraft

Apart from providing an efficient discretization scheme, the unstructured triangular grid generated in this process can be used in other high fidelity analysis such as an unstructured grid solver or an unstructured panel code for conceptual lift analysis. In such a scenario, the time from geometry generation to start CFD analysis takes just a few seconds compared to a few hours it takes to do this using the existing codes on a single processor machine. In addition, significant man hours could be eliminated because a CAD model could be obtained without actually using any CAD expertise. Furthermore, by performing the above geometric transformation, the duplicated areas and volumes, which would otherwise have lead to an incorrect area distribution as in Harris wave drag program, can be eliminated.



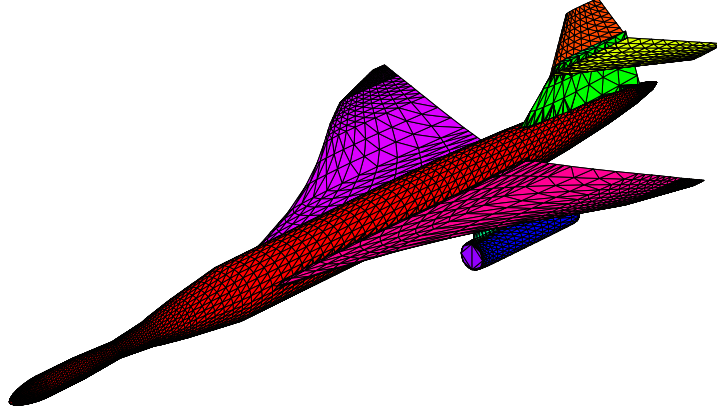


**Figure 37:** Fully triangulated aircraft

### ***3.3 Improvements to the equivalent area estimation***

For the equivalent area due to volume, flat planes are first generated and then rotated and translated to the required position and azimuthal orientation to obtain Mach planes. Rotation and translation matrices [75] for this transformation are generated by using the normal direction of the required Mach plane that is a function of the azimuthal angle. The method proposed in this paper uses efficient geometric algorithms to obtain the true Mach-plane intercepted area. The aircraft axis is discretized to user specified resolution and Mach planes generated at these axial locations are used to obtain the Mach plane intercepted areas of the aircraft at different axial locations. The developed code can compute the equivalent area due to volume distribution of any arbitrary body by directly operating on the true geometry as introduced by the [91]. The method has been validated over a Sears-Haack body and several other configurations and is believed to improve upon the results generated by AWAVE. Figure 38 shows the comparison of the equivalent area predicted for a Sears-Haack body at a Mach number of 1.0 . The area predicted from the newly developed tool exactly matches with the analytical expressions for the area distribution of the Sears-Haack body.

Figure 39 depicts a sample wing-body-canard geometry on which different analyses are run. Figure 40 shows the equivalent area due to volume comparison on the above geometry

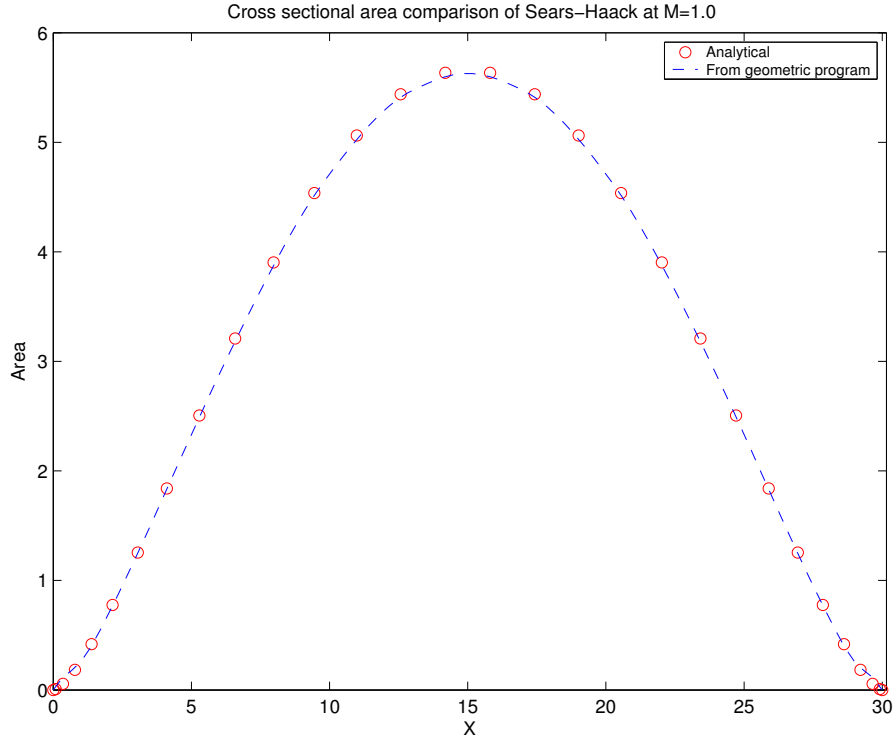


**Figure 38:** Equivalent area due to volume comparison for a Sears-Haack body

for a Mach number of 1.4. Two versions of the Harris wave drag code are run for comparison. The original AWAVE allows the wing to pass all the way to the fuselage center line. To avoid area duplication, original AWAVE has been modified to truncate the wing before it intersects the fuselage. However, this could introduce a gap between intersecting components. Clearly, the original wave drag code produces a distribution that over-predicts the values when the wing contribution kicks in. The simple modification to Harris wave drag code under-predicts the values. Using the Mach-plane intersection areas, the actual equivalent area is correctly computed since the geometry is treated as a single discretized configuration rather than a collection of various loosely placed components. A slight discrepancy from the canard is also observed in the equivalent area plots. This trend is depicted in Figure 40.

The case of geometries with engines is slightly tricky. Because the flow goes through the engines and not around it as for other components, the engine capture area has to be subtracted. However, the axial locations where the engine contribution starts and ends have to be computed exactly for a Mach number greater than 1. In order to do this accurately, the engines are extended in both directions and then use Mach planes to obtain the intercepted

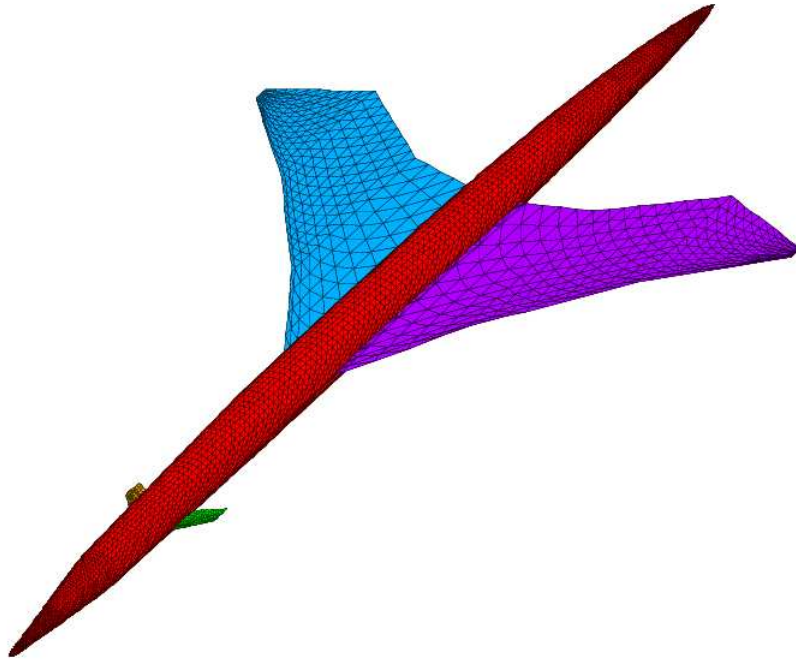


**Figure 39:** Sample wing-body-canard geometry

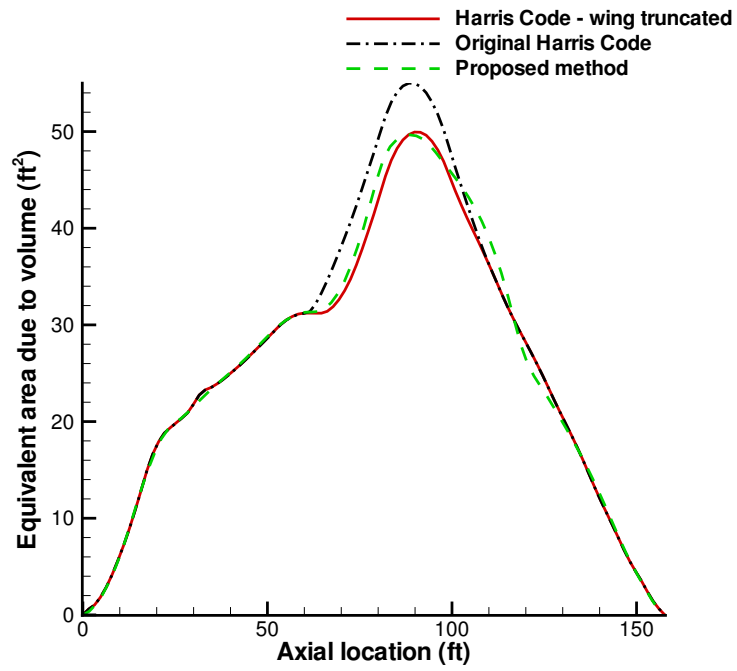


**Figure 40:** Equivalent area due to volume comparison on a wing-body-canard geometry

area. By doing this, flat regions of just engine contributions are obtained in the front and rear of the area distribution as shown in Figure 41. The last axial location of the front flat region and the first location of the rear flat region are then identified, as shown by the circles. The engine capture area is then subtracted from the area contribution and angle of attack corrections are made to yield the actual equivalent area due to volume as shown by the solid line in this figure. Note also that if the inlet capture area is different from the nozzle exhaust area, the area distribution would have a non-zero contribution at the end. The small spike seen in the figure is due to the combined contribution of the vertical and horizontal tail.

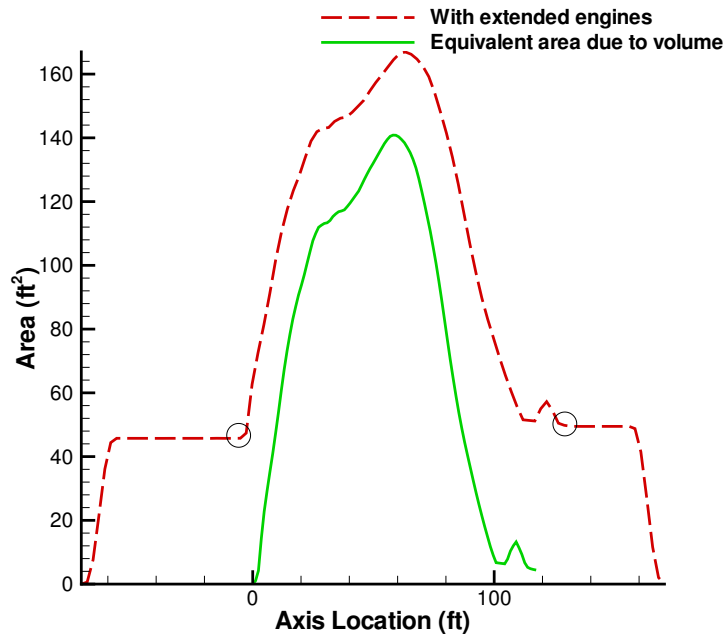


**Figure 41:** Equivalent area due to volume for geometries with engines

Sonic boom reduction is usually accompanied by increased drag values for the aircraft. Therefore, it is essential to have analysis routines to compute various components of drag and minimize boom and maximize aircraft performance simultaneously. One of the important components of drag for supersonic flight is the wave drag. According to slender body theory and equivalent body assumption, the average aircraft area intersected by the Mach planes oriented at different azimuthal angles at various locations on the aircraft axis is the area that affects the wave drag computation as opposed to sonic boom calculation where only a single azimuthal angle of  $-90^\circ$  is used. This is because, for primary sonic boom calculation,

only disturbances travelling exactly below the aircraft are needed, whereas for the wave drag, contributions from all directions are needed. The average aircraft area intercepted by many Mach planes oriented at various azimuthal angles is computed. The Mach planes are gradually translated along the axis and the average intersected area at each location is determined to obtain the distribution of the Mach plane intercepted area of the aircraft. The wave drag values obtained match with the analytical expressions for a Sears-Haack body to within 0.5% if sufficient surface resolution is allowed. The comparison of the wave drag results over an arbitrary geometry obtained using the proposed tools and a CFD flow solution is presented later on in this thesis after the procedure of exporting the geometries to high fidelity analysis is discussed. It was found that the wave drag values are not very sensitive to the number of azimuthal Mach plane cuts as long as the number of cuts is more than 8.

### ***3.4 Automatic CFD transfer capability***

As has been mentioned many times in this thesis, one of the important advantages of this research is to be able to provide a smooth transition to a computational fluid dynamics simulation from linearized analyses. With the present setup, after a geometry is generated, it is carried through different steps to produce a surface triangular grid over the aircraft. This is then used to generate a volume grid and the CFD flow field can be solved. The CFD tool used for demonstration in this study is called *NASCART*. Its a cartesian grid Euler/Navier-Stokes solver with grid adaptation. It is being developed at Georgia Tech and interested reader can obtain information from [98]. *NASCART* was used because it was readily available and the author was working with it at the time. Figure 42 shows the pressure contours after solution convergence over a sample configuration for a Mach number of 1.4. The front bow shock, wing leading edge shock, trailing edge shock and fuselage tail shock can be seen in this figure. This shows that the actual effects of the true geometry can be realized through CFD with run time far better compared to the traditional way of performing CFD analysis. As a further note, during the surface discretization stage, the neighboring triangle information is also stored and is supplied to the CFD solver. This information along with the

surface grid allows the CFD pre-processor to quickly generate the volume mesh necessary for computing the flow field. Thus, the CFD flow solution procedure efficiency is highly improved.

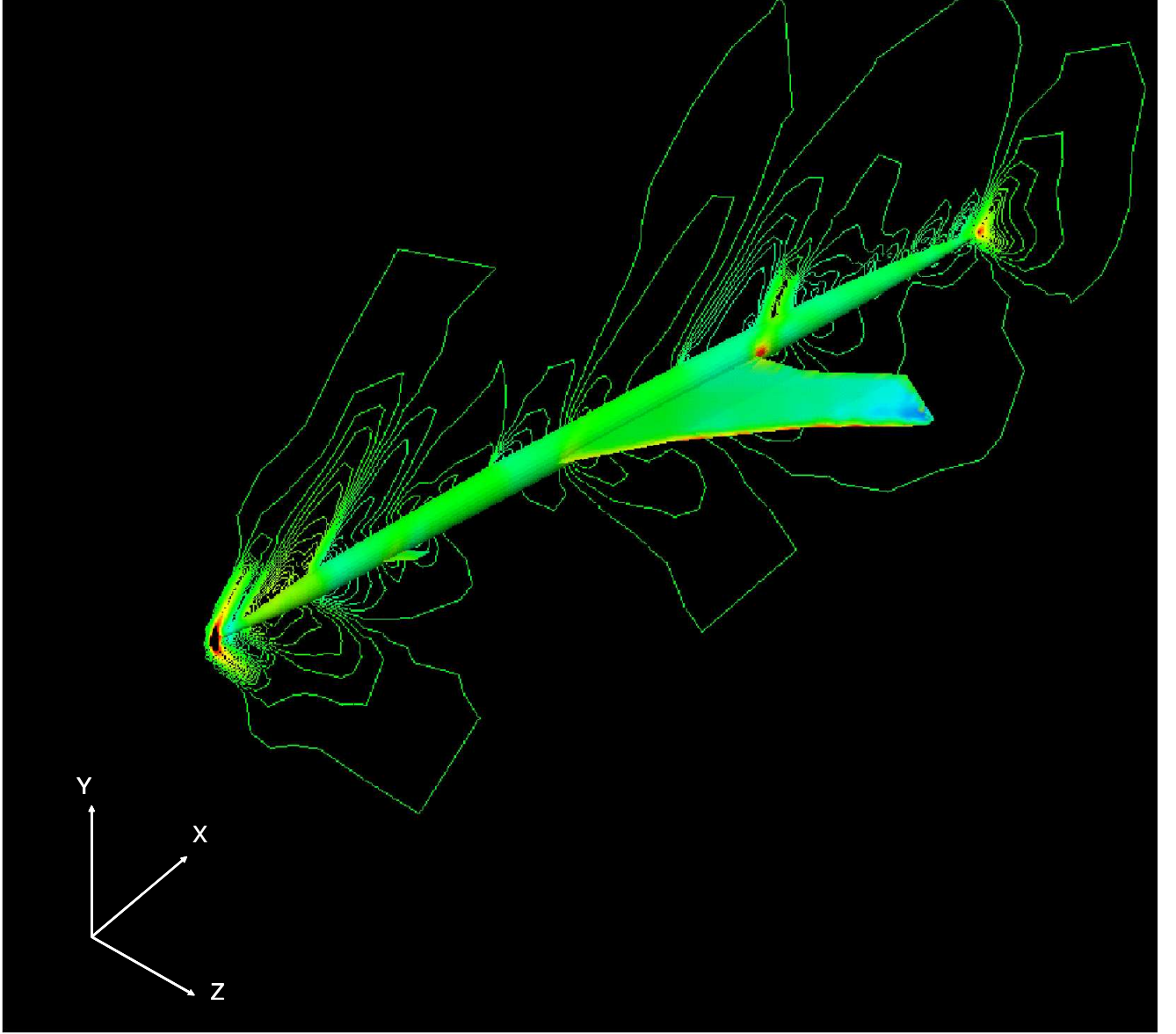


**Figure 42:** Pressure contours obtained from Cartesian CFD solver

Figure 43 shows the residual history of the of the flow solution. The spikes in this plot indicate the adaption process in the flow solution procedure. Figure 44 shows the convergence of the inviscid drag coefficient with a reference area of  $1.0m^2$ . These figures demonstrate the importance of this method in actually obtaining the CFD results with minimum effort.

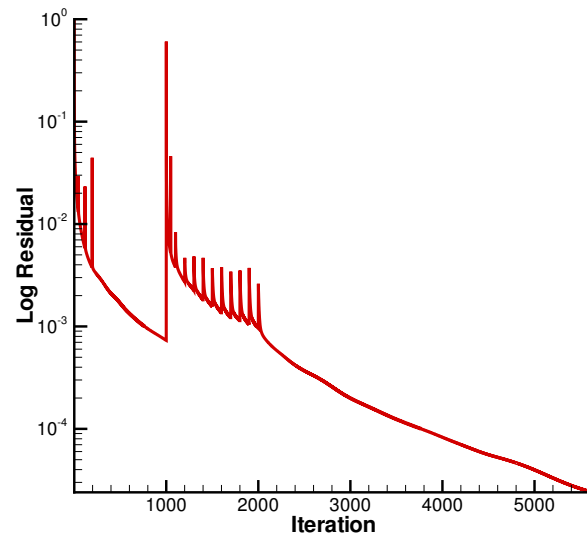


**Figure 43:** Residual history of the flow solution

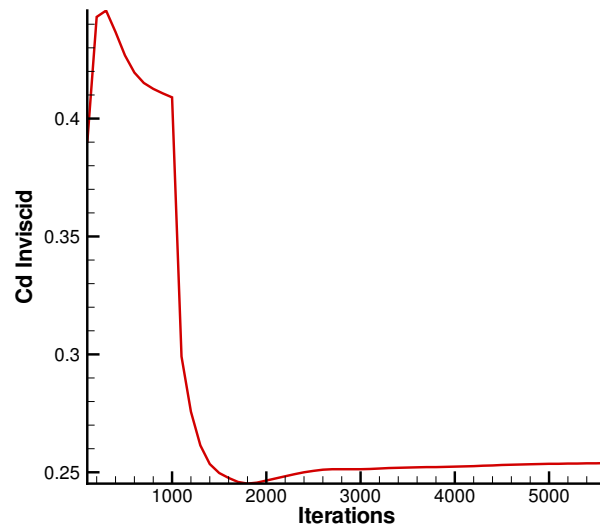


**Figure 44:** Iteration history of the drag coefficient

### 3.5 *Validation of the improved tools*

The foregoing analysis modifications are validated for simple bodies in this section. Using the linearized aerodynamics expressions, the analytical expressions for the drag and wave drag coefficient can be calculated for a Sears-Haack body and are shown in Equation 39.

$$\begin{aligned} D_w &= \frac{64V^2}{\pi l^4} \rho U^2 \\ C_{Dw} &= \frac{24V}{l^3} \end{aligned} \quad (39)$$

For the purpose of validation, a Sears-Haack body with a volume of 100 cubic ft. and length of 30 ft. has been used. A discretized Sears-Haack body is shown in Figure 45. Mach planes are generated and used to intersect the discretized body and the equivalent area and wave drag are computed. For the dimensions considered, the analytical expression predicts a  $D_w/q$  value of 0.503. Following the procedure laid out in section 3.3, a value of 0.507 is predicted. For a Sears-Haack body, the drag coefficient is independent of the Mach number and this result is obtained from our code. The program was also run on a Von-Karman ogive and the results match the analytical expressions.

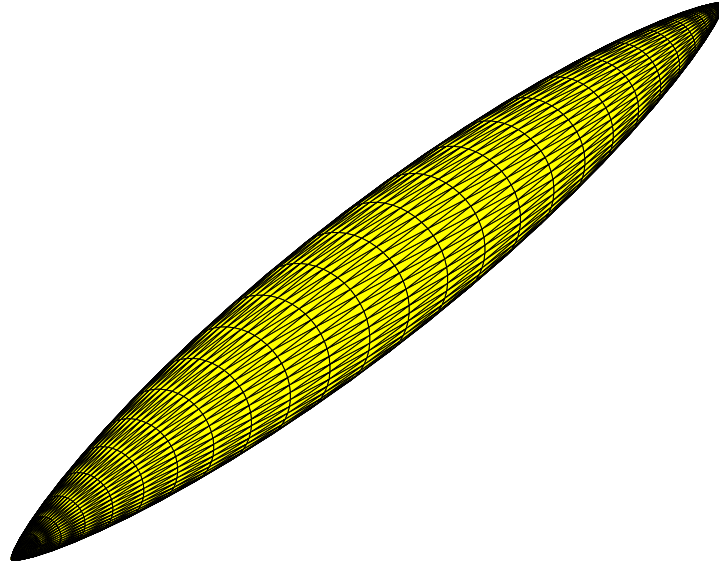


**Figure 45:** Discretized Sears-Haack body

As a further comparison, the wave drag and area distribution of the wing-body-canard



configuration shown in Figure 39 are presented next. The  $D_w/q$  value predicted by Mach plane intersection at Mach=1.4 is 3.08 and that by the original Harris Wave drag code is 5.19. CFD flow solution computed in Figure 42 produced an inviscid  $D_w/q$  of 2.74. Thus, the wave drag modification suggested here predicts a value much closer to the real CFD data. Harris wave drag code far over-predicts this value.

## ***3.6 Pressure propagation***

It has been mentioned in the introduction that the temperature profiles have an impact on the propagation of pressure waves. Similarly, the wind atmospheric distributions also have an impact on the pressure propagation. Heimann [38] provides experimental atmospheric wind profiles observed over a span of 10 years over Europe. Using these distributions as basis, the wind profiles have been parameterized using random variables with mean magnitudes around those specified in that study. Figure 46 shows some of the wind profiles generated using such a strategy.

### **3.6.1 PCBOOM**

Unlike ARAP, which is a linearized acoustic propagation program, PCBOOM is the industry standard non-linear propagation tool capable of predicting a three dimensional sonic boom footprint of a maneuvering aircraft. It is a heavy modification of the waveform parameter method of Thomas [120]. The waveform parameter method developed by Thomas is different from the code developed by Hayes and Kulsrud [126]. Rather than using the F-function as a starting point, Thomas code uses  $\Delta p$  at some radius to propagate the acoustic waves. Using Equation 5, one could argue that both these methods are equivalent. However, there are two fundamental differences between the two methods. The Thomas program was developed to directly use the near field pressure signature from the wind tunnel tests. This forms the practical difference between these two methods. The other difference is theoretical. The near field pressure may not correspond to the pressure obtained from the F-function. Hence, care has to be taken to measure the near field pressure sufficiently far away from the aircraft so that geometrical acoustics principles can be applied. Geometrical acoustics, like geometrical

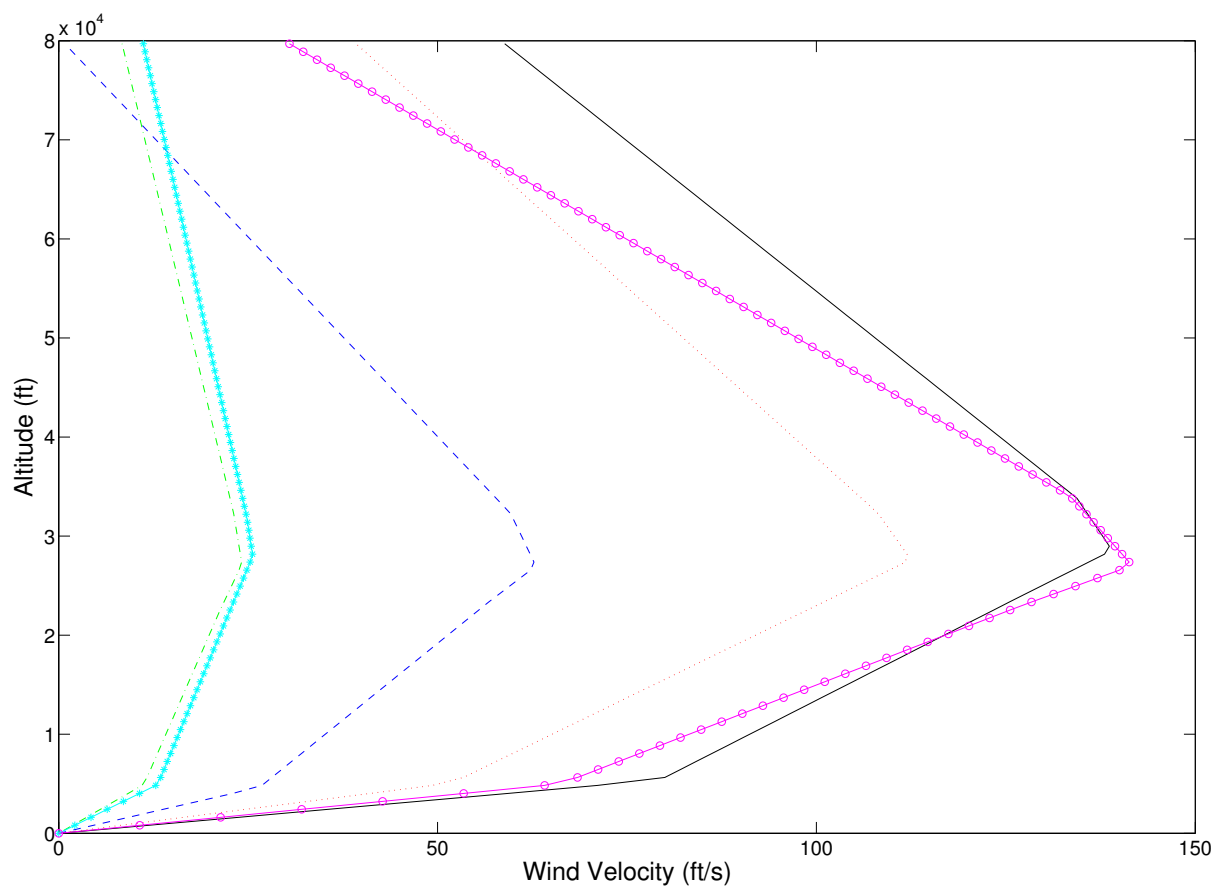


**Figure 46:** Random atmospheric Wind profiles

optics, is a field where sound waves are treated as rays. Refraction and propagation of acoustic waves through layers of changing refractive indices can be computed using the well known Snell's law for waves.

Sonic boom pressure signatures are traced to the ground altitude using ray acoustics. Therefore, it is possible that under certain flight and atmospheric conditions, the ray tube area might vanish. This causes the linearized acoustic solutions to break down. In order to overcome these singular solutions, equations for focus of weak shock waves were obtained by Guiraud and scaling laws were developed. Using these non-linear effects, the maximum amplitude for the focused booms is significantly increased and the resulting signatures are termed the "U waves" because of their shape as shown in Figure 14.

Using Guiraud's scaling laws, PCBOOM [87] computes the numerical solution of the signature at the focus, if such a situation occurs. Apart from ray acoustics, the other important quantity determining the loudness of sonic booms is the shock rise time. As has been mentioned earlier, rise times are the result of various complex phenomena such as molecular relaxation, turbulence, non-linear steepening, etc. PCBOOM uses a simplified method based on flight test data and assumes a hyperbolic tangent shock structure with a rise time of 1 ms. for . This shock thickening effect is shown in Figure 47.

While running PCBOOM, some convergence problems occurred for certain F-function distributions. Firstly, the iteration logic within the "BOOM" subroutine uses a fast but unreliable secant method to find the aging time along a ray. A secant method assumes that the function is approximately linear in the local region of interest and uses the zero-crossing of the line connecting the limits of the interval as the new reference point. However, since the secant method does not always bracket the root, the algorithm may not converge for functions that are not sufficiently smooth. This is indeed the case for certain situations as it has been found that the program goes into an infinite loop. To overcome this, the secant method has been replaced with a reliable bi-section method. A bisection method progressively halves the interval bound for the root till the interval width is less than tolerance specified. This slightly increases the time to achieve the final value compared to the secant method. However, convergence is assured. The second problem occurs when shock formation

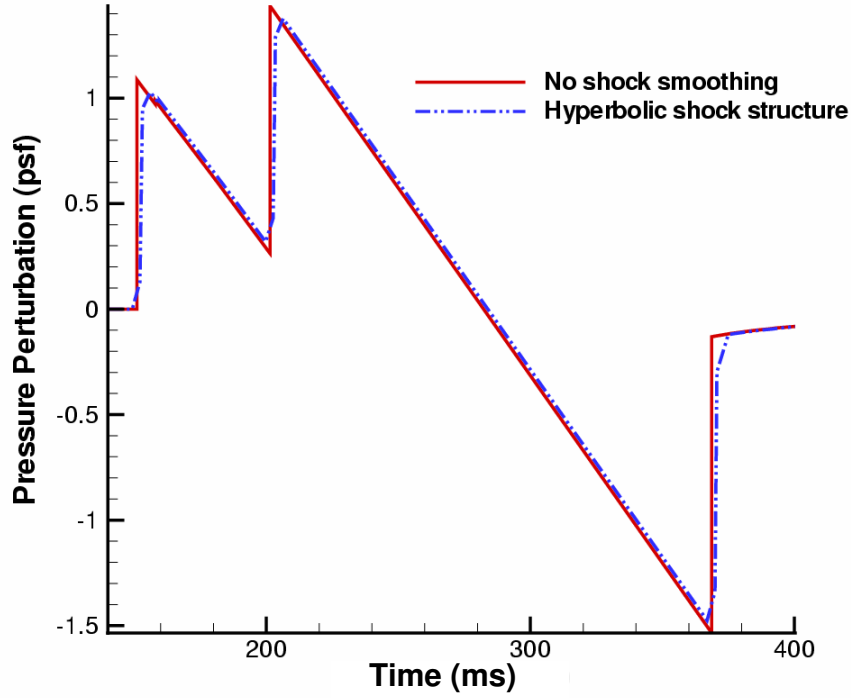


**Figure 47:** Hyperbolic shock structure

and shock coalescence occur simultaneously. This does not seem to be easy to overcome.

### ***3.7 Effect of Nacelle Interference***

In this section, the effect of nacelle interference [62] on the near field pressure signature for sonic boom analysis is presented. In the real situation, a nacelle causes the formation of shocks. There is a lip shock that is generated near the lip of the inlet and is propagated downstream. In addition, if the nacelle is directly under the wing, there are additional shocks in the near field due to reflection from the wing. These shocks have to be manifested in a linearized method as equivalent area contributions.

Two effects have to be considered when dealing with nacelle interference. The first is the global effect where the angle of attack of the aircraft is increased to maintain the weight of the aircraft due to the shocks and loss of lift. The other effect is the localized formation of shocks. Figure 48 shows the local effect of the nacelle under the wing as equivalent area contributions. The dashed lines represent the Mach planes cutting through the nacelle, the

solid lines represent the shocks due to the engine inlet and the dotted lines depict the shock reflections from the lower surface of the wing. The following observations can be made. There is a volume effect due to the thickness of the cowl and the inlet. Further due to reflections, there is a lift effect that is shifted downstream compared to the volume effect. The result is the new solid curve shown in the figure. The maximum magnitude of the solid curve is almost twice the maximum if the interference effects are not considered.

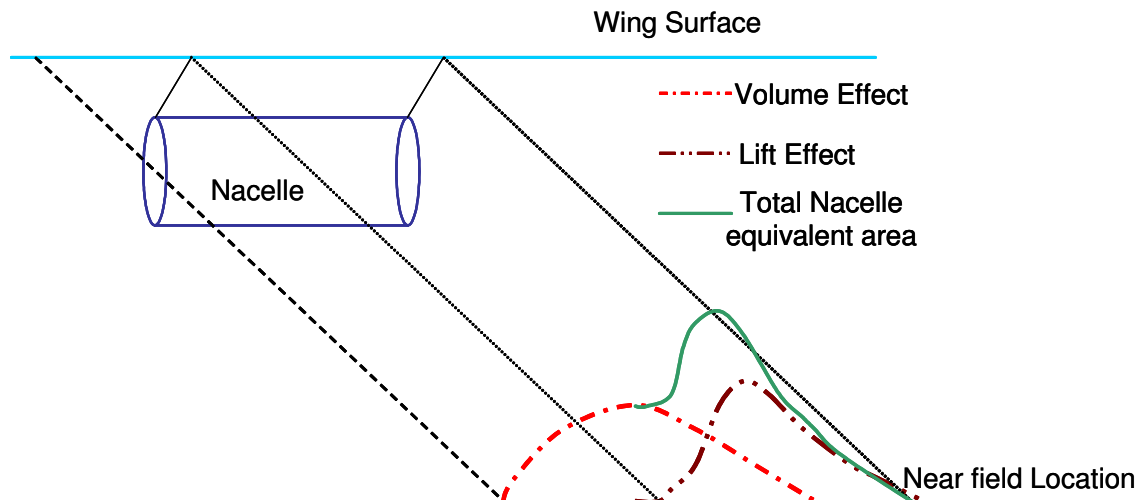


**Figure 48:** Near field signature with nacelle under the wing

For the case of nacelle on top of the wing, the shocks are generated as before. However, these shocks are now partially shielded by the wing surface and hence do not contribute to the near field for sonic-boom analysis if the three dimensional effects and diffraction are neglected. They do however cause an increase in the angle of attack to maintain the same lift and an increase in drag is seen. Figure 49 depicts the above reasoning in a simple sketch. Once again the dashed lines are the Mach lines, the solid line are the shocks and the dotted lines are the shock reflections from the top surface of the wing. Note that if there is no surface to shield the shocks from the nacelles, they do contribute to the sonic-boom near field signature.

In order to show the comparison of the nacelle interference effect, the configurations shown in Figure 50 are used. All the features of the geometries are the same except the location of the nacelles.

Figure 51 compares the equivalent area distribution for both the configurations. Three

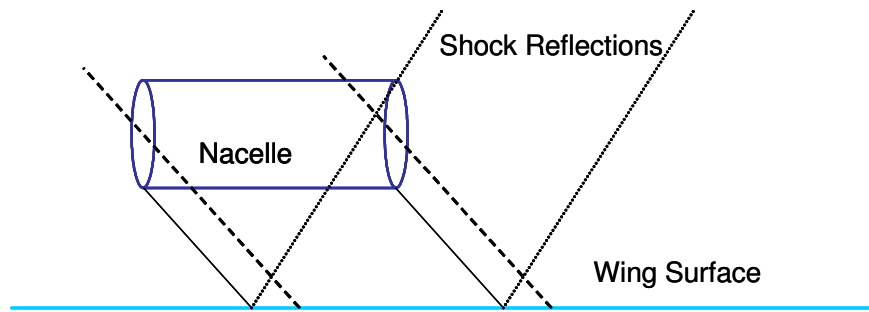


**Figure 49:** Near field signature with a nacelle on top of wing

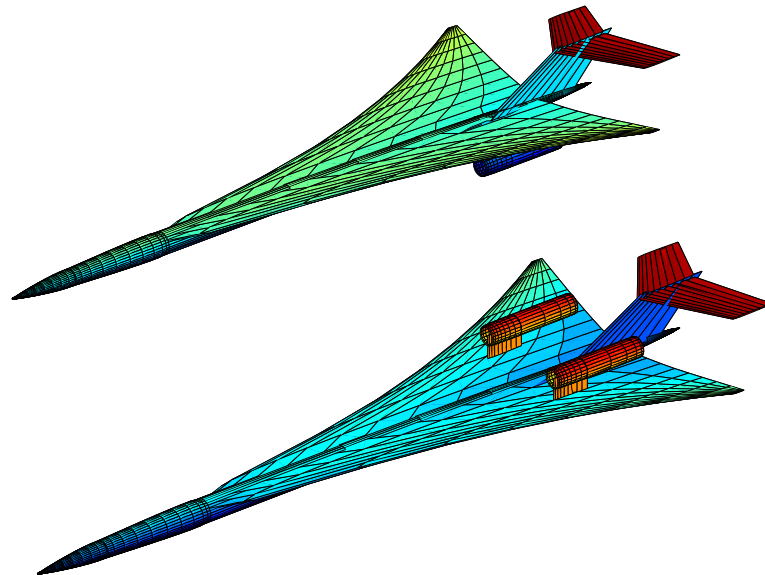


**Figure 50:** Two configuration differing only in the nacelle location

different regions can be seen in this figure as indicated. The first and second regions shows the effect of area due to volume. A lower nacelle causes a volume contribution at an earlier axial location compared to the volume contribution of a top nacelle. This is reflected in region 1 where the equivalent area for the bottom nacelle configuration is higher and in region 2 in which the geometry with top nacelles has a higher contribution. The reflected lift effects are seen in region 3. Due to reflections, the configuration with bottom nacelles has an increased area contribution.

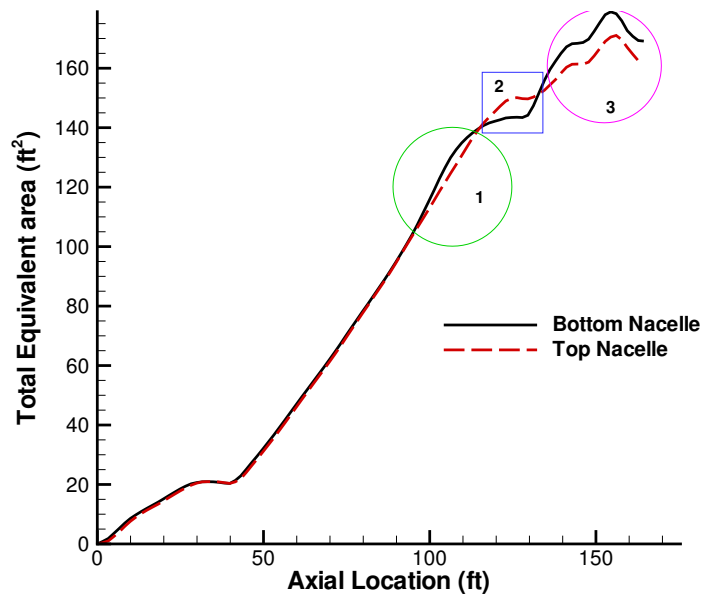


**Figure 51:** Comparison of equivalent area for top and bottom nacelles

Due to the change in the area distribution, the pressure signature in the near field is different for the configurations considered. Figure 52 shows the comparison of the ground pressure signatures in both cases. The over-pressure magnitude for the bottom nacelle geometry is higher than the nacelle over wing geometry. This may be due to the increased tendency for shock coalescence in the bottom nacelle case due to a forward location of the nacelle shocks. The rear shock strength is increased for the nacelle under the wing designs due to shock reflection phenomenon. For a Mach number of 1.6, the loudness values obtained are 92.69 PLdB and 92.01 PLdB for the bottom and top nacelle geometries respectively.

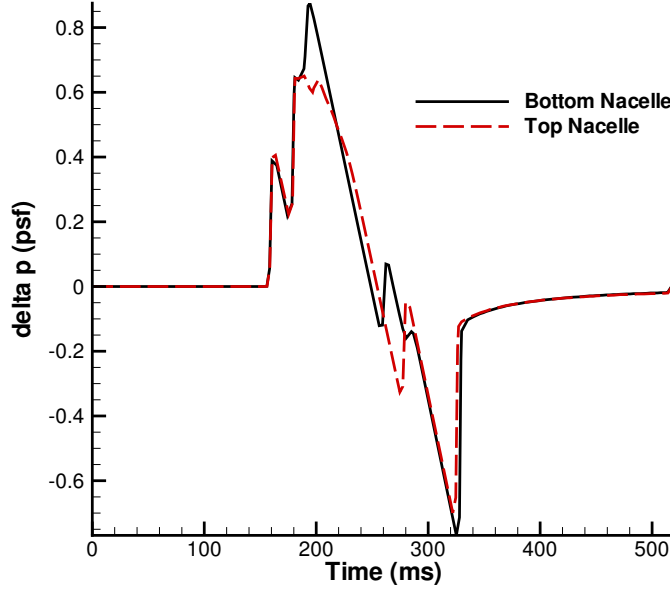


Figure 52: Ground pressure signature comparison

### 3.8 *Perceived loudness minimization tool*

In this section, the S-G-D equations are simplified and a strategy of solving them in an efficient manner is proposed. The F-function is assumed to be of the form shown in Equation 40

$$F(y) = \begin{cases} \frac{2yH}{y_f} & 0 \leq y \leq y_f/2 \\ C(\frac{2y}{y_f} - 1) - H(\frac{2y}{y_f} - 2) & y_f/2 \leq y \leq y_f \\ B(y - y_f) + C & y_f \leq y \leq \lambda \\ B(y - y_f) - D & \lambda \leq y \leq l \end{cases} \quad (40)$$

The known parameters are  $y_f, l, M, W$  and  $pr/pf$ . Based on the Seebass-George-Darden relations, the following equations can be written. The explanation of these equations is given in the papers by Seebass and George [105] and Darden [20] and was also briefly described earlier.



$$\int_l^{y_r} F(y)dy = \frac{-2}{\pi} \int_0^l F(x) \tan^{-1}\left(\sqrt{\frac{y_r - l}{l - x}}\right)dx = \frac{1}{2}[B(l - y_f) - D + F(y_r)](y_r - l) \quad (41)$$

$$\frac{p_f}{p_r} = \frac{C}{D - B(l - y_f) + F(y_r)} \quad (42)$$

$$F(y_r) = S(y_r - l) + B(l - y_f) - D \quad (43)$$

$$\int_0^{y_f} F(y)dy = \frac{\alpha_{y_f} C}{2} \quad (44)$$

$$\int_l^{y_r} F(y)dy = \frac{1}{2}[B(l - y_f) - D + F(y_r)](y_r - l) \quad (45)$$

$$F(y) = -\frac{1}{\pi(y - l)^{1/2}} \int_0^l \frac{(l - \xi)^{1/2}}{(y - \xi)} F(\xi) d\xi \quad (46)$$

The purpose of the exercise is to determine the unknowns C,D,H,  $\lambda$  and  $y_r$  given the Mach number, altitude, length and gross weight, etc. Note that a computer program called SEEB exists, based on the Darden's paper [20], which calculates the required outputs from the input parameters and flight conditions. However, in the present study, the objective is not only to obtain the minimizing F-function, but also to gain insight into the various terms contributing to the final outputs. This insight could then be used to modify the formulation by making it more generic. The derivation and simplification presented below have not been found elsewhere.

Using the geometric acoustics techniques, closed form expressions involving integrals can be used to calculate the value of the slope of the balancing line, S as shown in Equation 47

$$S = -\frac{\sqrt{2\beta}}{\Gamma M_h^3 \int_0^h \frac{p_h}{p} \sqrt{\frac{\rho a_h}{\rho_h a}} \sqrt{\frac{A_h}{z_h A} \frac{M}{\beta}} dz} \quad (47)$$

where Equation 48 is an expression relating the area of the ray tube as a function of the distance from the near field altitude.

$$\frac{A_h}{z_h A} = \left[ M_h \sqrt{\left(1 - \frac{1}{M_z^2}\right)} \int_0^z \frac{1}{\sqrt{(M_z^2 - 1)}} dz \right]^{-1} \quad (48)$$

The pressure signature stretches as it propagates due to the non-linear atmospheric effects. This non-linear advance can be calculated from Equation 49 by performing numerical integration.

$$\alpha_y = -\frac{\Gamma M_h^3 F(y)}{\sqrt{2\beta}} \int_0^z \frac{p_h}{p} \sqrt{\frac{\rho a_h}{\rho_h a}} \sqrt{\frac{A_h}{z_h A} \frac{M}{\beta}} dz \quad (49)$$

Using the supplied values of  $h$ ,  $M$ ,  $l$  and  $GW$ , the slope of the balancing can be calculated using equations 47 through 49. The greater the stretching of the signature, the more is the coalescence and hence the slope of the balancing line is increased. In other words, slope of the front balancing line,  $S$ , is proportional to the reciprocal of the advance. Therefore, Equation 47 can also be written as shown in Equation 50. Equation 51 gives the value of the advance at  $y_f$  in the near field signature.

$$S = \frac{F(y)}{\alpha_y} = \frac{F(y_f)}{\alpha_{y_f}} = \frac{C}{\alpha_{y_f}} \quad (50)$$

$$\alpha_{y_f} = (y_r - l) \frac{P_r}{P_f} \quad (51)$$

Using Equation 44 and Equation 51, Equation 52 is obtained as a function of  $\alpha_{y_f}$  which in turn is a function of  $y_f$ .

$$C = \frac{2Hy_f}{(2\alpha_{y_f} - y_f)} \quad (52)$$

Using equations 50 and 52, a quadratic equation in  $\alpha_{y_f}$  can be obtained as shown in Equation 53.

$$2S\alpha_{y_f}^2 - Sy_f\alpha_{y_f} - 2Hy_f = 0 \quad (53)$$

Because the advance cannot be negative, the negative root is discarded and the positive root is taken to be actual advance of the pressure signature. The quadratic can be solved for  $\alpha_{y_f}$  in terms of  $y_f, S$  and  $H$ . The solution is shown in Equation 54.

$$\alpha_{y_f} = \frac{y_fS + \sqrt{y_f^2S^2 + 16Hy_fS}}{4S} = (y_r - l)\frac{P_r}{P_f} \quad (54)$$

From Equation 54, H can be solved in terms of the unknown parameter  $y_r$  and is given by Equation 55.

$$H = \frac{S(y_r - l)^2(\frac{P_f}{P_r})^2}{y_f} - \frac{S(y_r - l)\frac{P_f}{P_r}}{2} \quad (55)$$

With  $H$  and  $\alpha_{y_f}$  known in terms of the unknown  $y_r$ , Equation 55 can now be used to obtain C in terms of  $y_r$  by substituting in Equation 52 and is given by Equation 56.

$$C = \frac{2S(y_r - l)^2(\frac{P_f}{P_r})^2 - Sy_f(y_r - l)\frac{P_f}{P_r}}{2(y_r - l)\frac{P_f}{P_r} - y_f} \quad (56)$$

All the above equations can be used to solve for the required F-function parameters. The first step is the assumption that the volume contribution to the equivalent area at the end of the aircraft length is zero. In other words, the equivalent area due to lift at the end is as shown in Equation 57.

$$A_e(l) = \frac{\beta W}{\rho U^2} = 4 \int_0^l F(y) \sqrt{(l-y)} dy \quad (57)$$

The above integral can be split into 4 different intervals and carry out the integration. Let  $l - \xi = x^2$ . The above integral reduces to

$$\begin{aligned} A_e(l) = & \frac{4H}{y_f} \int_{\sqrt{l}}^{\sqrt{l-\frac{y_f}{2}}} x^2(x^2-l)dx + \frac{4C}{y_f} \int_{\sqrt{l-\frac{y_f}{2}}}^{\sqrt{l-y_f}} x^2(4(x^2-l) + 2y_f)dx \\ & - \frac{4H}{y_f} \int_{\sqrt{l-\frac{y_f}{2}}}^{\sqrt{l-y_f}} x^2(4(x^2-l) + 4y_f)dx + 4 \int_{\sqrt{l-y_f}}^{\sqrt{l-\lambda}} 2x^2(B(x^2+y_f-l) - C)dx \\ & + 4 \int_{\sqrt{l-\lambda}}^0 2x^2(B(x^2+y_f-l) + D)dx \end{aligned} \quad (58)$$

The following relations are assumed to simplify the equations.

$$\beta = \sqrt{l}, \alpha = \sqrt{l - \frac{y_f}{2}}, \gamma = \sqrt{l - y_f}, \delta = \sqrt{l - \lambda} \quad (59)$$

Carrying out the integration, the expression for the equivalent area due to lift with the assumed form of the F-function is given Equation 60. This equation can then be used to solve for  $D$  in terms of  $y_r$  and  $\lambda$  and the expression is shown in Equation 61.

$$\begin{aligned} A_e(l) = & \frac{-16H}{y_f} \left[ \frac{l}{3}(\alpha^3 - \beta^3) - \frac{1}{5}(\alpha^5 - \beta^5) \right] + \frac{4C}{y_f} \left[ \frac{2y_f}{3}(\gamma^3 - \alpha^3) - 4\left(\frac{l}{3}(\gamma^3 - \alpha^3) \right. \right. \\ & \left. \left. - \frac{1}{5}(\gamma^5 - \alpha^5) \right) \right] - \frac{4H}{y_f} \left[ \frac{4y_f}{3}(\gamma^3 - \alpha^3) - 4\left(\frac{l}{3}(\gamma^3 - \alpha^3) - \frac{1}{5}(\gamma^5 - \alpha^5) \right) \right] \\ & + 4 \left[ \frac{2B}{5}(\delta^5 - \gamma^5) - \frac{2(B(l-y_f) + C)}{3}(\delta^3 - \gamma^3) \right] + 4 \left[ \frac{-2B}{5}\delta^5 + \frac{2(B(l-y_f) - D)}{3}\delta^3 \right] \end{aligned} \quad (60)$$

$$\begin{aligned} D = & \frac{3}{8(l-\lambda)^{\frac{3}{2}}} \left[ \frac{4(y_r-l)}{y_f} (h1(y_r-l) - h2) A1 \right. \\ & \left. + \frac{c1(y_r-l) - c2}{c3(y_r-l) - y_f} (y_r-l) (A2 - \frac{8}{3}((l-\lambda)^{\frac{3}{2}} - k1)) - \frac{\beta W}{\rho U^2} \right] \end{aligned} \quad (61)$$

Similarly, integral equations 41 and 46 can be split into four intervals and integration can be performed. Specifically, Equation 46 would yield Equation 62 using the symbols specified in Equation 59.

$$\begin{aligned}
x_p - \tan^{-1}(x_p) = & \frac{1}{(2C + 2D)(\sqrt{y_r - l})} \left[ \frac{4H}{y_f} \left( \frac{1}{3}(\alpha^3 - \beta^3) - y_r(\sqrt{\alpha} - \sqrt{\beta}) \right. \right. \\
& + y_r\sqrt{y_r - l} \left( \tan^{-1}\left(\frac{\alpha}{\sqrt{y_r - l}}\right) - \tan^{-1}\left(\frac{\beta}{\sqrt{y_r - l}}\right) \right) + \frac{4C}{y_f} \left( \frac{1}{3}(\gamma^3 - \alpha^3) \right. \\
& - y_r(\sqrt{\gamma} - \sqrt{\alpha}) + y_r\sqrt{y_r - l} \left( \tan^{-1}\left(\frac{\gamma}{\sqrt{y_r - l}}\right) - \tan^{-1}\left(\frac{\alpha}{\sqrt{y_r - l}}\right) \right) \\
& + 2C \left( (\sqrt{\gamma} - \sqrt{\alpha}) - \sqrt{y_r - l} \left( \tan^{-1}\left(\frac{\gamma}{\sqrt{y_r - l}}\right) - \tan^{-1}\left(\frac{\alpha}{\sqrt{y_r - l}}\right) \right) \right) \\
& - \frac{4H}{y_f} \left( \frac{1}{3}(\gamma^3 - \alpha^3) - y_r(\sqrt{\gamma} - \sqrt{\alpha}) + y_r\sqrt{y_r - l} \left( \tan^{-1}\left(\frac{\gamma}{\sqrt{y_r - l}}\right) - \tan^{-1}\left(\frac{\alpha}{\sqrt{y_r - l}}\right) \right) \right) \\
& - 4H \left( (\sqrt{\gamma} - \sqrt{\alpha}) - \sqrt{y_r - l} \left( \tan^{-1}\left(\frac{\gamma}{\sqrt{y_r - l}}\right) - \tan^{-1}\left(\frac{\alpha}{\sqrt{y_r - l}}\right) \right) \right) \\
& + (2By_f - 2C)\sqrt{y_r - l} \left( \tan^{-1}\left(\frac{\sqrt{\gamma}}{\sqrt{y_r - l}}\right) - \sqrt{\gamma} \right) + 2B(y_r\sqrt{\gamma} - \frac{\gamma^3}{3} \\
& \left. \left. - y_r\sqrt{y_r - l} \tan^{-1}\left(\frac{\sqrt{\gamma}}{\sqrt{y_r - l}}\right) \right) + \pi\sqrt{y_r - l}(S(y_r - l) + B(l - y_f) - D) \right] \quad (62)
\end{aligned}$$

where

$$x_p = \sqrt{\frac{l - \lambda}{y_r - l}} \quad (63)$$

Equation 41 would result in Equation 65 based on the symbols provided in Equation 64.

$$\beta = \sqrt{\frac{y_r - l}{l}}, \alpha = \sqrt{\frac{y_r - l}{l - \frac{y_f}{2}}}, \gamma = \sqrt{\frac{y_r - l}{l - y_f}}, \delta = \sqrt{\frac{y_r - l}{l - \lambda}} \quad (64)$$

There are two unknowns,  $\lambda$  and  $y_r$  in two equations 62 and 65. To numerically solve for the unknowns, the equations are recast as an optimization problem such that the squared difference of the right hand side and left hand side of the Equation 62 is minimized while Equation 65 is used as an equality constraint. Using  $\lambda$  and  $y_r$ , other parameters of the F-function C,D and H can be obtained. The optimizer used in this exercise is a sequential

quadratic programming (SQP) for constrained optimization. It is a gradient based optimization procedure which is very efficient [123] for functions which are smooth and have single optimum value. In this case, the functions are indeed smooth and SQP would result in fast convergence. The results of this optimization procedure are shown in Table 5 for a simple case with given input values. Figures 53 and 54 show sample F-function and total equivalent area distributions corresponding to the input values given in this table. The MATLAB code for solving the above equations is given in the appendix.

$$\begin{aligned}
\tan^{-1}\left(\frac{1}{x_p}\right)(1+x_p^2) + x_p = & \frac{1}{(C+D)(y_r-l)} \left[ \frac{4H(y_r-l)}{y_f} \left( \frac{l}{2} \left( \tan^{-1}(\beta) \left(1 + \frac{1}{\beta^2}\right) + \frac{1}{\beta} \right. \right. \right. \\
& - \tan^{-1}(\alpha) \left(1 + \frac{1}{\alpha^2}\right) - \frac{1}{\alpha} \Big) - \frac{(y_r-l)}{4} \left( \tan^{-1}(\alpha) \left(1 - \frac{1}{\alpha^4}\right) + \frac{1}{\alpha} \left(1 - \frac{1}{3\alpha^2}\right) \right. \\
& - \tan^{-1}(\beta) \left(1 - \frac{1}{\beta^4}\right) - \frac{1}{\beta} \left(1 - \frac{1}{3\beta^2}\right) \Big) \Big) + \frac{C}{y_f} \left( (2l-y_f)(y_r-l) \left( \tan^{-1}(\alpha) \left(1 + \frac{1}{\alpha^2}\right) \right. \right. \\
& + \frac{1}{\alpha} - \tan^{-1}(\gamma) \left(1 + \frac{1}{\gamma^2}\right) - \frac{1}{\gamma} \Big) - (y_r-l)(y_r-l) \left( \tan^{-1}(\gamma) \left(1 - \frac{1}{\gamma^4}\right) \right. \\
& + \frac{1}{\gamma} \left(1 - \frac{1}{3\gamma^2}\right) - \tan^{-1}(\alpha) \left(1 - \frac{1}{\alpha^4}\right) - \frac{1}{\alpha} \left(1 - \frac{1}{3\alpha^2}\right) \Big) \Big) - \frac{H}{y_f} \left( (2l-2y_f)(y_r-l) \right. \\
& \left( \tan^{-1}(\alpha) \left(1 + \frac{1}{\alpha^2}\right) + \frac{1}{\alpha} - \tan^{-1}(\gamma) \left(1 + \frac{1}{\gamma^2}\right) - \frac{1}{\gamma} \Big) - (y_r-l)(y_r-l) \right. \\
& \left( \tan^{-1}(\gamma) \left(1 - \frac{1}{\gamma^4}\right) + \frac{1}{\gamma} \left(1 - \frac{1}{3\gamma^2}\right) - \tan^{-1}(\alpha) \left(1 - \frac{1}{\alpha^4}\right) \right. \\
& \left. \left. - \frac{1}{\alpha} \left(1 - \frac{1}{3\alpha^2}\right) \right) \right) + (y_r-l) \left( B(l-y_f) + C \right) \left( \tan^{-1}(\beta) \left(1 + \frac{1}{\beta^2}\right) + \frac{1}{\beta} \right) \\
& + \frac{B}{2} (y_r-l)(y_r-l) \left( \tan^{-1}(\gamma) \left(1 - \frac{1}{\gamma^4}\right) + \frac{1}{\gamma} \left(1 - \frac{1}{3\gamma^2}\right) \right) - \frac{\pi B}{4} (y_r-l)(y_r-l) \\
& \left. - \frac{\pi}{2} (y_r-l) \left( B(l-y_f) - D \right) + \frac{\pi}{4} (y_r-l) \left( 2B(l-y_f) - 2D + S(y_r-l) \right) \right] \quad (65)
\end{aligned}$$

### 3.8.1 Modifications to the SGD analysis

While the F-function prescribed by Darden [20] has been used in most conceptual sonic boom minimization studies, it could be generalized a little more. In this section, a generalization of the F-function form is given along with the results accompanying such a form. Before proceeding to the derivation of the new set of equations, it is worthwhile to look into some

**Table 5:** Inputs and outputs for a sample run

Variable	Value	F-function Outputs	Value
B (Slope in F-function)	0.0004	C	0.04401
Mach Number	1.6	D	0.113553
Length	130.0 ft	H	0.248584
Gross Weight	100000.0 lbs	$\lambda$	104.97
Altitude	60000.0 ft	$y_r$	191.482
$y_f$ (Bluntness parameter)	10.0		

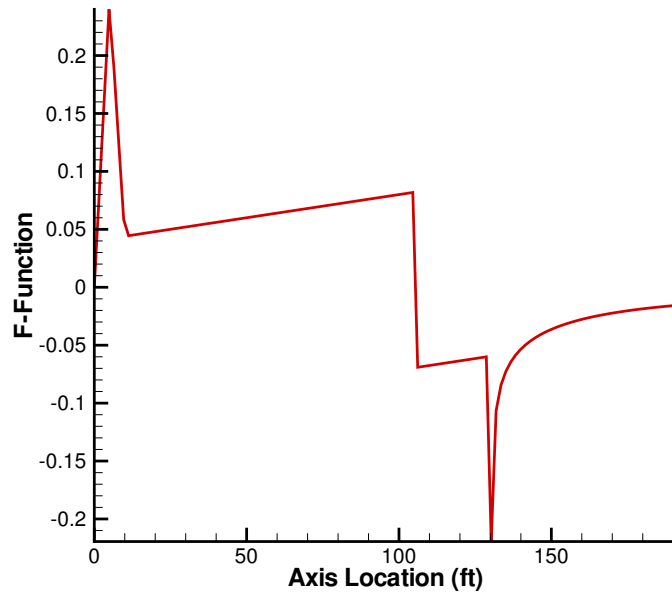


**Figure 53:** Sample SGD F-function shape for minimizing pressure perturbations

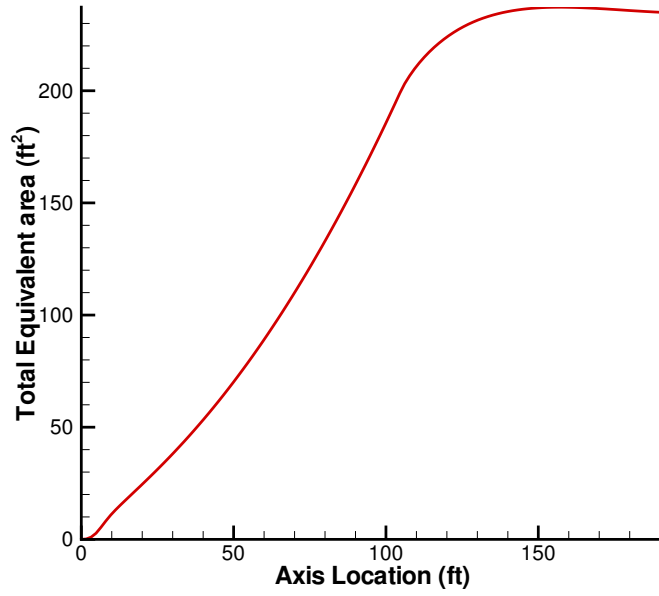


**Figure 54:** Sample SGD total equivalent area distribution

minor shortcomings of the form prescribed in Equation 40. The form assumes that the maximum of the F-function occurs at  $y_f/2$ . Secondly, the portion after  $y_f$  is controlled by just one parameter,  $B$ .

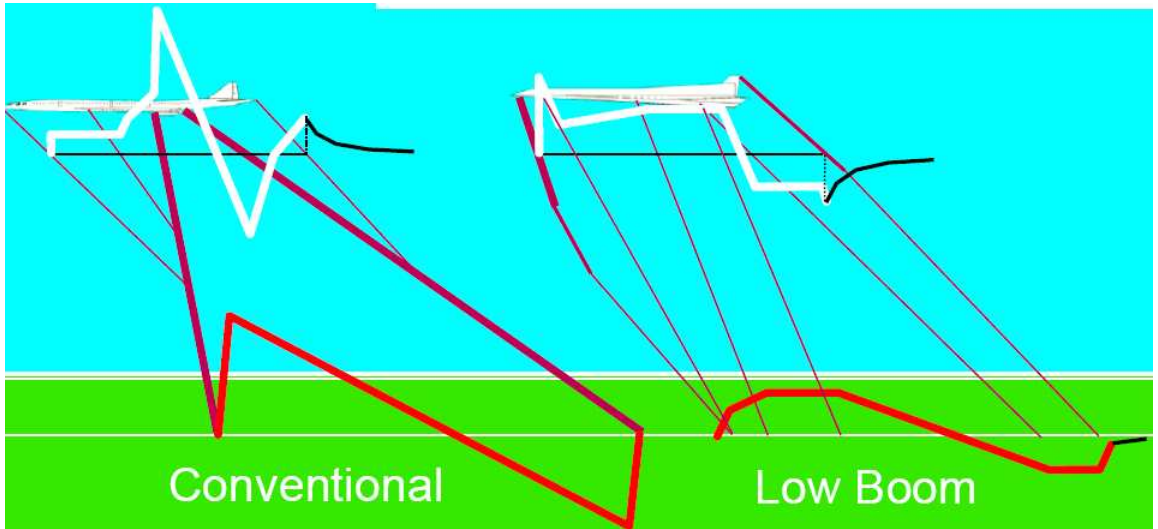


**Figure 55:** Sonic Boom minimization strategy [73]

While this may seem sufficient, consider Figure 55. This Figure [73] compares the design of conventional and low boom design strategies. While the left side of the figure produces a conventional N-wave, the ground signature on the right shows a rounded signature with a



significantly lower loudness level. These sort of near field F-functions have been tested by [63]. The near field signature for the low boom design strategy reveals that improved designs could be achieved by including additional parameters to the SGD F-function. It is with this idea that a generalization of the F-function is introduced with a new form as specified in Equation 66. Note that this form reduces to the original SGD form for the special case of  $\eta = 0.5$ ,  $\xi = y_f$ ,  $B_1 = B_2 = B_3 = B$  and  $t = 0.0$ . A sketch of the new form is presented in Figure 56.

$$F(y) = \begin{cases} \frac{yH}{\eta y_f} & 0 \leq y \leq \eta y_f \\ \frac{C}{(1-\eta)}\left(\frac{y}{y_f} - \eta\right) - \frac{H}{2(1-\eta)}\left(\frac{2y}{y_f} - 2\right) & \eta y_f \leq y \leq y_f \\ B_1(y - y_f) + C & y_f \leq y \leq \xi \\ B_2(y - \xi) + C_1 & \xi \leq y \leq \lambda \\ \frac{-(D+C_2)}{t}(y - \lambda) + C_2 & \lambda \leq y \leq \lambda + t \\ B_3(y - \lambda - t) - D & \lambda + t \leq y \leq l \end{cases} \quad (66)$$

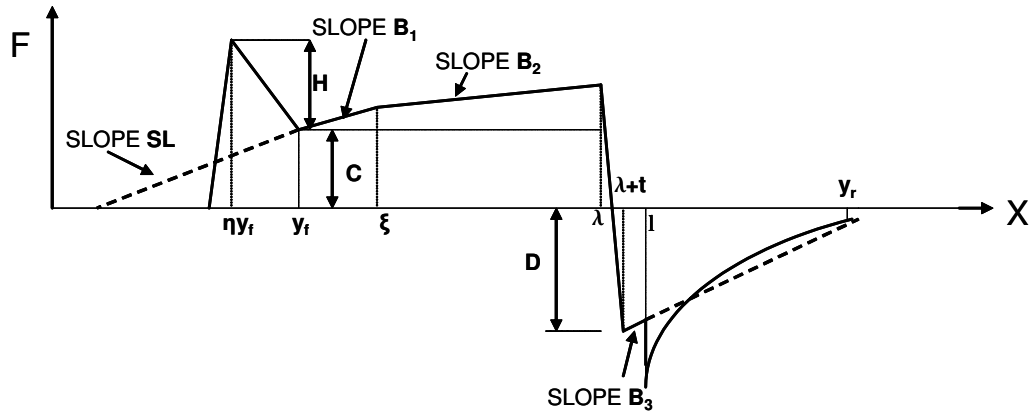


**Figure 56:** New F-function

Following the analysis procedure carried out earlier, each of the equations, derived earlier, has a counterpart involving  $\xi$  and  $\eta$ . Equation 67 specifies the equivalent area distribution corresponding to the minimizing F-function.

$$H = \frac{S(y_r - l)^2 \left(\frac{P_f}{P_r}\right)^2}{y_f} - \frac{S(1 - \eta)(y_r - l) \frac{P_f}{P_r}}{2} \quad (67)$$

**Table 6:** Fixed values of some parameters for sample run

Variable	Value
M	1.6
l (A/C length)	120.0 ft
GW	120000.0 lbs
h (Altitude)	60000.0 ft
$y_f$	25.0

$$C = \frac{Hy_f}{(y_r - l)\frac{P_f}{P_r} - y_f(1 - \eta)} \quad (68)$$

$$\begin{aligned}
A_e(x) = & \frac{16H}{15\eta y_f} x^{5/2} + 1(x - \eta y_f) \left[ \frac{8}{15\eta y_f(1 - \eta)} (x - \eta y_f)^{3/2} (2\eta y_f - 2x) \right] \\
& + 1(x - y_f) \left[ \frac{8}{15y_f} (x - y_f)^{3/2} (B_1 y_f - \frac{C - H}{1 - \eta}) (2x - 2y_f) \right] \\
& + 1(x - \xi) \left[ \frac{8}{15} (x - \xi)^{3/2} (B_2 - B_1) (2x - 2\xi) \right] \\
& + 1(x - \lambda) \left[ \frac{8}{15} (x - \lambda)^{3/2} (B_2 + \frac{D + C_2}{t}) (2\lambda - 2x) \right] \\
& + 1(x - (\lambda + t)) \left[ \frac{8}{15} (x - \lambda - t)^{3/2} (B_3 + \frac{D + C_2}{t}) (2x - 2(\lambda + t)) \right]
\end{aligned} \quad (69)$$

Since the weight has to be supported, it is also known that Equation 70 has to be satisfied.

$$A_e(l) = \frac{\beta W}{2q} = \frac{\beta W}{\rho V^2} \quad (70)$$

Substituting the length for the free variable, x, in Equation 69, and using Equation 70, an equation for D can be obtained. The other appropriate equations are also derived.

Now that a new form has been introduced, it has to be compared against the results from the original SGD form. To simplify the comparison process, the flight conditions are fixed as shown in Table 6. Using the values given in Table 7, new sample F-functions are generated and ground pressure signatures are generated by running PCBOOM.

Figure 57 depicts the changes in the F-function possible while maintaining all the necessary constraints while Figure 58 shows the corresponding ground pressure signatures. A few

**Table 7:** Variable values in sample run comparison

	Original SGD	Modified 1	Modified 2
$B_1$	0.00025	0.000042	0.000039
$B_2$	0.00025	0.000163	0.000265
$B_3$	0.00025	0.000326	0.000271
$\eta$	0.5	0.647074	0.167827
t	0.0	3.367603	4.564785
$\xi$	25.0	38.36105	36.416225

observations can be made from this figure. Firstly, as the axial location of the F-function maximum,  $\eta$ , gets smaller, the magnitude of the front shock increases. This is because with a lower  $\eta$ , the expansion behind the front shock is not very steep as in the case where  $\eta$  is large. This lower strength expansion region, during propagation, reduces the strength of the front shock to a lower extent. However, this is accompanied by a reduction in the rear shock strength. Secondly, the additional flat regions in the F-function can create a flat-top like pressure signature on the ground. This would not have been possible with the previous formulation.

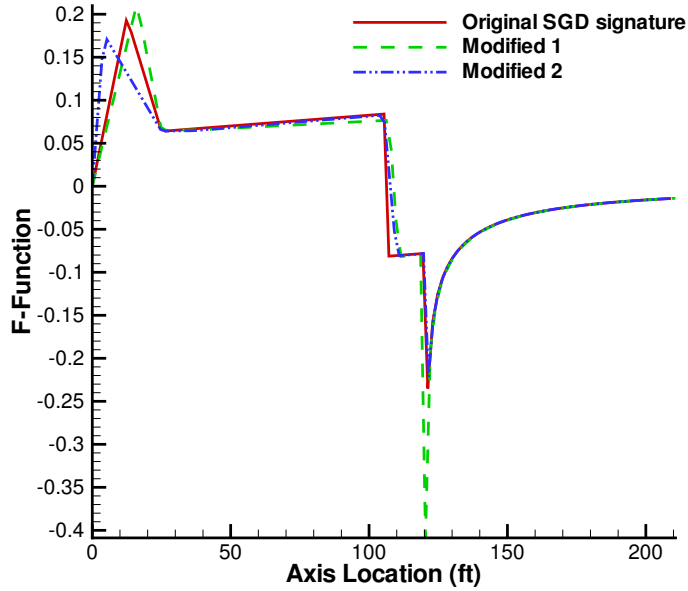
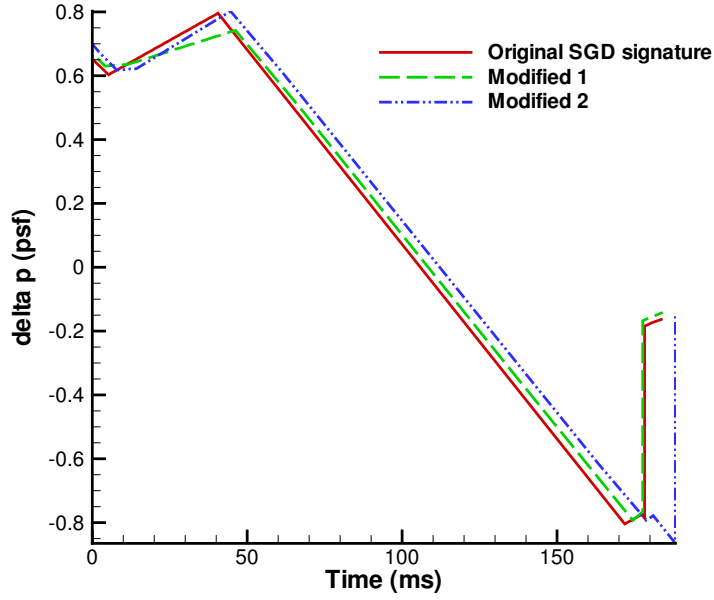
**Figure 57:** Modifications to the original S-G-D F-function

Table 8 shows the important parameters associated with the pressure signature on the



**Figure 58:** Corresponding ground pressure signatures

**Table 8:** Comparison of outputs for different F-functions

	<b>Original SGD</b>	<b>Modified 1</b>	<b>Modified 2</b>
PLdB	92.04	92.55	91.90
Shock pressure rise (psf)	0.612	0.653	0.659
Over-pressure (psf)	0.68	0.687	0.802

ground using the various F-functions. It is clear from the figure and the table that modifications in the F-function could lead to quite different values of the perceived loudness levels on the ground. Certain variable combinations lead to a reduction in perceived loudness.

### 3.8.2 Validation of the SGD analysis method

Before the SGD approximation and the modified SGD approximation can be used in the optimization analysis, these approximations have to be validated against previously known data. Two cases given by [20] are used here.

#### 3.8.2.1 Case 1: Minimum overpressure solution

The first case tested here is a minimum overpressure solution. This corresponds to the case where the F-function rise slope,  $B$ , is zero. The test case inputs are shown in Table 9. The

**Table 9:** Inputs for test case 1

Input Variable	Value
M	2.7
l	300 ft
Weight	600000 lbs
Altitude	60000 ft
B	0.0
$y_f$	30.0

**Table 10:** Additional inputs for modified SGD analysis

Input Variable	Value
$B_1$	0.0
$B_2$	0.0
$B_3$	0.0
$\eta$	0.5
t	0.0
$\xi$	30.0

modified analysis has additional parameters which need to be input. With the additional values shown in Table 10, the modified SGD analysis is equivalent to the Darden analysis.

With the above inputs, the present approximations are run and the outputs are compared in Table 11 with the original Darden results. All the relevant outputs are close to those predicted by Darden. Figure 59 depicts a comparison between the F-functions and Figure 60 shows the comparison between the equivalent area distributions. The match is almost exact. Another ready check can be performed to see if the resultant area distributions actually correspond to the aircraft weight and flight conditions. Based on the relation  $A_e(l) = \frac{\beta W}{\rho V^2}$ , and the values used in Table 9, a value of approximately 984.17 can be obtained for the equivalent area value at the end of the aircraft length. This value is observed in the area distribution plot.

### 3.8.2.2 Case 2: Minimum shock solution

The next test case is the minimum shock pressure solution suggested by Darden. In this case, all the inputs are same as before, except now the slope of the rise section in the F-function,

**Table 11:** Comparison of original analysis with modified SGD analyses

Variable	Original Darden	SGD approx.	Modified SGD approx.
H	0.3462239	0.351049	0.347603
C	0.0549862	0.055368	0.055106
D	0.0683242	0.067676	0.068459
$\lambda$	270.6449	268.118221	270.667902
$Y_r$	503.8965	505.209046	504.2377

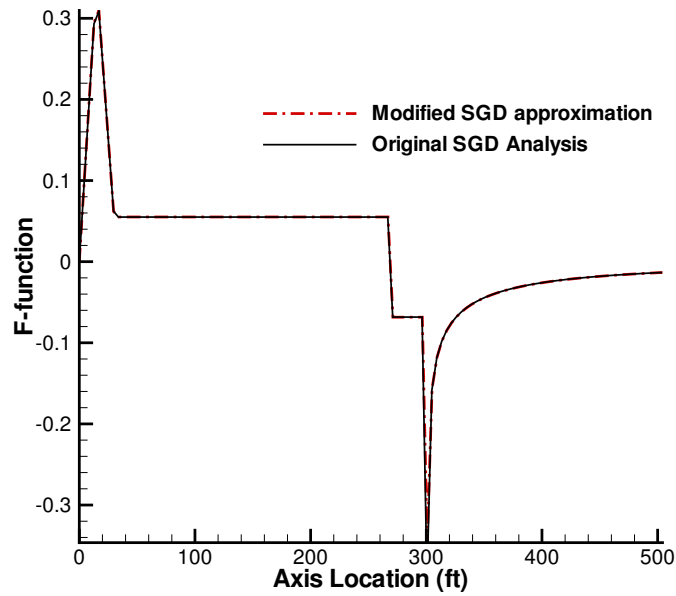


**Figure 59:** Comparison of F-functions for case 1

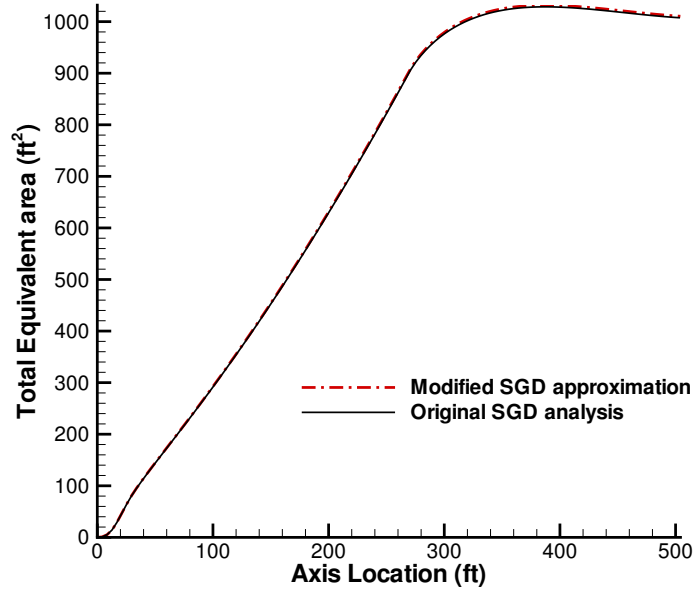


**Figure 60:** Comparison of total equivalent areas for case 1

**Table 12:** Comparison of original analysis with modified SGD analyses

Variable	Original Darden	SGD approx.	Modified SGD approx.
H	0.302491	0.309169	0.303828
C	0.0515336	0.052090	0.051656
D	0.0102131	0.101459	0.102261
$\lambda$	251.6591	249.139328	251.703854
$Y_r$	491.093	493.059499	491.452342

B, is given a value 0.000134838 instead of zero. The resultant outputs are shown in Table 12. It is seen that the outputs from the approximations match almost exactly with the results obtained by Darden.

Further, the F-functions and the area distributions obtained from original and modified SGD analyses are compared in figures 61 and 62 respectively. An almost identical match is obtained in both the figures.

The approximate SGD analysis introduced in this thesis can be used as an effective and efficient surrogate to the actual SGD analysis. Most of the optimization runs in this study use the modified SGD approximation presented earlier. Darden's equivalent area distributions are a special case of the modified analysis presented in this study. Hence, using the modified

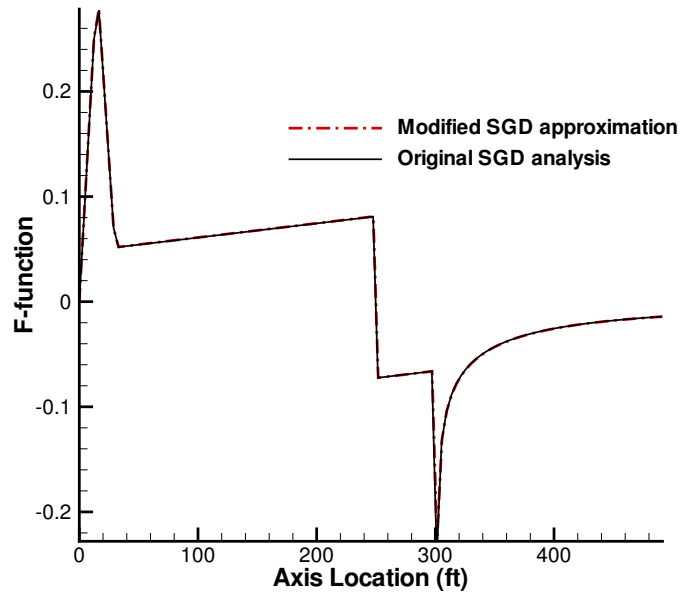


**Figure 61:** Comparison of F-functions for case 2

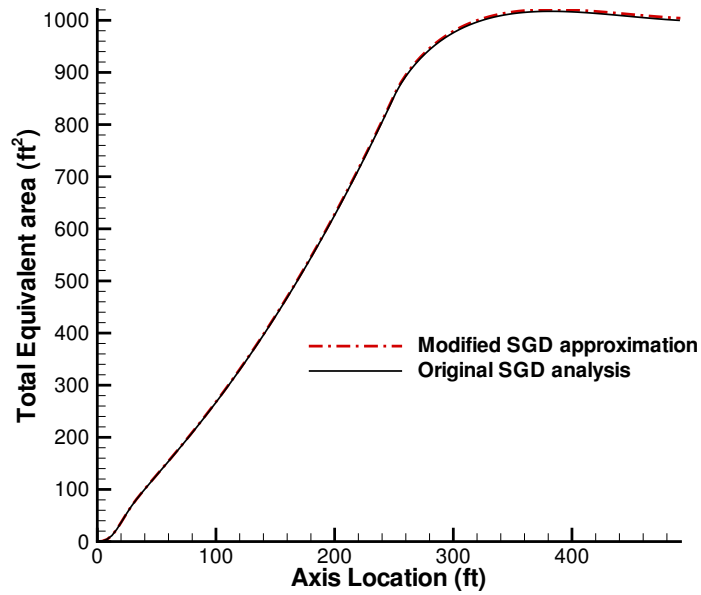


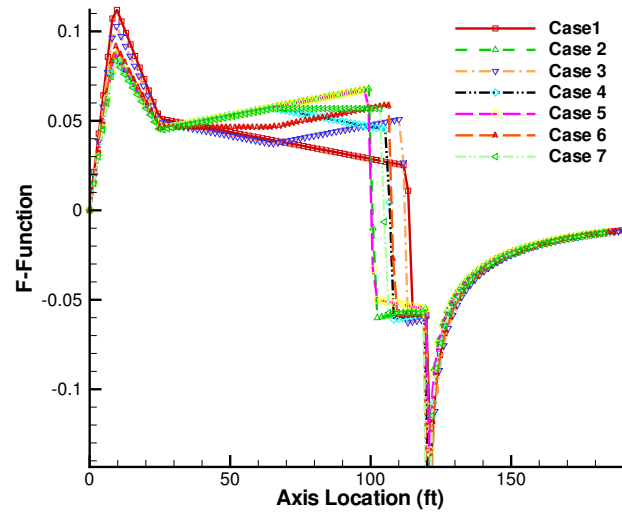
**Figure 62:** Comparison of total equivalent areas for case 2



SGD approximation boils down to the Seebass-George-Darden analysis in the worst case.

### 3.8.3 Additional insights of modified SGD analysis

In this section, the effect of the slopes  $B_i$  in the modified F-function formulation on the final loudness metrics and pressure signature is examined. Figure 63 depicts a few sample F-functions having varying slope values keeping most of the other inputs constant. Specifically, Mach = 1.6, length = 120.0 *ft*, weight = 120000.0 *lbs*,  $y_f = 25.0$  and altitude = 50000.0. The slopes in the sample F-functions have been given value equal to positive or negative 0.0003.



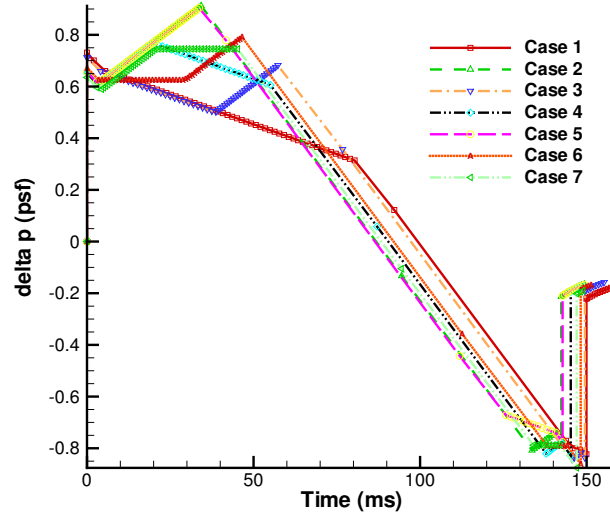
**Figure 63:** Sample F-functions with varying slopes

Figure 64 presents the ground pressure signatures corresponding to the F-functions shown in Figure 63. Various important conclusions can be deduced following these figures. With all the slopes having negative value, as in Case 1, the initial bump in the F-function is larger to compensate for the expansion in the mid region. Consequently, a larger loudness is associated with this signature. By having  $B_3$  go negative while maintaining  $B_1$  and  $B_2$  positive, the front portion of the F-function is not too large in magnitude. However, the rear shock system is reduced in strength thus leading to a lower loudness value. Case 2 and Case 5, with positive values for  $B_1$  and  $B_2$ , produce the minimum loudness values. The cases with negative  $B_1$  or negative  $B_2$  produce higher loudness values. Therefore, while performing the optimization studies, it is better to choose positive  $B_1$  and  $B_2$  while  $B_3$  can be allowed to

**Table 13:** Effect of varying slopes in F-function

Case	$B_1$	$B_2$	$B_3$	PLdB
1	-0.0003	-0.0003	-0.0003	92.8
2	0.0003	0.0003	0.0003	91.65
3	-0.0003	0.0003	0.0003	93.18
4	0.0003	-0.0003	0.0003	92.0
5	0.0003	0.0003	-0.0003	91.55
6	0.0	0.0003	0.0	92.5
7	0.0003	0.0	0.0	92.32

take on positive or negative values. Case 6 and Case 7 have been included to show the effect of flat regions in the portion of the F-function after the front shock and expansion. It is observed that a flat region followed by a ramp as in Case 6 produces a stronger front shock than Case 7 where the F-function has a ramp followed by a flat region. However, due to the lift constraint, Case 7 would have a stronger compression in the mid-region resulting in a higher shock overpressure value. The loudness values and shock perturbations corresponding to these figures are given in Table 13.

**Figure 64:** Sample ground signatures with varying slopes

### 3.9 Optimization tool

At the conceptual level, the designer is supposed to narrow down infinite number of possible designs to pick the most promising configurations for further analysis. The requirements and constraints usually reduce the design space. A single design is never a right choice at this stage of design. The most promising designs can be used to perform trade-off studies. It is necessary therefore to produce a population of non-dominated designs as a solution of the shape optimization process. Shape optimization used in this work is based on the idea that the ground pressure signature could be modified by changing the geometric design parameters that act as independent variables in the optimization process. A multi-objective problem is solved where conflicting objectives would be used. The objectives would be to simultaneously minimize the boom strength based on a chosen criterion and drag on the body.

Based on the above requirements, an optimizer is needed that achieves global optima of more than one objective. Evolutionary algorithms are usually suited for this purpose, even though they are computationally expensive. A non-dominated sorting genetic algorithm, *NSGA* [114, 51], is used in this study. The procedure is sketched in Figure 65 taken from [51]. Similar to other genetic algorithms, this algorithm generates a random initial population of points  $P_0$ . Selection, recombination and mutation operators are applied on the population and the resulting population,  $Q_0$  is combined with the original population to form a combined population  $R_0$ . The combined population is then sorted according to non-domination.  $F_i$  are the portions of the population with rank  $i$ . The top ranking populations are retained for next population. Crowding distance sorting procedure is then applied to obtain a population of the same size as the original. This procedure is continued till an optimized solution is reached.

A simple four design variable, 2 objective optimization run was performed to test the genetic algorithm performance. The sample optimization problem is formulated in Equation 71. In this example, four continuous variables are used  $x_1$ ,  $x_2$ ,  $x_3$  and  $x_4$ . The two objective functions to be minimized are also specified along with side constraints for the variables.

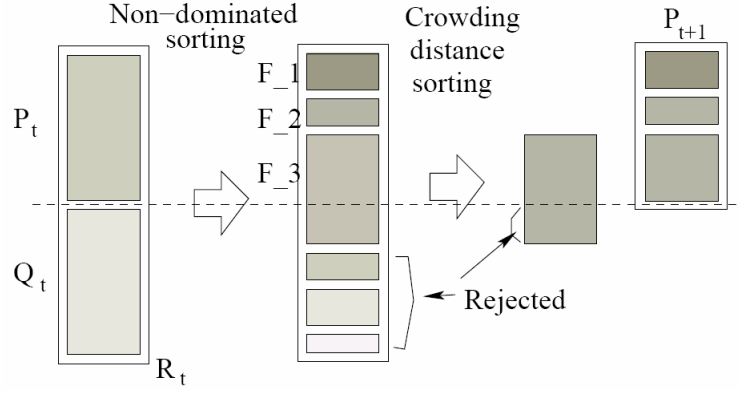


**Figure 65:** Sketch of NSGA II

$$\begin{aligned}
 \text{Min} : f_1(x) &= \frac{1}{n} \sum_{i=1}^n x_i^2 \\
 \text{Min} : f_2(x) &= \frac{1}{n} \sum_{i=1}^n (x_i - 2)^2 \\
 -4 &\leq x_i \leq 4, i = 1, 2, 3, 4
 \end{aligned} \tag{71}$$

A look at the objectives reveals that the required Pareto-optimal solutions are  $x_i \in [0, 2]$ . This means that both the objective functions cannot have minimum at the point point in the domain. A Pareto-optimal front represents a population of points in the domain space where the value of first objective cannot be reduced without increasing the value of the second objective. Figure 66 shows the Pareto-optimal front in the space of objectives. It can be seen from the figure that the initial population is gradually moved towards this Pareto front and all the points on this front are optimum points. The designer has to make a choice which point on the Pareto-optimal front is suitable from a practical or design perspective.

### 3.10 Summary of improved tools

In this chapter, all the analysis tool improvements done for this study have been presented. These tools form the building blocks for the shape optimization analysis to be conducted. However, a methodology has to be followed in order to bring together these diverse tools. The next next chapter introduces the implementation details wherein it is explained how most of the tools developed come together to perform aircraft shape optimization.

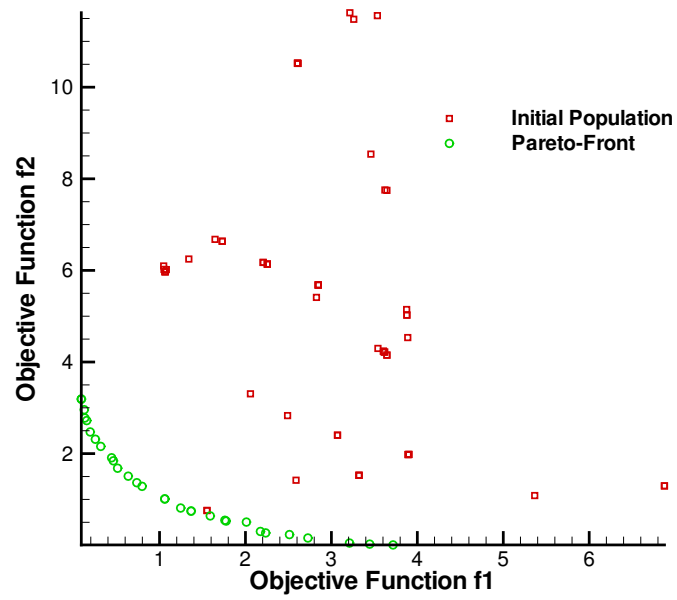


**Figure 66:** Performance of NSGA on a two objective optimization problem

## CHAPTER IV

# IMPLEMENTATION DETAILS AND FRAMEWORK FORMULATION

### *4.1 Metamodelling*

Due to the conceptual design paradigm shift, better and more accurate analyses are being used much earlier in the design phases than have been used in the past. This is termed as physics based design strategy because better models based on physics of the problem are used rather than empirical relationships. However, accurate analyses come at the price of higher computational time. If the design space being looked into is significantly large, considerable time would need to be invested in order to obtain useful designs. To overcome this problem and yet retain the physics-based approach, approximations of the analysis models have to be developed. Since these model the analysis models, they are termed as metamodels.

Various metamodels have been used by researchers in the past to approximate complex analysis routines. Some of these, not in any order of complexity, are response surface methodology, kriging, co-kriging and neural networks. In the following sections, each of these methodologies is briefly described. The neural network method is presented in much more detail as neural network regression has been performed and used in this study.

#### **4.1.1 Response Surface Equations**

Response Surface Methodology (RSM) [52] is the combination of mathematical and statistical techniques used in the study of relationships and optimization, where several independent variables influence a dependent variable or response. The objective is to obtain a working relation between the inputs and the response. In applying the RSM, the response or dependent variables' influence on a independent variable is viewed as a surface to which a

mathematical model is fitted. This procedure, simply stated, is just power series approximation to the required degree, usually two, of the responses in terms of multiple input variables as shown in Equation 72. Given the ranges for the input variables, a design of experiments (DoE) array is set-up and desired responses are computed using the actual analysis. Design of Experiments (DoE) provides a structured means of establishing the number of analysis executions required and the number of levels of the parameters' values for the regression run. Using a combination of RSE's and DoE arrays and the set of inputs and responses, the coefficients of the approximation are solved as a minimum least squares error problem. Once these coefficients are known, responses can be predicted for other input values, provided they are within the ranges specified earlier.

$$R = b_0 + \sum_{i=1}^n b_i x_i + \sum_{i=1}^n b_{ii} x_i^2 + \sum_{i=1}^n \sum_{j=1, j \neq i}^n b_{ij} x_i x_j \quad (72)$$

There are a couple of important advantages associated with this method. Firstly, it is computationally very cheap. Secondly, a closed form functional relationship between inputs and outputs is readily obtained. However, a quadratic surface model may be inadequate for many non-linear analyses. Due to this limitation, people resort to trust-region response surface methods wherein quadratic surfaces are created in localized areas which when put together could represent a highly non-linear representation, if the trust-regions are chosen to be suitably small. Trust region response surface methods may approximate an analyses response quite accurately. However, this method would offset any computational gains that the RSM is known to provide. Thus, an efficient meta-model for non-linear analyses has to be studied and other alternatives have to be looked into.

#### 4.1.2 Kriging and co-kriging

Kriging refers to a geo-statistical regression analyses first introduced by Krige. Kriging tries to obtain the value of a function at an unknown location by constructing a minimum error variance linear estimate of the function. The following paragraphs explain this procedure briefly. Before explaining the kriging procedure, an important statistical property of the

data sets has to be studied. This is called a variogram. The normal descriptive statistics like mean, standard deviation, median, etc. do not capture the spatial variation of the data sets. This is because the normal statistics do not incorporate the spatial locations of the data in their calculations. A Variogram [5] is a descriptive statistic that attempts to characterize the spatial continuity of a data set.

Consider the residual data values given in Equation 73.  $F(u_i)$  are the known data values,  $M(u)$  is the estimated mean of the data set.

$$G(u_i) = F(u_i) - M(u_i) \quad (73)$$

A variogram is defined mathematically as given in Equation 74

$$\gamma(h) = \frac{1}{2}E[G(u) - G(u + h)] \quad (74)$$

where  $h$  is the separation of interest to model spatial correlation. The covariance is defined as in Equation 75.

$$C(h) = E[G(u).G(u + h)] \quad (75)$$

Using equations 74 and 75 [115], a relation between covariance and variogram could be derived and given in Equation 76.

$$C(h) = C(0) - \gamma(h) \quad (76)$$

Simple kriging then approximates the residuals using a linear estimator as shown in Equation 77.

$$G^*(u) = \sum_{i=1}^n \lambda_i . G(u_i) \quad (77)$$



The error variance is defined as in Equation 78

$$e_R = E[(G^*(u) - G(u))^2] \quad (78)$$

The above equation after simplification yields Equation 79

$$e_R = \sum_{i=1}^n \sum_{j=1}^n \lambda_i \lambda_j C(u_i, u_j) - 2 \sum_{i=1}^n \lambda_i C(u, u_i) + C(0) \quad (79)$$

By taking the partial derivatives of the error variance with respect to the weights and equating to zero, a system of equations is obtained as shown in Equation 80. This system is solved to obtain the weights which can then be used to estimate the function values at new locations.

$$\sum_{j=1}^n \lambda_j C(u_i, u_j) = C(u, u_i), i = 1..n \quad (80)$$

Co-kriging uses the gradient information in addition to functional information.

### 4.1.3 Neural Networks

Unlike Response Surface Equation methods, Neural network modelling is a non-linear regression technique. Neural network [36] modelling is motivated by the way brain functions for learning and adapting information. An artificial neural network consists of simple processing units called artificial neurons that are connected in a specific way. The strength of each of these connections is termed as its weight. During the training phase, these weights are modified according to various training algorithms. The architecture and building blocks of a simple neural network are discussed next.

A simple neuron model shown in Figure 67 forms the fundamental building block for an artificial neural network. The input vector is  $x_i$  and,  $w_i$  are the weights associated with each input,  $y$  is the weighted sum of inputs and is the input to the transfer function  $f$  and the final output from the neuron model is  $a$ . Note also that,  $x_0$  along with its weight  $w_0$  acts

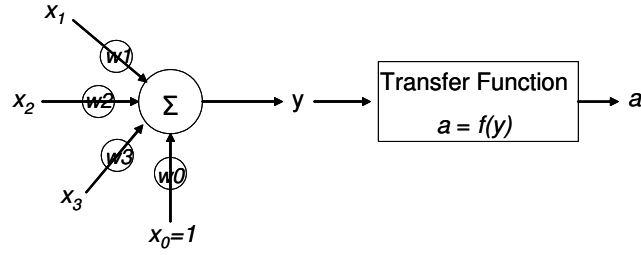


**Figure 67:** Artificial Neuron

as an intercept. This is called a bias to the neuron. In effect, each neuron computes the weighted sum of the inputs and uses this sum as input to a non-linear transfer function.

An artificial neural network could, in principle, have various layers of neurons. However, it has been proven that an artificial neural network with a single hidden layer is a universal approximator to any continuous smooth function provided the right number of neurons are chosen in the hidden layer. Choosing the right number of neurons in the hidden layer is often tricky. Over-fitting, generalization and other effects have to be taken into account to determine how many neurons should be used in the hidden layer. A rule of thumb is to use double the number of inputs as the number of neurons in the hidden layer.

A single hidden layer neural network has been used in this study to perform regression on various analyses. Such a neural network is shown in Figure 68.

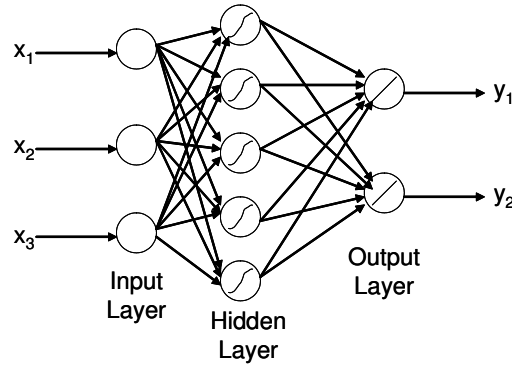


**Figure 68:** Single hidden layer Neural Network

For a single hidden layer neural network, the outputs,  $yN$ , can be specified in terms of the inputs,  $Nx$  by an equation such as the one shown in Equation 81 with weight matrices  $NW$ ,  $NV$  and bias vectors  $b_1$ ,  $b_2$ . The  $\sigma$  in this equation represents a non-linear sigmoidal transfer function, usually with activation 1.0. The reason for using a sigmoid function is to

generate a smooth bounded output from a weighted input summation.

$$yN = NW^T \sigma(NV^T Nx + b_1) + b_2 \quad (81)$$

Neural networks can be used in many ways. For our purposes here, supervised neural networks with batch training are used. Supervised neural networks have two stages. The first is the training stage where the actual analysis is run to record the input-output combinations. This data is then fed to the network that changes the weight matrices and bias vectors to fit the data in the best possible way. There are various algorithms to fit the data. In this study, Bayesian regularization learning algorithm available in the MATLAB neural network toolbox [67] is used. This algorithm minimizes a combination of squared errors and weights, and then determines the correct combination so as to produce a network that generalizes well. Once the optimum weight and bias vectors are obtained, the model has to be tested for performance. A test data of input-output pairs is generated using the actual analysis and it is compared with the output from neural network metamodel. If the neural network predicts the test data set satisfactorily, one can assume that the neural network has successfully approximated the analysis function.

## ***4.2 Metamodel estimation of minimum area distribution***

An approximate analysis is sought for the solution of the SGD equations [93]. The procedure laid out in the previous section can be used effectively to estimate the area distributions for minimum boom footprints. However, it has been observed that once in a while the optimization terminates prematurely by converging to a local minima. Even if it does converge to the right solution, the numerical integration and optimization routines could take about 6-8 seconds. That time is a lot if the analysis has to be run multiple times as in an optimization study. Therefore, an approximation to the SGD solution procedure is pursued. Since the responses are non-linear with respect to the inputs, a neural network meta-model has been used.

**Table 14:** Ranges for SGD input variables

Variable	Lower bound	Upper bound
B (Slope in F-function)	0.0	0.0004
Mach Number	1.4	1.8
Length	100.0 ft	200.0 ft
Gross Weight	80000.0 lbs	130000.0 lbs
Altitude	50000.0 ft	80000.0 ft
$y_f$ (Bluntness parameter)	2.0	30.0

#### 4.2.1 SGD analysis approximation

The first analysis to be approximated is the SGD analysis. The relevant equations and constraints describing this analysis was presented in an earlier section. Training and test data was generated for the single hidden layer neural network with the ranges for the variables provided in Table 14.

An artificial neural network with 18 hidden layers was chosen. This number was chosen by trial and error to obtain the best possible fit. This trial and error procedure required a couple of iterations. Figure 69 compares the actual training values with the values obtained from the neural network regression. Since a non-linear regression fit for the responses is being attempted, adequate training data has to be provided to the network. The domain is defined by a six dimensional space. The domain was separated into 64 regions by dividing each dimension into 2 parts. In each such region, 3 points were randomly chosen as training data. While this may not be optimal, most of the regions are well represented in the training set and a sufficiently accurate fit can be expected. Test data cases were randomly generated by picking points in the domain space. It can be seen from this figure that the neural network was able to successfully track the actual responses by modifying the weights and biases. A good match with training data is only half the story. The most important thing is that the network has to perform well for the test data. Figure 70 compares the test data with the output from the neural network. From this figure, it can be concluded that the trained neural network can be used as a viable replacement to the SGD analysis.

The information contained in the above figures can also be shown in terms of expected-predicted value plots. Figures 71 - 75 show the expected versus predicted values for the test data of the neural network approximation. Each plot also shows a high correlation coefficient for each fit in the test data. Note that these plots are for the random test data. The same plots can be generated for the data used to train the artificial neural network. An almost perfect fit is obtained in that case or in other words there are no points which are outliers in the training phase.

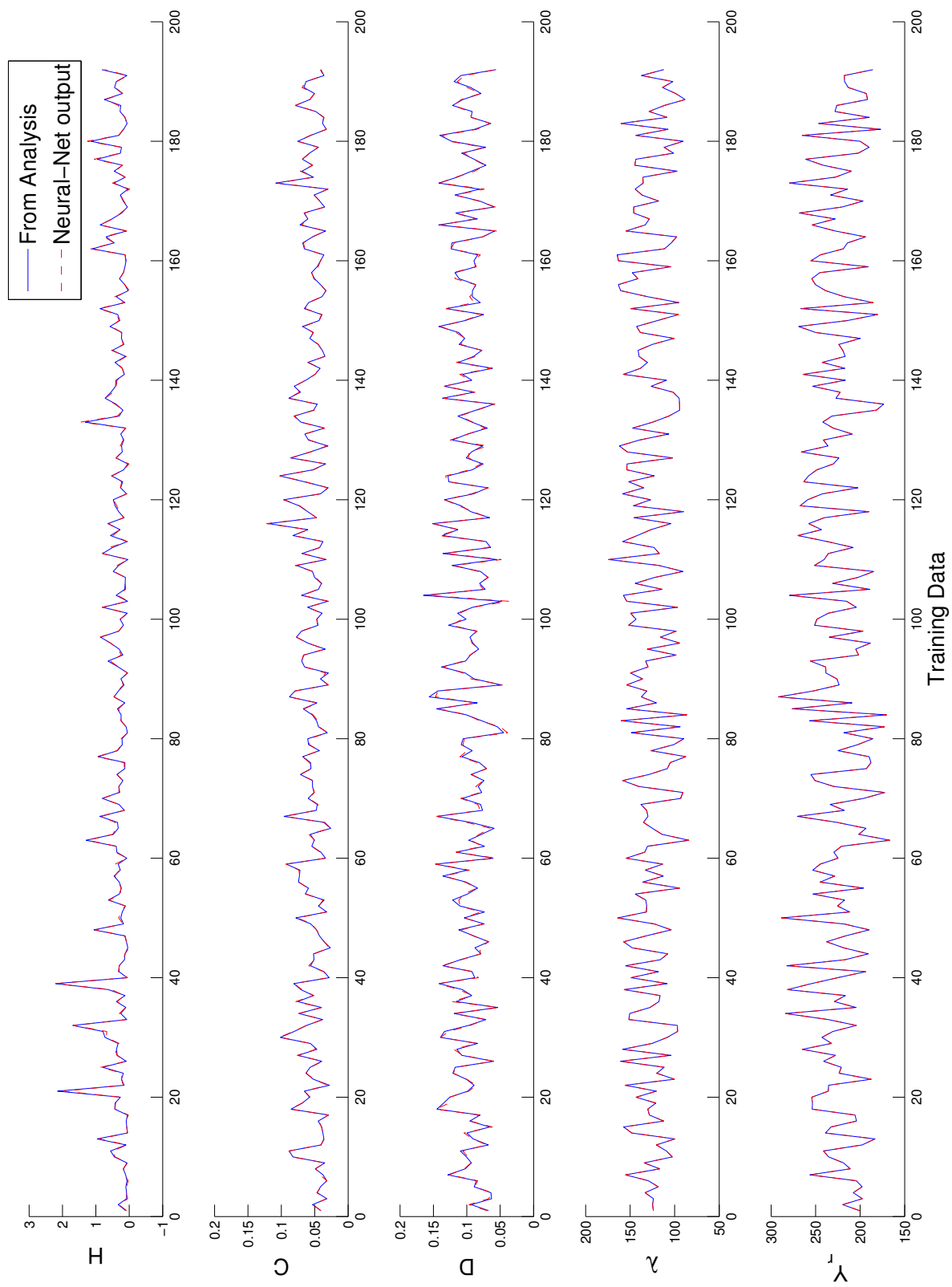


**Figure 69:** Neural Network training for SGD equations

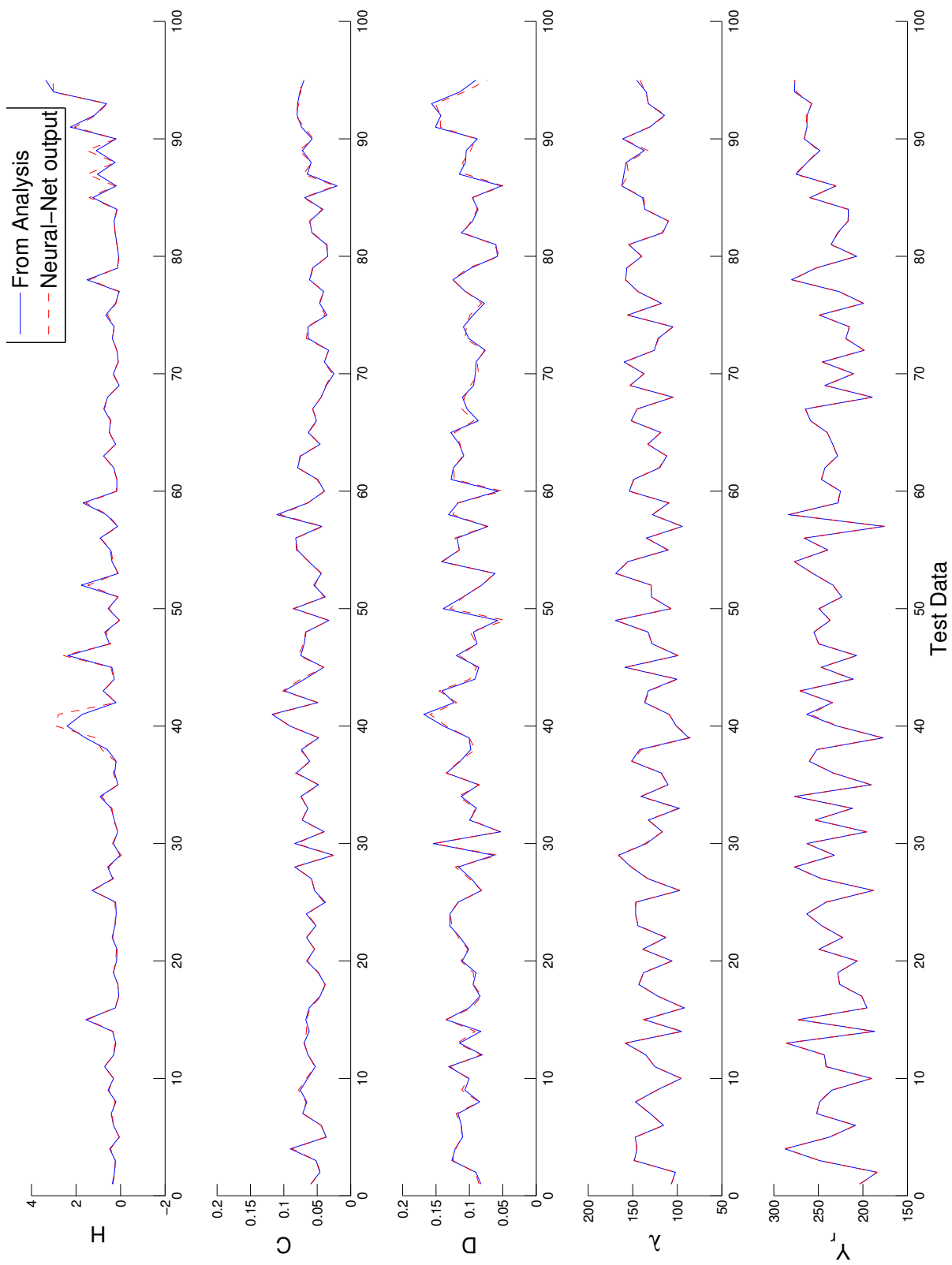


**Figure 70:** Neural Network testing for SGD equations

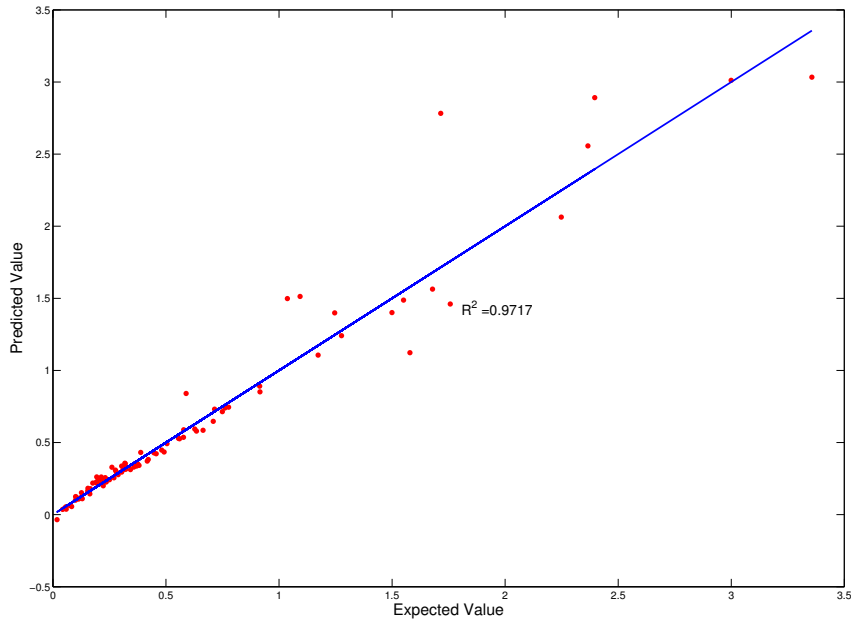


**Figure 71:** Expected vs. Predicted plot for H

#### 4.2.2 Modified SGD approximation

An approximate regression procedure for the modified SGD analysis is presented in this section. Training and test data required to train the neural network is once again generated with the variable ranges as specified in Table 15. Using the same logic as the previous case results in 6144 training cases. Using too many training cases not only increases the computational time, but also causes memorization of the input-response mapping that causes poor generalization for other data. To overcome this difficulty, the domain was arbitrarily divided into three overlapping sub-domains, (1) three consisting of seven variables, (2) one with six variables and (3) one with four variables. Each such sub-domain was cut in half in each dimension resulting in a total of 464 training cases. The number of random test cases were increased to observe the performance of the neural network approximation over a wide range of variables in the domain. Each of the inputs and outputs has been normalized with respect to the maximum value of particular variable.

As before, the number of neurons in the hidden layer was chosen by trial and error. For the modified analysis with 11 variables this number was 25. Figure 76 depicts the normalized training data as well as the output obtained from the neural network. It can be seen from



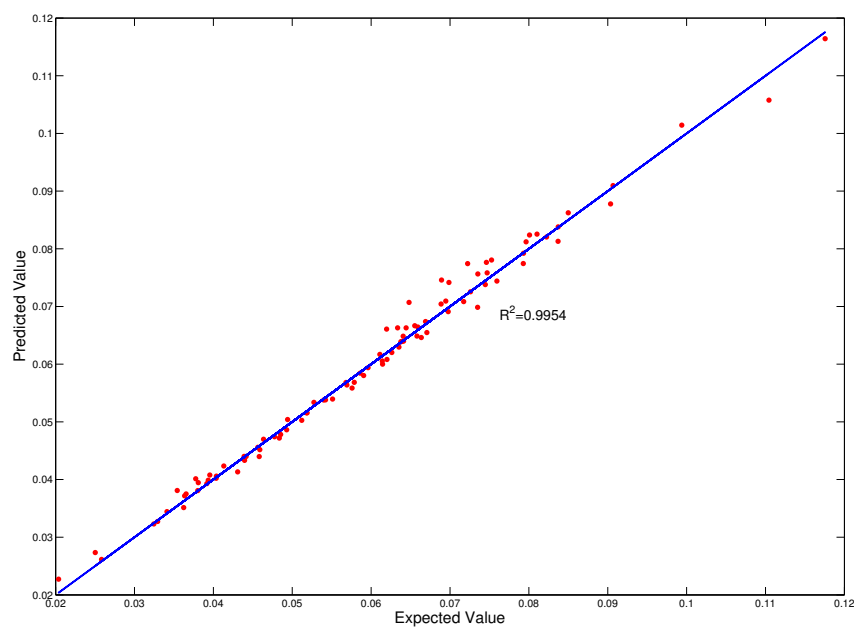


**Figure 72:** Expected vs. Predicted plot for C

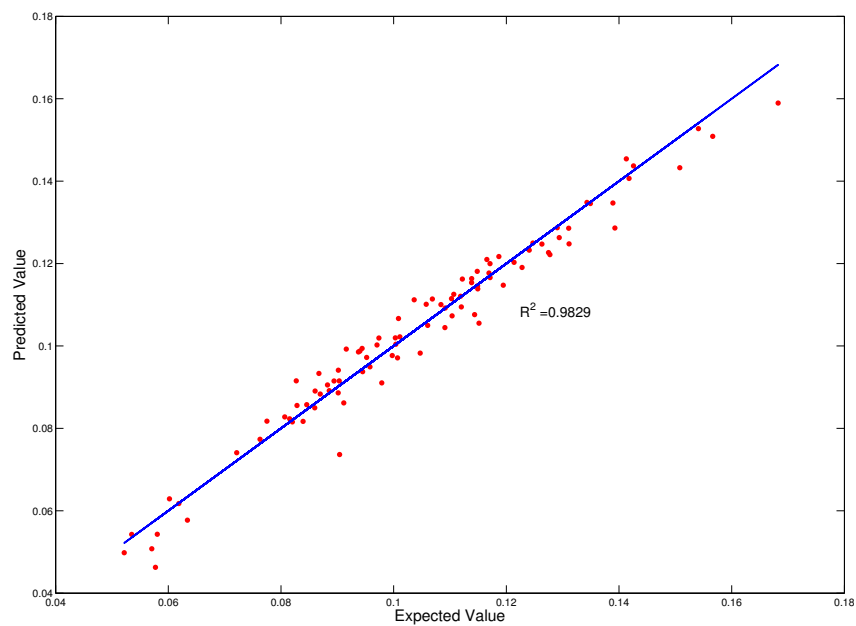


**Figure 73:** Expected vs. Predicted plot for D

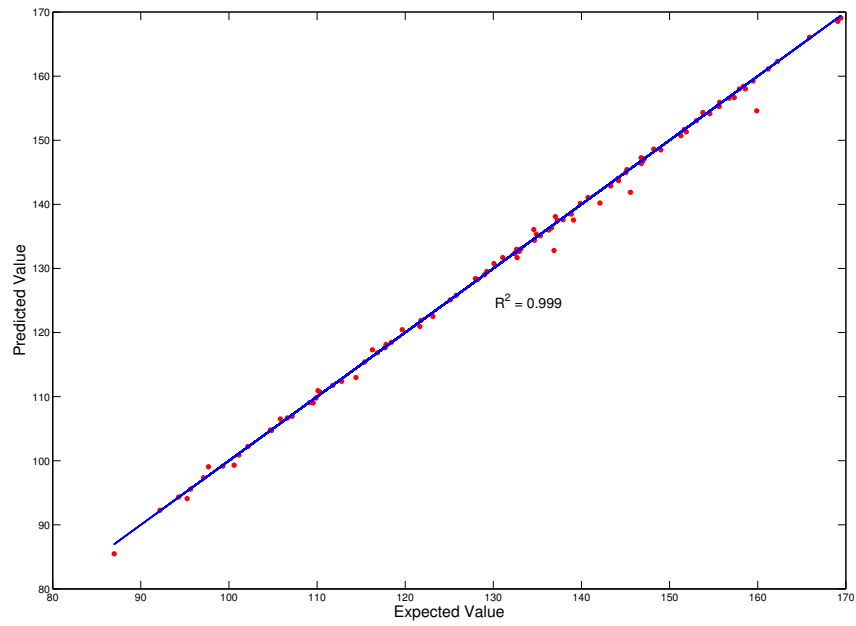


**Figure 74:** Expected vs. Predicted plot for  $\lambda$

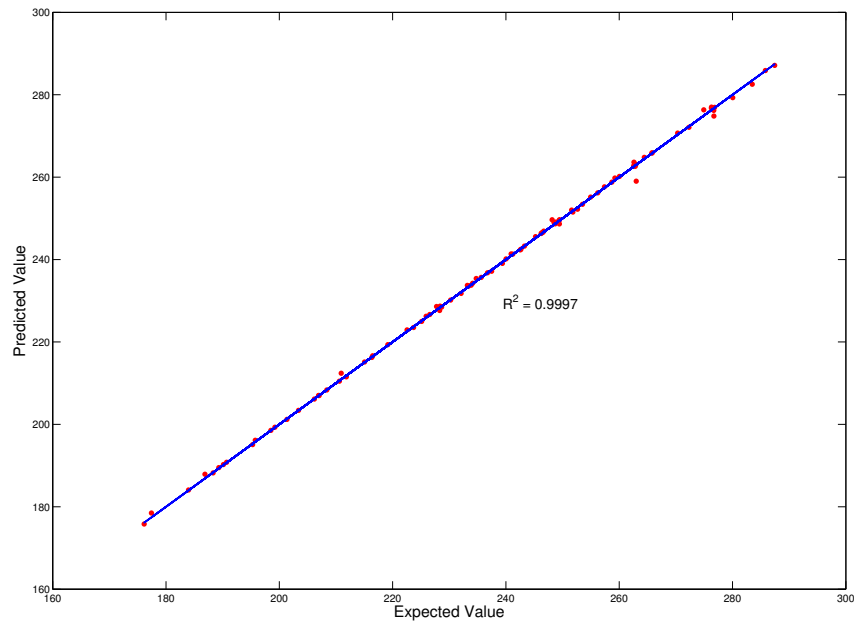


**Figure 75:** Expected vs. Predicted plot for  $Y_r$

**Table 15:** Ranges for modified SGD input variables

Variable	Lower bound	Upper bound
B1	-0.0003	0.0004
B2	-0.0003	0.0004
B3	-0.0003	0.0004
Mach Number	1.4	1.8
Length	100.0 ft	200.0 ft
Gross Weight	80000.0 lbs	130000.0 lbs
Altitude	40000.0 ft	80000.0 ft
$y_f$ (Bluntness parameter)	2.0	30.0
$\xi$	$y_f$	$y_f + 40.0$
$\eta$	0.2	0.8
t	0.0	5.0

this figure that the neural network was able to successfully track the actual responses by modifying the weights and biases. The performance of the neural network has to be evaluated with normalized test data. Figure 77 shows the test data and the output from the neural network. It can be seen that the neural network was able to mimic the performance of the actual analysis for most of the test cases. The neural network approximation for the modified SGD analysis can be used as an effective surrogate to the actual analysis.

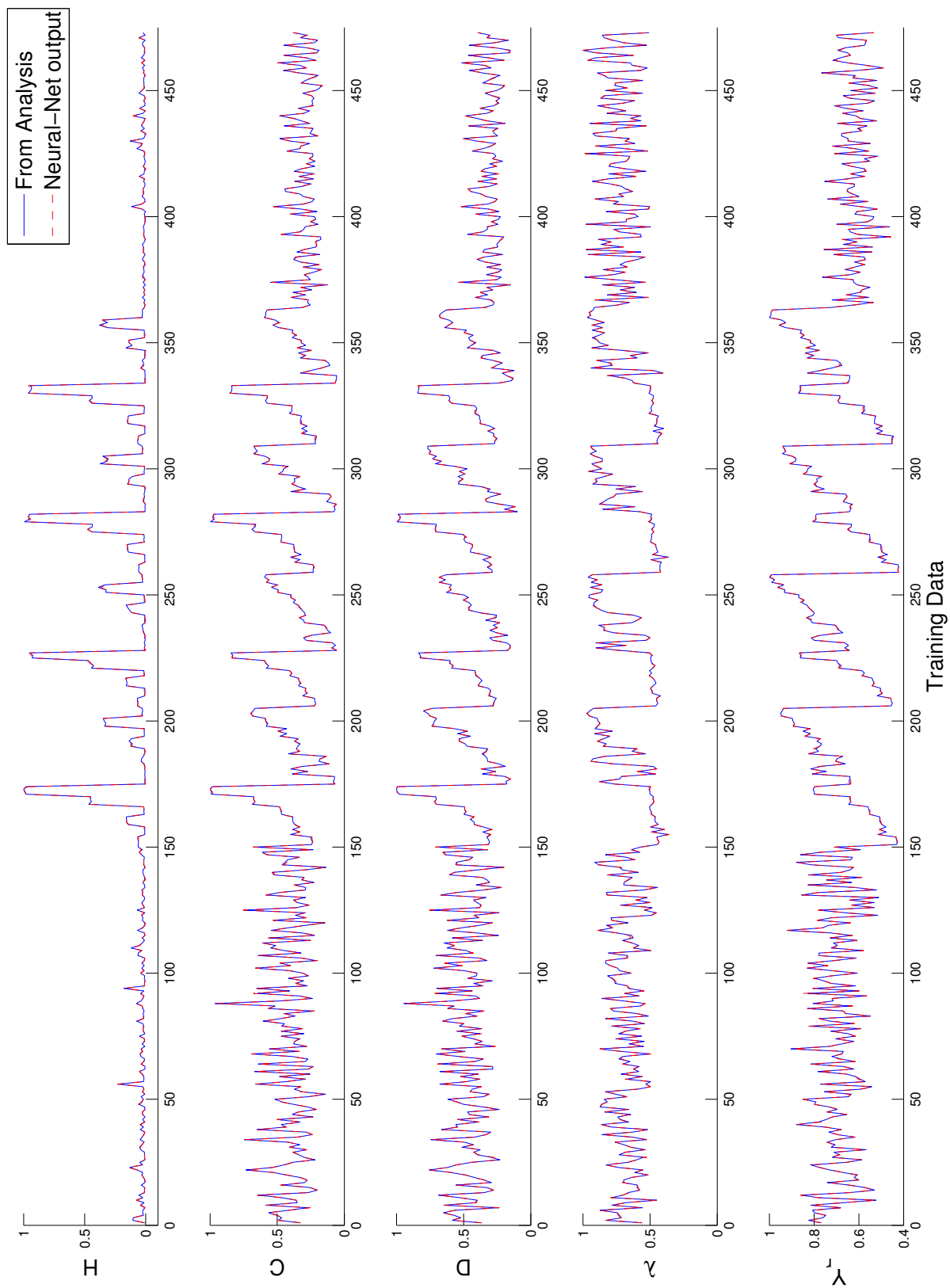


**Figure 76:** Neural Network training for modified SGD equations

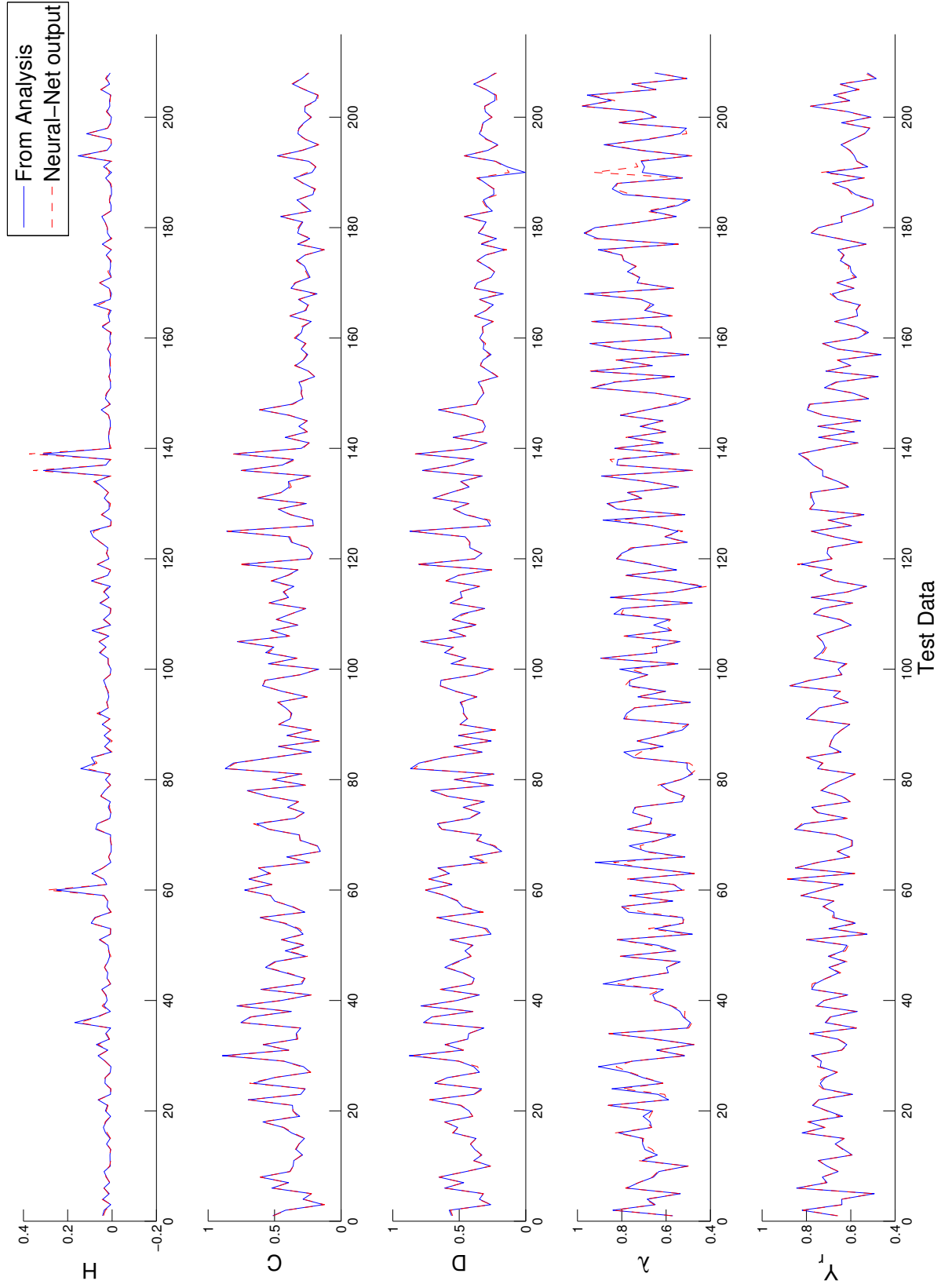


**Figure 77:** Neural Network testing for modified SGD equations

## 4.3 *Parallelization*

Shape optimization for sonic boom minimization is a multi-objective design problem and is multi-modal. This means that various local minima exist in the design space. To add to that, the shape variables consist of discrete and continuous variables. A traditional optimizer like SQP cannot be used for such a problem. Therefore, a genetic algorithm optimizer is used in this study. Genetic algorithms have a few important advantages over gradient based optimization schemes. Firstly, they achieve a global optimum instead of getting stuck in a local optimum. Secondly, since they operate on population of candidates, a Pareto-optimal front can be obtained in a multi-dimensional space with many conflicting objective functions. Furthermore, since these do not require any gradient information, they can be applied to problems that may be discontinuous. In spite of the advantages mentioned here, genetic algorithms have been the subject of criticism for various reasons. They are computationally very intensive as they lack the elegance of reaching the optimum as in the case of gradient based optimization. Moreover, as the algorithm continues, some individuals with high fitness values may dominate the population. This causes premature convergence of the population and hence has to be avoided.

In order to answer some of these concerns and yet retain the advantages of genetic algorithms, a parallel genetic algorithm optimizer has been developed for this study. Parallelization would enable genetic algorithm shape optimization runs to be completed much faster than they usually take to run, provided enough computers are present in the cluster and computational decomposition between processors is handled well. The following section presents a small digression to introduce a parallel computer architecture used in this study. The actual procedure for performing the parallel genetic algorithm operations is presented next.

### 4.3.1 **Message Passing Interface**

Message passing interface (MPI) [90] is a powerful toolkit for performing parallel computations over a cluster of computers. MPI provides portability and platform independent computing and thus is widely used over networks with heterogenous computers. MPI [122]

**Table 16:** Various implementations of MPI

<b>Implementation</b>	<b>Applicable System</b>
MPICH	Unix/Windows NT
MPICH-T3E	Cray T3E
LAM/MPI	Unix/SGI Irix/IBM AIX
Chimp	Sun OS/AIX/Irix/HP-UX
WinMPI	Windows 3.1

provides synchronous and asynchronous communication calls between processors, parallel file operations and time measurement operations. There are various implementations of the MPI standard being used and are listed in Table 16. The most widely used implementations are MPI-CH and LAM/MPI. LAM/MPI implementation has been used in this study because it was readily available. However, the implementation may be readily used on other implementations with minimal change as most of the implementations are based on the MPI standard. Local area multicomputer (LAM) [55] is an MPI programming environment and development system for computers over a network.

#### 4.3.2 Coarse grained Parallel Genetic Algorithms

Premature convergence is avoided in most genetic algorithms using a technique called niching [65], which tries to include a diverse population after every generation or epoch. A genetic algorithm might have the ability to include a diverse population at each generation. However, an efficient parallel implementation of the genetic algorithm could obtain the results in far less computational time. Various parallelization schemes have been proposed including those by Gondra [31] and de Toro [27]. In this study, a parallel genetic algorithm along the lines suggested by Gondra is attempted. A brief overview of parallelization strategy is presented next with the keywords directly taken from Gondra [31].

A coarse grained genetic algorithm is based on the principle of "punctuated equilibria", which is based on "allopatric speciation" and "stasis". Any population initially undergoes rapid evolution to new solution. However, as the number of generations increase, the changes to the population are gradual and slow. In that sense, the population attains stability or

stasis and could end up in a local optimum. "Punctuated equilibrium" principle states that in order to continue the evolution to the best population, new population members have to be thrust into the existing population to increase the evolution rate. "Allopatric speciation" involves the introduction of stabilized individuals into different populations.

## 4.4 *Probabilistic and statistical propagation*

As has been mentioned earlier, atmospheric fluctuations cause variations in the pressure signature on the ground. The effect of atmospheric fluctuations is modelled in the following way. Given the area distribution or the F-function, the propagation analysis is run for a fixed number of times with varying temperature and wind profiles. The perceived loudness values for these cases are then used to fit a distribution using goodness-of-fit tests. For the present study, Anderson-Darling test statistic is used.

### 4.4.1 Anderson-Darling test statistic

The Anderson-Darling test [116] is one of the most powerful and important goodness-of-fit tests in the statistical literature especially for small sample sizes. This test is a modification of the Kolmogorov-Smirnov test [37] in that it weighs the tails more heavily and utilizes a hypothesized distribution resulting in a better goodness-of-fit test. Using the sample points, the parameters of the hypothesized distribution are estimated. Then a critical value of the test statistic corresponding to the hypothesized distribution is determined. Depending on the values of the test statistic and the critical values, the hypothesized distribution is either accepted or rejected.

The Anderson-Darling test statistic is defined in equations 82 and 83 for a normal distribution. Here  $F_o$  represents the hypothesized cumulative distribution function with estimated distribution parameter,  $N$  is the sample size.

$$A^2 = -N - S \quad (82)$$



where

$$S = \sum_{i=1}^N \frac{(2i-1)}{N} [\ln(F_0(x_i)) + \ln(1 - F_0(x_{n+1-i}))] \quad (83)$$

If the mean and variance have to be estimated using the same data used for the test, then the test statistic,  $A^2$ , is modified according to the Equation 84.

$$A^2 = A^2 \times (1 + \frac{4}{N} + \frac{25}{N^2}) \quad (84)$$

The critical value for a normal distribution is given by Equation 85.

$$CV = 0.752 / (1 + \frac{0.75}{N} + \frac{2.25}{N^2}) \quad (85)$$

Now if  $A^2 > CV$ , then the hypothesized distribution is rejected as not fitting the sample points. The critical and test statistic values are different for various distributions and is explained in detail in the RAC [97] paper. In this study, Anderson-Darling test has been used to accept or reject 4 distributions, Normal, Log-Normal, Weibull and Exponential.

After the distribution of the perceived loudness level has been obtained using the Anderson-Darling test, a cumulative probability function for that distribution is obtained. A value corresponding to the 95% probable value is then used as the perceived loudness level. There is no scientific reason for choosing a 95% values. It is just to make sure a conservative perceived loudness value is used in the optimization process. Figure 78 depicts a cumulative distribution function obtained by using 50 perceived loudness values and fitting a distribution using the Anderson-Darling test. It so happened that a Weibull distribution was the best fit for the generated values and the indicated point is selected. The perceived loudness values were calculated by propagating a sample F-function from an altitude of 50000 ft. using random temperature and wind profiles discussed in chapter 1. The aircraft shape used to generate the F-function is a complete configuration with a multi-section wing, a T-tail, two nacelles under the wing and a simple fuselage. The shape was generated using the geometry generation scheme discussed in section 3.1.

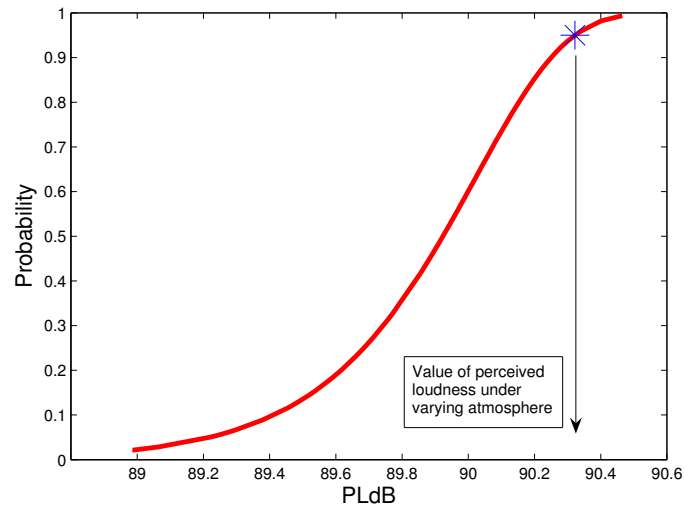


**Figure 78:** The perceived loudness level from CDF

## 4.5 PROBLEM FORMULATION

The study attempts to perform two different approaches to the aircraft shape optimization problem. The following subsections provide a brief description of the mathematical formulation for each of these approaches. Before the actual problem statement is formulated, a brief description is provided for the analysis constraints.

### 4.5.1 Analysis Constraints

Specifying constraints in an optimization process is extremely important to avoid designs and solutions which do not meet basic design requirements. In this study, two different kinds of constraints have been used as explained below.

#### 4.5.1.1 Geometric Constraints

Some of the geometries created by the geometric engine might not be suitable for completing a given mission. The reasons might be that the wing volume may not be enough to hold sufficient fuel or the cabin volume is not adequate to provide comfortable seating to all the passengers. These sort of constraints have to be included in an optimization study.

A typical mission for a supersonic business jet would be a take-off operation, supersonic cruise and landing with about  $4000nm$  of range. Following the conceptual analysis [42], the fuel fraction needed to complete a typical mission is in the range of 0.4 to 0.55. In this study,

**Table 17:** Geometric constraints

Variable	Lower Constraint value
Cabin Volume	888 $ft^3$
Wing Volume	$0.007643 \times W \text{ } ft^3$

to specify a constraint on the wing volume, a fuel fraction value of 0.4 has been used. Based on the fuel fraction and the gross weight of the aircraft, the weight of the fuel required can be obtained. With the knowledge of the density of the jet fuel used, the volume needed to carry that fuel can be obtained. This volume is then used as a lower limit for wing volume. Note that a jet-A fuel with density  $840kg/m^3$  is used in the constraint calculation.

The cabin volume constraint has to be specified so that the passengers can be comfortably seated during the supersonic flight. The cabin dimensions can be specified close to the values for an existing subsonic business jet. Simple cabin sketches and dimensions are specified by [42] and a cabin volume constraint can be specified as shown in Table 17.

#### 4.5.1.2 *Flight condition constraints*

Since linearized methods are being used, they are valid only for small angles of attack. However, if proper constraints are not placed, the optimizer would exploit this and produce shapes which would have to be flown at high angles of attack to optimize the objectives. To avoid this situation, an upper limit of  $4.0^\circ$  has been placed on the angle of attack. Note also that higher the angle of attack,  $\alpha_a$ , the lower is the effective length of the aircraft as defined by  $x_n$  in Equation 86. As a simple example, if the computed effective length is 145.0 ft. and the angle of attack is  $3^\circ$ , the length is reduced to 135.32 ft. at a Mach number of 1.6. This is a considerable reduction in the effective length and would lead to less separation between front and rear shocks in the near field signature and hence more intense sonic booms as the shocks have a greater chance to coalesce. In order to overcome this effect, the wings could be installed at an angle with respect to the fuselage so that sufficient lift can be generated at lower angles of attack.

$$x_n = \frac{\sin(\mu - \alpha_a)}{\sin(\mu)} x \quad (86)$$

#### 4.5.2 Direct Design

The first procedure is the usual direct optimization process. In this method, the shape is parameterized using shape parameters  $s_1, s_2, \dots, s_n, d_1, d_2, \dots, d_m$  and flight conditions  $M, W, h$  and  $l$ . The optimization problem is specified in Equation 87. Three different conflicting objectives are used to achieve a Pareto-optimal front of configurations in this three dimensional space. The first objective is to minimize the perceived loudness,  $PLdB$ , of the sonic-boom ground signature which is a function of the shape parameters. The second objective is to maximize the  $\frac{C_L}{C_D}$  ratio, which is also a function of the shape parameters. However, unlike the sonic boom noise metric, this objective is a near field phenomenon. The final objective is to maximize the reciprocal of the figure of merit,  $FoM$ , suggested by Seebass and Argrow [109]. A higher value of the figure of merit is generally known to yield lesser intensity sonic boom signatures.

As in the case of any real world optimization problem, suitable constraints have to be placed on certain variables in order to yield practical solutions. The specific constraints used in this study are given in Equation 87. The probability of exceeding the perceived loudness value is given an upper limit called the critical probability parameter  $P_c$ .

$$\begin{aligned} & \text{Minimize : } PLdB(s_1, s_2, \dots, s_n, d_1, d_2, \dots, d_m, M, l, h, W) \\ & \text{Maximize : } \frac{C_L}{C_D}(s_1, s_2, \dots, s_n, d_1, d_2, \dots, d_m, M, l, h, W) \\ & \text{Maximize : } FoM(M, W, l, h) \\ & \text{Constraints : } 100 \leq l \leq 150.0ft, 100000 \leq W \leq 150000lbs \\ & 40000 \leq h \leq 60000ft, \alpha_a \leq 4.0 \\ & P_{PLdB} \leq P_c = 0.05 \end{aligned} \quad (87)$$

### 4.5.3 Bi-level Reverse Design

The second method pursued here is the bi-level reverse approach where the shape optimization problem is broken into two separate optimization runs. By performing optimization in this way, additional insight is gained into the features of the equivalent area distribution which produce low sonic boom signatures. However, as always, the design should not lead to a solution which optimizes a particular objective at the cost of other metrics. So, conflicting objectives have to be introduced.

In the first step, the variables are the inputs to the SGD analysis as described in an earlier section. Varying these parameters causes the equivalent area distribution to change and so does the loudness metric on the ground. The figure of merit is provided as the conflicting objective. Side constraints are placed on each of the variables as shown in Equation 88 in order to restrict the problem to the projected size and dimensions of a supersonic business jet.

$$\begin{aligned}
& \textit{Minimize} : PLdB(W, M, l, h, y_f, B_1, B_2, B_3, t, \eta, \xi) \\
& \textit{Maximize} : FoM(M, W, l, h) \\
& \textit{Constraints} : 100 \leq l \leq 150.0ft, 1.45 \leq M \leq 1.7 \\
& 100000 \leq W \leq 150000lbs, 50000 \leq h \leq 80000ft \\
& 0.0 \leq B_1 \leq 0.0004, 0.0 \leq B_2 \leq 0.0004 \\
& -0.0003 \leq B_3 \leq 0.0004, 2.0 \leq y_f \leq 20.0 \\
& 0 \leq t \leq 5, 0.25 \leq \eta \leq 0.75 \\
& y_f \leq \xi \leq y_f + 40.0
\end{aligned} \tag{88}$$

The result of the first step is a Pareto-optimal population of variables which provide the best compromise between the perceived loudness and the figure of merit. Each individual in the Pareto-optimal population has an F-function and equivalent area distribution associated with it. Once a suitable individual is chosen, the second step can be started with the goal of achieving the area distribution of the chosen point.

The optimization statement is given in Equation 89. This step of the optimization process has continuous and discrete shape parameters as in the case of the direct design. However, in this case, the objective is to minimize the sum of squared difference between the area distribution of the aircraft and the target area distribution from step 1,  $\delta A$ , while ensuring that the lift to drag ratio is not severely deteriorated.

$$\begin{aligned}
& \text{Minimize : } \delta A(s_1, s_2, \dots, s_n, d_1, d_2, \dots, d_m, M, l, h) \\
& \text{Maximize : } \frac{C_L}{C_D}(s_1, s_2, \dots, s_n, d_1, d_2, \dots, d_m, M, l, h, W) \\
& \text{Constraints : } 100 \leq l \leq 150.0 \text{ ft} \\
& 100000 \leq W \leq 150000 \text{ lbs}, 50000 \leq h \leq 80000 \text{ ft} \\
& \alpha \leq 4.0, P_{LdB} \leq P_c = 0.05
\end{aligned} \tag{89}$$

## 4.6 Hierarchical cross-over operation

Because the shape parameter space is composed of discrete and continuous parameters, the cross-over operation has to be handled properly. Following the crossover operation given by Buonanno and Mavris [8], a hierarchical cross-over operation is used in this study. In this crossover operation, the standard uniform crossover is performed if the components are of the same category. However, if the components are dissimilar, then the components are swapped with a probability of 0.5. Using this kind of cross-over operation causes minimal gene disruption and leads to improved convergence rates.

Figure 79 presents a sample crossover operation. Shown in the figure are two parent configurations and the corresponding children configurations. Figure 80 sketches the process whereby the swing-wing and joined-wing tail features of the first parent are swapped with the multi-section wing and T-tail design of the second parent while creating children. The fuselage and pod settings are not altered in this particular example.

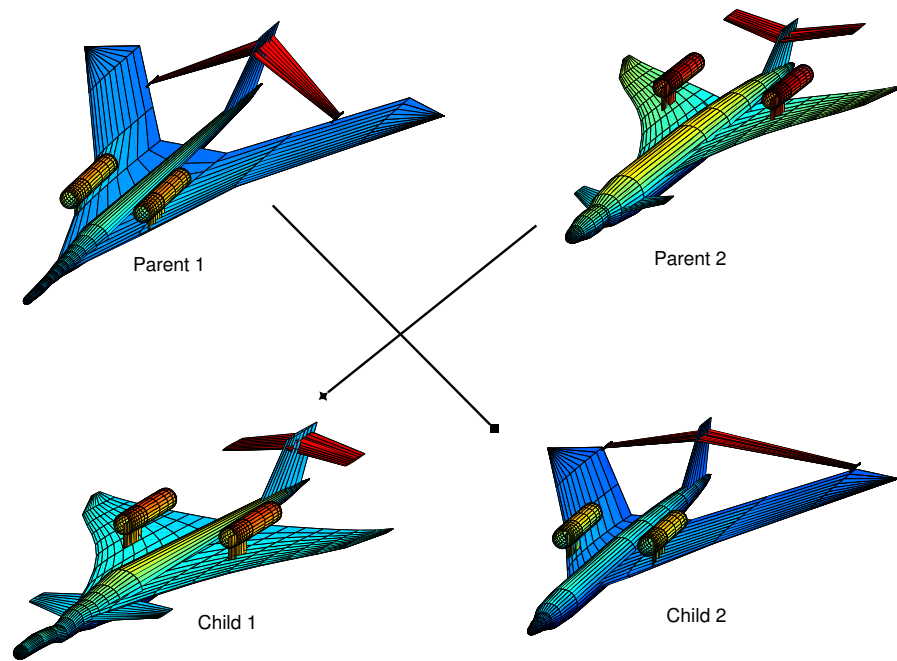


Figure 79: Sample Cross-over

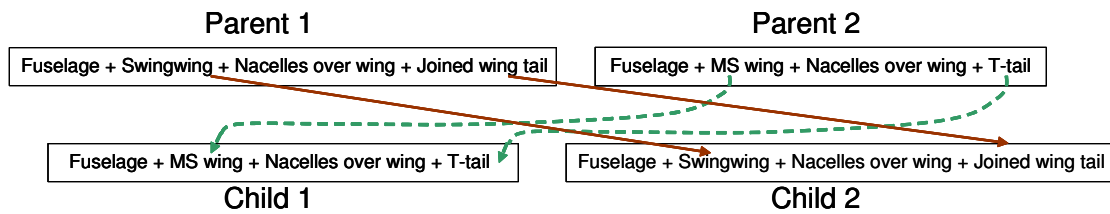
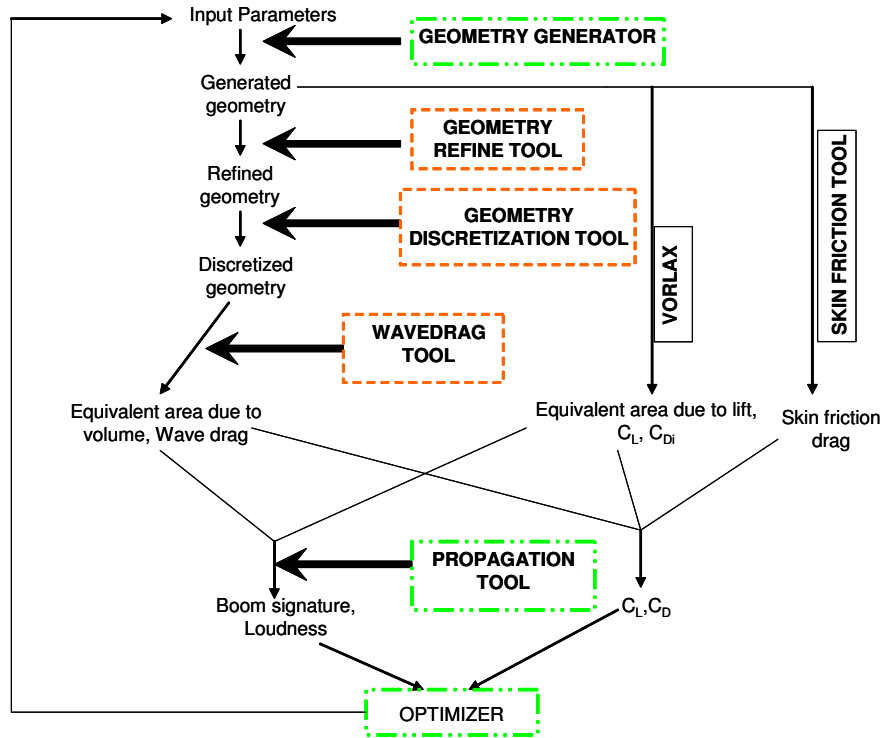


Figure 80: Sample Crossover sketch

## 4.7 Optimization flowcharts

### 4.7.1 Direct Design

This section presents the process flowcharts used for the shape optimization study. Figure 81 presents a flow chart of the direct design procedure. The boxes with a dashed line border show tools that have been developed from scratch for this study. The tools in dotted-dashed boxes were created by someone else and have been modified for the present study. Table 18 presents the names of all tools used in this study along with their functions.



**Figure 81:** Flow chart of the optimization process

### 4.7.2 Bi-level reverse design

The first step in bi-level design uses F-function parameters used in SGD analysis to create F-function and area distributions, which are then propagated numerous times by varying the atmospheric profiles and the optimizer is used to minimize the loudness and maximize the figure of merit. This step is depicted in Figure 82.

Using the optimized area distribution, shape parameters are modified in the second step to drive the optimizer towards matching the equivalent area distribution while at the same



**Table 18:** Different tools and their functions

GEOMETRY GENERATOR	Creates a wire-frame geometry using shape and planform parameters
REFINE TOOL	Refines the wire-frame geometry to user specified refine level
DISCRETIZATION TOOL	Performs boolean operations to create an unstructured geometry
WAVEDRAG TOOL	Obtains Mach plane intersection to produce equivalent area due to volume and wave drag
VORLAX	Computes lift, induced drag and equivalent area due to lift [71]
SKIN FRICTION TOOL	Computes skin friction drag based on wetted areas [66]
PROPAGATION TOOL	Uses either modified ARAP or PCBOOM for pressure propagation
OPTIMIZER	NSGA2 genetic algorithm optimizer

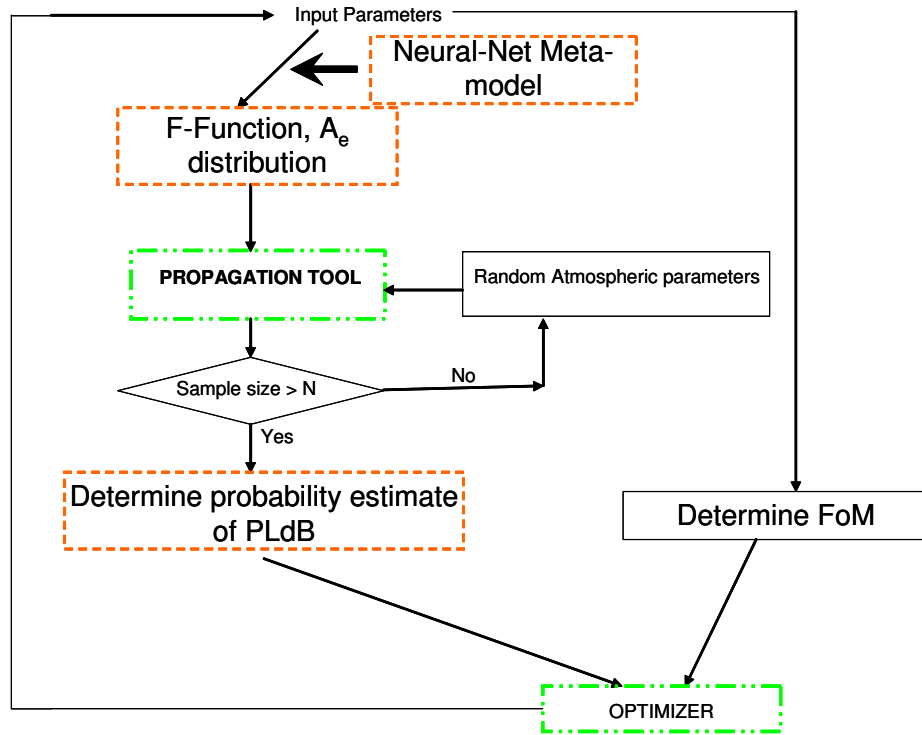


**Figure 82:** Reverse design: Step 1

time maximizing the  $\frac{C_L}{C_D}$  ratio. The tools used are the same as introduced in direct design. The second step is depicted in Figure 83.

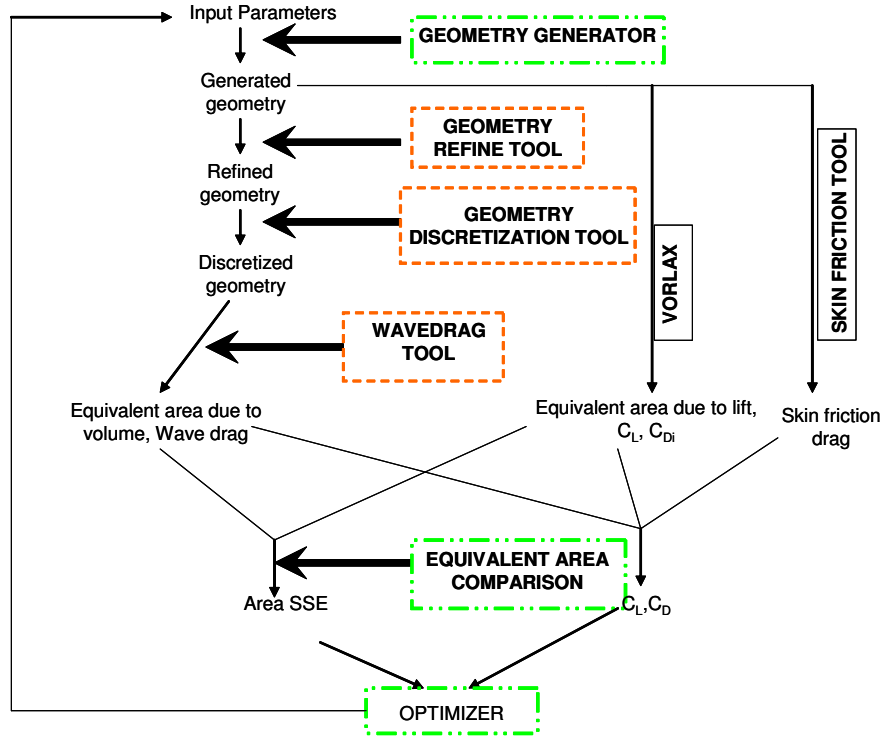
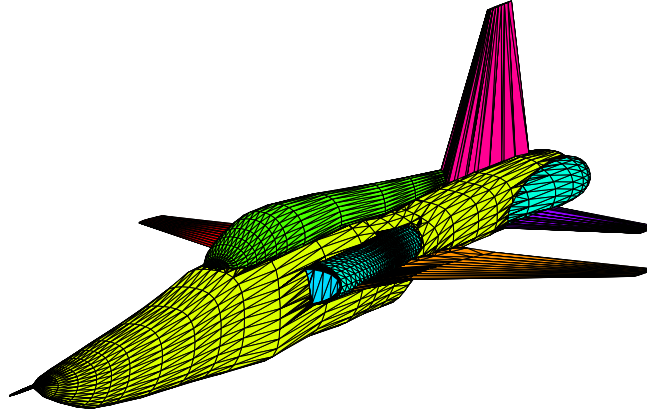


Figure 83: Reverse Design: Step 2

## 4.8 Proof of concept - SSBD

NASA has recently performed flight experiments [17] to verify the effect of shape changes on sonic boom strength by modifying the nose of a F5E aircraft. This aircraft has been run through our programs to first generate a triangular surface geometry as shown in Figure 84.

The equivalent area distribution due to volume comparison is shown in Figure 85 for a Mach number of 1.4. Three different curves are shown. The original Harris wave drag code over-predicts the area near the wing-fuselage intersection because of duplicated areas and under-predicts towards the rear of the aircraft because incorrect capture area is used. The real capture area can be calculated only by forming a combined aircraft model as is done in the present study. Further, the modification to crop wings before they intersect the fuselage causes an under-prediction of the area both near wing-fuselage intersection and also in the aft region. It can be clearly seen that the Harris wave drag code computes an erroneous



**Figure 84:** Modified F-5E

equivalent area distribution.

Figure 86 shows the comparison of ground boom signatures predicted by the improved tools considering varying atmospheric profiles along with the signature from the experimental data and that obtained by propagating the signature through standard atmosphere for a cruise Mach number of 1.4 and cruise altitude of 32000 ft. Since the exact geometric details of the F-5E were not known, the wing and fuselage geometry were tweaked so as to resemble the modified F5E used in the shaped sonic boom demonstrator program. Since the flight tests were conducted on August 27, 2003 at Edwards Air Force base in California, the temperature and wind measurements taken four times during that day were obtained from the NOAA [78] website. Each of the atmospheric variations referred to in this figure correspond to the four atmospheric measurements. Three different regions of interest are identified and shown in circles in the figure. The first circle shows that the without atmospheric fluctuations and rise time effects, the standard propagation code over-predicts both the shock pressure rise and shock overpressure. The second circle shows the presence of a shock in the middle of the signature and finally the third circle shows that the rear shock strength is over-predicted and the signature is not stretched as much as the real signature. Using each of the varying atmospheric temperature and wind profiles and using tangent hyperbolic rise time, a better match is obtained in the front region and there is not shock in the middle of the signature. Further, the rear shock strength gets closer to the actual measured value and signature

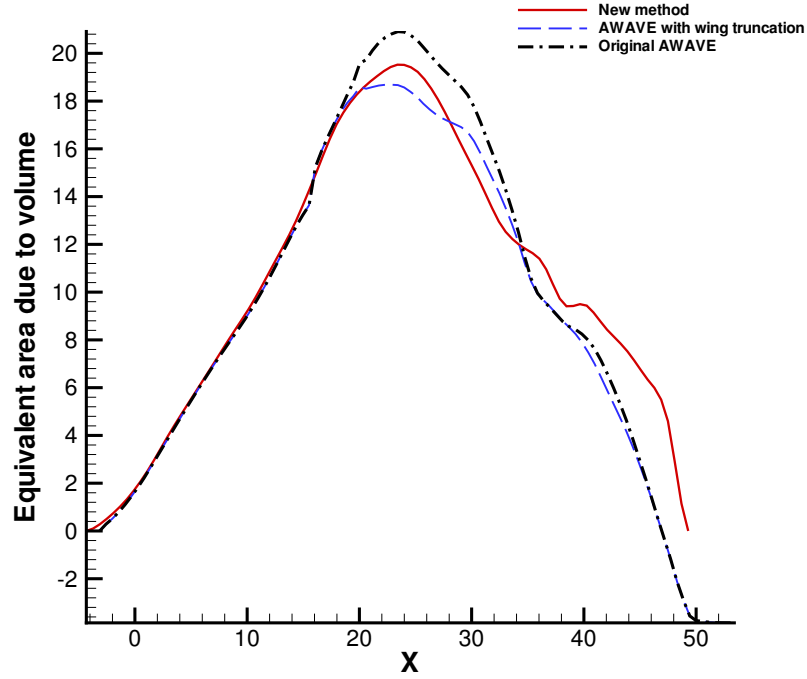


**Figure 85:** Equivalent area due to volume for Modified F-5E

stretching is seen for some atmospheric profiles. The failure to match the almost flat region just after the shock overpressure is a limitation of the near field analysis tools being used. A better near field prediction in conjunction with varying atmospheric profiles could lead to better signature matching. Furthermore, if the geometry is known more accurately, a better comparison can be expected.

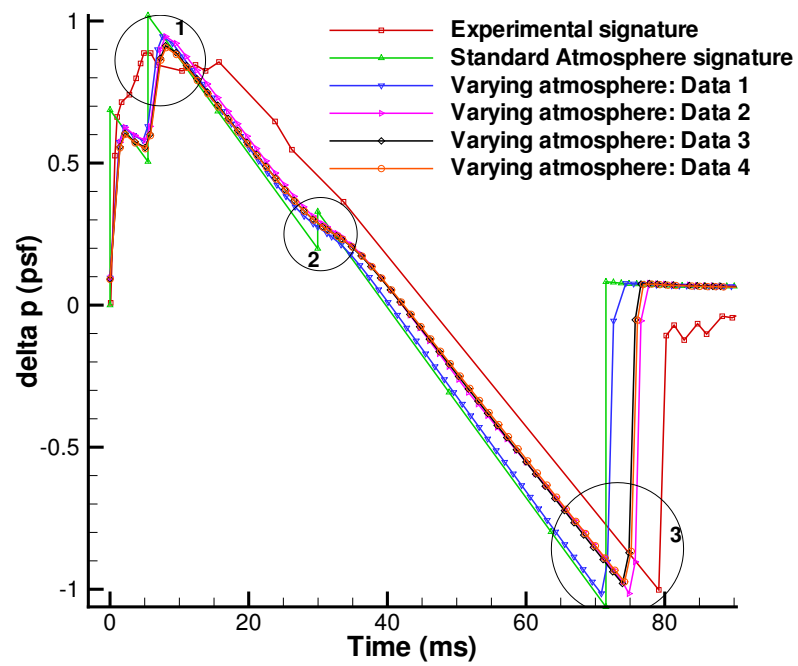


Figure 86: Boom signature comparison

# CHAPTER V

## SHAPE OPTIMIZATION RESULTS

Two preliminary optimization runs have been performed. The optimization tool used in both runs is a non-dominated sorting genetic algorithm [114]. In the first run, a population of configurations is generated using the MATLAB geometry generator described earlier and the improved linearized aerodynamic analyses and pressure propagation analysis codes are run on these geometries with the objectives being minimizing shock pressure rise and maximizing  $\frac{C_L}{C_D}$ . The second run performs the optimization in two steps in reverse order. The first step is to obtain the equivalent area distribution to minimize the perceived loudness at ground level. This distribution is then used as target to drive the shape of the aircraft in the second step.

### ***5.1 Direct optimization***

Most of the design tools developed in this research are put to use in this optimization run. The optimization procedure should use the valuable insights gained by numerous studies while attempting to minimize sonic boom of an aircraft. The trade-off between boom strength and wave drag is one such insight. The wave drag of an aircraft is sensitive to the shape of the nose cone as the nose shape determines the strength of the front shock. In order to provide sufficient control near the nose, the geometry variables are chosen such that fuselage nose shapes include a NURBS surface, as discussed in an earlier section, as well as a Sears-Haack half-body. This was done because Sears-Haack body is known to have the least wave drag.

Various different configurations can be obtained by changing the geometric parameters. A random initial population is created by the genetic algorithm and a snapshot of this geometric design space is shown in Figure 87. The vastness of the design space can be seen from this figure. A variety of configurations with dissimilar shapes and sizes can be obtained

as the initial population. Such a vast population aids the optimizer in selecting a suitable configuration without restricting the aircraft shapes.

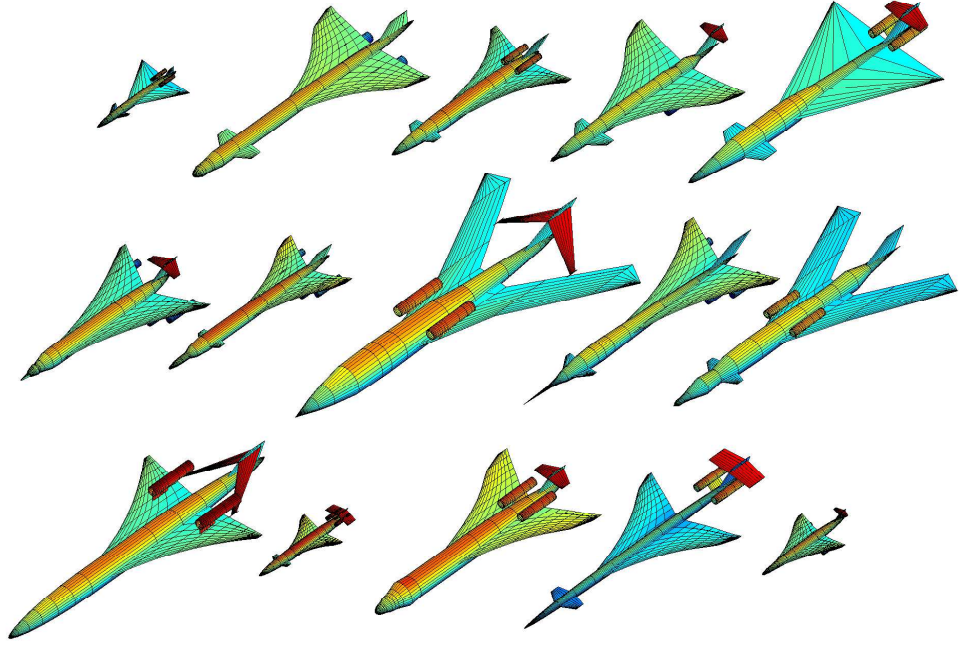


**Figure 87:** Some configurations from the initial population

Figure 88 shows the shift of the populations as the generation number increases. Note that in the first few generations, a rapid progression occurs followed by a slowly varying population towards the regions of desired objective values. Shown in this figure is also non-dominated portion of the population after 25 generations. The optimization could be continued for more generations to realize further improvements in the loudness metrics.

Corresponding to the population after 25 generations, the best designs are shown in Figure 89 which include the configurations with the lowest sonic boom loudness, maximum  $\frac{C_L}{C_D}$  ratio as well as the over-all best design. The salient features of the over-all best design can be explained as follows. The nose region is slightly cambered down so that a downward propagating pressure signature sees a nose bluntness while the azimuthal average of the Mach plane intercepted area is not too high. This prevents high wave drag values. The engines are on top of the wings due to the favorable nature of nacelle interference as mentioned before. The nacelle interference analysis is not very rigorous. Its just a qualitative simulation of the

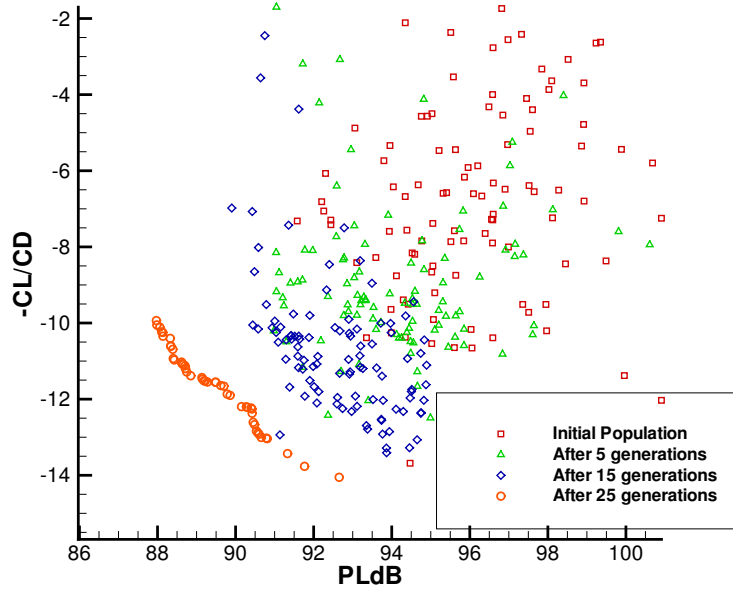


**Figure 88:** Progression of populations through generations

shock reflection phenomena. The wings have a multi-section configuration to allow for lift contribution along most of the aircraft length. The T-tail arrangement provides a medium to increase the effective length of the aircraft. However, it has generally been observed that if the T-tail is highly swept back, the equivalent area due to volume has a drop and rise in its distribution. This is because the wing contribution ends and the T-tail contribution does not begin immediately. Therefore, in a small portion of the axial region, the only area contribution is from the vertical tail. This drop and rise creates a non-smooth equivalent area distribution towards the rear regions and could lead to additional shocks in the far field. This situation can be avoided by either having a sweep-forward for the T-tail or extending the wing to a little aft axial location. However, by having a sweep forward T-tail, the effective length of the aircraft is reduced. These two features have to be balanced in order to arrive at the best design.

Figure 90 shows the iteration history of the minimum perceived loudness level at each generation. After 25 generations, the loudness level has decreased from around  $91.8dB$  to around  $87.9dB$ .

A direct optimization procedure attempts to minimize the near field metric of wave drag



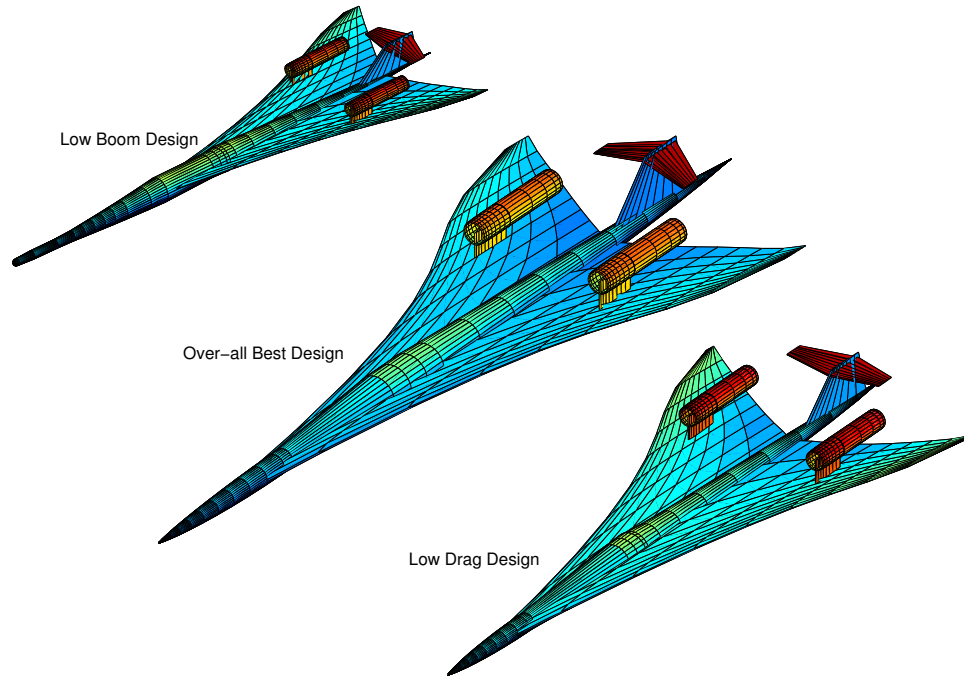


**Figure 89:** Best Designs from direct optimization

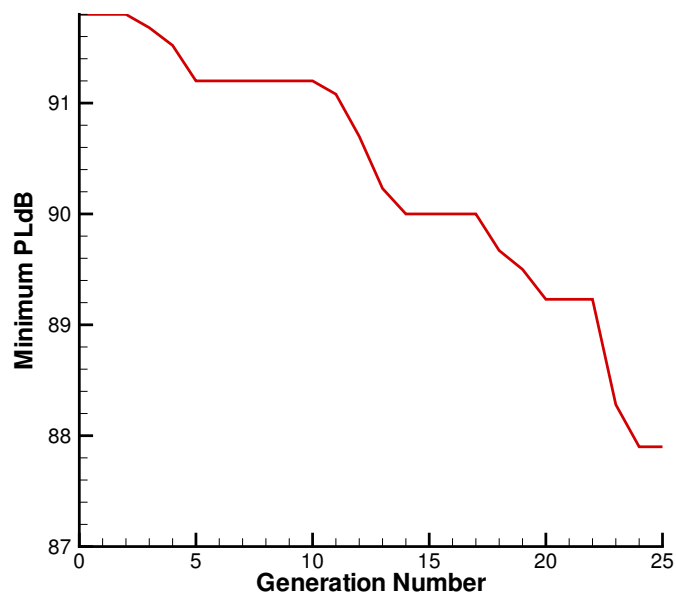


**Figure 90:** Iteration history of the minimum loudness at each generation

and far field metric of sonic boom loudness in a single step. By doing this optimization, there is no simple way of knowing if further reductions could be achieved in the desired metrics. It would be desirable if the designer has an idea of the best theoretical result that could be achieved with given aircraft dimensions and flight conditions. Furthermore, in the conceptual design stages, there should be an easy way to obtain the required results with changing flight conditions. In the direct design that is attempted here, the Mach number and altitude are arbitrarily chosen as 1.6 and 45000 ft. respectively. How does the design change when these numbers are altered? There is no easy way of answering this question quantitatively without resorting to some kind of regression or approximation of the near field signature with respect to the flight conditions and shape design variables. Because of the large number of shape parameters, the near field approximation is limited by the curse of dimensionality.

Near field distributions for theoretically minimizing sonic boom using modified SGD analysis can be used to overcome the problem of unknown desired goal. The next section presents a procedure where aircraft shapes are modified to achieve best known theoretical distributions for minimizing the desired objectives. Following this procedure, an extension is presented by which results for varying design conditions can be obtained easily.

## ***5.2 Bi-level reverse optimization from SGD perspective***

To numerically minimize sonic boom loudness, a "bi-level reverse" optimization is performed. The analysis is split into two optimization routines. Firstly, using probabilistic propagation techniques, the optimum area distribution, aircraft length, gross weight, Mach number, altitude and other parameters in the SGD analysis which minimize the perceived loudness level on the ground are determined. This optimum distribution is then fed to the next optimization level, where optimum shape parameters, described in section 2, are obtained to match the area distribution. The following sections briefly explain these steps and provide the shape optimization results. The optimization process is carried out using the SGD approximation as well as the modified SGD approximation introduced in this thesis. The

**Table 19:** Ranges of design variables for step 1

Design Variable	Lower bound	Upper bound
B (Slope in F-function)	0.0	0.0004
Mach Number	1.4	1.8
Length	100.0 ft	150.0 ft
Gross Weight	100000.0 lbs	130000.0 lbs
Altitude	50000.0 ft	60000.0 ft
$y_f$ (Bluntness parameter)	2.0	30.0

results from both these runs are compared to show the advantages of using the modified SGD analysis over the original SGD analysis.

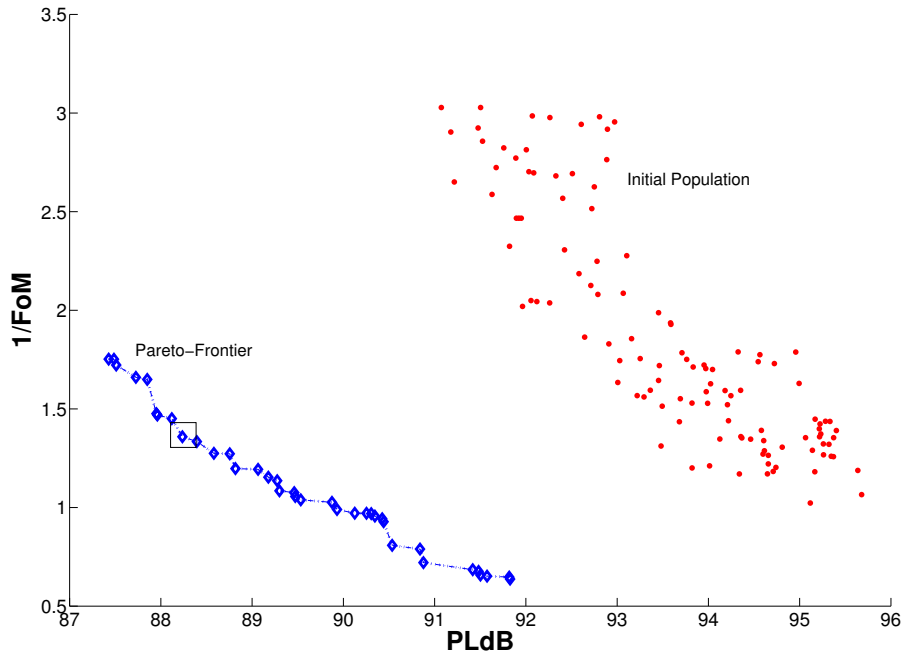
### 5.2.1 Using SGD analysis

#### 5.2.1.1 Optimum area distribution

The design variables in this step are the Mach number, gross weight, length, altitude, bluntness parameter,  $y_f$ , and slope of the rise in F-function, B. Using the neural network meta-model, optimum values for these variables are obtained by simultaneously minimizing the probabilistic estimate of the perceived loudness and maximizing the figure of merit [109]. The reason for providing the second conflicting objective is to obtain a Pareto-front of area distributions. The best compromised area distribution can then be chosen according to the requirements of the design.

The ranges of the design variables are shown in Table 19. Note that these ranges are a subset of the ranges utilized for the neural network approximation and therefore the neural network can be safely used in lieu of the actual analysis. The results for the first step of optimization are shown in figures 91 and 92. Figure 91 shows the Pareto-front of the probabilistic perceived loudness level against the reciprocal of figure of merit. The genetic algorithm was run for 30 generations. The genetic algorithm population is constantly pushed towards lower-bottom regions of the plot as the optimization process varies the design variables to minimize the desired objectives.

Figure 92 shows the target equivalent area distribution to be used for the second optimization step. This area distribution corresponds to the point enclosed by the rectangle in



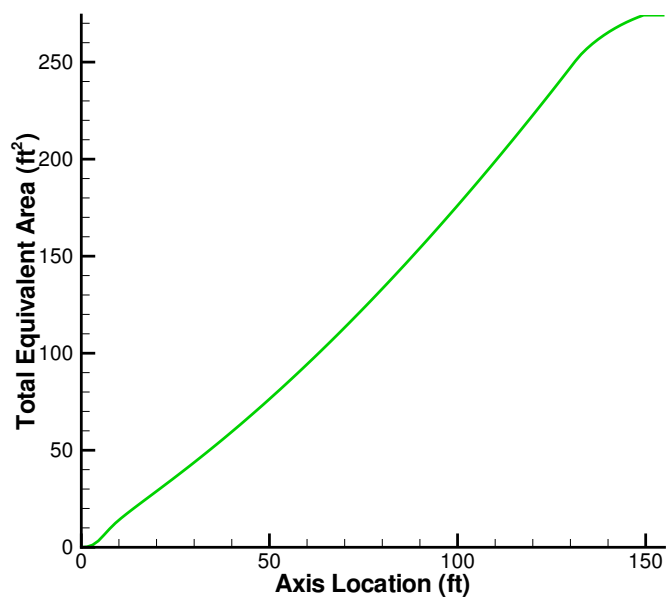
**Figure 91:** Pareto-front for the first step of optimization

Figure 91. The final values chosen for the second step of optimization are  $M = 1.44$ ,  $GW = 113401.76$  lbs, Altitude = 59501.73 ft, length = 149.54 ft.

#### 5.2.1.2 Estimation of optimum aircraft shape

The design variables in this step are the shape parameters of the aircraft. Suitable care is taken to include a vast design space for the aircraft shapes to achieve a proper final shape. A parallel genetic algorithm is utilized to minimize the normalized squared difference between the total equivalent area from the aircraft and the target area distribution. Figure 93 depicts the comparison of the total equivalent areas after about 20 generations. As can be observed from the figure, a close match is obtained for most of the longitudinal locations. The comparison is not as good for the tail regions. The reason for this could be that there is not sufficient shape control in the tail sections of the aircraft.

Figure 94 depicts the Pareto-front for the optimization run. The trade-off between boom minimization and aircraft performance is seen in this figure, although the measure for boom minimization has been mapped from the usual loudness level to the matching of the total equivalent areas. The dashed rectangle provides the best candidates which offer a fair



**Figure 92:** The target equivalent area distribution chosen for step 2

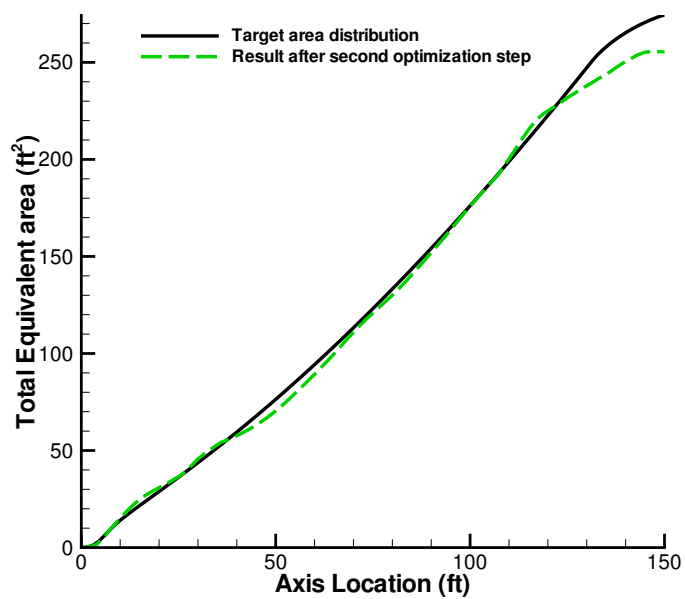


**Figure 93:** Comparison of total equivalent areas

compromise between sonic boom and performance constraints. Three such candidate configurations are provided in Figure 95. The features of the best design can be explained as follows. A T-tail design causes the signature length to be extended so that the effective length of the aircraft is increased. Nacelles over the top of wings cause shock reflection to a certain extent. These effects lead to a reduction in the sonic boom loudness on the ground.

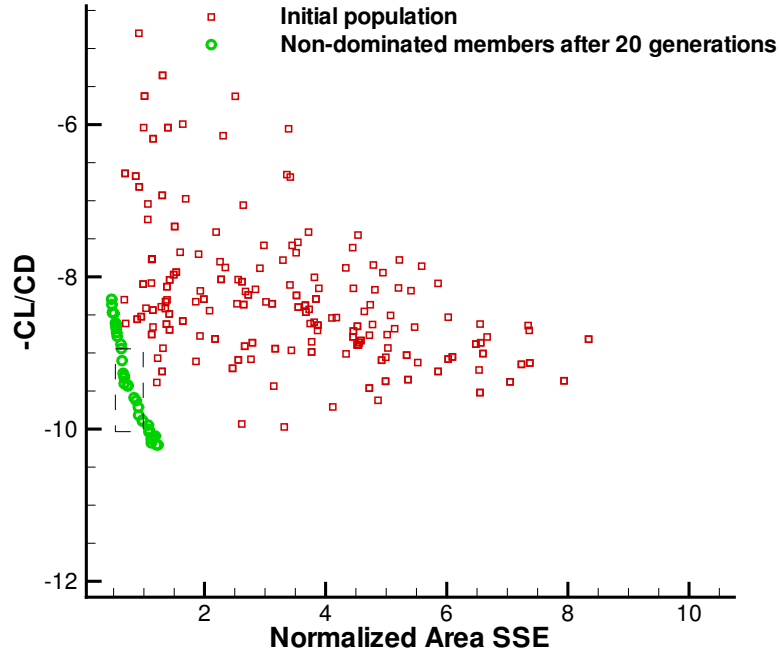


**Figure 94:** Pareto-front for the second step of optimization

The important thing to note about this formulation is that only a few parameters have been varied in the near field F-function so that the minimum loudness area distributions obtained are limited to a certain extent. In order to improve upon these, further parameters have to be added in the optimization. The modified SGD procedure with additional parameters provides the necessary extension to the design space to investigate many other near field signatures.

Before results from the modified SGD analysis are presented, a small digression is made here to show the performance of the parallel genetic algorithm. An important measure of the efficiency of a parallel algorithm is the speed-up achieved. Figure 96 depicts the superposition of a linear speed-up and the speed-up achieved by the parallel genetic algorithm used in this

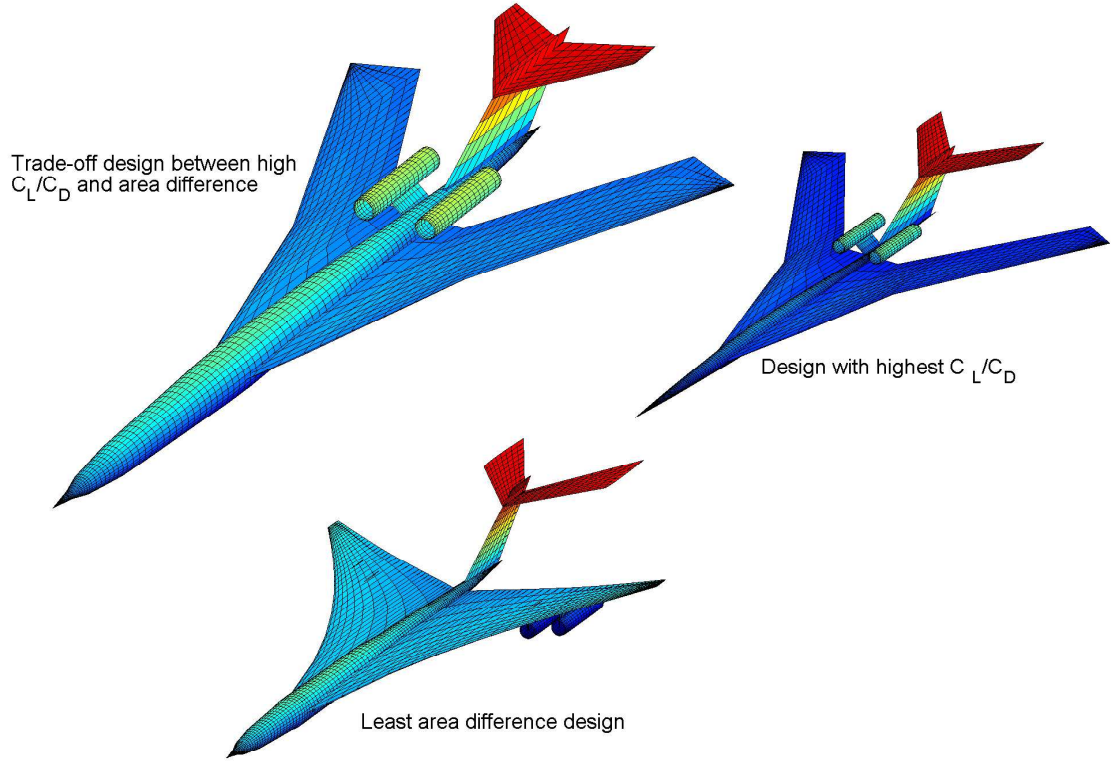


**Figure 95:** Three candidate configurations in the Pareto-front

study. As can be seen from the figure, a sub-linear speed-up is achieved. It might be possible to improve the speed-up by better communication calls between processors and would be pursued in the future.

## 5.2.2 Using generalized SGD analysis

### 5.2.2.1 Optimum area distribution

For the sake of conducting an optimization to determine a near field F-function that reduces the sonic boom loudness, the ranges for the parameters given in Table 20 are considered. The weight is given a minimum value of 100000 lbs. because a lower value is not structurally feasible with the other requirements. The ranges for the optimization run are a subset of the ranges used for neural network approximation. Thus, the approximation models can still be used in the optimization process.

Following the optimization as described earlier, a Pareto-front of the area distributions is obtained as shown in Figure 97. Compared to the results from Figure 91, significantly

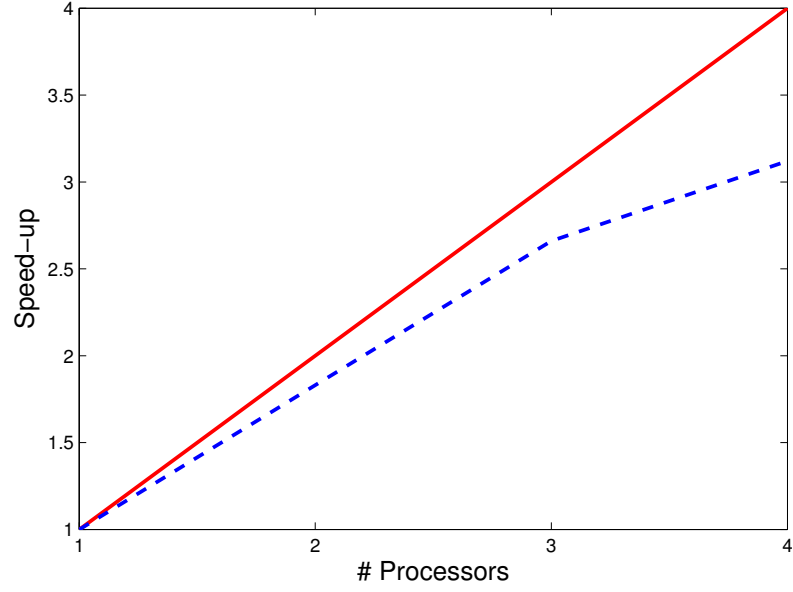


**Figure 96:** Speed-up of the Parallel GA

**Table 20:** Variable Ranges for parameters modified SGD optimization

Variable	Lower bound	Upper bound
B1	-0.00002	0.0004
B2	-0.00002	0.0004
B3	-0.0003	0.0004
Mach Number	1.45	1.7
Length	100.0 ft	150.0 ft
Gross Weight	100000.0 lbs	130000.0 lbs
Altitude	40000.0 ft	60000.0 ft
$y_f$ (Bluntness parameter)	2.0	10.0
$\xi$	$y_f$	$y_f + 40.0$
$\eta$	0.2	0.5
t	0.0	5.0



reduced perceived loudness values are obtained by opening up the design space. For the purpose of demonstration here, the values and distributions corresponding to the rectangle,  $PLdB = 84.27$ , shown in the figure are used for further design and analysis. The iteration history of the optimization process is shown in Figure 98. Depicted in this figure is the minimum perceived loudness level of the individual members of the population at each generation.

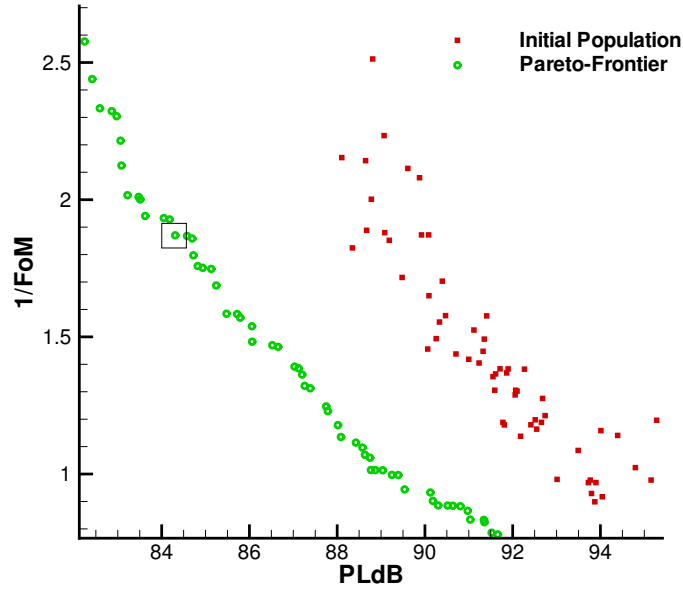
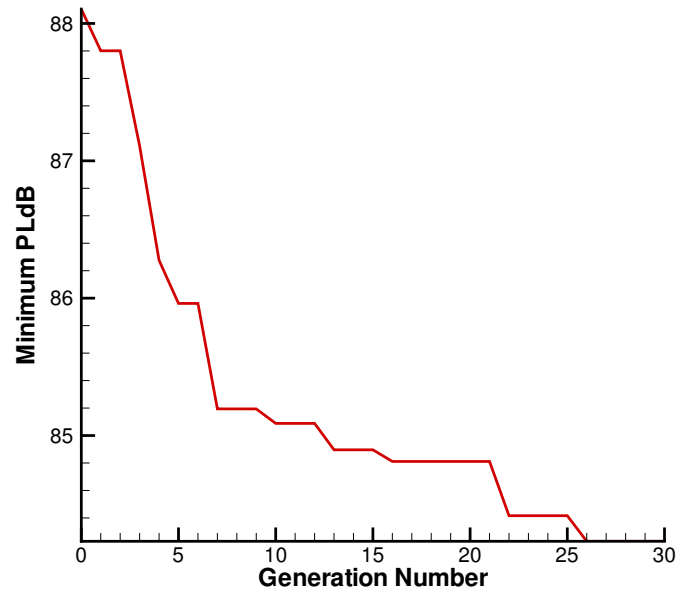


**Figure 97:** Pareto-front for the first step of optimization

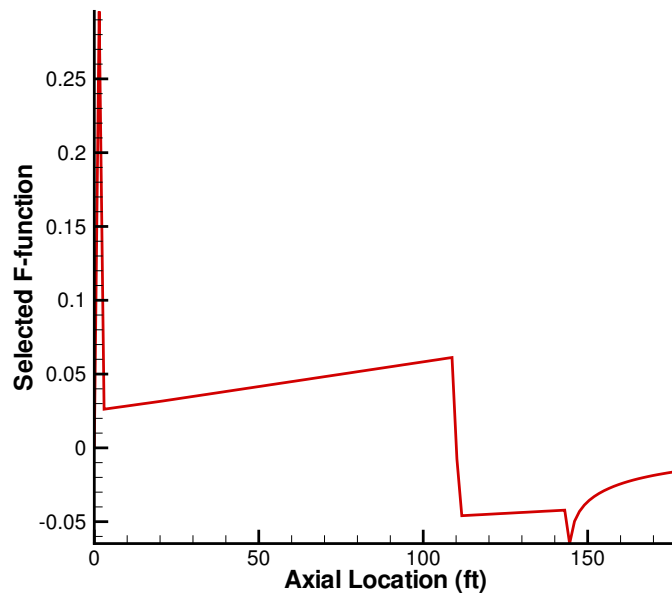
The results of the first step are given in figures 99 and 100. The resulting F-function has a peak near the nose followed by a small flat region and a ramp signifying a slow compression. This is then followed by a quick expansion after which there is a slow expansion. Finally, there is a rear compression to the ambient conditions.

Figure 100 depicts the corresponding area distribution which is used as the target for the second step of optimization. Figure 101 depicts the ground pressure signature corresponding to the highest loudness level when the F-function given in Figure 99 is propagated through varying atmospheric profiles. As can be seen, the initial shock rise is about 0.242 psf and the maximum over-pressure is about 0.7 psf.

Comparison with the results using the SGD analysis reveals that by opening up the



**Figure 98:** Iteration history of the minimum PLdB at each generation



**Figure 99:** The optimum F-function chosen from step 1

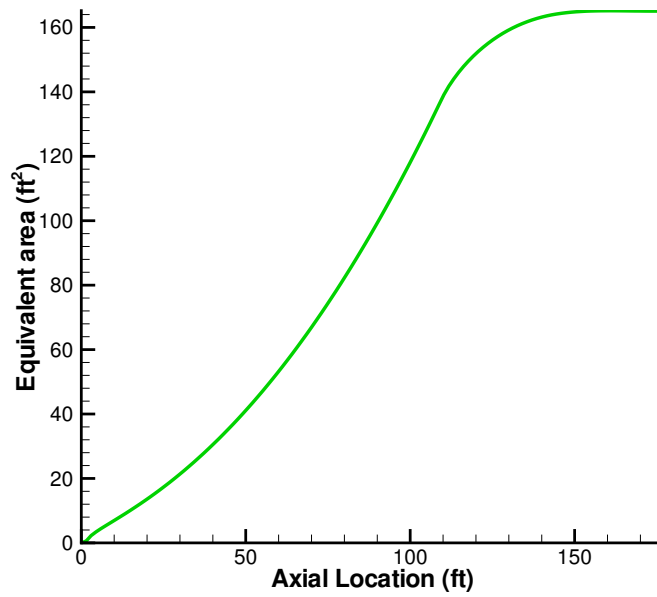


**Figure 100:** The target equivalent area distribution chosen for step 2

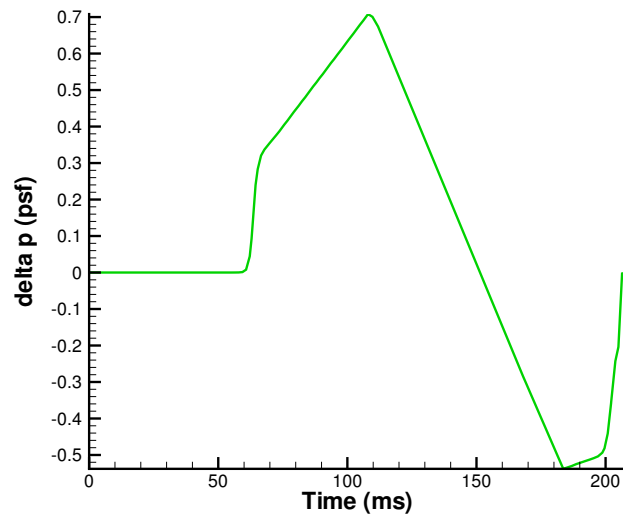


**Figure 101:** The ground pressure signature

**Table 21:** Final loudness values

Loudness Metric	Value
PLdB	84.27
dBA	68.393
dBC	95.026

design space, significant reduction in the perceived loudness values can be obtained. The final optimization values chosen for the second step of optimization are  $M = 1.46$ ,  $GW = 102460.76$  lbs,  $Altitude = 51660.2ft$ ,  $length = 149.27ft$ .. Table 21 presents the loudness values corresponding to the above ground signature.

#### *5.2.2.2 Perturbation from a given baseline*

It has been realized that getting to the target area distribution by varying shape parameters can take a lot of iterations and computational time. Using the linearized and conceptual analysis tools, it may not be possible to achieve an exact match for the equivalent area distribution. Nevertheless, if a close match is obtained, later design stages could use advanced analysis to realize the complete matching of the area distributions. In this section, the effect of perturbations from the target area distributions are studied to provide a better insight into performing optimization runs.

Deviations from the target curve can lead to some beneficial effects [72] if these deviations are below the target area distribution. In order to demonstrate this, minor deviations are introduced in a sample area distribution calculated from the modified SGD analysis. The area distribution perturbations are shown in Figure 102. The perturbations are quite small when viewed in this figure.

Using the perturbed area distributions, the F-function distribution in each of the cases can be calculated. These are shown in Figure 103. Since the F-function is representative of the near field signature, it can be seen that a perturbation in the area below SGD curve causes an expansion followed by a compression. As the signature propagates through the atmosphere, the compression moves forward and is reduced in strength as it meets the expansion wave. Thus, coalescence with the front shock is avoided to a certain extent.

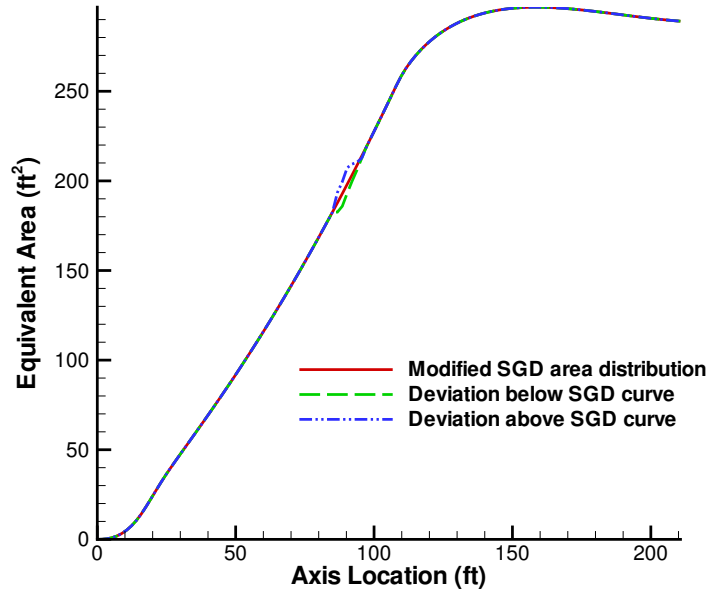
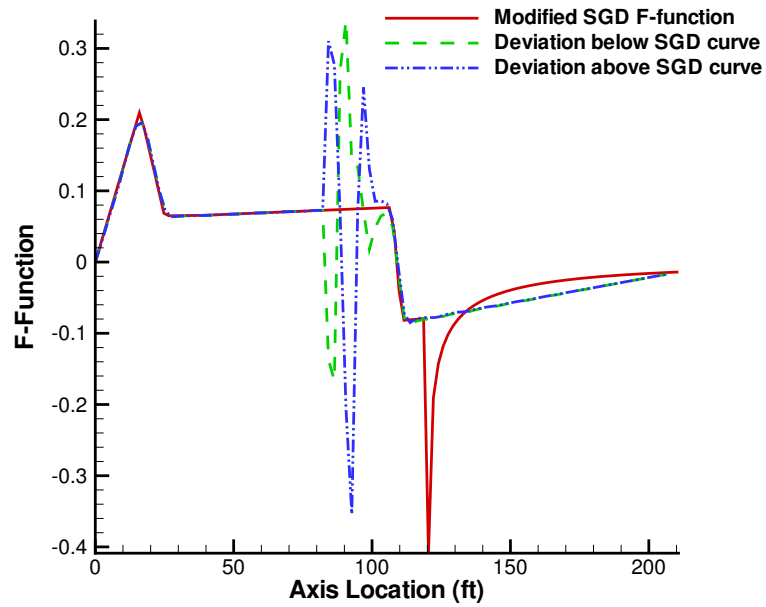


**Figure 102:** Area perturbations

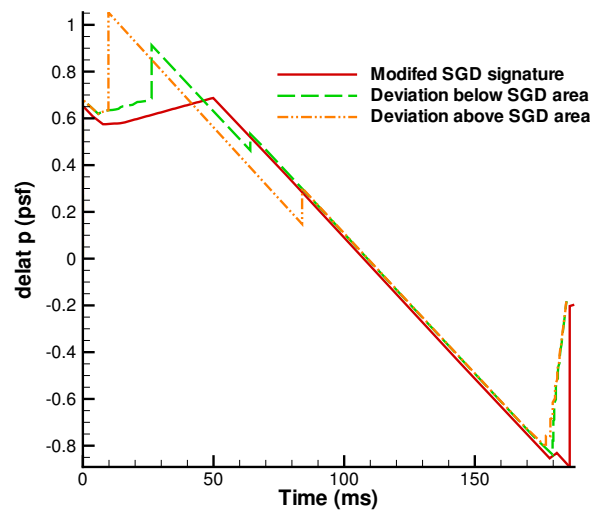
In contrast, if the deviation is above the modified SGD analysis curve, the near field has a compression followed by an expansion. Since compressions travel faster than expansion regions, this compression has a far greater chance of merging with the front shock system.

Figure 104 compares the ground shock signatures in all three cases. As has been pointed out, the shock strength values for the area deviation below SGD curve are lesser than the corresponding values for the case in which there is deviation above the prescribed SGD curve. Bearing these results in mind, a member of the Pareto-optimal front can be chosen as a baseline configuration and its shape perturbed till the area distribution is met. Deviations below the target distribution should be allowed to increase the flexibility of the analysis. A penalty has to be placed for area distributions which have a deviation above target distribution followed by a deviation below it for the reasons mentioned here. In order to impose this penalty, the derivative of the target and obtained area distributions are calculated when the first area deviation occurs. For the case of derivative value higher than the value calculated for the target distribution, a penalty is added to the sum of squared area error value.

Also, in order to reduce the computational time, the second step of the reverse optimization can be further split into 2 steps. In the first step, the fuselage shape can be altered to



**Figure 103:** Comparison of F-functions corresponding to perturbed area distributions



**Figure 104:** Comparison of ground signatures corresponding to perturbed area distributions

meet the nose shape. Once a suitable match is obtained, the fuselage shape can be frozen and the other components can be perturbed to reach the final target distribution. By doing this, the problem can be decomposed into optimization runs involving lesser number of variables.

### 5.2.2.3 Estimation of optimum aircraft shape

The next step, as explained before, is the determination of the shape of the aircraft that meets the required area distribution from step 1 without incurring a heavy drag penalty. As has been mentioned in the previous section, changes to the nose region of the aircraft are attempted first. Figure 105 shows the non-dominated population points after 20 generations along with the initial population. Figure 106 shows the area match corresponding to a point in the saddle region of the non-dominated front. It can be seen that the nose region is approximated well.

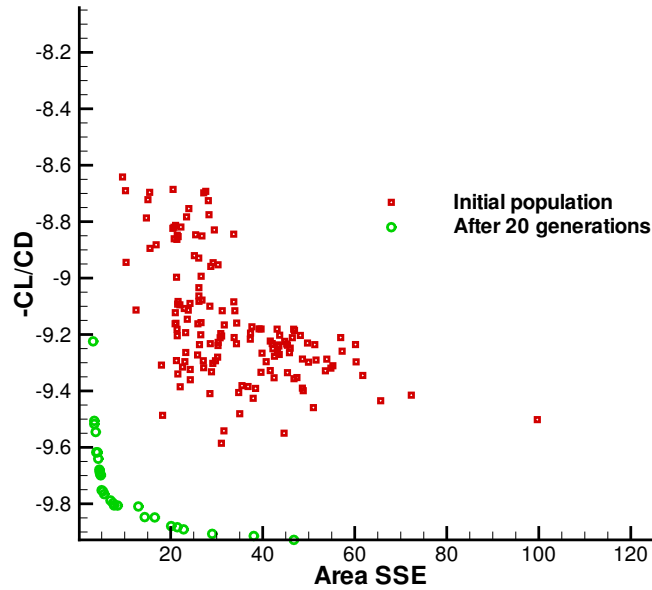


**Figure 105:** Pareto front of the Nose matching

With a known nose shape, the other components of the aircraft are altered in order to achieve the target area distribution. Figure 107 depicts the non-dominated individuals after 20 generations. By changing the wing and tail parameters while maintaining the nose shape as obtained from the previous step, the lift to drag coefficient increases slightly.

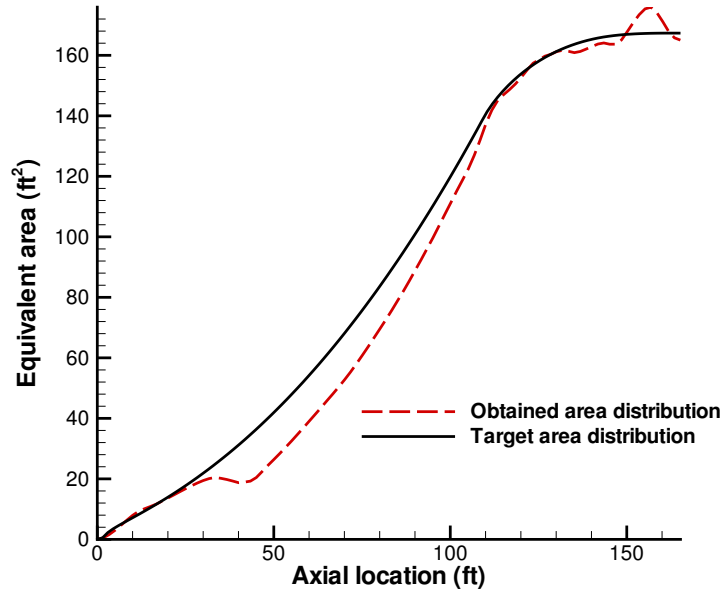


**Figure 106:** Comparison of total equivalent areas after nose area matching

The equivalent area distributions are then compared by choosing a point from the non-domination front. Figure 108 shows the final comparison of the equivalent areas. It can be observed from this figure that by changing the geometric parameters of components other than the fuselage, a fairly close area distribution can be obtained. Figure 109 shows four views of one of the best configurations obtained after 20 generations. It can be seen that this configuration has a swept forward T-tail and multi-section wing. This configuration has nacelles under the wing and using the linearized tool nacelle modification explained in the third chapter, this configuration might have slightly increased boom loudness compared to the same configuration with nacelles over the wing. This is not captured in the reverse design because the objective is not to minimize the perceived loudness but to achieve a target equivalent area distribution. Thus, there is no bias towards nacelle-over-wing designs in reverse design procedure.

Although a decent match is obtained in terms of the area distribution, the F-function and the pressure signature need not be the same as expected. Figure 110 shows the comparison of the near field effects in terms of the F-functions. As can be seen, because of minor deviations in the area distribution, the obtained F-function no longer has the shape of the



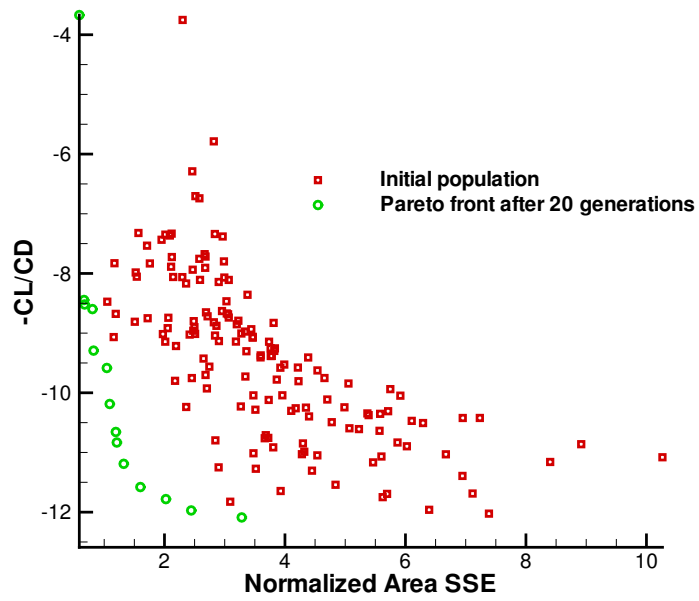


Figure 107: Pareto front after perturbing wing and tail geometries

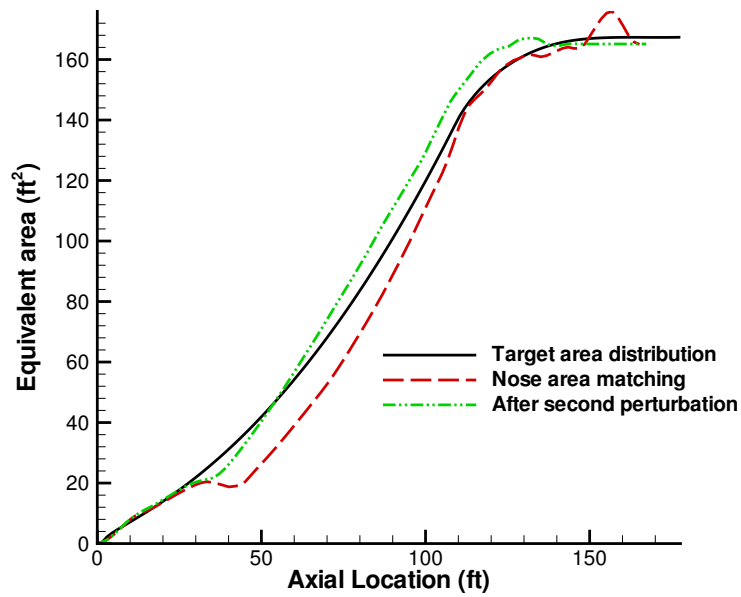
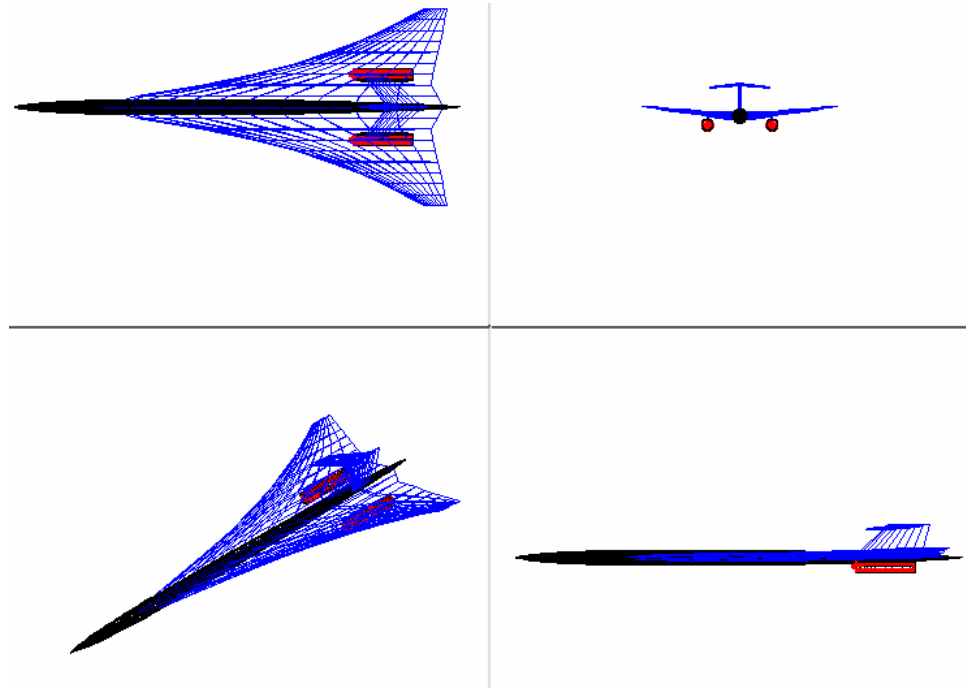


Figure 108: Comparison of final total equivalent areas



**Figure 109:** Four view sketch of one of the best designs

target distribution. New wiggles are introduced due to the changes in the second derivative in the area distribution. This shows that the near field signature is extremely sensitive to the total equivalent area distribution.

Since the F-function is changed, the ground pressure signature is expected to be different. This is indeed the case as shown in Figure 111 where the ground signatures are compared and are quite different. In order to match the area distributions to a greater extent, one suggestion is to alternate between fuselage and wing perturbations to achieve distributions of minimum deviation. After a few iterations, a near to exact match may be obtained. Further, using non-linear lift analysis, wing reflexing, fillets and fairings and other advanced methods, an exact match in the area distribution may be obtained. However, that can be accomplished in the later stages of design.

### ***5.3 Low boom designs under varying conditions***

In order to help the designer in calculating the performance of the aircraft with varying dimensions and flight conditions, a four variable Design of Experiments (DoE) array has been created. The four variables of interest are Mach number  $M$ , Gross Weight  $W$ , length of

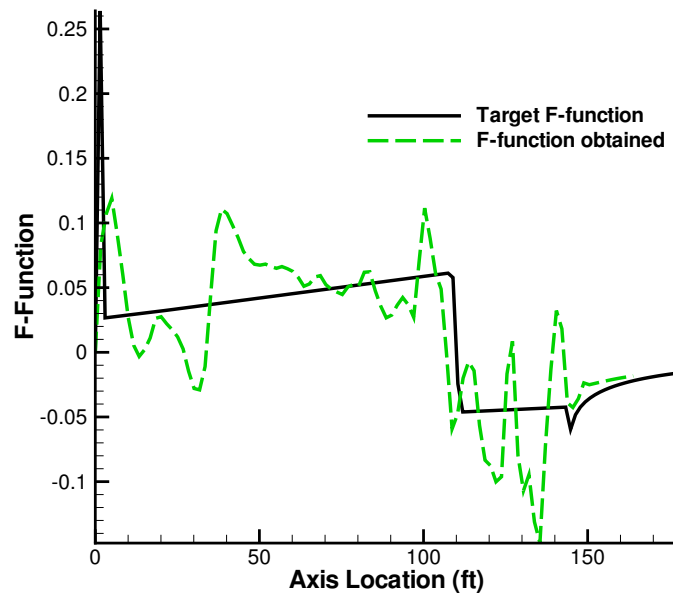


Figure 110: Comparison of F-functions

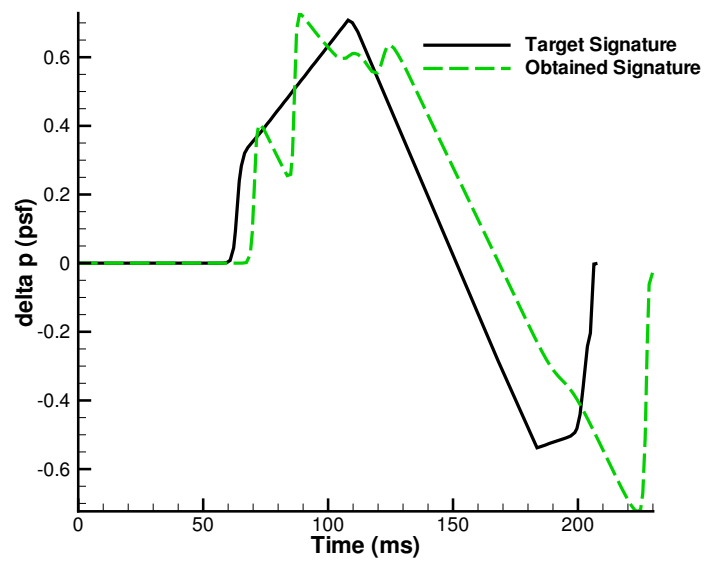


Figure 111: Comparison of ground signatures

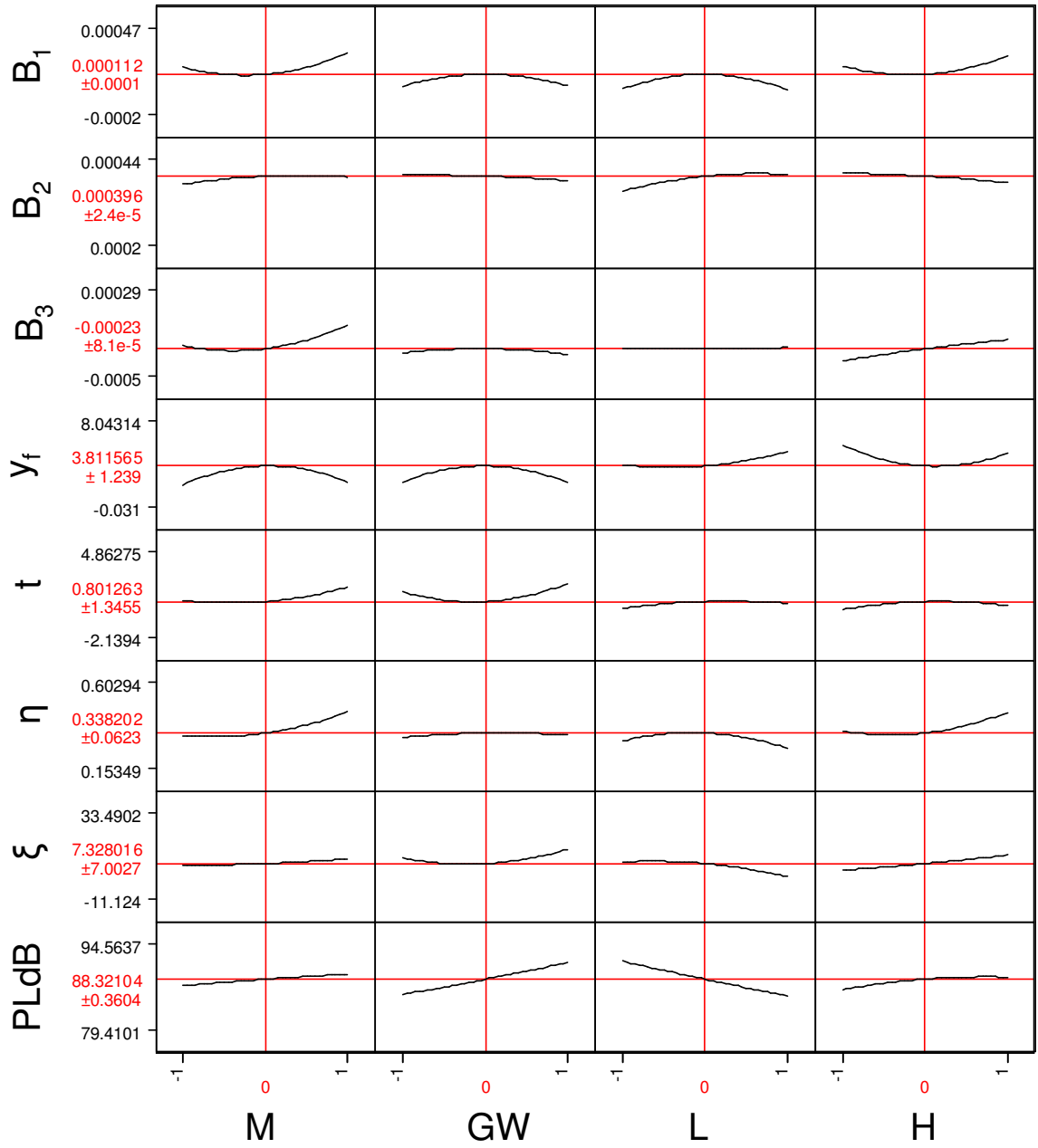
the aircraft and flight altitude. The modified SGD approximation is run for each case in the DoE table and the variables  $B_1, B_2, B_3, y_f, t, \eta$  and  $\xi$  are tracked as responses to minimize the perceived loudness level. Table 22 presents the inputs and outputs of such a run.

Figure 112 shows the trend of each of the responses to the variation of the input variables. Each of the profiles specify the sensitivity of the responses to the changes in the input variables. In addition, the trend of the minimum perceived loudness level with varying inputs is also shown. These profiles facilitate a sanity check allowing the designer to determine if the trends make sense. If not, further investigation is warranted to answer the questionable trends. For example, it can be observed from this figure that the perceived loudness value reduces with increasing aircraft length and increases as the Mach number, gross weight and altitude are increased. Further, the perceived loudness level is more sensitive to aircraft length and gross weight than it is to the Mach number and altitude. These are the expected results. It can also be observed from these trends that some of the responses are insensitive to certain variables.

Using this setup, for a given set of inputs within the ranges, the modified SGD coefficients that minimize the perceived loudness level can be obtained efficiently provided the regression model used to obtain the values is accurate. This would cause easy computation of the target equivalent area distribution and F-function. Furthermore, the lowest achievable loudness level for a given set of conditions is predicted by these trends. Therefore, for a set of conditions if the requirement for loudness level is specified, it can be seen from this figure if those requirements can be actually met. If not, valuable time can be saved by relaxing the requirements so that a feasible design is achievable. For example, if a design is required to achieve a perceived loudness level of 79.0 PLdB, it can be readily seen that this requirement cannot be achieved with ranges given in Table 22. The requirements have to be relaxed or the input variable ranges have to be expanded in order to meet the loudness requirement.

## 5.4 *Final comments*

The computational time required to achieve a converged solution using a direct optimization run is higher when compared to the reverse optimization. This is due to the large number



**Figure 112:** Prediction profiler for the responses

of design variables and lack of a target distribution in the direct optimization. In addition, with changing conditions, the reverse design offers an easy computation of the target area distributions thus improving the overall efficiency of the conceptual design process. In order to exactly realize the target area distribution, advanced analysis tools have to be used and manual strategies may have to be employed. This is a procedure left for further stages of design.

**Table 22:** DoE table inputs and outputs

M	W (lbs)	L (ft)	H (ft)	$B_1$	$B_2$	$B_3$	$y_f$	t	$\eta$	$\xi$	PLdB
1.4	10000	100	40000	0.000016	0.00039	-0.000242	2.09	1.17	0.258	2.88	86.07
1.4	100000	100	60000	0.000024	0.000346	-0.000165	2.90	1.41	0.307	3.43	88.05
1.4	100000	150	40000	0.000008	0.000334	-0.000297	3.98	0.37	0.426	14.96	79.41
1.4	100000	150	60000	0.000122	0.000392	-0.000218	3.17	2.07	0.25	4.25	82.16
1.4	150000	100	40000	0.000092	0.000321	-0.000284	2.27	0.72	0.295	4.94	92.10
1.4	150000	100	60000	0.0	0.000202	-0.000281	2.99	1.65	0.34	29.08	92.54
1.4	150000	150	40000	0.000336	0.000393	-0.000242	2.09	0.72	0.26	5.35	85.06
1.4	150000	150	60000	0.000039	0.00038	-0.000215	2.99	0.45	0.289	0.68	88.10
1.8	100000	100	40000	0.000026	0.000397	-0.000286	2.09	0.137	0.301	7.68	88.02
1.8	100000	100	60000	0.000398	0.000303	0.00029	2.09	0.824	0.60	33.49	89.94
1.8	100000	150	40000	0.000155	0.000356	-0.000267	4.07	3.21	0.26	6.86	81.35
1.8	100000	150	60000	0.000153	0.0004	-0.000028	2.90	3.35	0.526	0.82	84.56
1.8	150000	100	40000	0.000064	0.000377	-0.000286	2.45	4.86	0.47	6.04	94.10
1.8	150000	100	60000	0.000374	0.000306	-0.000053	2.54	1.23	0.54	31.84	94.56
1.8	150000	150	40000	0.00008	0.000397	-0.000187	5.15	1.02	0.27	7.0	87.15
1.8	150000	150	60000	0.000028	0.000387	0.000183	2.63	3.84	0.48	12.21	89.91
1.4	125000	125	50000	0.000048	0.000375	-0.0003	2.0	1.66	0.366	14.0	87.14
1.8	125000	125	50000	0.00039	0.000395	0.000068	2.63	1.47	0.421	3.02	89.15
1.6	100000	125	50000	0.000064	0.000387	-0.000295	2.81	0.0	0.287	3.84	85.47
1.6	150000	125	50000	0.0	0.000398	-0.000259	2.09	4.137	0.372	21.41	91.31
1.6	125000	100	50000	0.0	0.000369	-0.000223	2.90	0.294	0.277	4.53	91.64
1.6	125000	150	50000	0.0	0.000388	-0.000226	6.42	0.84	0.293	4.94	85.08
1.6	125000	125	40000	0.000034	0.000387	-0.000281	8.04	0.196	0.364	3.43	85.99
1.6	125000	125	60000	0.000393	0.000398	-0.000218	2.90	0.686	0.44	12.76	89.11
1.6	125000	125	50000	0.000118	0.000387	-0.000215	2.99	0.0	0.295	5.49	88.62

# CHAPTER VI

## CONCLUSIONS AND RECOMMENDATIONS

### *6.1 Summary of research contributions*

A shape optimization procedure for supersonic aircraft design using better geometry generation and improved near field tools has been successfully demonstrated. The geometry engine provides dynamic reconfiguration and efficient manipulation of various components to yield unstructured geometries. The architecture supports an assimilation of different components and allows configuration changes to be made quickly and efficiently because the changes can be localized to each component. The geometry generation and discretization procedure enables an efficient and automatic way to combine linear and non-linear analysis.

Traditional analyses and implementations tend to have a complex algorithmic flow, tight coupling between tools used and computational limitations. Some of these shortcomings are overcome in this study and a diverse mix of tools are seamlessly integrated to provide a simple, yet powerful and automatic procedure for sonic boom minimization. Conceptual design can be performed to exploit the vastness of the design space to achieve suitable configurations resulting in an increased insight into the effect of the design requirements.

It was shown in this study that varying atmospheric conditions could have a huge impact on the perceived loudness levels on the ground. A quick way of obtaining probability estimates of the required responses under atmospheric uncertainty was demonstrated. A new design methodology has been introduced for sonic boom minimization based on linearized methods. The well accepted SGD equations have been generalized to yield near-field signatures with better far field characteristics. The relevant equations for this generalization were derived.

The implications of this research could be profound if a set of best configurations could be selected in the conceptual phases of design weighing in various conflicting requirements. The



unique shape optimization procedure in conjunction with parallel genetic algorithms allows the designer to explore vast design spaces efficiently and accurately. The probabilistic propagation provides a strategy to include atmospheric fluctuations into the aircraft design process. The bi-level procedure not only serves as a pseudo-inverse technique but also induces design flexibility by separating the near and far field analysis. The basic framework of the architecture has been set. Various important studies could be conducted with this setup.

## ***6.2 Answering Research questions through the results obtained***

Each of the research questions, given earlier, has been addressed in this thesis. The following sections present a brief discussion of what has been accomplished in this study in regards to each of the questions posed at the start of this thesis.

### **6.2.1 Improved geometry handling (Question 1)**

It has been shown in this thesis that a vast design space of geometric configurations can be generated using a combination of continuous and discrete shape parameters. The geometry created is a wire-frame model with no component intersection data. In other words, the initial geometry would simply be a collection of various components. The individual components generated using the parameterization strategy are converted into an unstructured geometry using geometric libraries and other tools. It has been demonstrated in this thesis that these geometries can be used to run both computational fluid dynamics simulations and linearized analysis. This not only makes it straight forward to analyze any configuration using linearized methods but also paves the way for a CFD simulation to be used in the early stages of design. The gap between CFD and linearized codes can thus be reduced to a certain extent.

### **6.2.2 Improvements in near field prediction tools (Question 2)**

According to slender body theory and equivalent body assumption, the average aircraft area intersected by the Mach planes oriented at different azimuthal angles at various locations on the aircraft axis is the area that affects the wave drag computation. Having obtained

a discretized geometry, Mach plane intersection areas for various values of the azimuthal angles are calculated. To obtain the equivalent area distribution due to volume, the aircraft axis is discretized to user specified resolution.

Using the same theoretical basis as used in AWAVE, an improved code has been developed, which would accept any arbitrary configuration as input and compute the wave drag and equivalent area due to volume of the configuration. The frontal area projections of the intersections between Mach planes and the aircraft would be calculated without any simplifying geometric assumptions. This computational geometry problem has been handled by a surface library created specifically to handle surface operations.

Similarly, the equivalent area due to lift estimation routines have been modified to run on the geometry created. The lift analysis could be replaced either by a generalized vortex lattice method, panel method or a full blown computational fluid dynamics simulation. Better geometry handling, as suggested in this thesis, can create surface meshes in an easy fashion to be given as computational mesh for advanced analysis.

### **6.2.3 Pressure propagation tools(Question 3)**

With the changing atmospheric profiles, it was realized that scalar estimates of the sonic boom response metrics with a standard atmosphere are not adequate. Simple statistical goodness-of-fit tests have been used to obtain a distribution of the relevant responses under varying atmospheric conditions. Existing propagation codes have been modified to account for these variations in the atmospheric parameters. Distributions have been placed on the lapse rate and the altitudes separating the different layers of the atmosphere to create a parametric temperature model for the atmosphere. Further, the atmospheric wind profiles have also been parameterized based on meteorological data. This probabilistic sonic boom prediction method has been demonstrated in this thesis and a conservative estimate of the responses is obtained.

#### **6.2.4 Sonic boom minimization technique (Question 4)**

The classical SGD equations for minimum pressure perturbations in the sonic boom signature have been re-derived and recast into an optimization form. The optimization results are then approximated using an artificial neural-network to reduce the computational time of the SGD analysis. The approximation has been used to minimize the probabilistic estimate of the perceived loudness instead of minimizing the shock pressure rise or the overpressure values as used in traditional sonic boom minimization studies.

Two numerical approaches have been used to minimize the loudness of the boom signature. The first way is to use the improved linear analysis methods to affect the shape of the geometry to minimize loudness. Asymmetric signature corrections have been made in the loudness calculations. In the second way to numerically minimize sonic boom loudness, a "bi-level reverse" optimization procedure is performed. The numerical computation was separated into aerodynamics module and aero-acoustics module. The aero-acoustics module involves the use the SGD approximation equations to obtain an F-function and the corresponding equivalent area distribution to minimize the sonic boom loudness metric on the ground. In the second step, aircraft shape parameters are varied to match the area distribution from step 1 as well as minimize the lift to drag ratio  $\frac{C_L}{C_D}$ .

#### **6.2.5 Generalized SGD equations for Sonic Boom minimization (Question 5)**

Many insights were gained from the SGD approximation. It was realized that the SGD equations can be generalized further to improve upon the results obtained from SGD approximation. Additional parameters have been introduced in the F-function formulation and the relevant equations were re-derived and approximated using a non-linear artificial neural network regression model. Improvements in the near field signature have been realized using this generalization.

#### **6.2.6 Flexible design framework (Question 6)**

Many conceptual design studies have been conducted in the past to overcome the problem of sonic boom. However, most of the tools were not very flexible. Further, there is a

fundamental disconnect between the tools used in the conceptual design stages and later stages of design. The methodology used in this study has immense potential because of its improved flexibility and ability to transition to a higher fidelity analyses. The framework provides an easy, effective and adequate control over the design space for conceptual design and offers a great platform to conduct preliminary design.

## ***6.3 Recommendations***

It is to be noted that shape optimization as used in this thesis is limited to a certain extent because linearized tools have been used. In order to move to the next level of sophistication and realize much more benefits from shape design, high-fidelity non-linear tools have to be used which compute higher order effects that cannot be captured by linearized methods. In order to do this efficiently, many approximation based techniques can be used to reduce the computational workload. Some of these techniques are briefly explained here.

### **6.3.1 Variable Fidelity Optimization**

Detailed disciplinary analyses like CFD cannot be readily used to provide pertinent information to the conceptual designer due to the high computational costs involved in running these simulations. At the same time, low fidelity tools linked to the traditional design tools lack the capability to handle radically new or revolutionary geometries accurately. Even though this was the main motivation for the present study, actual variable fidelity analysis in the traditional sense was not implemented due the lack of available computational resources. Future work would be to include one of the following proven approximation models and strategies to perform optimization using a combination of low and high fidelity tools that effectively improve the accuracy of the final solution without incurring a huge computational burden.

According to the literature, variable fidelity modelling has been accomplished in various forms. The most widely used forms are briefly discussed.

### *6.3.1.1 Approximate Model Management Framework*

Alexandrov [77] introduced this method by applying it to the wing design problem. The idea is to use a scale factor prescribing the ratio of the high fidelity to the low fidelity analysis. This scale factor is then expanded according to first-order Taylor series about a point in the design space where both the high and low fidelity analyses have been evaluated. An approximation is then constructed to the high fidelity analysis which uses the linear Taylor approximated scale factor and the low fidelity analysis. Thus, the high fidelity approximation is guaranteed to behave like the exact high fidelity analysis up to the first derivative. This procedure can be used in conjunction with the trust region methodology to drive the solution towards the high fidelity optimum while using more of low fidelity analysis.

### *6.3.1.2 Proper Orthogonal Decomposition*

Proper orthogonal decomposition [15] is a powerful and elegant method which is aimed at generating low dimensional approximations of high dimensional analysis. Analyses, like functions, are usually composed of many modes. These modes are equivalent to basis functions, which could be numerous. However, all the modes might not contribute to the final result of the analysis in a significant way. Using this idea, approximate analysis models can be created by ignoring certain modes of the original analysis.

In the approximation of functions to finite dimensional space, the basis functions are not unique. Basis functions could be either Fourier series, Legendre polynomials or the usual power series. In the proper orthogonal decomposition, the basis modes have to be chosen carefully so that only the main modes can be kept and the rest ignored. Singular value decomposition (SVD) methods are usually used to determine all the modes of a finite dimensional case. Then, the designer ignores certain modes to approximate the analysis. Instead of SVD scheme, balanced model reduction [130] techniques can also be used to determine the optimum basis functions.

This technique, after it has been fully validated, can be used to obtain the near field pressure signatures from an approximate CFD analysis. This would result in an almost accurate near field, using a POD based CFD analysis, which can then be propagated using

the pressure propagation tools.

#### *6.3.1.3 Functional mapping*

The most simple and straight forward way to approach the variable fidelity optimization is through functional mapping. In this procedure, the design parameters are selected for a desired analysis to be approximated. Both the coarse and fine models are run and the outputs from both the analysis are collected. Based on the input variables and the responses, a regression model can be constructed which maps the inputs onto to a response perturbation space. Once the accuracy of the mapping is ascertained, the regression mapping response can be summed with the low fidelity analysis output in lieu of the high fidelity analysis.

This procedure though straight forward in principle, can be bogged down by the curse of dimensionality. As the number of parameters increases, the regression becomes very difficult. This can be overcome if the problem can be decomposed into numerous regression models with less number of parameters.

### **6.3.2 Near field approximation improvements**

The near field pressure signature can be improved further if high order panel methods, which consider the thickness effect can be used. However, these panel methods have to be used with caution for supersonic flows if the body falls outside the Mach cone. Since an unstructured surface geometry is obtained using the procedure described in this thesis, the use of unstructured panel code could save valuable design time.

In addition to the above, an approximation model can be fit to obtain the near field area distribution using the geometric parameters as design variables. If this is done and the approximation model's effectiveness is proved, the optimization analysis can be done in much less computational time, especially the step involving area matching.

The procedure used here does not vary the airfoil in the geometry optimization process. Optimum wing airfoil can also be obtained with possible reflex in the nacelle interference region to result in shock reductions not obtained otherwise.

### 6.3.3 Inverse Design

The procedure followed in this study is not the inverse design in the traditional sense. An inverse design involves the determination of aircraft shape given a target ground signature. In this study, the target was the near field equivalent area distribution that was obtained by performing the acoustic propagation analysis in a direct fashion.

A simple strategy for performing is laid out here. The equivalent area distribution could be assumed to be a cubic spline with certain number of control points. The signature could be propagated to the ground using the propagation tool modifications to obtain the ground signature. A Fourier series basis with a certain number of terms, say 10, could be used to approximate the ground signature. This procedure could be repeated many times. Now, an input output mapping could be established with the coefficients of the Fourier series being the inputs and the control points of the equivalent area distributions being the outputs. A non-linear regression analysis could be attempted. If an acceptable regression model is obtained, the approximation model could be used in inverse design. A target ground signature can be used to obtain an equivalent area distribution and using the technique laid out in the second step of the bi-level optimization procedure, the aircraft shapes producing the desired ground pressure signature could be obtained. The regression mapping might not be easy to achieve. This is an area for further research and investigation.

### 6.3.4 Indoor and other effects

In this study as in many other design studies, only the outdoor effect on humans has been considered as the minimizing criterion. However, due to the high energy content of the sonic boom ground signature at low frequencies that excite structural vibrations, the indoor noise and building response [54] could be critical. Future design studies should involve a frequency analysis of the pressure signature. The important parameters in this respect would be the rise time and the duration of the pressure signature.

Another important aspect that was not treated completely was the atmospheric absorption [48] of the sound waves as they propagate through air. Atmospheric humidity causes the significant absorption particularly at high frequencies. Analytical expressions have been

derived [41] to predict the absorption coefficient as a function of frequency. Following the calculation of the frequency spectrum of the sonic boom pressure signature, atmospheric absorption effect can also be incorporated into the design method. These would make the ground signature prediction more realistic.

### **6.3.5 Practical considerations**

This study focussed on expanding the SGD equations and allowing the use of high fidelity modelling into conceptual design. The objectives used in this study to design the aircraft are limited. In real world situations, various other objectives exist including minimizing cost, stability constraints and aeroelasticity to name a few. Future research should make use of the concepts presented in this thesis along with methods to analyze the other objectives to perform a truly multi-disciplinary analysis. By having better analysis techniques in the earlier stages, a better final system can be designed.



# APPENDIX A

## AIRCRAFT EQUIVALENT AREA REPRESENTATION

This area has been thoroughly studied and explained in the literature. However, for a reader who is unfamiliar with this concept, this appendix should provide a quick and simple introduction. The excellent explanation given by Carlson and Maglieri [13] is used as the basis for this section.

When an aircraft travels at supersonic speeds, the disturbances created by the aircraft always lag the position of the aircraft. This is because the disturbances travel at the local speed of sound and since the aircraft is travelling at supersonic speeds, the locus of all spherical disturbance fronts generated at successive times form a conical surface. The generated disturbances cannot be felt outside this conical domain of dependence. A simple sketch showing the conical domain of dependence is shown in Figure 113.

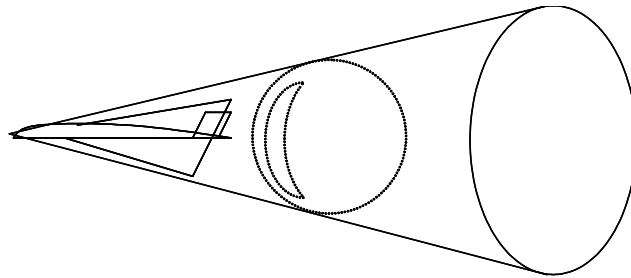


**Figure 113:** Conical domain of dependence

The conical domain of dependence is relevant only in the aircraft frame of reference. The main concern for sonic boom analysis should be the observer's frame of reference. Shifting to this frame requires that a fore cone originating at the observer's location be considered. This fore cone represents the domain of influence for the observer and thus contains all the disturbances that exert an influence at the observer's location.

As the airplane maneuvers and crosses the fore cone, the disturbances created by the

aircraft will start to reach the observer. An important aspect of this flow is the fact that the observer perceives the disturbance to be maximum when the disturbance source is exactly on the fore cone. As the aircraft moves through the cone, the disturbances from the front portion of the aircraft produce a lesser effect than the disturbances lying exactly on the fore cone at any instant in time. It is assumed that the influence of the points on the cone surface is much larger than that of the points away from this surface and so the effect of disturbances generated from the portion of the aircraft that has penetrated the fore cone are neglected.

Under the assumption of large distance between the airplane and the observer, the fore cone surface in the vicinity of the airplane may be approximated by a planar surface tangent to the cone. The planar nature of the fore cone near the aircraft can be observed from Figure 114. In this figure a aircraft is shown along with a fore Mach cone generated with a cone vertex a little distance below from the aircraft. For sonic boom analysis, the observer point and hence the cone vertex is far below the aircraft. Therefore, it was realized that the Mach cones could be approximated by Mach planes without introducing any error.

As the aircraft moves, parallel Mach planes are generated at various axial locations. The Mach planes define the location of airplane created disturbances that exert an influence at the observer location. As long as the large distance assumption is maintained, a translation of airplane created disturbances within the Mach planes is assumed to have negligible effect at the observer's location. Thus, the airplane may be replaced by an equivalent body of revolution as long as the volume and lift disturbances are lumped onto axial points that lie on the Mach planes and their effect is felt by the observer. This is the essence of equivalent body concept.

In order to perform the numerical analysis, the procedure by which the volume and lift effects are modelled and lumped has to be studied. Linearized methods use singularities for modelling these effects. Sources are used for volume effect and doublets or vortices are used for lift effects. Starting with the linearized potential equation, an expression has been derived for the pressure perturbation and is shown in appendix B after solving the linearized potential equation. What is observed is that following the application of the boundary condition, the pressure perturbation is related to the second derivative of the cross-sectional

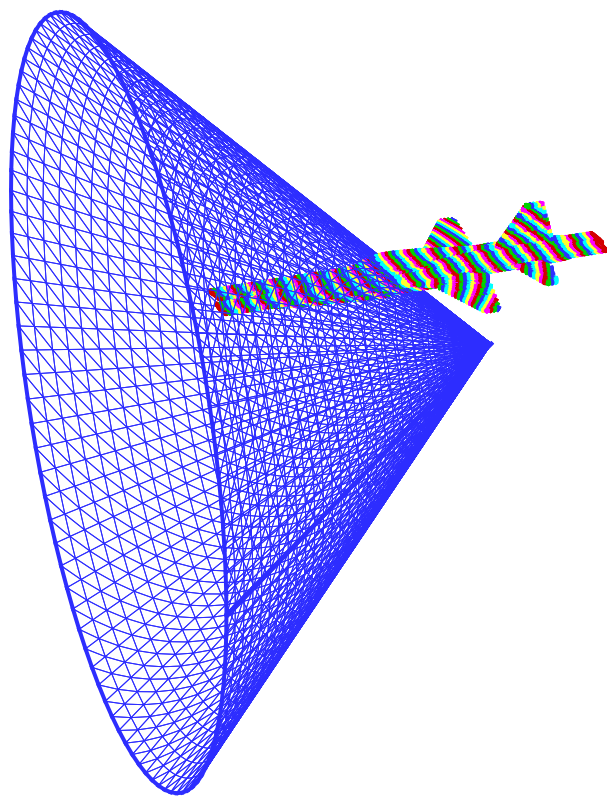


**Figure 114:** Mach plane replacing Mach cones

area. This implies that disturbances are affected by the rate of growth of area. For the purpose of simplification, the area effect is separated into volume and lift contributions and modelled separately.

Following the equivalent area and Mach plane concepts, the cross-sectional area is replaced by the frontal projection of the Mach plane intercepted area for volume contribution. As has been mentioned in the previous paragraph, the area contributions are lumped into axial points for simplicity. The translation and concentration of areas does not make any physical sense. However, since the rate of area growth is the primary concern for near field prediction, area lumping is just a means to simplify the numerical analysis and does not induce any other effect. Configurations with engines are slightly trickier because engine inlet capture air flows through the engine not around it, and thus does not contribute to the area. However, the engine exhaust area could be different from the capture area. This effect has to be captured in the equivalent area contribution. These effects have been discussed as a part of this thesis.

In order to calculate the equivalent area due to lift, the lift effects have to be computed first using any lift prediction models. The lifting force has to be translated onto the Mach planes as has been explained earlier. However, unlike volume effect where the disturbances away from the Mach plane surface have been neglected, lift contribution at any axial location is computed as the superposition of the lift generated by all disturbances in the fore cone of that point. Therefore the lift contribution is usually a monotonically increasing function as the lift effects keep accumulating. The accumulated lifting force is then converted into area contribution by using the factor  $\frac{\beta}{2q}$ .

# APPENDIX B

## WHITHAM'S F-FUNCTION

Most of the linearized analysis used in the prediction of sonic boom near field is based on the simple yet powerful method proposed by Whitham [129] in his pioneering work. Whitham's study was aimed at obtaining the flow field at large distances away from a slender, axisymmetric body. This chapter provides a basic introduction to this concept.

The linearized theory relations were well known at the time Whitham proposed this theory. Linearized theory assumed the disturbances to be propagated along parallel characteristic lines. However, it was observed from experiments that the actual flow field had curved characteristics. Further more, a linearized theory cannot predict any shocks because existence of shocks is a highly non-linear phenomena. So, rather than discard all linearized relations and resort to non-linear analysis, Whitham thought of an ingenious way to use linearized analysis with some corrections built in so that non-linear effects can also be modelled. In order to make simplifying approximations, only far field effects were considered. Assuming that the disturbances created by a slender body are small allowed certain terms in the resulting expressions to be neglected.

When performing linearized acoustics, it is usually assumed that the disturbances propagate at the speed of sound. However, local speed variations or convection of sound with moving fluid are not considered. These approximations provide a reasonable estimate when the propagation distances are small. However, in the case of sonic boom where the propagation could extend for very long distances, such approximations tend to accumulate errors resulting in an incorrect pressure signature. To remedy this, it was deduced that the straight characteristics should be replaced by exact characteristic curves. With this basic understanding, we now move on to the mathematics of the linearized theory improvements. The derivation is directly taken from Whitham's paper [129] and is provided to the reader

for ready reference.

## ***B.1 Linearized theory corrections***

Assuming that the flow field is irrotational, the perturbation potential equation can be written as shown in Equation 90.

$$\phi_{rr} + \frac{1}{r}\phi_r - \beta^2\phi_{xx} = 0 \quad (90)$$

Solving the potential equation results in Equation 91 for the perturbation potential. In this equation,  $f(t)$  is an arbitrary function determined from boundary condition on the body.

$$\phi = - \int_0^{x-\beta r} \frac{f(t)dt}{\sqrt{(x-t)^2 - \beta^2 r^2}} \quad (91)$$

By taking partial derivatives, the perturbation velocities can be obtained as shown in Equations 92-93.

$$u = - \int_0^{x-\beta r} \frac{f'(t)dt}{\sqrt{(x-t)^2 - \beta^2 r^2}} \quad (92)$$

$$v = \frac{1}{r} \int_0^{x-\beta r} \frac{(x-t)f'(t)dt}{\sqrt{(x-t)^2 - \beta^2 r^2}} \quad (93)$$

Now, modifying the straight characteristics,  $x - \beta r$ , by curved ones,  $y(x, r)$ , results in Equations 94-95.

$$u = - \int_0^y \frac{f'(t)dt}{\sqrt{(y-t)(y-t+2\beta r)}} \quad (94)$$

$$v = \frac{1}{r} \int_0^y \frac{(y-t+\beta r)f'(t)dt}{\sqrt{(y-t)(y-t+2\beta r)}} \quad (95)$$

Along the characteristic curve, Equation 96 has to be satisfied. This equation gives the slope of the characteristic curve at any instantaneous location. In this equation,  $\theta = \tan^{-1}(v/(U + u))$  represents the local direction of flow.

$$\frac{dx}{dr} = \cot(\mu + \theta) \quad (96)$$

Based on Bernoulli's equation relating the local speed of sound with undisturbed conditions, Equation 97 could be written with  $q$  being the magnitude of velocity.

$$\mu = \sin^{-1}\left(\frac{a}{q}\right) = \mu_0 - \left(1 + \frac{\gamma - 1}{2}M^2\right)\frac{u}{\beta} + O(u^2 + v^2) \quad (97)$$

Using the above equations, on  $y = \text{constant}$ , Equation 98 can be obtained.

$$\frac{dx}{dr} = \beta + \frac{(\gamma + 1)M^4}{2\beta}u - M^2(v + \beta u) + O(u^2 + v^2) \quad (98)$$

By substituting equations 94 and 95 in equation 98 and performing integration leads to an approximate Equation 99 after second order terms have been neglected. It can be clearly seen from this expression that the by using the original linearized analysis, the term  $c(y, r)$  is completely neglected. It has been observed that this term could have a significant impact at large distances and near the Mach cone.

$$x = \beta r - c(y, r) + y \quad (99)$$

Having obtained the main relations, we now move on to the far field approximation in which we assume that  $\beta r/y \gg 1$ . Using this relation, Equations 94, 95 and 99 become Equations 100, 101 and 102 respectively with  $F$  and  $k$  given by Equations 103 and 104. The function  $F$  is fundamental to the theory and has since been known as the Whitham's  $F$ -function.

$$u = -\frac{F(y)}{\sqrt{2\beta}}r^{-\frac{1}{2}} \quad (100)$$

$$v = \beta u \quad (101)$$

$$x = \beta r - kF(y)r^{\frac{1}{2}} + y \quad (102)$$

$$F(y) = \int_0^y \frac{f'(t)dt}{\sqrt{y-t}} \quad (103)$$

$$k = \frac{(\gamma + 1)M^4}{\beta\sqrt{2\beta}} \quad (104)$$

## ***B.2 Characteristics of the F-function***

In equation 91, it was mentioned that  $f(t)$  is an arbitrary function to be determined by the boundary condition. In potential flow analysis, a common boundary condition is to have normal velocity at the body surface be equal to zero. Assuming the equivalent body assumption introduced in Appendix A, for a body described by  $r = R(x)$ , where  $R(x)$  is the body radius at distance  $x$  from the nose, the linearized boundary condition turns out to be  $v = R'(x)$ . When  $r$  is very small, as in the case of body surface, Equation 93 can be simplified to obtain  $v = f(x)/r$ . Using these expressions, Equation 105 can be written with  $S$  being the cross-sectional area of the equivalent body.

$$f(x) = R'(x)R(x) = \frac{S'(x)}{2\pi} \quad (105)$$

Now using Equation 103, Equation 106 can be written for the F-function. This is the form used in most of the analysis presented in this and other studies.

$$F(y) = \frac{1}{2\pi} \int_0^y \frac{S''(t)dt}{\sqrt{y-t}} \quad (106)$$



By decomposing the domain into large and small  $y$ , various approximations for the F-function can be derived. The important result after such approximation analysis is that Equation 107 should be satisfied for a finite body. This is to say that the disturbances due to the supersonic travel of the body are nullified and conditions return to ambient conditions when the point of interest is chosen at a far downstream location.

$$\int_0^{\infty} F(y) dy = 0.0 \quad (107)$$

The F-function provides a good description of the flow field. For example, when  $F'(y) > 0$ , the characteristics converge signifying compression and the opposite is true for the case  $F'(y) < 0$ . Based on this, all bodies have a shock in the front and due to the condition given in equation 107, all bounded bodies necessarily have a shock at the rear. Shock locations and strengths as a function of the distance  $r$  can be derived using simplified equations.

Before proceeding into further discussion about F-function, the concept of limit line is introduced here. Characteristic lines specify the locus of points along which the disturbances are constant. Numerous characteristic lines can be drawn from various points in the flow-field. There are certain characteristics which form an interface between supersonic and subsonic pockets of the flow-field. These are called limiting characteristics. At any point of the limiting characteristic, the characteristics from the subsonic and supersonic regions meet. During propagation, the limiting characteristics usually result in shocks. The front shock characteristics have been derived and mentioned in section 2.1. Here, the rear shock system is introduced along the same lines as given by Whitham [129].

Consider Figure 115 where a sample F-function is depicted. Using linearized relations, it has been shown that Equations 108 and 109 are satisfied. Using these equations and referring to the figure, it can be realized that the area of the lobes cut-off from each side of the curve by a straight line segment, whose slope is given by equation 109, should be equal. Furthermore, when the line segment is tangential to the curve, the area cut-off is zero and the gradient of the line segment has a maximum value. The tangent location occurs at an inflexion point on the F-function curve and since maximum gradient occurs near the body,

the inflexion point corresponds to the shock initiation location. Hence it can be deduced that the shock starts at the location where the line segment forms a tangent to the curve.

$$\int_{y_1}^{y_2} F(y)dy = \frac{1}{2}(y_2 - y_1) \left( F(y_2) + F(y_1) \right) \quad (108)$$

$$\frac{1}{kr^{\frac{1}{2}}} = \frac{F(y_2) - F(y_1)}{y_2 - y_1} \quad (109)$$

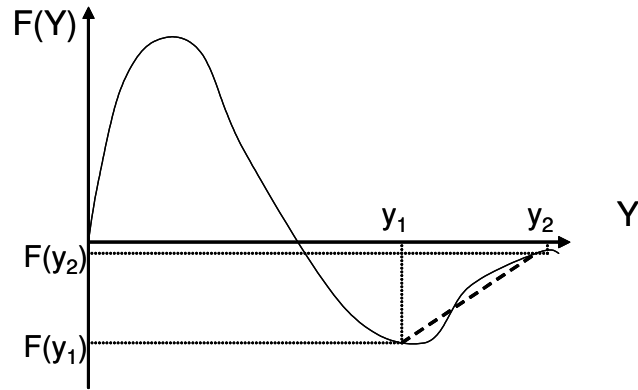


**Figure 115:** F-function rear shock characteristics [129]

Much more can be realized about the near field shock structure just from the shape of the F-function. Consider an F-function as shown in Figure 116. As can be seen, there is a sharp kink in the rear region of the F-function. Using the area balancing rule and the shock location, the progression of shock can be traced. The kink causes the formation of two shocks from each of the tangent line segments. Line segments  $a'a$  and  $aa''$  are balancing lines across the first and second shock respectively. Similarly, line segments  $b'b$  and  $bb''$  are balancing lines across the first and second shock at a different time instant. The broken line segments  $a'aa''$  and  $b'bb''$  are bent in opposite directions. By relying on the continuity of the line segment progression, a line segment can be constructed,  $m'mm''$ , which is a single straight line that satisfies the area balancing rule. When such a single straight line segment occurs, the separate line segments lose their identity and merge into one. From the time instant when this occurs, only a single shock is seen in the signature. Thus, the coalescence of the two shocks is predicted from the shape of the F-function.

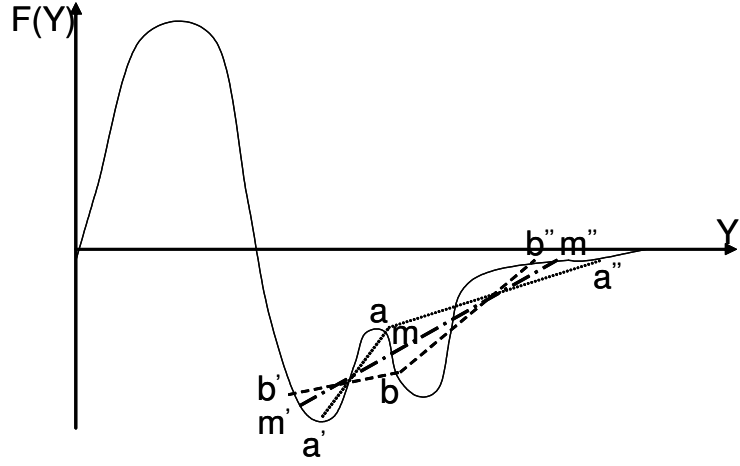


**Figure 116:** F-function with a kink in rear region [129]

Various other cases might be considered and an in-depth knowledge about the detailed information stored in an F-function can be gained. F-function, though very important in the theoretical sense, is not a physical quantity and is usually not known to the aircraft designers. A relevant physical quantity is the pressure perturbation and the next section introduces the connection between the F-function and pressure signature.

### ***B.3 The pressure signature***

Using the Bernoulli's equation, the local pressure perturbation can be related to the ambient pressure as given in Equation 110.

$$\frac{p}{p_0} = -\gamma M^2 \left( u + \frac{1}{2}(u^2 + v^2) \right) \quad (110)$$

Using the expressions for the perturbation velocities in terms of the F-function derived earlier in this appendix, the pressure perturbation equation can be derived in terms of the F-fnction as shown in equation 111.

$$\frac{p}{p_0} = \frac{\gamma M^2}{\sqrt{2\beta}} \frac{F(y)}{r^{\frac{1}{2}}} \quad (111)$$

Using the expression for F-function and the corresponding approximations at large distances, the pressure perturbation expressions at large distances can be obtained. Initially, the

pressure signature resembles the shape of the F-function. However, as the distance increases, the characteristics diverge and the signature is stretched and magnitude is attenuated due to atmospheric effects.

# APPENDIX C

## MATLAB CODE FOR MODIFIED SGD ANALYSIS

The relevant equations for this analysis have been presented in section 3.8. The MATLAB file included here has the inputs and outputs presented in Table 23. The definitions of these variables have been presented earlier. Using the outputs obtained, the program also computes the F-function and equivalent area distribution.

```
function sgddareanew(file)

fd = fopen(file,'r');
A = fscanf(fd,'%f');
B1 = A(1);
B2 = A(2);
B3 = A(3);
M = A(4);
l = A(5);
h = A(6);
W = A(7);
yf = A(8);
t = A(9);
eta = A(10);
epsil = A(11)+yf;

fclose(fd);
prbypf = 1.0;

sgam=1.4;
gam = (1+sgam)/2;
beta = sqrt(M^2-1);
zh = 750; % Initial waveform at 1000 ft from aircraft axis
z = 10*l; % Calculate F-function at 10 body lengths away

% Standard atmosphere computations
hgp = 0.3048*h/(1.0+0.3048*h/6356766.0); %Convert to metres
ttb(1)= 518.67;
htb(1)=0.0;
htb(2) = 11000.0;
htb(3) =20000.0;
htb(4) = 32000.0;
htb(5) = 47000.0;
ttb(2) = 389.97;
ttb(3) = 389.97;
ttb(4) = 411.57;
ttb(5) = 487.17;

Pg = 2116.2281; %psf at ground
zm = zh/3.2808399; %Convert zh into metres
Ttaxs = interp1(htb,ttb,hgp,'linear');%Temperature at aircraft axis
Th = interp1(htb,ttb,hgp-zm,'linear');%Temperature at initial waveform

if (hgp-zm < 11000)
    tmpth = ((Th-491.67)/1.8)+273.15;
    Ph=Pg*((tmpth/288.15)^5.256);
else
    Ph1 = Pg*((216.5/288.15)^5.255912);
    Ph = Ph1*exp(-(hgp-zm-11000)*9.807/287.26/216.5);
end

spsh = sqrt(sgam*1716.56*Th);
rhoh = Ph/1716.56/Th;

Ptmp = Pg*((216.5/288.15)^5.256);
tmptxs = ((Ttaxs-491.67)/1.8) + 273.15;
Pinf = Ptmp*exp(-(hgp-11000)*9.807/287.26/tmptxs);

rhoinf = Pinf/1716.56/Taxs;

ainf = sqrt(sgam*1716.56*Taxs);
Vinf = M*ainf;
mh = Vinf/sqrt(sgam*1716.56*Th);

rhovtmp = beta/rhoinf/Vinf/Vinf;

yr = 1.0*l;;
lamb = 0.5*l;

X0 = [yr lamb];
LB = [1+5.0 yf+3.0];
UB = [3*l 1-1.0];
OPTIONS=[];
OPTIONS=optimset('Tolx',1e-8,'TolFun',1e-8,'TolCon',1e-8,'MaxFunEvals',10000,'MaxIter',2000);
% Correct S value being computed
S = 1/ obtainalpha(h,M,l,W)
```

**Table 23:** Inputs and outputs for the Program

Inputs	Outputs
$B_1$	H
$B_2$	C
$B_3$	D
M (Mach number)	$\lambda$
l (Length)	$Y_r$
W (Gross Weight)	
h (Altitude)	
$y_f$ (Bluntness parameter)	
t	
$\eta$	
$\xi$	

```

X1 = lsqnonlin(@fornlsq,X0,LB,UB,OPTIONS,l,M,W,h,prbypf,yf,rhovtmp,S,B1,B2,B3,t,eta,epsil);

x = fmincon(@functp,X1,[],[],[],[],LB,UB,@constrap,OPTIONS,l,M,W,h,prbypf,yf,rhovtmp,S,B1,B2,B3,t,eta,epsil);

H = (S*(x(1)-1)*(x(1)-1)/yf/prbypf/prbypf) - (S*(1-eta)*(x(1)-1)/prbypf);
C = H*yf/(((x(1)-1)*prbypf)-(yf*(1-eta)));

ptmp = 1/prbypf;

K1 = eta*C./(1-eta);
H1 = H./(2*(1-eta));
C1 = B1*(epsil-yf)+C;
C2 = B2*(x(2)-epsil)+C1;

a1 = 32*H*(l^2.5)/(30*eta*yf);
a2 = -8*H*((1-eta.*yf).^1.5)*(6*eta*yf+4*1)./(30*eta*yf);
a3 = 8*((K1/eta)-2*H1)*((1-eta*yf).^1.5)*(3*eta*yf+2*1)/(15*yf);
a4 = 8*(2*H1-K1)*((1-eta.*yf).^1.5)/3;
a5 = -8.*((1-yf).^1.5).*(3*yf+2.*1).*(1./(15*yf)).*((K1/eta)-2*H1);
a6 = -8*(2*H1-K1)*((1-yf).^1.5)/3;
a7 = 8*(C-B1*yf)*((1-yf).^1.5)/3;
a8 = 8.*((1-yf).^1.5).*(3*yf+2.*1).*(B1/15);
a9 = -8*(C-B1*yf)*((1-epsil).^1.5)/3;
a10 = -8.*((1-epsil).^1.5).*(3*epsil+2.*1).*(B1/15);
a11 = 8*(C1-B2*epsil)*((1-epsil).^1.5)/3;
a12 = 8.*((1-epsil).^1.5).*(3*epsil+2.*1).*(B2/15);
a13 = -8*(C1-B2*epsil)*((1-x(2)).^1.5)/3;
a14 = -8.*((1-x(2)).^1.5).*(3*x(2)+2.*1).*(B2/15);
a15 = 8.*((1-x(2)-t).^1.5).*(3*x(2)+3*t+2.*1).*(B3/15);

a17 = 8*B3*(x(2)+t)*((1-x(2)-t).^1.5)/3;

if (t==0)
    a16=0;
    a18 =0;
    a19 = (8*((1-x(2)-t).^1.5)/3);
    a21 = 0.0;
    a23 = 0.0;
    a22=0.0;
else
    a16 = -8*(C2+(x(2)*C2./t))*((1-x(2)).^1.5)/3;
    a18 = 8.*((1-x(2)).^1.5).*(3*x(2)+2.*1).*(C2/(15*t));
    a19 = (8.*((1-x(2)).^1.5).*(3*x(2)+2.*1).*(1/(15*t))) - (8*x(2)*((1-x(2)).^1.5)/(3*t)) + (8*((1-x(2)-t).^1.5)/3);
    a21 = -8*(C2+(x(2)*C2./t))*((1-x(2)-t).^1.5)/3;
    a22 = 8.*((1-x(2)-t).^1.5).*(3*x(2)+2.*1+3*t).*(C2/(15*t));
    a23 = -(8*((1-x(2)-t).^1.5).*(3*x(2)+2.*1+3*t).*(1/(15*t))) + (8*x(2)*((1-x(2)-t).^1.5)/(3*t));
end

% Value of D in terms of other variables
D = abs((a1+a2+a3+a4+a5+a6+a7+a8+a9+a10+a11+a12+a13+a14+a15-rhovtmp.*W-a16-a17-a18+a21+a22)./(a19+a23));

fid = fopen('coeffs.dat','w');
fprintf(fid,'%f\n',S);
fprintf(fid,'%f\n',H);
fprintf(fid,'%f\n',C);
fprintf(fid,'%f\n',D);
fprintf(fid,'%f\n',x(2));
fprintf(fid,'%f\n',x(1));
fclose(fid);

lamb = x(2);
yr = x(1);
% Once we have all the coefficients, plot and write the F-function and area distribution

% x1 = linspace(0,1-0.1);
% x1 = linspace(0,yr-0.1,120);

fd=fopen('compf.plt','w');
fprintf(fd,'%d\n',length(x1));
for i=1:length(x1)
    if (x1(i)<eta*yf)
        F(i) = x1(i).*H./(eta*yf);
    end
end

```

```

elseif (xl(i)<yf)
    F(i) = (C.*(xl(i)./yf)-eta)./(1-eta)-(H.*(xl(i)./yf)-1)./(1-eta));
elseif (xl(i)<epsil)
    F(i) = B1*(xl(i)-yf) + C;
elseif (xl(i)<lamb)
    F(i) = B2.*(xl(i)-epsil) + C1;
elseif (xl(i)<lamb+t)
    F(i) = -(D+C2).*(xl(i)-lamb)/t + C2;
elseif (xl(i)<l)
    F(i) = B3.*(xl(i)-lamb-t) - D;
else
    F(i)=arbitp(xl(i),l,yf,B1,B2,B3,t,eta,epsil,lamb,D,H,C);
end
fprintf(fd,'%f\t%f\n',xl(i),F(i));
end
fclose(fd);

alph = 1-0.5*yf;
beta = 1;
gammat = 1-yf;
deltat = 1-lamb;

H1 = H/(2*(1-eta));
K1 = eta*C./(1-eta);

fid = fopen('aenewdata.dat','w');
for i=1:length(xl)
    if (xl(i)<eta*yf)
        A(i) = 16.*H.*(xl(i).^2.5)./(15.*eta.*yf);
    elseif (xl(i)<yf)
        tmp1 = 16.*H.*(xl(i).^2.5)./(15.*eta.*yf);
        tmp20 = -8.*(xl(i)-eta*yf).^1.5).*(3*eta*yf+2.*xl(i)).*H/(15*eta*yf);
        tmp21 = 8.*(xl(i)-eta.*yf).^1.5).*(3*eta*yf+2.*xl(i)).*(1./(15*yf)).*((K1/eta)-(2*H1));
        tmp22 = 8*(2*H1-K1)*(xl(i)-eta.*yf).^1.5)./3;
        A(i) = tmp1+tmp20+tmp21+tmp22;
    elseif (xl(i)<epsil)
        tmp1 = 16.*H.*(xl(i).^2.5)./(15.*eta.*yf);
        tmp20 = -8.*(xl(i)-eta*yf).^1.5).*(3*eta*yf + 2*xl(i)).*H/(15*eta*yf);
        tmp21 = 8.*(xl(i)-eta.*yf).^1.5).*(3*eta*yf+2.*xl(i)).*(1./(15*yf)).*((K1/eta)-2*H1);
        tmp22 = 8*(2*H1-K1)*(xl(i)-eta.*yf).^1.5)./3;
        tmp31 = -8.*(xl(i)-yf).^1.5).*(3*yf+2.*xl(i)).*(1./(15*yf)).*((K1/eta)-2*H1);
        tmp32 = -8*(2*H1-K1)*(xl(i)-yf).^1.5)./3;
        tmp33 = 8*(C-B1*yf)*(xl(i)-yf).^1.5)./3 + (8*B1*((xl(i)-yf).^1.5)*(3*yf+2.*xl(i))./15);
        A(i) = tmp1+tmp20+tmp21+tmp22+tmp31+tmp32+tmp33;
    elseif (xl(i)<lamb)
        tmp1 = 16.*H.*(xl(i).^2.5)./(15.*eta.*yf);
        tmp20 = -8.*(xl(i)-eta*yf).^1.5).*(3*eta*yf + 2*xl(i)).*H/(15*eta*yf);
        tmp21 = 8.*(xl(i)-eta.*yf).^1.5).*(3*eta*yf+2.*xl(i)).*(1./(15*yf)).*((K1/eta)-2*H1);
        tmp22 = 8*(2*H1-K1)*(xl(i)-eta.*yf).^1.5)./3;
        tmp31 = -8.*(xl(i)-yf).^1.5).*(3*yf+2.*xl(i)).*(1./(15*yf)).*((K1/eta)-2*H1);
        tmp32 = -8*(2*H1-K1)*(xl(i)-yf).^1.5)./3;
        tmp33 = 8*(C-B1*yf)*(xl(i)-yf).^1.5)./3 + (8*B1*((xl(i)-yf).^1.5)*(3*yf+2.*xl(i))./15);
        tmp41 = -8*(C-B1*yf)*(xl(i)-epsil).^1.5)./3 - (8*B1*((xl(i)-epsil).^1.5)*(3*epsil+2.*xl(i))./15);
        tmp42 = 8*(C1-B2*epsil)*(xl(i)-epsil).^1.5)./3 + (8*B2*((xl(i)-epsil).^1.5)*(3*epsil+2.*xl(i))./15);
        A(i) = tmp1+tmp20+tmp21+tmp22+tmp31+tmp32+tmp33+tmp41+tmp42;
    elseif (xl(i)>lamb+t) & (xl(i)<l)
        tmp1 = 16.*H.*(xl(i).^2.5)./(15.*eta.*yf);
        tmp20 = -8.*(xl(i)-eta*yf).^1.5).*(3*eta*yf + 2*xl(i)).*H/(15*eta*yf);
        tmp21 = 8.*(xl(i)-eta.*yf).^1.5).*(3*eta*yf+2.*xl(i)).*(1./(15*yf)).*((K1/eta)-2*H1);
        tmp22 = 8*(2*H1-K1)*(xl(i)-eta.*yf).^1.5)./3;
        tmp31 = -8.*(xl(i)-yf).^1.5).*(3*yf+2.*xl(i)).*(1./(15*yf)).*((K1/eta)-2*H1);
        tmp32 = -8*(2*H1-K1)*(xl(i)-yf).^1.5)./3;
        tmp33 = 8*(C-B1*yf)*(xl(i)-yf).^1.5)./3 + (8*B1*((xl(i)-yf).^1.5)*(3*yf+2.*xl(i))./15);
        tmp41 = -8*(C-B1*yf)*(xl(i)-epsil).^1.5)./3 - (8*B1*((xl(i)-epsil).^1.5)*(3*epsil+2.*xl(i))./15);
        tmp42 = 8*(C1-B2*epsil)*(xl(i)-epsil).^1.5)./3 + (8*B2*((xl(i)-epsil).^1.5)*(3*epsil+2.*xl(i))./15);
        tmp54 = -8*(C1-B2*epsil)*(xl(i)-lamb).^1.5)./3 - (8*B2*((xl(i)-lamb).^1.5)*(3*lamb+2.*xl(i))./15);
        if (t==0)
            tmp55=0;
            tmp65=0;
        else
            tmp55 = 8*(C2+(lamb*(D+C2)/t))*((xl(i)-lamb).^1.5)./3 - (8*(D+C2))*((xl(i)-lamb).^1.5)*(3*lamb+2.*xl(i))./(15*t));
            tmp65 = -8*(C2+(lamb*(D+C2)/t))*((xl(i)-lamb-t).^1.5)./3 + (8*(D+C2))*((xl(i)-lamb-t).^1.5)*(3*lamb+3*t+2.*xl(i))./(15*t));
        end
        tmp66 = -8*(B3*(lamb+t)+D)*((xl(i)-lamb-t).^1.5)./3 + (8*B3*((xl(i)-lamb-t).^1.5)*(3*lamb+3*t+2.*xl(i))./15);
        A(i) = tmp1+tmp20+tmp21+tmp22+tmp31+tmp32+tmp33+tmp41+tmp42+tmp54+tmp55+tmp65+tmp66;
    elseif (xl(i)>l)
        tmp1 = 16.*H.*(xl(i).^2.5)./(15.*eta.*yf);
        tmp20 = -8.*(xl(i)-eta*yf).^1.5).*(3*eta*yf + 2*xl(i)).*H/(15*eta*yf);
        tmp21 = 8.*(xl(i)-eta.*yf).^1.5).*(3*eta*yf+2.*xl(i)).*(1./(15*yf)).*((K1/eta)-2*H1);
        tmp22 = 8*(2*H1-K1)*(xl(i)-eta.*yf).^1.5)./3;
        tmp31 = -8.*(xl(i)-yf).^1.5).*(3*yf+2.*xl(i)).*(1./(15*yf)).*((K1/eta)-2*H1);
        tmp32 = -8*(2*H1-K1)*(xl(i)-yf).^1.5)./3;
        tmp33 = 8*(C-B1*yf)*(xl(i)-yf).^1.5)./3 + (8*B1*((xl(i)-yf).^1.5)*(3*yf+2.*xl(i))./15);
        tmp41 = -8*(C-B1*yf)*(xl(i)-epsil).^1.5)./3 - (8*B1*((xl(i)-epsil).^1.5)*(3*epsil+2.*xl(i))./15);
        tmp42 = 8*(C1-B2*epsil)*(xl(i)-epsil).^1.5)./3 + (8*B2*((xl(i)-epsil).^1.5)*(3*epsil+2.*xl(i))./15);
        tmp54 = -8*(C1-B2*epsil)*(xl(i)-lamb).^1.5)./3 - (8*B2*((xl(i)-lamb).^1.5)*(3*lamb+2.*xl(i))./15);
        if (t==0)
            tmp55=0;
            tmp65=0;
        else
            tmp55 = 8*(C2+(lamb*(D+C2)/t))*((xl(i)-lamb).^1.5)./3 - (8*(D+C2))*((xl(i)-lamb).^1.5)*(3*lamb+2.*xl(i))./(15*t));
            tmp65 = -8*(C2+(lamb*(D+C2)/t))*((xl(i)-lamb-t).^1.5)./3 + (8*(D+C2))*((xl(i)-lamb-t).^1.5)*(3*lamb+3*t+2.*xl(i))./(15*t));
        end
        tmp66 = -8*(B3*(lamb+t)+D)*((xl(i)-lamb-t).^1.5)./3 + (8*B3*((xl(i)-lamb-t).^1.5)*(3*lamb+3*t+2.*xl(i))./15);
        tmp73 = 8*(B3*(lamb+t)+D)*((xl(i)-l).^1.5)./3;
        tmp74 = -(8*B3*((xl(i)-l).^1.5)*(3*l+2.*xl(i))./15);
        tmp71 = 8*(B3*(l-lamb-t)-D-(S*1))*((xl(i)-l).^1.5)./3;
        tmp72 = (8*S*((xl(i)-l).^1.5)*(3*l+2.*xl(i))./15);
        A(i) = tmp1+tmp20+tmp21+tmp22+tmp31+tmp32+tmp33+tmp41+tmp42+tmp54+tmp55+tmp65+tmp66+tmp71+tmp72+tmp73+tmp74;
    else
        if (t==0)
            tmp1 = 16.*H.*(xl(i).^2.5)./(15.*eta.*yf);
            tmp20 = -8.*(xl(i)-eta*yf).^1.5).*(3*eta*yf + 2*xl(i)).*H/(15*eta*yf);
            tmp21 = 8.*(xl(i)-eta.*yf).^1.5).*(3*eta*yf+2.*xl(i)).*(1./(15*yf)).*((K1/eta)-2*H1);
            tmp22 = 8*(2*H1-K1)*(xl(i)-eta.*yf).^1.5)./3;
            tmp31 = -8.*(xl(i)-yf).^1.5).*(3*yf+2.*xl(i)).*(1./(15*yf)).*((K1/eta)-2*H1);

```

```

tmp32 = -8*(2*H1-K1)*((xl(i)-yf).^1.5)./3;
tmp33 = 8*(C-B1*yf)*((xl(i)-yf).^1.5)./3 + (8*B1*((xl(i)-yf).^1.5)*(3*yf+2.*xl(i))./15);
tmp41 = -8*(C-B1*yf)*((xl(i)-epsilon).^1.5)./3 - (8*B1*((xl(i)-epsilon).^1.5)*(3*epsilon+2.*xl(i))./15);
tmp42 = 8*(C1-B2*epsilon)*((xl(i)-epsilon).^1.5)./3 + (8*B2*((xl(i)-epsilon).^1.5)*(3*epsilon+2.*xl(i))./15);

tmp54 = -8*(C1-B2*epsilon)*((xl(i)-lamb).^1.5)./3 - (8*B2*((xl(i)-lamb).^1.5)*(3*lamb+2.*xl(i))./15);
tmp55 = 8*(C2+(lamb*(D+C2)/t))*((xl(i)-lamb).^1.5)./3 - (8*(D+C2))*((xl(i)-lamb).^1.5)*(3*lamb+2.*xl(i))./(15*t));

end

A(i) = tmp1+tmp20+tmp21+tmp22+tmp31+tmp32+tmp33+tmp41+tmp42+tmp54+tmp55;
end
fprintf(fid,'%f\t0.0\t0.0\t0.0\t%f\n',xl(i),A(i));
end
fclose(fid);

function alphas = obtainalpha(h,M,l,W)
format long;
zh = 750; % Initial waveform at 1000 ft from aircraft axis
z = 10*l; % Calculate F-function at 10 body lengths away

sgam=1.4;
gam = (1+sgam)./2;
beta = sqrt(M.^2-1);

% Standard atmosphere computations
hgp = 0.3048.*h./(1.0+0.3048.*h./6356766.0); %Convert to metres
ttb(1)= 518.67;
htb(1)=0.0;
htb(2) = 11000.0;
htb(3) =20000.0;
htb(4) = 32000.0;
htb(5) = 47000.0;
ttb(2) = 389.97;
ttb(3) = 389.97;
ttb(4)= 411.57;
ttb(5) = 487.17;

Pg = 2116.2281; %psf at ground
zm = zh/3.2808399; %Convert zh into metres
Txs = interp1(htb,ttb,hgp,'linear'); %Temperature at aircraft axis
Th = interp1(htb,ttb,hgp-zm,'linear'); %Temperature at initial waveform

if (hgp-zm < 11000)
    tmpth = ((Th-491.67)./1.8)+273.15;
    Ph=Pg*((tmpth/288.15).^5.256);
else
    Ph1 = Pg.*((216.5/288.15).^5.255912);
    Ph = Ph1.*exp(-(hgp-zm-11000).*9.807./287.26./216.5);
end

spsh = (sgam*1716.56*Th).^0.5;
rhoh = Ph./1716.56./Th;

Ptmp = Pg.*((216.5/288.15).^5.256);
tmptxs = ((Txs-491.67)./1.8) + 273.15;
Pinf = Ptmp.*exp(-(hgp-11000).*9.807./287.26./tmptxs);

rhoinf = Pinf./1716.56./Txs;

ainf = (sgam*1716.56*Txs).^0.5;
Vinf = M.*ainf;
mh = Vinf./((sgam*1716.56*Th).^0.5);

Tz = interp1(htb.*3.2808399,ttb,0,'linear');
mz = Vinf./((sgam*1716.56*Tz).^0.5);
mh = Vinf./spsh;

rhog = Pg./1716.56./Tz;
ag = (sgam*1716.56*Tz).^0.5;
mg = Vinf./ag;

alptmp = quadl(@alfunc,0,hgp*3.2808399,[],[],M,Ph,rhoh,Vinf,htb,ttb,hgp);

betag = (mg.^2-1).^0.5;
alphay = gam.*mh.*mh.*mh.*alptmp./((2*betag).^0.5);

function re=ahfunc(Z,Vinf,htb,ttb,hgp)

sgam=1.4;
Tz = interp1(htb.*3.2808399,ttb,hgp*3.2808399-Z,'linear');
mz = Vinf./((sgam*1716.56*Tz).^0.5);
re = 1./((mz.^2)-1).^0.5);

function re = alfunc(Z,M,Ph,rhoh,Vinf,htb,ttb,hgp,ahterm)

sgam=1.4;
Pg = 2116.2281;

Th = Ph./1716.56./rhoh;
sph = (sgam*1716.56*Th).^0.5;
mh = Vinf./sph;

for i=1:length(Z)
    Tz(i) = interp1(htb.*3.2808399,ttb,hgp*3.2808399-Z(i),'linear');
    mz(i) = Vinf./((sgam*1716.56*Tz(i)).^0.5);
    if Z(i)==0
        Z(i) = 0.001;
    end
    Ahtmp = quadl(@ahfunc,0,Z(i),[],[],Vinf,htb,ttb,hgp);
    ahterm(i) = 1./(mh*((1-(1./(mz(i)).*mz(i))))).^0.5).*Ahtmp;
    if Z(i)<36089
        tmptz = ((Tz(i)-491.67)./1.8)+273.15;
        Pz(i) = Pg.*((tmptz/288.15).^5.256);
    else
        Pzn = Pg.*((216.5/288.15).^5.255912);
        tmptz = ((Tz(i)-491.67)./1.8)+273.15;
        Pz(i) = Pzn.*exp(-(hgp-11000).*9.807./287.26./tmptz);
    end
end

rhoz = Pz./1716.56./Tz;
spsz = (sgam*1716.56*Tz).^0.5;

```



```

betaz = (mz.^2-1).^0.5;

re = (Ph./Pz).*((rhoz.*sph./rhoh./spsz).^0.5).*(ahterm.^0.5).*mz./betaz;

function res=functp(x,l,M,W,h,prbypf,yf,rhovtmp,S,B1,B2,B3,t,eta,epsil)

ptmp = 1/prbypf;

aly =(x(1)-1)/prbypf;
H = (S*(x(1)-1)*(x(1)-1)/yf/prbypf/prbypf) - (S*(1-eta)*(x(1)-1)/prbypf);
C = H*yf/(((x(1)-1)*ptmp)-(yf*(1-eta)));
ptmp = 1/prbypf;

K1 = eta*C./(1-eta);
H1 = H./(2*(1-eta));
C1 = B1*(epsil-yf)+C;
C2 = B2*(x(2)-epsil)+C1;

a1 = 32*H*(1^2.5)/(30*eta*yf);
a2 = -8*H*((1-eta.*yf).^1.5)*(6*eta*yf+4*1)./(30*eta*yf);
a3 = 8*((K1/eta)-2*H1)*((1-eta*yf).^1.5)*(3*eta*yf+2*1)/(15*yf);
a4 = 8*(2*H1-K1)*((1-eta.*yf).^1.5)/3;
a5 = -8.*((1-yf).^1.5).*(3*yf+2.*1).*(1./(15*yf)).*((K1/eta)-2*H1);
a6 = -8*(2*H1-K1)*((1-yf).^1.5)/3;
a7 = 8*(C-B1*yf)*((1-yf).^1.5)/3;
a8 = 8.*((1-yf).^1.5).*(3*yf+2.*1).*(B1/15);
a9 = -8*(C-B1*yf)*(1-epsil).^1.5)/3;
a10 = -8.*((1-epsil).^1.5).*(3*epsil+2.*1).*(B1/15);
a11 = 8*(C1-B2*epsil)*(1-epsil).^1.5)/3;
a12 = 8.*((1-epsil).^1.5).*(3*epsil+2.*1).*(B2/15);
a13 = -8*(C1-B2*epsil)*((1-x(2)).^1.5)/3;
a14 = -8.*((1-x(2)).^1.5).*(3*x(2)+2.*1).*(B2/15);
a15 = 8.*((1-x(2)-t).^1.5).*(3*x(2)+3*t+2.*1).*(B3/15);

a17 = 8*B3*(x(2)+t)*((1-x(2)-t).^1.5)/3;

if (t==0)
    a16=0;
    a18 =0;
    a19 = (8*((1-x(2)-t).^1.5)/3);
    a21 = 0.0;
    a23 = 0.0;
    a22=0.0;
else
    a16 = -8*(C2+(x(2)*C2./t))*((1-x(2)).^1.5)/3;
    a18 = 8.*((1-x(2)).^1.5).*(3*x(2)+2.*1).*(C2/(15*t));
    a19 = (8.*((1-x(2)).^1.5).*(3*x(2)+2.*1).*(1/(15*t))) - (8*x(2)*((1-x(2)).^1.5)/(3*t)) + (8*((1-x(2)-t).^1.5)/3);
    a21 = -8*(C2+(x(2)*C2./t))*((1-x(2)-t).^1.5)/3;
    a22 = 8.*((1-x(2)-t).^1.5).*(3*x(2)+2.*1+3*t).*(C2/(15*t));
    a23 = -8.*((1-x(2)-t).^1.5).*(3*x(2)+2.*1+3*t).*(1/(15*t)) + (8*x(2)*((1-x(2)-t).^1.5)/(3*t));
end

% Value of D in terms of other variables
D = abs((a1+a2+a3+a4+a5+a6+a7+a8+a9+a10+a11+a12+a13+a14+a15-rhovtmp.*W-a16-a17-a18+a21+a22)/(a19+a23));

% First equation
alph = 1-eta*yf;
beta = 1;
gammat = 1-yf;
upsil = 1-epsil;
deltat = 1-x(2);
phit = 1-x(2)-t;

tmp1 = ((gett1(alph)-gett1(beta))/3);
tmp2 = x(1)*(sqrt(alph)-sqrt(beta));
tmp3 = x(1)*sqrt(x(1)-1)*(gett2(alph,x(1),1)-gett2(beta,x(1),1));
ft = 2*H*(tmp1-tmp2+tmp3)/(yf*eta);

tmp1 = ((gett1(gammat)-gett1(alph))/3);
tmp2 = x(1)*(sqrt(gammat)-sqrt(alph));
tmp3 = x(1)*sqrt(x(1)-1)*(gett2(gammat,x(1),1)-gett2(alph,x(1),1));
tmp4 = sqrt(x(1)-1)*(gett2(gammat,x(1),1)-gett2(alph,x(1),1));
tmp5 = (sqrt(gammat)-sqrt(alph));
st1 = (2*C*(tmp1-tmp2+tmp3)/((1-eta)*yf)) + 2*eta*C*(tmp5-tmp4)/(1-eta);

tmp1 = ((gett1(gammat)-gett1(alph))/3);
tmp2 = x(1)*(sqrt(gammat)-sqrt(alph));
tmp3 = x(1)*sqrt(x(1)-1)*(gett2(gammat,x(1),1)-gett2(alph,x(1),1));
tmp4 = sqrt(x(1)-1)*(gett2(gammat,x(1),1)-gett2(alph,x(1),1));
tmp5 = (sqrt(gammat)-sqrt(alph));
st2 = (-2*H*(tmp1-tmp2+tmp3)/((1-eta)*yf));
sttmp = 2*H*(tmp4-tmp5)/(1-eta);
st2 = st2+sttmp;

tmp1 = (2*B1*yf-2*C)*((sqrt(upsil)-sqrt(gammat))-sqrt(x(1)-1)*(gett2(upsil,x(1),1)-gett2(gammat,x(1),1)));
tmp2 = 2*B1*((gett1(upsil)-gett1(gammat))/3)-x(1)*((sqrt(upsil)-sqrt(gammat)))+x(1)*sqrt(x(1)-1)*(gett2(upsil,x(1),1)-gett2(gammat,x(1),1)));
st3 = tmp1+tmp2;

tmp1 = (2*B2*epsil-2*C1)*((sqrt(deltat)-sqrt(upsil))-sqrt(x(1)-1)*(gett2(deltat,x(1),1)-gett2(upsil,x(1),1)));
tmp2 = 2*B2*((gett1(deltat)-gett1(upsil))/3)-x(1)*((sqrt(deltat)-sqrt(upsil)))+x(1)*sqrt(x(1)-1)*(gett2(deltat,x(1),1)-gett2(upsil,x(1),1)));
st4 = tmp1+tmp2;

if (t==0)
    st5=0;
else
    N = -(D+C2)/t;
    tmp1 = (2*N*x(2)-2*C2)*((sqrt(phit)-sqrt(deltat))-sqrt(x(1)-1)*(gett2(phit,x(1),1)-gett2(deltat,x(1),1)));
    tmp2 = 2*N*((gett1(phit)-gett1(deltat))/3)-x(1)*((sqrt(phit)-sqrt(deltat)))+x(1)*sqrt(x(1)-1)*(gett2(phit,x(1),1)-gett2(deltat,x(1),1)));
    st5 = tmp1+tmp2;
end

tmp1 = (2*B3*(x(2)+t)+2*D)*((-sqrt(phit))+sqrt(x(1)-1)*gett2(phit,x(1),1));
tmp2 = 2*B3*(((-gett1(phit))/3)+x(1)*sqrt(phit)-x(1)*sqrt(x(1)-1)*gett2(phit,x(1),1)));
st6 = tmp1+tmp2;

newvar = ft+st1+st2+st3+st4+st5+st6;

rh = -pi*sqrt(x(1)-1)*(S*(x(1)-1)+B3*(1-x(2)-t)-D);

newvar2 = rh;

res = ((newvar-newvar2).^2);

function re = gett1(a)
tmp = sqrt(a);

```

```

re = tmp^3;

function re = gett2(a,x1,l);
tmp = sqrt(a);
re = atan(tmp./sqrt(x1-l));

function re = getw1(a)
tmp = sqrt(a);
re = tmp^3;

function re = getw2(a)
tmp = sqrt(a);
re = tmp^5;

function res = fornlseq(x,l,M,W,h,prbypf,yf,rhovtmp,S,B1,B2,B3,t,eta,epsil)

ptmp = 1/prbypf;

aly = (x(1)-l)/prbypf;
H = (S*(x(1)-l)*(x(1)-l)/yf/prbypf/prbypf) - (S*(1-eta)*(x(1)-l)/prbypf);
C = H*yf/(((x(1)-l)*ptmp)-(yf*(1-eta)));

ptmp = 1/prbypf;

K1 = eta*C./(1-eta);
H1 = H./(2*(1-eta));
C1 = B1*(epsil-yf)+C;
C2 = B2*(x(2)-epsil)+C1;

a1 = 32*H*(1^2.5)/(30*eta*yf);
a2 = -8*H*((1-eta.*yf)^1.5)*(6*eta*yf+4*1)./(30*eta*yf);
a3 = 8*((K1/eta)-2*H1)*((1-eta*yf)^1.5)*(3*eta*yf+2*1)/(15*yf);
a4 = 8*(2*H1-K1)*((1-eta.*yf)^1.5)/3;
a5 = -8.*((1-yf)^1.5).*(3*yf+2.*1).*(1./((15*yf))).*((K1/eta)-2*H1);
a6 = -8*(2*H1-K1)*((1-yf)^1.5)/3;
a7 = 8*(C-B1*yf)*((1-yf)^1.5)/3;
a8 = 8.*((1-yf)^1.5).*(3*yf+2.*1).*(B1/15);
a9 = -8*(C-B1*yf)*((1-epsil)^1.5)/3;
a10 = -8.*((1-epsil)^1.5).*(3*epsil+2.*1).*(B1/15);
a11 = 8*(C1-B2*epsil)*((1-epsil)^1.5)/3;
a12 = 8.*((1-epsil)^1.5).*(3*epsil+2.*1).*(B2/15);
a13 = -8*(C1-B2*epsil)*((1-x(2))^1.5)/3;
a14 = -8.*((1-x(2))^1.5).*(3*x(2)+2.*1).*(B2/15);
a15 = 8.*((1-x(2)-t)^1.5).*(3*x(2)+3*t+2.*1).*(B3/15);

a17 = 8*B3*(x(2)+t)*((1-x(2)-t)^1.5)/3;

if (t==0)
a16=0;
a18 =0;
a19 = (8*((1-x(2)-t)^1.5)/3);
a21 = 0.0;
a23 = 0.0;
a22=0.0;
else
a16 = -8*(C2+(x(2)*C2./t))*((1-x(2))^1.5)/3;
a18 = 8.*((1-x(2))^1.5).*(3*x(2)+2.*1).*(C2/(15*t));
a19 = (8.*((1-x(2))^1.5).*(3*x(2)+2.*1).*(1/(15*t))) - (8*x(2)*((1-x(2))^1.5)/(3*t)) + (8*((1-x(2)-t)^1.5)/3);
a21 = -8*(C2+(x(2)*C2./t))*((1-x(2)-t)^1.5)/3;
a22 = 8.*((1-x(2)-t)^1.5).*(3*x(2)+2.*1+3*t).*(C2/(15*t));
a23 = -(8.*((1-x(2)-t)^1.5).*(3*x(2)+2.*1+3*t).*(1/(15*t))) + (8*x(2)*((1-x(2)-t)^1.5)/(3*t));
end

% Value of D in terms of other variables
D = abs((a1+a2+a3+a4+a5+a6+a7+a8+a9+a10+a11+a12+a13+a14+a15-rhovtmp.*W-a16-a17-a18+a21+a22)./(a19+a23));

alph = 1-eta*yf;
beta = 1;
gammat = 1-yf;
upsil = 1-epsil;
deltat = 1-x(2);
phit = 1-x(2)-t;

tmp1 = ((gett1(alph)-gett1(beta))/3);
tmp2 = x(1)*(sqrt(alph)-sqrt(beta));
tmp3 = x(1)*sqrt(x(1)-l)*(gett2(alph,x(1),l)-gett2(beta,x(1),l));
ft = 2*H*(tmp1-tmp2+tmp3)/(yf*eta);

tmp1 = ((gett1(gammat)-gett1(alph))/3);
tmp2 = x(1)*(sqrt(gammat)-sqrt(alph));
tmp3 = x(1)*sqrt(x(1)-l)*(gett2(gammat,x(1),l)-gett2(alph,x(1),l));
tmp4 = sqrt(x(1)-l)*(gett2(gammat,x(1),l)-gett2(alph,x(1),l));
tmp5 = (sqrt(gammat)-sqrt(alph));
st1 = (2*C*(tmp1-tmp2+tmp3)/((1-eta)*yf)) + 2*eta*C*(tmp5-tmp4)/(1-eta);

tmp1 = ((gett1(gammat)-gett1(alph))/3);
tmp2 = x(1)*(sqrt(gammat)-sqrt(alph));
tmp3 = x(1)*sqrt(x(1)-l)*(gett2(gammat,x(1),l)-gett2(alph,x(1),l));
tmp4 = sqrt(x(1)-l)*(gett2(gammat,x(1),l)-gett2(alph,x(1),l));
tmp5 = (sqrt(gammat)-sqrt(alph));
st2 = (-2*H*(tmp1-tmp2+tmp3)/((1-eta)*yf));
sttmp = 2*H*(tmp4-tmp5)/(1-eta);
st2 = st2+sttmp;

tmp1 = (2*B1*yf-2*C)*((sqrt(upsil)-sqrt(gammat))-sqrt(x(1)-l)*(gett2(upsil,x(1),l)-gett2(gammat,x(1),l)));
tmp2 = 2*B1*((gett1(upsil)-gett1(gammat))/3)-x(1)*((sqrt(upsil)-sqrt(gammat))+x(1)*sqrt(x(1)-l)*(gett2(upsil,x(1),l)-gett2(gammat,x(1),l)));
st3 = tmp1+tmp2;

tmp1 = (2*B2*epsil-2*C1)*((sqrt(deltat)-sqrt(upsil))-sqrt(x(1)-l)*(gett2(deltat,x(1),l)-gett2(upsil,x(1),l)));
tmp2 = 2*B2*((gett1(deltat)-gett1(upsil))/3)-x(1)*((sqrt(deltat)-sqrt(upsil))+x(1)*sqrt(x(1)-l)*(gett2(deltat,x(1),l)-gett2(upsil,x(1),l)));
st4 = tmp1+tmp2;

if (t==0)
st5=0;
else
N = -(D+C2)/t;
tmp1 = (2*N*x(2)-2*C2)*((sqrt(phit)-sqrt(deltat))-sqrt(x(1)-l)*(gett2(phit,x(1),l)-gett2(deltat,x(1),l)));
tmp2 = 2*N*((gett1(phit)-gett1(deltat))/3)-x(1)*((sqrt(phit)-sqrt(deltat))+x(1)*sqrt(x(1)-l)*(gett2(phit,x(1),l)-gett2(deltat,x(1),l)));
st5 = tmp1+tmp2;
end

tmp1 = (2*B3*(x(2)+t)+2*D)*((-sqrt(phit))+sqrt(x(1)-l)*gett2(phit,x(1),l));
tmp2 = 2*B3*((-gett1(phit))/3)+x(1)*sqrt(phit)-x(1)*sqrt(x(1)-l)*gett2(phit,x(1),l);
st6 = tmp1+tmp2;

newvar = ft+st1+st2+st3+st4+st5+st6;

```

```

rh = -pi*sqrt(x(1)-1)*(S*(x(1)-1)+B3*(1-x(2)-t)-D);

newvar2 = rh;

res(1) = (newvar-newvar2).^2;

alph = (x(1)-1)/(1-eta*yf);
beta = (x(1)-1)/1;
gammat = (x(1)-1)/(1-yf);
upsil = (x(1)-1)/(1-epsil);
deltat = (x(1)-1)/(1-x(2));
phit = (x(1)-1)/(1-x(2)-t);

tmp1 = H.*(x(1)-1).*(1./(eta*yf));
tmp2 = tmp1.*(tant1(beta)-tant1(alph));
tmp3 = H.*(x(1)-1).*(x(1)-1).*(tant2(alph)-tant2(beta))./(2*eta*yf);
ft = (tmp2-tmp3);

tmp1 = C.*(1/yf)-eta.*(x(1)-1).*(tant1(alph)-tant1(gammat))./(1-eta);
tmp2 = -C.*(x(1)-1).*(x(1)-1).*(tant2(gammat)-tant2(alph))./(2*(1-eta)*yf);
st1 = (tmp1+tmp2);

tmp1 = ((1/yf)-1).*(x(1)-1).*(tant1(alph)-tant1(gammat))./(1-eta);
tmp2 = (x(1)-1).*(x(1)-1).*(tant2(gammat)-tant2(alph))./(2*yf*(1-eta));
st2 = -H.*(tmp1-tmp2);

tmp1 = (B1*(1-yf)+C)*(x(1)-1).*(tant1(gammat)-tant1(upsil));
tmp2 = -0.5*B1*((x(1)-1)^2).*(tant2(upsil)-tant2(gammat));
st3 = tmp1+tmp2;

tmp1 = (B2*(1-epsil)+C1)*(x(1)-1).*(tant1(upsil)-tant1(deltat));
tmp2 = -0.5*B2*((x(1)-1)^2).*(tant2(deltat)-tant2(upsil));
st4 = tmp1+tmp2;

if (t==0)
    st5=0;
else
    N = -(D+C2)/t;
    tmp1 = (N*(1-x(2))+C2)*(x(1)-1).*(tant1(deltat)-tant1(phit));
    tmp2 = -0.5*N*((x(1)-1)^2).*(tant2(phit)-tant2(deltat));
    st5 = tmp1+tmp2;
end

tmp1 = (B3*(1-x(2)-t)-D)*(x(1)-1).*(-0.5*pi+tant1(phit));
tmp2 = -0.5*B3*((x(1)-1)^2).*(0.5*pi-tant2(phit));
st6 = tmp1+tmp2;

rhs = -0.25.*pi.*(2.*B3.*(1-x(2)-t)-2.*D + (S.*(x(1)-1))).*(x(1)-1);

res1 = ft+st1+st2+st3+st4+st5+st6;
res2 = rhs;

res(2) = res1-res2;

function [c,ceq] = consttrap(x,l,M,W,h,prbypf,yf,rhovtmp,S,B1,B2,B3,t,eta,epsil)

c=[];
ceq = [];

ptmp = 1/prbypf;

aly =(x(1)-1)/prbypf;
H = (S*(x(1)-1)*(x(1)-1)/yf/prbypf/prbypf) - (S*(1-eta)*(x(1)-1)/prbypf);
C = H*yf/(((x(1)-1)*ptmp)-(yf*(1-eta)));

K1 = eta*C./(1-eta);
H1 = H./(2*(1-eta));
C1 = B1*(epsil-yf)+C;
C2 = B2*(x(2)-epsil)+C1;

a1 = 32*H*(1^2.5)/(30*eta*yf);
a2 = -8*H*((1-eta.*yf)^1.5).*(6*eta*yf+4*1)./(30*eta*yf);
a3 = 8*((K1/eta)-2*H1)*((1-eta*yf)^1.5).*(3*eta*yf+2*1)/(15*yf);
a4 = 8*(2*H1-K1)*((1-eta.*yf)^1.5)./3;
a5 = -8*((1-yf)^1.5).*(3*yf+2.*1).*(1./(15*yf)).*((K1/eta)-2*H1);
a6 = -8*(2*H1-K1)*((1-yf)^1.5)./3;
a7 = 8*(C-B1*yf)*((1-yf)^1.5)./3;
a8 = 8.*(1-yf)^1.5).*(3*yf+2.*1).*(B1/15);
a9 = -8*(C-B1*yf)*(1-epsil)^1.5)./3;
a10 = -8*((1-epsil)^1.5).*(3*epsil+2.*1).*(B1/15);
a11 = 8*(C1-B2*epsil)*(1-epsil)^1.5)./3;
a12 = 8.*(1-epsil)^1.5).*(3*epsil+2.*1).*(B2/15);
a13 = -8*(C1-B2*epsil)*((1-x(2))^1.5)./3;
a14 = -8*((1-x(2))^1.5).*(3*x(2)+2.*1).*(B2/15);
a15 = 8.*(1-x(2)-t)^1.5).*(3*x(2)+3*t+2.*1).*(B3/15);

a17 = 8*B3*(x(2)+t)*((1-x(2)-t)^1.5)./3;

if (t==0)
    a16=0;
    a18 =0;
    a19 = (8*((1-x(2)-t)^1.5)./3);
    a21 = 0.0;
    a23 = 0.0;
    a22=0.0;
else
    a16 = -8*(C2+(x(2)*C2./t))*((1-x(2))^1.5)./3;
    a18 = 8.*(1-x(2))^1.5).*(3*x(2)+2.*1).*(C2/(15*t));
    a19 = (8.*(1-x(2))^1.5).*(3*x(2)+2.*1).*(1/(15*t))) - (8*x(2)*((1-x(2))^1.5)./(3*t)) + (8*((1-x(2)-t)^1.5)./3);
    a21 = -8*(C2+(x(2)*C2./t))*((1-x(2)-t)^1.5)./3;
    a22 = 8*((1-x(2)-t)^1.5).*(3*x(2)+2.*1+3*t).*(C2/(15*t));
    a23 = -(8.*(1-x(2)-t)^1.5).*(3*x(2)+2.*1+3*t).*(1/(15*t))) + (8*x(2)*((1-x(2)-t)^1.5)./(3*t));
end

% Value of D in terms of other variables
D = abs((a1+a2+a3+a4+a5+a6+a7+a8+a9+a10+a11+a12+a13+a14+a15-rhovtmp.*W-a16-a17-a18+a21+a22)./(a19+a23));

alph = (x(1)-1)/(1-eta*yf);
beta = (x(1)-1)/1;
gammat = (x(1)-1)/(1-yf);
upsil = (x(1)-1)/(1-epsil);
deltat = (x(1)-1)/(1-x(2));
phit = (x(1)-1)/(1-x(2)-t);

tmp1 = H.*(x(1)-1).*(1./(eta*yf));

```

```

tmp2 = tmp1.*(tant1(beta)-tant1(alph));
tmp3 = H.*(x(1)-1).*(x(1)-1).*(tant2(alph)-tant2(beta))./(2*eta*yf);
ft = (tmp2-tmp3);

tmp1 = C.*(1/yf)-eta).*(x(1)-1).*(tant1(alph)-tant1(gammat))./(1-eta);
tmp2 = -C.*(x(1)-1).*(x(1)-1).*(tant2(gammat)-tant2(alph))./(2*(1-eta)*yf);
st1 = (tmp1+tmp2);

tmp1 = ((1/yf)-1).*(x(1)-1).*(tant1(alph)-tant1(gammat))./(1-eta);
tmp2 = (x(1)-1).*(x(1)-1).*(tant2(gammat)-tant2(alph))./(2*yf*(1-eta));
st2 = -H.*(tmp1-tmp2);

tmp1 = (B1*(1-yf)+C).*(x(1)-1).*(tant1(gammat)-tant1(upsil));
tmp2 = -0.5*B1*((x(1)-1)^2).*(tant2(upsil)-tant2(gammat));
st3 = tmp1+tmp2;

tmp1 = (B2*(1-epsil)+C1).*(x(1)-1).*(tant1(upsil)-tant1(deltat));
tmp2 = -0.5*B2*((x(1)-1)^2).*(tant2(deltat)-tant2(upsil));
st4 = tmp1+tmp2;

if (t==0)
    st5=0;
else
    N = -(D+C2)/t;
    tmp1 = (N*(1-x(2))+C2).*(x(1)-1).*(tant1(deltat)-tant1(phit));
    tmp2 = -0.5*N*((x(1)-1)^2).*(tant2(phit)-tant2(deltat));
    st5 = tmp1+tmp2;
end

tmp1 = (B3*(1-x(2)-t)-D).*(x(1)-1).*(-0.5*pi+tant1(phit));
tmp2 = -0.5*B3*((x(1)-1)^2).*(0.5*pi-tant2(phit));
st6 = tmp1+tmp2;

rhs = -0.25.*pi.*(2.*B3.*(1-x(2)-t)-2.*D + (S.*(x(1)-1))).*(x(1)-1);

res1 = ft+st1+st2+st3+st4+st5+st6;
res2 = rhs;

ceq(1) = res1-res2;

c(1) = x(2)+5.0+t-1;
c(2) = 1+5.0-x(1);
c(3) = 1.3*C2-H;
c(4) = -C;
c(5) = -H;
c(6) = epsil-x(2);
c(7) = B3.*(1-x(2)-t)-D+0.005;

function re = tant1(a)
tmp = atan(sqrt(a));
re = tmp*(1+(1/a)) + (1/sqrt(a));

function re = tant2(a)
tmp = atan(sqrt(a));
re = tmp*(1-(1/(a*a))) + (1/sqrt(a))*(1-(1/(3*a)));

function res=arbitp(x,l,yf,B1,B2,B3,t,eta,epsil,lamb,D,H,C)

K1 = eta*C./(1-eta);
H1 = H./(2*(1-eta));
C1 = B1*(epsil-yf)+C;
C2 = B2*(lamb-epsil)+C1;

% First equation
alph = 1-eta*yf;
beta = 1;
gammat = 1-yf;
upsil = 1-epsil;
deltat = 1-lamb;
phit = 1-lamb-t;

tmp1 = ((gett1(alph)-gett1(beta))/3);
tmp2 = x*(sqrt(alph)-sqrt(beta));
tmp3 = x*sqrt(x-1)*(gett2(alph,x,1)-gett2(beta,x,1));
ft = 2*H*(tmp1-tmp2+tmp3)/(yf*eta);

tmp1 = ((gett1(gammat)-gett1(alph))/3);
tmp2 = x*(sqrt(gammat)-sqrt(alph));
tmp3 = x*sqrt(x-1)*(gett2(gammat,x,1)-gett2(alph,x,1));
tmp4 = sqrt(x-1)*(gett2(gammat,x,1)-gett2(alph,x,1));
tmp5 = (sqrt(gammat)-sqrt(alph));
st1 = (2*C*(tmp1-tmp2+tmp3)/((1-eta)*yf)) + 2*eta*C*(tmp5-tmp4)/(1-eta);

tmp1 = ((gett1(gammat)-gett1(alph))/3);
tmp2 = x*(sqrt(gammat)-sqrt(alph));
tmp3 = x*sqrt(x-1)*(gett2(gammat,x,1)-gett2(alph,x,1));
tmp4 = sqrt(x-1)*(gett2(gammat,x,1)-gett2(alph,x,1));
tmp5 = (sqrt(gammat)-sqrt(alph));
st2 = (-2*H*(tmp1-tmp2+tmp3)/((1-eta)*yf));
sttmp = 2*H*(tmp4-tmp5)./(1-eta);
st2 = st2+sttmp;

tmp1 = (2*B1*yf-2*C)*((sqrt(upsil)-sqrt(gammat))-sqrt(x-1)*(gett2(upsil,x,1)-gett2(gammat,x,1)));
tmp2 = 2*B1*((gett1(upsil)-gett1(gammat))/3)-x*((sqrt(upsil)-sqrt(gammat)))+x*sqrt(x-1)*(gett2(upsil,x,1)-gett2(gammat,x,1));
st3 = tmp1+tmp2;

tmp1 = (2*B2*epsil-2*C1)*((sqrt(deltat)-sqrt(upsil))-sqrt(x-1)*(gett2(deltat,x,1)-gett2(upsil,x,1)));
tmp2 = 2*B1*((gett1(deltat)-gett1(upsil))/3)-x*((sqrt(deltat)-sqrt(upsil)))+x*sqrt(x-1)*(gett2(deltat,x,1)-gett2(upsil,x,1));
st4 = tmp1+tmp2;

if (t==0)
    st5=0;
else
    N = -(D+C2)/t;
    tmp1 = (2*N*lamb-2*C2)*((sqrt(phit)-sqrt(deltat))-sqrt(x-1)*(gett2(phit,x,1)-gett2(deltat,x,1)));
    tmp2 = 2*N*((gett1(phit)-gett1(deltat))/3)-x*((sqrt(phit)-sqrt(deltat)))+x*sqrt(x-1)*(gett2(phit,x,1)-gett2(deltat,x,1));
    st5 = tmp1+tmp2;
end

tmp1 = (2*B3*(lamb+t)+2*D)*((-sqrt(phit))+sqrt(x-1)*gett2(phit,x,1));
tmp2 = 2*B3*((-gett1(phit))/3)+x*sqrt(phit)-x*sqrt(x-1)*(gett2(phit,x,1));
st6 = tmp1+tmp2;

newvar = ft+st1+st2+st3+st4+st5+st6;
rh = -1/(pi*sqrt(x-1));
res = rh*newvar;

```

# APPENDIX D

## MATLAB CODE FOR NEURAL NETWORK APPROXIMATION

Following the artificial neural network approximation discussion from section 4.2, this chapter lists the MATLAB program used. The program accepts the training and test data as input and using in-built training algorithms, attempts to fit a model through the training data. The program then simulates the performance of the approximation against the test data.

```
% function nntraintest
clear all;clc

close all;

temp=load('FinalSGD.dat'); % training
temptest=load('FinalSGDtest.dat'); %testing

[m,n]=size(temp);

nnin = 11;
nnout = 5;
nnmid = 25;

% Structure for training neural network %
% mydata=struct('x',temp(:,1:nnin),'y',[temp(:,nnin+2) temp(:,nnin+5:n)],'R',zeros(nnin,2)); % 6 in the number of inputs %
mydata=struct('x',temp(:,1:nnin),'y',temp(:,nnin+2:n),'R',zeros(nnin,2)); % 6 in the number of inputs %

%structure for testing neural network %
% mydatatest=struct('x',temptest(:,1:nnin),'y',[temptest(:,nnin+2) temptest(:,nnin+5:n)],'R',zeros(nnin,2)); % 6 in the number of inputs %
mydatatest=struct('x',temptest(:,1:nnin),'y',temptest(:,nnin+2:n),'R',zeros(nnin,2)); % 6 in the number of inputs %

% max and min values of each input for normalization %
mydata.R=[min(mydata.x(:,1:nnin))' max(mydata.x(:,1:nnin))'];
mydatatest.R=[min(mydatatest.x(:,1:nnin))' max(mydatatest.x(:,1:nnin))'];

outbndtr = [min(mydata.y(:,1:nnout))' max(mydata.y(:,1:nnout))'];

fid = fopen('upbound.dat','w');
for i=1:nnin
    fprintf(fid,'%f\n',mydata.R(i,2));
end
fclose(fid);

fid = fopen('outbound.dat','w');
for i=1:nnout
    fprintf(fid,'%f\n',outbndtr(i,2));
end
fclose(fid);

% low = [0.0 1.4 100 50000 80000 5];
% high = [0.0003 1.8 150 65000 115000 30];
%
% mydata.R = [low' high'];

% clearing unnecessary work variables
clear temp,m,n,temptest;

% Normalize inputs and outputs %

% using feedforward neural network %
net=newff(mydata.R,[nnmid,nnout],{'logsig','purelin'},'trainbr');

% normalization of inputs %
for i=1:nnin
    temp=mydata.x(:,i)/mydata.R(i,2);
    temptest=mydatatest.x(:,i)/mydata.R(i,2);
    mydata.x(:,i)=temp;
    mydatatest.x(:,i)=temptest;
end

% normalization of outputs %
for i=1:nnout
    temp=mydata.y(:,i)/outbndtr(i,2);
```

```

        temptest=mydata.test.y(:,i)/outbndtr(i,2);
        mydata.y(:,i)=temp;
        mydata.test.y(:,i)=temptest;
    end

    net.performFcn='msereg';

    net.userdata.note='Neural network developed for Thesis';

    % All network weights are initialized to zero %
    net.IW{1,1}=zeros(net.inputWeights{1,1}.size);
    net.LW{2,1}=zeros(net.layerWeights{2,1}.size);

    net.inputWeights{1,1}.initFcn='initnw';
    net.layerWeights{2,1}.initFcn='initwb';

    % The bias here refers to bias in the individual basis functions not the
    % way bias is defined in controls work

    net.b{1}=zeros(net.biases{1}.size,1);
    net.b{2}=zeros(net.biases{2}.size,1);

    net.biases{1,1}.initFcn='rands';
    net.biases{2,1}.initFcn='rands';

    net=init(net);

    net.biases{1,1}.learnFcn='learngdm';
    net.biases{2,1}.learnFcn='learngdm';

    net.InputWeights{1,1}.learnFcn='learngdm'; % Gradient descent with momentum %
    net.layerWeights{2,1}.learnFcn='learngdm'; % Gradient descent with momentum %

    net.InputWeights{1,1}.learnParam.lr=0.15; % learning rate %
    net.layerWeights{2,1}.learnParam.lr=2.0; % learning rate %

    net.biases{1}.learnParam.lr=0.05;
    net.biases{2}.learnParam.lr=0.05;

    net.adaptParam.passes=50;

    p=num2cell(mydata.x',1);t=num2cell(mydata.y',1);
    ptest=num2cell(mydata.test.x',1);
    % [net,a,e]=adapt(net,p,t); % Incremental training of the neural network %

    net.trainParam.goal=1e-10;
    net.trainParam.epochs=10000;
    net=train(net,p,t);

    a=sim(net,p); % neural network output for training data
    at=sim(net,ptest); % neural network output for testing data

    nnout=cell2mat(a); % neural network output in matrix form for training data
    nnouttest=cell2mat(at); % neural network output in matrix form for testing data

    figure(1)
    fh1=gcf;set(fh1,'Name','Training');
    subplot(511)
    hold on;
    plot(mydata.y(:,1),'b-');plot(nnout(1,:), 'r--');
    subplot(512)
    hold on;
    plot(mydata.y(:,2),'b-');plot(nnout(2,:), 'r--');
    subplot(513)
    hold on;
    plot(mydata.y(:,3),'b-');plot(nnout(3,:), 'r--');
    subplot(514)
    hold on;
    plot(mydata.y(:,4),'b-');plot(nnout(4,:), 'r--');
    subplot(515)
    hold on;
    plot(mydata.y(:,5),'b-');plot(nnout(5,:), 'r--');

    figure(2)
    fh2=gcf;set(fh2,'Name','Testing');
    subplot(511)
    hold on;
    plot(mydata.test.y(:,1),'b-');plot(nnouttest(1,:), 'r--');
    subplot(512)
    hold on;
    plot(mydata.test.y(:,2),'b-');plot(nnouttest(2,:), 'r--');
    subplot(513)
    hold on;
    plot(mydata.test.y(:,3),'b-');plot(nnouttest(3,:), 'r--');
    subplot(514)
    hold on;
    plot(mydata.test.y(:,4),'b-');plot(nnouttest(4,:), 'r--');
    subplot(515)
    hold on;
    plot(mydata.test.y(:,5),'b-');plot(nnouttest(5,:), 'r--');

    V1 = net.IW{1,1};
    W1 = net.LW{2,1};
    b1 = net.b{1};
    b2 = net.b{2};

    fid = fopen('V1.dat','w');
    for i=1:size(V1,1)
        for j=1:size(V1,2)
            fprintf(fid,'%f\t',V1(i,j));
        end
        fprintf(fid,'\n');
    end
    fclose(fid);

    fid = fopen('W1.dat','w');
    for i=1:size(W1,1)
        for j=1:size(W1,2)
            fprintf(fid,'%f\t',W1(i,j));
        end
        fprintf(fid,'\n');
    end
    fclose(fid);

    fid = fopen('b1.dat','w');

```

```

for i=1:size(b1,1)
    for j=1:size(b1,2)
        fprintf(fid,'%f\t',b1(i,j));
    end
    fprintf(fid,'\n');
end
fclose(fid);

fid = fopen('b2.dat','w');
for i=1:size(b2,1)
    for j=1:size(b2,2)
        fprintf(fid,'%f\t',b2(i,j));
    end
    fprintf(fid,'\n');
end
fclose(fid);

```

# REFERENCES

- [1] AERION. <http://www.aerioncorp.com>, 2004.
- [2] ALONSO, J. J. and KROO, I. M., “Advanced algorithms for design and optimization of quiet supersonic platforms,” in *Proceedings of the 40th AIAA Aerospace Sciences Meeting and Exhibit*, American Institute for Aeronautics and Astronautics, Jan. 2002.
- [3] ASHLEY, H. and LANDAHL, M., *Aerodynamics of wings and bodies*. Dover Publications, 1965.
- [4] AUGER, T. and COULOUVRAT, F., “Numerical simulation of sonic boom focusing,” *AIAA Journal*, vol. 40, no. 9, pp. 1726–1734, 2002.
- [5] BARNES, R., “Variogram tutorial.” <http://www.goldensoftware.com/variogramTutorial.pdf>, 2002.
- [6] BLOOR, M. I. and WILSON, M. J., “Efficient parameterization of generic aircraft geometry,” *Journal of Aircraft*, vol. 32, pp. 1269–1275, Dec. 1995.
- [7] BROWN, J. G. and HAGLUND, G. T., “Sonic boom loudness study and airplane configuration development,” in *Proceedings of the AIAA/AHS/ASEE Aircraft Design, Systems and Operations*, American Institute for Aeronautics and Astronautics, Sept. 1990.
- [8] BUONANNO, M. A. and MAVRIS, D. N., “A new method for aircraft concept selection using multicriteria interactive genetic algorithms,” in *Proceedings of the 43rd Aerospace Sciences Meeting and Exhibit*, American Institute for Aeronautics and Astronautics, Jan. 2005.
- [9] BUSEMANN, A., “The relation between minimizing drag and noise at supersonic speeds,” *Proceedings of the conference on high-speed aeronautics*, pp. 133–144, Jan. 1955.
- [10] CARLSON, H. W., “The lower bound of attainable sonic-boom overpressure and design methods of approaching this limit,” Tech. Rep. TN D-1494, National Aeronautics and Space Administration, Langley, Virginia, Nov. 1964.
- [11] CARLSON, H. W., *Correlation of Sonic-Boom theory with wind tunnel and flight measurements*. NASA Langley Research Center, Jan. 2002.
- [12] CARLSON, H. W. and HARRIS, R. V., “A unified system of supersonic aerodynamic analysis,” *NASA SP-228 Analytic methods in aircraft aerodynamics*, pp. 639–658, Oct. 1969.
- [13] CARLSON, H. and MAGLIERI, D., “Review of sonic boom generation theory and prediction methods,” *Journal of Acoustical Society of America*, vol. 51, no. 2, pp. 675–685, 1972.



- [14] CHARBEL FARHAT, KURT MAUTE, B. A. and NIKBAY, M., "A shape optimization methodology for reducing the sonic boom initial pressure rise," in *Proceedings of the 40th AIAA Aerospace Sciences Meeting and Exhibit*, American Institute for Aeronautics and Astronautics, Jan. 2002.
- [15] CHATTERJEE, A., "An introduction to the proper orthogonal decomposition," *Current Science*, vol. 78, pp. 808–817, Apr. 2000.
- [16] CHUNG, H.-S. and ALONSO, J. J., "Design of a low-boom supersonic business jet using cokriging approximation models," in *Proceedings of the 9th AIAA Symposium on Multidisciplinary analysis and optimization*, American Institute for Aeronautics and Astronautics, Sept. 2002.
- [17] COEN, P., "Shaped sonic boom demonstration." [http://www.aee.faa.gov/noise/aee100\\_files/SonicWkshp/2-Panel1-Graham-Northrop.pdf](http://www.aee.faa.gov/noise/aee100_files/SonicWkshp/2-Panel1-Graham-Northrop.pdf), 2003.
- [18] COEN, P. G., "Development of a computer technique for the prediction of transport aircraft flight profile sonic boom signatures," tech. rep., George Washington University, Mar. 1983.
- [19] CONCORDE, "Concorde schematic." <http://www.aerospaceweb.org/aircraft/jetliner/concorde/pics02.shtml>, 2000.
- [20] DARDEN, C., "Sonic boom minimization with nose-bluntness relaxation," Tech. Rep. NASA TP-1348, NASA Langley Research Center, Hampton, VA, Sept. 1979.
- [21] DARDEN, C. M., "Study of the limitations of linear theory methods as applied to sonic boom calculations," in *Proceedings of the 28th Aerospace Sciences Meeting*, American Institute for Aeronautics and Astronautics, Jan. 1990.
- [22] DARDEN, C. M., "The importance of sonic boom research in the development of future high speed aircraft," *Journal of the NTA*, pp. 54–62, 1992.
- [23] DE BOOR, C., *A practical guide to splines*. Springer-Verlag, 2001.
- [24] DOMENIC J. MAGLIERI, H. W. C. and HUBBARD, H. H., "Status of knowledge of sonic booms," Tech. Rep. TM 80113, NASA Langley Research Center, Hampton, VA, 1979.
- [25] EMINTON, E. and LORD, W., "The numerical evaluation of the wave drag of smooth slender bodies using optimum area distributions for minimum wave drag," *Journal of the royal aeronautical society*, vol. 60, pp. 61–63, Jan. 1956.
- [26] FERRI, A. and ISMAIL, A., "Effects of lengthwise lift distribution on sonic boom of sst configurations," *AIAA Journal*, vol. 7, no. 8, pp. 1538–1541, 1969.
- [27] FRANCISCO DE TORO, JULIO ORTEGA, J. F. and DIAZ, A., "Psfga: A parallel genetic algorithm for multiobjective optimization," in *Proceedings of the 10th Euromicro workshop on Parallel, Distributed and Network-based Processing*, IEEE, June 2002.
- [28] GEORGE, A. R., "Lower bounds for sonic booms in the midfield," *AIAA Journal*, vol. 7, no. 8, pp. 1542–1545, 1969.

- [29] GEORGE, A. R. and SEEBASS, R., “Sonic boom minimization including both front and rear shock waves,” *AIAA Journal*, vol. 10, no. 10, pp. 2091–2093, 1969.
- [30] GEORGE, A. and PLOTKIN, K. J., “Sonic boom waveforms and amplitudes in a real atmosphere,” *AIAA Journal*, vol. 7, pp. 1978–1981, Oct. 1969.
- [31] GONDRA, I. and SAMADZADEH, M. H., “A coarse-grain parallel genetic algorithm for finding ramsey numbers,” in *Proceedings of the 18th Annual ACM Symposium on Applied Computing*, Mar. 2003.
- [32] HAGLUND, G. T., “Hsct designs for reduced sonic boom,” in *Proceedings of the AIAA Aircraft Design Systems and Operations Meeting*, American Institute for Aeronautics and Astronautics, Sept. 1991.
- [33] HARRIS, R. V., “An analysis and correlation of aircraft wave drag,” Tech. Rep. NASA TM X-947, NASA, Princeton,NJ, Apr. 1964.
- [34] HAYES, W. D., “Brief review of basic theory,” *Sonic Boom Research NASA SP-147*, pp. 3–7, 1967.
- [35] HAYES, W. D. and JR., H. L. R., “Propagation of sonic boom through a stratified atmosphere,” *NASA SP-228 Analytic methods in aircraft aerodynamics*, pp. 229–241, Oct. 1969.
- [36] HAYKIN, S., *NEURAL NETWORKS A Comprehensive Foundation*. McGraw-Hill Publishing Company, Inc., 2003.
- [37] HAYTER, A. J., *Probability and Statistics for Engineers and Scientists*. PWS Publishing Company, 1996.
- [38] HEIMANN, D., “Effects of long-term atmospheric variability on the width of a sonic-boom carpet produced by high-flying supersonic aircraft,” *Acoustics research Letters Online*, pp. 73–78, Mar. 2001.
- [39] HENNE, P. A., “A gulfstream perspective on the darpa qsp program and furture supersonic initiatives.” [http://www.aee.faa.gov/noise/aee100\\_files/SonicWkshp/3-Panel1-HenneGulfstream.pdf](http://www.aee.faa.gov/noise/aee100_files/SonicWkshp/3-Panel1-HenneGulfstream.pdf), 2003.
- [40] HENRY E. BASS, RICHARD RASPET, J. P. C. and KELLY, M., “Modification of sonic boom wave forms during propagation from the source to the ground,” *Journal of Acoustical Society of America*, vol. 111, pp. 481–486, Jan. 2002.
- [41] HENRY E. BASS, L. C. S. and ZUCKERWAR, A. J., “Atmospheric absorption of sound: Further developments,” *Journal of Acoustical Society of America*, pp. 680–683, Jan. 1995.
- [42] HORINOUCI, S., “Conceptual design of a low sonic boom ssbj,” in *Proceedings of the 43rd AIAA Aerospace Sciences Meeting and Exhibit*, American Institute for Aeronautics and Astronautics, Jan. 2005.

- [43] HOWE, D. C., "Engine placement for sonic boom mitigation," in *Proceedings of the 40th AIAA Aerospace Sciences Meeting and Exhibit*, American Institute for Aeronautics and Astronautics, Jan. 2002.
- [44] HOWE, D. C., "Sonic boom reduction through the use of non-axisymmetric configuration shaping," in *Proceedings of the 41st AIAA Aerospace Sciences Meeting and Exhibit*, American Institute for Aeronautics and Astronautics, Jan. 2003.
- [45] HOWE, D. C., "Improved sonic boom minimization with extendable nose spike," in *Proceedings of the 43rd AIAA Aerospace Sciences Meeting and Exhibit*, American Institute for Aeronautics and Astronautics, Jan. 2005.
- [46] HYOUNG-SEOG CHUNG, S. C. and ALONSO, J. J., "Supersonic business jet design using knowledge-based genetic algorithm with adaptive, unstructured grid methodology," in *Proceedings of the 21st AIAA Applied Aerodynamics Conference*, American Institute for Aeronautics and Astronautics, June 2003.
- [47] JAMESON, A., "The role of cfd in preliminary aerospace design," in *Proceedings of FEDSM03 4th ASME JSME Joint Fluids Engineering Conference*, ASME, July 2003.
- [48] JOHN E. PIERCY, TOM F. EMBLETON, L. C. S., "Review of noise propagation in the atmosphere," *Journal of Acoustical Society of America*, pp. 1403–1418, June 1977.
- [49] JOHN W. BANDLER, Q. S. C. E. A., "Space mapping: The state of the art," *IEEE transactions on Microwave Theory and Techniques*, vol. 52, pp. 337–361, Jan. 2004.
- [50] JONES, R. T., "Theory of wing-body drag at supersonic speeds," Tech. Rep. Report 1284, NACA, Langley, Virginia, 1953.
- [51] KALYANMOY DEB, AMRIT PRATAP, S. A. and MEYARIVAN, T., "A fast and elitist multi-objective genetic algorithm: Nsga-ii," Tech. Rep. KanGAL report 200001, IIT Kanpur, Kanpur, India, 2000.
- [52] KIRBY, M., *A Methodology for Technology, Identification, Evaluation, and Selection in Conceptual and Preliminary Aircraft Design*. PhD thesis, Georgia Institute of Technology School of Aerospace Engineering, Atlanta, GA 30332, Mar. 2001.
- [53] KIRBY, M. R. and MAVRIS, D. N., "A method for technology selection based on benefit, available schedule and budget resources," in *Proceedings of the 2000 World Aviation Congress*, American Institute for Aeronautics and Astronautics, Oct. 2000.
- [54] KRISHAN K. AHUJA, J. C. S. and WALTERICK, R. E., "A giant simulator of sonic boom and aircraft noise," in *Proceedings of the 15th AIAA Aeroacoustics conference*, American Institute for Aeronautics and Astronautics, Oct. 1993.
- [55] LAM-MPI, "Lam-mpi." <http://www.lam-mpi.org>, 2003.
- [56] L.B.JONES, "Lower bounds for sonic bangs," *Journal of the royal aeronautical society*, vol. 65, pp. 433–436, June 1961.
- [57] L.B.JONES, "Lower bounds for the pressure jump of the bow shock of a supersonic transport," *Aeronautical Quarterly*, vol. XXI, pp. 1–17, Feb. 1970.

- [58] LEATHERWOOD, J. D. and SULLIVAN, B. M., "Effect of sonic boom asymmetry on subjective loudness," Tech. Rep. TM-107708, National Aeronautics and Space Administration, Langley, Virginia, Dec. 1992.
- [59] LUCIA, D. J. and BERAN, P. S., "Aeroelastic system development using proper orthogonal decomposition and volterra theory," No. AIAA 2003-1922, American Institute for Aeronautics and Astronautics, 2003.
- [60] LYMAN, V. and MORGENSTERN, J. M., "Calculated and measured pressure fields for an aircraft designed for sonic-boom alleviation," in *Proceedings of the 22nd Applied Aerodynamics Conference and Exhibit*, American Institute for Aeronautics and Astronautics, Aug. 2004.
- [61] M. VAZQUEZ, A. D. and KOOBUS, B., "Aerodynamical and sonic boom optimization of a supersonic aircraft," Tech. Rep. N 4250, INRIA, Sophia-Antipolis, France, 2002.
- [62] MACK, R. J., "A numerical method for evaluation and utilization of supersonic nacelle-wing interference," Tech. Rep. NASA TN D-5057, NASA Langley Research Center, Hampton, VA, Feb. 1969.
- [63] MACK, R. J., "A supersonic business-jet concept designed for low sonic boom," Tech. Rep. NASA/TM-2003-212435, NASA Langley Research Center, Hampton, VA, Oct. 2003.
- [64] MACK, R. J. and NEEDLEMAN, K. E., "A methodology for designing aircraft to low sonic boom constraints," Tech. Rep. NASA TM 4246, NASA Langley Research Center, Hampton, VA, Feb. 1991.
- [65] MAHFOUD, S. W., "Niching methods for genetic algorithms," Tech. Rep. 95001, Illinois Genetic Algorithms Laboratory, Urbana, Illinois, May 1995.
- [66] MASON, W. H., "Pre-cfd computational aerodynamics programs." [http://www.aoe.vt.edu/~mason/Mason\\_f/CAtxtAppD.html](http://www.aoe.vt.edu/~mason/Mason_f/CAtxtAppD.html), 2001.
- [67] MATHWORKS, T., "Neural network toolbox user's guide." <http://www.mathworks.com/access/helpdesk/help/toolbox/nnet/>, 2002.
- [68] MAVRIS, D. N. and DELAURENTIS, D., "Methodology for examining the simultaneous impact of requirements, vehicle characteristics, and technologies on military aircraft design," in *22nd Congress of the International Council on the Aeronautical Sciences*, ICAS, Aug. 2000.
- [69] MIDDLETON, W. D. and CARLSON, H. W., "A numerical method for calculating near-field sonic boom pressure signatures," Tech. Rep. TN D-3082, NASA Langley Research Center, Hampton, VA, July 1965.
- [70] MIDDLETON, W. D. and CARLSON, H. W., "Numerical method for estimation and optimizing supersonic aerodynamic characteristics of arbitrary planform wings," *Journal of Aircraft*, vol. 2, pp. 261–265, July 1965.

- [71] MIRANDA, E. and BAKER, "A generalized vortex lattice method for subsonic and supersonic flow applications," Tech. Rep. CR-2865, National Aeronautics and Space Administration, Langley, Virginia, Nov. 1977.
- [72] MORGENSTERN, J. M., "Tail-braced wing aircraft and configurations for achieving long supersonic range and low sonic boom," 2004.
- [73] MORGENSTERN, J. M., "Wind tunnel testing of a sonic boom minimized tail-braced wing transport configuration," in *Proceedings of the 10th AIAA/ISSMO Multidisciplinary Analysis and Optimization Conference*, American Institute for Aeronautics and Astronautics, Aug. 2004.
- [74] MORGENSTERN, J. M., "F-5 shaped sonic boom demonstrators persistence of boom shaping reduction through turbulence," in *Proceedings of the 43rd Aerospace Sciences Meeting and Exhibit*, American Institute for Aeronautics and Astronautics, Jan. 2005.
- [75] MORTENSON, M. E., *Geometric modeling*. Wiley Computer Publishing, second ed., 1997.
- [76] NADARAJAH, S., *The Discrete Adjoint Approach to Aerodynamic Shape Optimization*. PhD thesis, Stanford University, School of Aerospace Engineering, Stanford, CA, Jan. 2003.
- [77] NATALIA M. ALEXANDROV, R. M. L. E. A., "Optimization with variable-fidelity models applied to wing design," Tech. Rep. NASA/CR-1999-209826, ICASE Report No. 99-49, National Aeronautics and Space Administration, Langley, Virginia, Dec. 1999.
- [78] NOAA, "Radiosonde database access." <http://raob.fsl.noaa.gov/>, 2004.
- [79] PAGE, J. A. and PLOTKIN, K. J., "An efficient method for incorporating computational fluid dynamics into sonic boom prediction," in *Proceedings of the AIAA 9th Applied Aerodynamics Conference*, American Institute for Aeronautics and Astronautics, Sept. 1991.
- [80] PATRICIA A. KERR, R. E. S. and POSENAU, M.-A. K., "Geolab surface modeling and grid generation technology and services," Tech. Rep. NASA 95-CP3291, NASA Langley Research Center, Hampton, VA, May 1995.
- [81] PEDERSON, "Sonic boom technologies and challenges." [http://www.aee.faa.gov/noise/aee100\\_files/SonicWkshp/3-Panel12-Pederson-Lockheed.pdf](http://www.aee.faa.gov/noise/aee100_files/SonicWkshp/3-Panel12-Pederson-Lockheed.pdf), 2003.
- [82] PEI LI, R. S. and SOBIECZKY, H., "The sonic boom of an oblique flying wing sst," in *Proceedings of the First Joint CEAS/AIAA Aeroacoustics Conference*, American Institute for Aeronautics and Astronautics, June 1995.
- [83] PETER M. HARTWICH, BILLY A. BURROUGHS, J. S. and WILER, C. D., "Design development strategies and technology integration for supersonic aircraft of low perceived sonic boom," in *Proceedings of the 41st AIAA Aerospace Sciences Meeting and Exhibit*, American Institute for Aeronautics and Astronautics, Jan. 2003.

- [84] PIERCE, A. D., “Turbulence scales, rise times, caustics and the simulation of sonic boom propagation,” *NASA Conference publication 3335*, vol. 1, pp. 1–19, July 1995.
- [85] PIERCE, A. D. and MAGLIERI, D. J., “Effects of atmospheric irregularities on sonic boom propagation,” *Journal of Acoustical Society of America*, vol. 51, no. 2, pp. 702–721, 1972.
- [86] PLOTKIN, K. J., “Theoretical basis for finite difference extrapolation of sonic boom signatures,” *NASA Conference publication 3335*, vol. 1, pp. 54–67, July 1995.
- [87] PLOTKIN, K. J., “Pcboom3 sonic boom prediction model - version 1.0c,” Tech. Rep. AFRL-HE-WP-TR-2001-0155, Wyle Research laboratories, Arlington,VA, May 1996.
- [88] PLOTKIN, K. J., “State of the art of sonic boom modeling,” *Journal of Acoustical Society of America*, vol. 111, pp. 530–535, Jan. 2002.
- [89] POPINET, S., “Gnu triangulation surface library.” <http://gts.sourceforge.net>, 2004.
- [90] QUINN, M. J., *Parallel programming in C with MPI and OpenMP*. McGraw-Hill Publications, 2003.
- [91] RALLABHANDI, S. K. and MAVRIS, D. N., “An unstructured wave drag code for preliminary design of future supersonic aircraft,” in *Proceedings of the 33rd Fluid dynamics conference and exhibit*, American Institute for Aeronautics and Astronautics, June 2003.
- [92] RALLABHANDI, S. K. and MAVRIS, D. N., “Sonic boom modelling under atmospheric uncertainty,” in *Proceedings of the 10th AIAA/ISSMO Multidisciplinary Analysis and Optimization Conference*, American Institute for Aeronautics and Astronautics, Aug. 2004.
- [93] RALLABHANDI, S. K. and MAVRIS, D. N., “Sonic boom minimization using improved linearized tools and probabilistic propagation,” in *Proceedings of the 43rd Aerospace Sciences Meeting and Exhibit*, American Institute for Aeronautics and Astronautics, Jan. 2005.
- [94] RICHARD B. MILES, L. M. E. A., “Suppression of sonic boom by dynamic off-body energy addition and shape optimization,” in *Proceedings of the 40th AIAA Aerospace Sciences Meeting and Exhibit*, American Institute for Aeronautics and Astronautics, Jan. 2002.
- [95] ROBERT E. SMITH, MALCOLM I.G. BLOOR, M. J. W. and THOMAS, A. M., “Rapid airplane parametric input design,” in *Proceedings of the 12th AIAA Computational Fluid dynamics conference*, American Institute for Aeronautics and Astronautics, June 1995.
- [96] ROGERS, D. F., *An Introduction to NURBS With Historical Perspective*. Morgan Kaufmann Publishers, 2001.
- [97] ROMEU, J. L., “Anderson-darling: A goodness of fit test for small samples assumptions.” [http://rac.alionscience.com/pdf/A\\_DTest.pdf](http://rac.alionscience.com/pdf/A_DTest.pdf), 2003.

- [98] RUFFIN, S., "Nascart-gt." <http://www.ae.gatech.edu/~sruffin/nascart>, 2004.
- [99] SAI. <http://www.saiproject.com/about.htm>, 2004.
- [100] SAI. <http://www.saiproject.com/images/SonicBoomBackground.pdf>, 2004.
- [101] SAMAREH, J. A., "A novel shape parameterization approach," Tech. Rep. NASA TM-1999-209116, NASA Langley Research Center, Hampton, VA, May 1999.
- [102] SAMAREH, J. A., "Survey of shape parameterization techniques for high-fidelity multidisciplinary shape optimization," *AIAA Journal*, vol. 39, pp. 877–884, May 2001.
- [103] SASAKI, D. and OBAYASHI, S., "Low-boom design optimization for sst nacard-wing-fuselage configuration," in *Proceedings of the 16th AIAA Computational Fluid Dynamics Conference*, American Institute for Aeronautics and Astronautics, June 2003.
- [104] SEEBASS, R., "Minimum sonic boom shock strengths and overpressures," *AIAA Journal*, vol. 221, pp. 651–653, 1969.
- [105] SEEBASS, R. and GEORGE, A., "Sonic boom minimization," *Journal of Acoustical Society of America*, vol. 51, no. 2, pp. 686–694, 1972.
- [106] SEEBASS, R. and GEORGE, A., "Design and operation of aircraft to minimize their sonic boom," *Journal of aircraft*, vol. 11, no. 9, pp. 509–517, 1974.
- [107] SEEBASS, R., "Sonic boom theory," *Journal of Aircraft*, vol. 6, pp. 177–184, May 1969.
- [108] SEEBASS, R., "History and economics of, and prospect for, commercial supersonic transport," in *RTO AVT course on Fluid dynamics research on supersonic aircraft*, RTO, May 1998.
- [109] SEEBASS, R. and ARGROW, B., "Sonic boom minimization revisited," in *Proceedings of the 2nd Theoretical Fluid Mechanics Meeting*, American Institute for Aeronautics and Astronautics, June 1998.
- [110] SHEPHERD, K., "Human response to sonic booms-recent nasa research." <http://citeseer.ist.psu.edu/160468.html>, 1995.
- [111] SIMMONS, F. and FREUND, D., "Morphing concept for quiet supersonic jet boom mitigation," in *Proceedings of the 43rd AIAA Aerospace Sciences Meeting and Exhibit*, American Institute for Aeronautics and Astronautics, Jan. 2005.
- [112] SIMMONS, F. and FREUND, D., "Wing morphing for quiet supersonic jet performance - variable geometry design challenges for business jet utilization," in *Proceedings of the 43rd AIAA Aerospace Sciences Meeting and Exhibit*, American Institute for Aeronautics and Astronautics, Jan. 2005.
- [113] SIVA K. NADARAJAH, A. J. and ALONSO, J. J., "Sonic boom reduction using an adjoint method for wing-body configurations in supersonic flow," in *Proceedings of the 9th AIAA/ISSMO Symposium on Multidisciplinary analysis and Optimization Conference*, American Institute for Aeronautics and Astronautics, Sept. 2002.

- [114] SRINIVAS, N. and DEB, K., “Multiobjective optimization using nondominated sorting in genetic algorithms,” *Journal of Evolutionary Computation*, vol. 2, pp. 221–248, Jan. 1995.
- [115] STATIOS, “Reservoir modeling with gslib.” <http://www.statios.com/Resources/05-kriging.pdf>, 2004.
- [116] STEPHENS, M., “Edf statistics for goodness of fit and some comparisons,” *Journal of the American Statistical Association*, no. 69, pp. 730–737, 1974.
- [117] STEVENS, S., “Perceived level of noise by mark vii and decibels(e),” *Journal of the acoustical society of America*, vol. 51, no. 2, pp. 575–601, 1972.
- [118] SUKHOI, “Sukhoi ssbj.” <http://www.scac.ru/en/projects/ssbj/>, 2004.
- [119] SWARTZ, K. <http://gc.kls2.com/>, 2004.
- [120] THOMAS, C., “Extrapolation of sonic boom pressure signatures by the waveform parameter method,” Tech. Rep. NASA TN D-6832, NASA, June 1972.
- [121] TRAPP, J. and SOBIECZKY, H., “Interactive parametric geometry design,” Tech. Rep. AIAA-99-0829, DLR, German Aerospace Center, Gottingen, Germany, 1999.
- [122] VAN DEN BERG, “Introduction to parallel computing.” [www.nus.edu.sg/ACES/seminars/2001/ewout/ppt/Part2b.ppt](http://www.nus.edu.sg/ACES/seminars/2001/ewout/ppt/Part2b.ppt), 2001.
- [123] VANDERPLAATS, G. N., *Numerical optimization techniques for engineering design*. Vanderplaats research and development Inc., third ed., 1999.
- [124] VON GIERKE, H. and C.W.NIXON, “Human response to sonic boom in the laboratory and the community,” *Journal of Acoustical Society of America*, vol. 51, no. 2, pp. 766–782, 1972.
- [125] WALKDEN, F., “The shock pattern of a wing-body combination, far from the flight path,” *The Aeronautical Quarterly*, pp. 164–194, 1958.
- [126] WALLACE D. HAYES, R. C. H. and KULSRUD, H. E., “Sonic boom propagation in a stratified atmosphere with computer program,” Tech. Rep. NASA CR-1299, Aeronautical research associates of Princeton Inc., Princeton,NJ, Apr. 1969.
- [127] WARD, G. N., *Linearized theory of steady high-speed flow*. Cambridge Univ., 1955.
- [128] WARREN, C., “A significant single quatity that typifies a sonic bang,” *Journal of the acoustical society of America*, vol. 51, no. 1, pp. 418–420, 1972.
- [129] WHITHAM, G., “The flow pattern of a supersonic projectile,” *Communications on pure and applied mathematics*, vol. V, pp. 301–347, 1952.
- [130] WILLCOX, K. and PERAIRE, J., “Balanced model reduction via the proper orthogonal decomposition,” in *Proceedings of the 15th Computational Fluid Dynamics Conference*, American Institute for Aeronautics and Astronautics, June 2001.



- [131] WOLZ, R., “Recent supersonic vehicle studies at gulfstream aerospace.” [http://www.aee.faa.gov/noise/aee100\\_files/SonicWkshp/4-Panel2-WolzGulfstream.pdf](http://www.aee.faa.gov/noise/aee100_files/SonicWkshp/4-Panel2-WolzGulfstream.pdf), 2003.
- [132] WOLZ, R. R., “A summary of recent supersonic vehicle studies at gulfstream aerospace,” in *Proceedings of the 41st AIAA Aerospace Sciences Meeting and Exhibit*, American Institute for Aeronautics and Astronautics, Jan. 2003.
- [133] YOSHIDA, K., “Aerodynamic research for a second generation sst in japan including laminar flow control and low sonic boom design,” in *RTO AVT course on Fluid dynamics research on supersonic aircraft*, RTO, May 1998.
- [134] YOSHIKAZU MAKINO, KEN’ICHIRO SUZUKI, M. N. and YOSHIDA, K., “Non-axisymmetric fuselage shape modification for drag reduction of a low sonic-boom airplane,” in *Proceedings of the 41st AIAA Aerospace Sciences Meeting and Exhibit*, American Institute for Aeronautics and Astronautics, Jan. 2003.
- [135] YOSHIKAZU MAKINO, TAKASHI AOYAMA, T. I. E. A., “Numerical optimization of fuselage geometry to modify sonic-boom signature,” *Journal of aircraft*, vol. 36, no. 4, pp. 668–674, 1999.

## VITA

Sriram Rallabhandi was born on 26th September, 1978 in Guntur, India. He grew up in Hyderabad, India and completed his preliminary studies from St. Paul's High school in 1994. Sriram went to Indian Institute of Technology, Kanpur to pursue Bachelor of Technology in Aerospace Engineering.

After graduating with a Bachelors degree in May, 2000, Sriram enrolled at Georgia Institute of Technology for Master of Science in Aerospace Engineering. After successfully obtaining the Masters degree, he stayed on for his PhD.